

THE DEVELOPMENT OF NOVEL PROBES FOR OPTICAL ELASTOGRAPHY

Rowan William Sanderson
BSc, MPE



This Thesis is presented for the degree of
Doctor of Philosophy

of The University of Western Australia

Department of Electrical, Electronic & Computer Engineering
in the School of Engineering

2021

*In dedication to
William Mackellar Sanderson
Always close, despite the distance*

THESIS DECLARATION

I, Rowan William Sanderson, certify that:

This Thesis has been substantially accomplished during enrolment in this degree.

This Thesis does not contain material which has been submitted for the award of any other degree or diploma in my name, in any university or other tertiary institution.

In the future, no part of this Thesis will be used in a submission in my name, for any other degree or diploma in any university or other tertiary institution without the prior approval of The University of Western Australia and where applicable, any partner institution responsible for the joint-award of this degree.

This Thesis does not contain any material previously published or written by another person, except where due reference has been made in the text and in the Authorship Declaration that follows.

This Thesis does not violate or infringe any copyright, trademark, patent, or other rights whatsoever of any person.

The research involving human data reported in this Thesis was assessed and approved by The University of Western Australia Human Research Ethics Committee approval number: RA/4/1/5745. Written patient consent has been received and archived for the research involving patient data reported in this Thesis.

This Thesis contains published work and work prepared for publication, some of which has been co-authored.

Signature: 

Date: 31/08/2021

ABSTRACT

The mechanical properties of tissue are closely linked to function and pathology. From individual cells through to the whole organ scale, mechanical properties provide vital information related to the progression of disease throughout the body. The ability to resolve these mechanical properties has long been a focus of medical imaging, producing a wide array of diagnostic techniques that have been successfully translated into routine clinical use including ultrasound elastography and magnetic resonance elastography. While these techniques have demonstrated excellent diagnostic capabilities in several clinical applications, their resolution is limited to ~ 1 mm, preventing them from being deployed in other applications where disease manifests on a finer scale, such as the assessment residual tumour following breast-conserving surgery.

One potential solution is optical elastography, an emerging field describing several optical techniques that map the mechanical properties of soft tissue. Optical elastography utilises light to observe the local displacement in a sample under an applied load with micrometre-scale resolution. The relative tissue deformation is related to the tissue mechanical properties which can be reconstructed by applying an appropriate mechanical model. While optical elastography has been demonstrated in ophthalmology, oncology, and cardiology, as well as several other clinical applications, it is still a relatively new technique, as such, much of the work to date has focussed on technical developments and preliminary implementations on *ex vivo* tissue in laboratory conditions. These studies are crucial in the development of any optical imaging technology; however, further development is required to translate this research into a viable clinical tool, capable of improving patient outcomes. Medical imaging probes are a means to bridge this gap and translate research into clinical applications. These probes serve as a sample-system interface, providing the diagnostic benefits of medical imaging in a design that meets the specific needs of routine clinical use.

The work presented in this Thesis seeks to build on the significant technical developments in the field of optical elastography and translate this existing research into a format that could potentially be implemented in a clinical setting, through the development of novel optical elastography probes. Three optical elastography techniques, finger-mounted quantitative micro-elastography, camera-based optical palpation and smartphone-based optical palpation were developed towards applications of intraoperative breast margin assessments and burn scar assessments. Imaging probes which use these techniques were developed to suit the clinical requirements of the specific application. Preliminary demonstrations on tissue specimens were validated against existing gold standards, where

each imaging probe was able to accurately identify local mechanical contrast. These studies demonstrate the clinical viability of optical elastography imaging probes and provide a platform for future developments towards clinical translation.

CONTENTS

Thesis declaration	v
Abstract	vi
Contents	viii
List of figures	xii
List of tables	xvi
Acknowledgements	xvii
Authorship declaration	xviii
List of publications	xxi
List of acronyms	xxiv
Introduction	1
1.1 Research objectives	3
1.2 Thesis structure.....	3
Biomedical applications	6
2.1 Breast cancer	6
2.1.1 Breast cancer physiology.....	8
2.1.2 Breast cancer surgeries	12
2.1.3 Intraoperative tumour margin assessment tools	14
2.2 Burn scars	21
2.2.1 Burn wound repair process	22
2.2.2 Pathological burn scars	24
2.2.3 Burn scar treatment and management	26
2.2.4 Burn scar assessment tools	27
Optical elastography	34
3.1 Elastography.....	34
3.1.1 Ultrasound elastography	35
3.1.2 Magnetic resonance elastography	38
3.2 Optical elastography.....	40
3.2.1 Optical coherence elastography.....	40
3.2.2 Brillouin.....	41
3.2.3 Optical palpation.....	43
3.3 Continuum mechanics model of tissue deformation	45
3.3.1 Deformation	45
3.3.2 Infinitesimal stress and strain.....	46

3.3.3	Governing equations.....	49
3.3.4	Elastic moduli	51
3.3.5	First-order approximations in elastography.....	52
3.4	Other mechanical properties	53
3.5	Tissue elasticity.....	55
3.6	Mechanical model for optical elastography techniques in this Thesis	56
Optical coherence elastography		58
4.1	Optical coherence tomography.....	58
4.1.1	OCT imaging parameters	60
4.2	Optical coherence elastography	63
4.2.1	Measurement of displacement with OCT.....	63
4.2.2	OCE loading methods.....	64
4.3	Optical elastography techniques in this Thesis.....	66
4.3.1	Quantitative micro-elastography	67
4.3.2	OCT-based optical palpation.....	71
Clinical validation of optical elastography		74
5.1	Preface	74
5.2	Diagnostic accuracy of quantitative micro-elastography for margin assessment in breast-conserving surgery	75
5.2.1	Introduction	76
5.2.2	Patients and Methods.....	79
5.2.1	Histopathology and coregistration with imaging data.....	81
5.2.2	Reader study and statistical analysis.....	82
5.2.3	Results	85
5.2.4	Discussion	89
5.3	Optical palpation for tumour margin assessment in breast-conserving surgery	93
5.3.1	Introduction	94
5.3.2	Materials and methods.....	96
5.3.3	Discussion	106
Optical coherence elastography imaging probes		111
6.1	Preface	111
6.2	OCE imaging probes.....	112
6.2.1	Introduction	112
6.2.2	Bench-top imaging probes	114
6.2.2.1	Ophthalmic bench-top probes	115

6.2.2.2 Oncological bench-top probes.....	119
6.2.3 Handheld imaging probes.....	121
6.2.4 Endoscopic imaging probes	126
6.2.5 Other compact imaging probes	131
6.2.6 Conclusions.....	136
Finger-mounted quantitative micro-elastography	137
7.1 Preface.....	137
7.2 Finger-mounted quantitative micro-elastography.....	138
7.2.1 Introduction.....	138
7.2.2 Methods and materials	140
7.2.3 Results.....	144
7.2.4 Discussion.....	150
7.2.5 Conclusions.....	153
7.3 Breast tissue scanning	153
Camera-based optical palpation	156
8.1 Preface.....	156
8.2 Camera-based optical palpation	157
8.2.1 Introduction.....	158
8.2.2 Methods and materials	160
8.2.3 Results.....	169
8.2.4 Discussion.....	174
8.2.5 Conclusion	176
Smartphone-based optical palpation	178
9.1 Preface.....	178
9.2 Smartphone-based optical palpation: towards elastography of skin for telehealth applications.....	179
9.2.1 Introduction.....	180
9.2.2 Materials and methods	182
9.2.3 Results.....	189
9.2.4 Discussion.....	192
9.2.5 Conclusion	196
Conclusion and perspectives	197
10.1 Research contributions and significance.....	197
10.2 Study limitations and future work.....	199
10.3 Final remarks.....	203

LIST OF FIGURES

Figure 2.1: Chart showing the most commonly diagnosed cancers in Australia during 2020	7
Figure 2.2: Anatomy of the female breast	9
Figure 2.3: Stages of breast cancer development	11
Figure 2.4: Breast cancer surgical treatments	13
Figure 2.5: Illustration of breast cancer margins	14
Figure 2.6: Frozen section analysis procedure for tumour margin assessment	15
Figure 2.7: Imprint cytology for tumour margin assessment	16
Figure 2.8: Intraoperative specimen radiography of freshly excised breast specimen	17
Figure 2.9: Intraoperative OCT for breast cancer margin imaging	19
Figure 2.10: Classification of burn severity	22
Figure 2.11: The four stages of wound repair	23
Figure 2.12: Illustration of different types of skin scars	25
Figure 2.13: Example of compression garment worn by patient with severe burn scars on their left hand	26
Figure 2.14: Devices for measuring scar mechanical properties	30
Figure 2.15: Ultrasound elastography of a 14-month-old burn scar on the arm of a 23-year-old male patient	31
Figure 3.1: Shear wave USE of liver fibrosis on 21-day-old child	36
Figure 3.2: Representative image of strain USE performed on breast tissue	37
Figure 3.3: Stiffness maps obtained using MRE of five patients with non-alcoholic fatty liver disease at different stages of liver fibrosis	38
Figure 3.4: MRE images of two patients with meningiomas	39
Figure 3.5: Brillouin microscopy in cell mechanics and ophthalmology applications	41
Figure 3.6: Diagram of deformation	44
Figure 3.7: Stress and strain	46
Figure 3.8: Reported values and ranges of Young's modulus for selected tissues and tissue constituents	54
Figure 4.1: Conventional OCT scan modes	57
Figure 4.2: Diagram of a TD-OCT system	58
Figure 4.3: Diagram of an SD-OCT system	58

Figure 4.4: Diagram of OCT imaging parameters for a Gaussian beam.....	60
Figure 4.5: Diagrams of common OCE loading methods	64
Figure 4.6: Diagram of displacement and strain measured in compression OCE.....	67
Figure 4.7: Methodology for QME.....	68
Figure 4.8: OCT, strain OCE and QME of a freshly excised mastectomy specimen containing invasive ductal carcinoma	69
Figure 4.9: Optical palpation working principle	70
Figure 4.10: Optical palpation of breast-conserving surgery specimen with a margin involved by invasive tumour	71
Figure 5.1: Reader criteria for determining presence of cancer	81
Figure 5.2: Examples images of benign breast tissues	84
Figure 5.3: Example images of invasive ductal carcinoma.....	85
Figure 5.4: Example images of ductal carcinoma in situ (DCIS) and mucinous carcinoma.....	86
Figure 5.5: Optical palpation working principle	97
Figure 5.6: Optical palpation in adipose tissue	98
Figure 5.7: Flowcharts illustrating the classifier algorithm and the classifier parameter optimisation procedure used to determine the optimum circle diameter and stress threshold	99
Figure 5.8: Examples of optical palpation images	100
Figure 5.9: Boxplots showing the distribution of average stress in regions with tumour ≥ 1 mm from the surface or absent compared to regions with tumour < 1 mm from the surface	102
Figure 5.10: AUC plots used to determine the optimum circle diameter and ROC curves with maximum AUC used to determine the optimum stress threshold, sensitivity and specificity.....	102
Figure 6.1: Examples of bench-top OCE imaging probes	113
Figure 6.2: Schematic diagrams of bench-top OCE imaging probes for use in ophthalmology	114
Figure 6.3: Photograph and schematic diagrams of ophthalmic bench-top OCE imaging probes.....	116
Figure 6.4: Overview of handheld OCE imaging probes.....	120
Figure 6.5: Standard unidirectional and custom bidirectional scan patterns	124
Figure 6.6: Examples of endoscopic OCE imaging probes.....	125
Figure 6.7: Schematic diagrams of optical designs used in side-facing and forward- facing endoscopic OCE imaging probes.....	126

Figure 6.8: Comparison of images produced by a radially scanning endoscopic OCE imaging probe and raster scanning endoscopic OCE imaging probe .	129
Figure 6.9: Compact OCE imaging probe optical designs	131
Figure 6.10: Method for the measurement of tissue displacement in forward-facing needle OCE imaging probes	133
Figure 6.11: Images acquired by finger-mounted OCE imaging probe	134
Figure 7.1: Finger-mounted QME probe	139
Figure 7.2: 1-D Finger-mounted QME scans.....	141
Figure 7.3: Finger-mounted QME filtering scheme used to reduce hand motion artifacts.....	142
Figure 7.4: Mean tangent moduli measured in five homogeneous phantoms of varying elasticity compared to expected values measured with uniaxial compression.....	143
Figure 7.5: Finger-mounted QME on a bi-layer phantom	145
Figure 7.6: Finger-mounted QME of kangaroo muscle.....	146
Figure 7.7: 2-D finger-mounted QME scan over silicone inclusion phantom.....	148
Figure 7.8: Preliminary 2-D finger-mounted QME scan over freshly excised human breast tissue.....	152
Figure 8.1: Fabrication process of micro-porous silicone layers.....	160
Figure 8.2: Working principle of CBOP.....	161
Figure 8.3: Layer characterisation and generation of optical palpograms	164
Figure 8.4: Photographs and optical palpograms for four different-sized inclusion phantoms.....	167
Figure 8.5: Analysis of the lateral resolutions of CBOP and OCT-based optical palpation.....	170
Figure 8.6: CBOP performed on two freshly excised mastectomy specimens.....	172
Figure 9.1: Diagram of the SBOP system.....	181
Figure 9.2: Working principle of SBOP	182
Figure 9.3: Histograms of colour channels captured from photographs of the layers under uniform increments of compressive strain	184
Figure 9.4: Optical palpogram and characterisation of SBOP	185
Figure 9.5: Comparison of mounted and freehand SBOP images	188
Figure 9.6: Photograph and optical palpogram of the unscarred site	189
Figure 9.7: Photograph and optical palpogram of a burn scar located on the back of the right hand.....	190

Figure 9.8: Photograph and optical palpogram of a burn scar located on the right
forearm..... 190

LIST OF TABLES

Table 2.1: Classification of breast cancer stages	10
Table 2.2: POSAS Observer scale.	27
Table 2.3: POSAS Patient scale.....	28
Table 5.1: BCS patient and clinical specimen characteristics	78
Table 5.2: Summary of regions of interest included in study.	83
Table 5.3: Reader study results.....	87
Table 5.4: Optimum diagnostic accuracies and classifier parameters.....	104
Table 6.1: Summary of OCE imaging probes and relevant applications.	112
Table 6.2: Summary of handheld OCE imaging probes.....	121
Table 6.3: Summary of several endoscopic OCE imaging probes.....	125

ACKNOWLEDGEMENTS

This Thesis has been one of the most challenging yet rewarding experiences in my life and has only been made possible by the support of so many people. Firstly, I would like to thank my supervisors, Brendan Kennedy, Qi Fang and Andrea Curatolo, whose continual support and guidance have motivated me throughout my research. Brendan, thank you for all your valuable lessons in optics and elastography and for helping me develop as a researcher. I'm incredibly grateful for all the support you've provided throughout my PhD and for the opportunity to undertake such a fulfilling project. Qi, for your patience, wisdom, and calmness which has helped me overcome seemingly insurmountable challenges. Andrea, for your drive and enthusiasm which inspires me to keep working in the lab well after everyone else has gone home.

To everyone in BRITElab, I would like to thank you for your support and encouragement. It has been an honour to have been a part of such a wonderful group of people who are so generous with their time and knowledge. Thanks to Wes, the founding father of the BRITElab biathletes, for teaching me the art of phantom making and LabView. Lixin, for guiding me when writing codes and fixing the Git repository every time I crashed it. Philip, for all your help and support when I was first starting out and for your appreciation of colour maps. Ken and Leo for the many informative discussions and for always having positive attitudes. In particular, I'd like to acknowledge my PhD brother, Matt. The last four years have been incredible fulfilling and I am privileged to have gone through the PhD experience with you. Your determination and perseverance always inspired me to overcome the challenging moments during the PhD. Thanks to all the enthusiastic students I've had the opportunity to work with during my PhD.

Thanks to the support of the War Widows' Guild of Western Australia Top-up Scholarship for Research into Breast Cancer and travel funding from the UWA Graduate Research School. This research was supported by an Australian Government Research Training Program (RTP) Scholarship. I'd also like to acknowledge all our collaborators and colleagues, who provide knowledge and insight which enriches our research.

Thanks to my friends and family for all your support. Thanks for the countless hours you've spent listening to me talk about my Thesis and for all of your help along the way.

Finally, and most importantly, thank you Róisín. From the bottom of my heart, thank you for all that you've done and sacrificed to allow me to complete my Thesis. Your immeasurable kindness and encouragement motivates me, and without you, this Thesis would not be possible.

AUTHORSHIP DECLARATION

This Thesis contains the results of the research that I, Rowan William Sanderson, performed within the Department of Electrical, Electronic, and Computer Engineering in the School of Engineering at The University of Western Australia, between August 2017 and September 2021.

Sections 6.2, 7.2, 8.2, and 9.2 of this Thesis are reproductions of four first-authored publications, and Chapters 5.2 and 5.3 are reproductions are co-authored publications modified only in formatting. This Thesis was prepared in accordance with The University of Western Australia's guidelines on "Thesis as a series of papers" (<http://www.postgraduate.uwa.edu.au/students/thesis/series>, Accessed: March 2021). I am the sole author of the remainder of this document.

The details of the included publications and the locations where they appear are stated below. Publications are listed in the order in which they appear in the Thesis.

1. Kelsey M. Kennedy, Renate Zilkens, Wes M. Allen, Ken Y. Foo, Qi Fang, Lixin Chin, **Rowan W. Sanderson (10%)**, James Anstie, Philip Wijesinghe, Andrea Curatolo, Hsern Ern I. Tan, Narelle Morin, Bindu Kunjuraman, Chris Yeomans, Synn Lynn Chin, Helen DeJong, Katharine Giles, Benjamin F. Dessauvague, Bruce Latham, Christobel M. Saunders, Lixin Chin, and Brendan F. Kennedy, "*Diagnostic accuracy of quantitative micro-elastography for margin assessment in breast-conserving surgery*," *Cancer Research*, 80(8): p. 17731783, 2020.

Chapter 5.2. RWS is a co-author of this article. RWS performed imaging of the tissue specimens used in this work, processed the acquired data, performed imaging of prepared histology slides, and revised and edited the manuscript.

2. Ken Y. Foo, Kelsey M. Kennedy, Renate Zilkens, Wes M. Allen, Qi Fang, **Rowan W. Sanderson (10%)**, James Anstie, Benjamin F. Dessauvague, Bruce Latham, Christobel M. Saunders, Lixin Chin, and Brendan F. Kennedy, "*Optical palpation for tumour margin assessment in breast-conserving surgery*," *Biomedical Optics Express*, 12(3): p. 1666-1682, 2021.

Chapter 5.3. RWS is a co-author of this article. RWS performed imaging of the tissue specimens used in this work, processed the acquired data, performed imaging of prepared histology slides, and revised and edited the manuscript.

3. **Rowan W. Sanderson (70%)**, Qi Fang, Andrea Curatolo, and Brendan F. Kennedy, “*Optical coherence elastography imaging probes*,” in Brendan F. Kennedy (Ed.), *Optical Coherence Elastography: Imaging Tissue Mechanics on the Micro-Scale*, AIP, (to be published October 2021).

Chapter 6.2. RWS is the principal author of this article. RWS performed the literature review, adapted, performed imaging of prepared histology slides, and generated the figures used and led the writing of this manuscript which was reviewed and edited by all authors.

4. **Rowan W. Sanderson (70%)**, Andrea Curatolo, Philip Wijesinghe, Lixin Chin, and Brendan F. Kennedy, “*Finger-mounted quantitative micro-elastography*,” *Biomedical Optics Express*, 10(4): p. 1760-1773, 2019.

Chapter 7.2. RWS is the principal author of this article. RWS designed and built the probes used in this work; fabricated and characterised the testing phantoms; performed the experiments; and led the writing of the manuscript which was reviewed and edited by all authors.

5. **Rowan W. Sanderson (70%)**, Qi Fang, Andrea Curatolo, Wayne Adams, Devina D. Lakhiani, Hina M. Ismail, Ken Y. Foo, Benjamin F. Dessauvague, Bruce Latham, Chris Yeomans, Christobel M. Saunders, and Brendan F. Kennedy. “*Camera-based optical palpation*,” *Scientific Reports*, 10(1): pp. 1-13, 2020.

Chapter 8.2. RWS is the principal author of this article. RWS along with QF and BFK conceived and developed the methodology; RWS designed and built the imaging system; fabricated and characterised the testing phantoms; fabricated and characterised the porous stress layers; wrote the processing code; performed experiments on both silicon phantoms and freshly excised breast tissue; and led the writing of the manuscript which was reviewed and edited by all authors.

6. **Rowan W. Sanderson (80%)**, Qi Fang, Andrea Curatolo, Aiden Taba, Helen M. DeJong, Fiona M. Wood, and Brendan F. Kennedy. “*Smartphone-based optical palpation: towards elastography of skin for telehealth applications*,” *Biomedical Optics Express*, 12(6): p. 3117-3132, 2021.

Chapter 9.2. RWS is the principal author of this article. RWS designed and constructed the imaging system used in this work, including 3-D modelling and 3-D printing of key components; fabricated and characterised the silicone phantoms and porous stress layers; performed testing on phantoms; wrote the processing code; and led the writing of the manuscript which was reviewed and edited by all authors.

Student signature:



Date: 31/08/2021

I, Brendan Kennedy, certify that the student statements regarding their contribution to each of the works listed above are correct.

As all co-authors' signatures could not be obtained, I hereby authorise inclusion of the co-authored work in this Thesis.

Coordinating supervisor's signature:



Date:

31st August 2021

LIST OF PUBLICATIONS

Fully refereed journal articles

1. <Under Review> Peijun Gong, Synn Lynn Chin, Wes M. Allen, Helen Ballal, James D. Anstie, Lixin Chin, Hina M. Ismail, Renate Zilkens, Devina D. Lakhiani, Matthew McCarthy, Qi Fang, Daniel Firth, Kyle Newman, Caleb Thomas, Jiayue Li, **Rowan W. Sanderson**, Ken Y. Foo, Chris Yeomans, Benjamin F. Dessauvague, Bruce Latham, Christobel M. Saunders, and Brendan F. Kennedy, “*In vivo detection of residual cancer in the surgical cavity during breast-conserving surgery using quantitative micro-elastography*,” Cancer Research, 2022.
2. Evelyn Collier, Brooke Maitland, **Rowan W. Sanderson**, Behzad Shiroud Heidari, Christopher Lamb, Matt S. Hepburn, Paul D. Dalton, Qi Fang, Elena M. De-Juan-Pardo & Brendan F. Kennedy. “*In Situ Characterization of Melt Electrowritten Scaffolds in 3D Using Optical Coherence Tomography*,” Advanced Photonics Research, 2022.
3. **Rowan W. Sanderson**, Qi Fang, Andrea Curatolo, Aiden Taba, Helen M. DeJong, Fiona M. Wood, and Brendan F. Kennedy. “*Smartphone-based optical palpation: towards elastography of skin for telehealth applications*,” Biomedical Optics Express, 12(6): p. 3117-3132, 2021.
4. Ken Y. Foo, Kelsey M. Kennedy, Renate Zilkens, Wes M. Allen, Qi Fang, **Rowan W. Sanderson**, James Anstie, Benjamin F. Dessauvague, Bruce Latham, Christobel M. Saunders, Lixin Chin, Brendan F. Kennedy, “*Optical palpation for tumour margin assessment in breast-conserving surgery*,” Biomedical Optics Express, 12(3): p. 1666-1682, 2021.
5. **Rowan W. Sanderson**, Qi Fang, Andrea Curatolo, Wayne Adams, Devina D. Lakhiani, Hina M. Ismail, Ken Y. Foo, Benjamin F. Dessauvague, Bruce Latham, Chris Yeomans, Christobel M. Saunders, and Brendan F. Kennedy. “*Camera-based optical palpation*,” Scientific Reports, 10(1): p. 1-13, 2020.
6. Helen M. DeJong, Steven Abbott, Marilyn Zelesco, Katrina Spilsbury, Lisa Martin, **Rowan W. Sanderson**, Melanie Ziman, Brendan F. Kennedy, and Fiona M. Wood, “*A novel, reliable protocol to objectively assess scar stiffness using shear wave elastography*,” Ultrasound in Medicine & Biology, 46(7): p. 1614-1629, 2020.
7. Ken Y. Foo, Lixin Chin, Renate Zilkens, Devina D. Lakhiani, Qi Fang, **Rowan W. Sanderson**, Benjamin F. Dessauvague, Bruce Latham, Sally McLaren, Christobel M. Saunders, Brendan F. Kennedy, “*Three-dimensional mapping of the attenuation coefficient in*

- optical coherence tomography to enhance breast tissue microarchitecture contrast,”* Journal of Biophotonics, 13(6): p. e201960201, 2020.
8. Qi Fang, Luke Frewer, Renate Zilkens, Brooke Krajancich, Andrea Curatolo, Lixin Chin, Ken Y. Foo, Devina D. Lakhiani, **Rowan W. Sanderson**, Philip Wijesinghe, James D. Anstie, Benjamin F. Dessauvague, Bruce Latham, Christobel M. Saunders, Brendan F. Kennedy, “*Handheld volumetric manual compression-based quantitative microelastography,*” Journal of Biophotonics, 13(6): p. e201960196, 2020.
 9. Kelsey M. Kennedy, Renate Zilkens, Wes M. Allen, Ken Y. Foo, Qi Fang, Lixin Chin, **Rowan W. Sanderson**, James Anstie, Philip Wijesinghe, Andrea Curatolo, Hsien Ern I. Tan, Narelle Morin, Bindu Kunjuraman, Chris Yeomans, Synn Lynn Chin, Helen M. DeJong, Katharine Giles, Benjamin F. Dessauvague, Bruce Latham, Christobel M. Saunders, Brendan F. Kennedy, “*Diagnostic accuracy of quantitative micro-elastography for margin assessment in breast-conserving surgery,*” Cancer Research, 80(8): p. 1773-1783, 2020.
 10. Luke G. Major, Andrew W. Holle, Jennifer L. Young, Matt S. Hepburn, Kwanghee Jeong, Ian L. Chin, **Rowan W. Sanderson**, Ji Hoon Jeong, Zachary M. Aman, Brendan F. Kennedy, Yongsung Hwang, Dong-Wook Han, Hyun Woo Park, Kun-Liang Guan, Joachim P. Spatz, Yu Suk Choi, “*Volume adaptation controls stem cell mechanotransduction,*” ACS Applied Materials & Interfaces, 11(49): p. 45520-45530, 2019.
 11. **Rowan W. Sanderson**, Andrea Curatolo, Philip Wijesinghe, Lixin Chin, and Brendan F. Kennedy, “*Finger-mounted quantitative micro-elastography,*” Biomedical Optics Express, 10(4): p. 1760-1773, 2019.

Book chapters

1. **Rowan W. Sanderson**, Qi Fang, Andrea Curatolo, and Brendan F. Kennedy, “*Optical coherence elastography imaging probes,*” in Brendan F. Kennedy (Ed.), Optical Coherence Elastography: Imaging Tissue Mechanics on the Micro-Scale, AIP, 2021.

Conference presentations

1. **Rowan W. Sanderson**, Qi Fang, Andrea Curatolo, Wayne Adams, Devina D. Lakhiani, Hina M. Ismail, Ken Y. Foo, Benjamin F. Dessauvague, Bruce Latham, Chris Yeomans, Christobel M. Saunders, and Brendan F. Kennedy, “*Camera-based optical palpation towards in vivo breast cancer assessment,*” International Tissue Elasticity Conference, Virtual, 13-16 September, 2020.
2. Qi Fang, Luke Frewer, Renate Zilkens, Brooke Krajancich, Andrea Curatolo, Lixin Chin, Ken Y. Foo, Devina D. Lakhiani, **Rowan W. Sanderson**, Philip Wijesinghe,

James D. Anstie, Benjamin F. Dessauvage, Bruce Latham, Christobel M. Saunders, and Brendan F. Kennedy, “*Comparison between two handheld quantitative micro elastography methods,*” SPIE Photonics West, Optical Elastography and Tissue Biomechanics VII, San Francisco, California 1-6 February 2020.

3. **Rowan W. Sanderson**, Andrea Curatolo, Philip Wijesinghe, Lixin Chin, and Brendan F. Kennedy, “*Development of a novel palpation-mimicking probe for optical coherence elastography,*” SPIE Photonics West, Optical Elastography and Tissue Biomechanics VI, San Francisco, California 2-7 February 2019.
4. Kelsey M. Kennedy, Wes M. Allen, Renate Zilkens, Ken Y. Foo, Qi Fang, Lixin Chin, **Rowan W. Sanderson**, James D. Anstie, Synn Lynn Chin, Benjamin F. Dessauvage, Bruce Latham, Christobel M. Saunders, and Brendan F. Kennedy, “*An assessment of OCT plus micro-elastography for detection of close tumour margins following breast-conserving surgery,*” SPIE Photonics West, Diseases in the Breast and Reproductive System V, San Francisco, California 2-7 February 2019.
5. **Rowan W. Sanderson**, Andrea Curatolo, Philip Wijesinghe, Lixin Chin, and Brendan F. Kennedy, “*Towards a smart surgical glove for the intraoperative detection of breast cancer,*” Australian Conference on Optical Fibre Technology, Perth, 9-13 December 2018.

Other publications

1. **Rowan W. Sanderson**, Andrea Curatolo, Philip Wijesinghe, Lixin Chin, and Brendan F. Kennedy, “*Finger-Mounted Optical Probe Designed to Improve Breast Cancer Removal,*” Optical Society News (OSA), March 2019.

LIST OF ACRONYMS

Acronym	Definition
2-D	Two-dimensional
3-D	Three-dimensional
CBOP	Camera-based optical palpation
CNR	Contrast-to-noise ratio
DCIS	Ductal carcinoma <i>in situ</i>
FEA	Finite element analysis
FWHM	Full-width-at-half-maximum
GRIN	Graded index fibre
IDC	Invasive ductal carcinoma
ILC	Invasive lobular carcinoma
LCIS	Lobular carcinoma <i>in situ</i>
LED	Light-emitting diode
OCE	Optical coherence elastography
OCT	Optical coherence tomography
PDMS	Polydimethylsiloxane
POSAS	Patient and observer scar assessment scale
QME	Quantitative micro-elastography
SBOP	Smartphone-based optical palpation
SMF	Single-mode fibre
SNR	Signal-to-noise ratio
UCT	Uniaxial compression test

CHAPTER 1

INTRODUCTION

For centuries, it has been known that the onset of various diseases is accompanied by physiological changes to the affected tissue's mechanical properties [1]. These changes often result in the tissue becoming stiffer than the surrounding unaffected tissue and serve as a biomarker for disease progression. For example, cancers often present as stiff masses [2]; pathological burn scars cause the surrounding skin to stiffen and contract [3]; and fibrotic livers also exhibit increased stiffness [4]. In order to localise and map the progression of such diseases, physicians seek to identify this contrast in mechanical properties, often via manual palpation of the affected tissue. Manual palpation is ubiquitous throughout diagnostic applications owing to the dexterity afforded to the user and its ease of use [5–8]. However, it is limited by inherent subjectivity and relatively low spatial resolution, on the order of 1-3 mm [9,10]. This can lead to negative consequences ranging from incorrectly prescribed treatments to residual tumour remaining undetected inside a surgical cavity following excision of a cancerous mass.

A variety of diagnostic methods have been developed to better understand and localise disease progression. One particular branch of medical imaging that draws parallels to manual palpation is elastography, a family of techniques that use imaging devices to map the mechanical properties of disease. Similar to manual palpation, elastography also aims to detect mechanical contrast brought about by disease, through the application of some external force to disturb the tissue and an imaging modality to detect the reaction of the tissue [11]. Elastography can produce quantitative 3-D images of tissue mechanical properties and in some instances, at a higher spatial resolution than manual palpation. The images produced by elastography, commonly referred to as elastograms, visualise the stiffness of the imaged tissue and aid in the detection of disease. Initially based on ultrasound (US) [11] and magnetic resonance imaging (MRI) [12], elastography has undergone significant development over the last three decades, so much so that it is now commercially available for applications in oncology and hepatology [13,14].

The spatial resolution of elastography is largely determined by the underlying imaging modality used. In the case of US elastography (USE) and magnetic resonance elastography

(MRE), this is typically 100s μm and 1-3 mm, respectively. While USE and MRE can generate images over centimetre to whole-body depths, making them well suited to screening and imaging large structures on the organ scale, higher resolution is often required for localisation and mapping disease progression. At the other end of the resolution scale, imaging techniques such as atomic force microscopy (AFM) [15], optical tweezers [16] and micropipette aspiration [17] interrogate mechanical properties on the cellular scale. However, these techniques are almost exclusively laboratory-based rather than clinical, due to the very limited scanning range and their incompatibility with compact, practical imaging probes.

Optical elastography is a relatively new set of elastography techniques which have the potential to bridge the gap between the more established USE and MRE, and those imaging techniques on the cellular scale through the use of optics. Initially proposed by Schmitt [18] and Jacques *et al.* [19] independently in 1998, optical elastography offers several distinct advantages over the more established elastography approaches of USE and MRE, namely, faster image acquisition rates, higher spatial resolution, increased sensitivity, and the potential for incorporation in compact imaging probes. However, optical elastography techniques are not without their own limitations, as optical imaging is typically limited to either surface measurements or shallow imaging depths of 1-2 mm. Despite this, optical elastography is capable of imaging on the intermediate scale between organs and cells [20,21], making it highly advantageous for detecting diseases which manifest on this scale as well as mapping the progression of diseases over time.

While optical elastography is a broad field and describes several different techniques such as optical coherence elastography (OCE) [22], Brillouin microscopy [23], laser speckle elastography [24] and digital holography-based elastography [25], it is OCE and Brillouin microscopy which have undergone the most development to date. OCE makes use of the micrometre-scale resolution and nanometre-scale displacement sensitivity of optical coherence tomography (OCT) to map tissue mechanical properties through a variety of external loading methods such as compression and acoustic radiation force [21]. Brillouin microscopy, in contrast, employs confocal microscopy to measure the Brillouin frequency shift created by vibrations of phonons in the tissue. The local longitudinal (bulk) modulus of the tissue is obtained from this frequency shift and is related to elasticity under simplifying assumptions [23,26].

Both techniques have undergone significant development towards clinical applications and several diagnostic probe prototypes have been proposed. These probes, designed for applications in endoscopy [27], tumour margin assessment [28] and dermatology [29], represent the clinical translation of laboratory-based techniques and hold potential for improving the future outcomes of healthcare for patients. Despite the ability of OCE and

Brillouin microscopy probes to rapidly image tissue mechanical properties at high resolution, these techniques predominantly rely on expensive and bulky optical components which restrict them to niche applications. Furthermore, the high cost of these systems makes them prohibitive in developing and low-resource scenarios. In addition, optical devices are commonly complex in design and require a high level of expertise to operate, further restricting the potential adoption of these probes.

This Thesis will investigate novel optical elastography probes which seek to overcome the limitations of existing probes, specifically, ease-of use, cost and size.

1.1 RESEARCH OBJECTIVES

This Thesis aims to develop novel imaging probes towards the translation of optical elastography from a laboratory-based tool to broader clinical and biological applications. To achieve these research objectives, the Thesis investigates the following three projects:

1. Development of a finger-mounted quantitative micro-elastography (QME) device for breast cancer detection which aims to improve on the existing clinical practice of manual palpation by augmenting it with the diagnostic ability of QME; This capability would preserve the clinical workflow during surgery, potentially increasing the clinical adoption of this technique as an intraoperative margin assessment tool.
2. Development of a low-cost optical elastography technique using a digital camera and porous silicone layer for the detection of breast cancer. This would create a new platform for optical elastography, with the potential to provide high-resolution elastography to low-resource and remote settings.
3. Incorporation of camera-based optical palpation into a smartphone device for the identification of pathological burn scars in a compact and portable device. This would enable optical elastography to be performed in telehealth applications, improving the standard of care in remote and rural burns patients.

1.2 THESIS STRUCTURE

The Thesis is structured in two broad Sections. The first half provides the reader with a thorough background of the biomedical applications relevant to the research in this Thesis, before providing an overview of the principles of optical elastography with a focus of OCE, QME and optical palpation. The second half presents a clinical validation of QME and optical palpation before providing a comprehensive review of the development of OCE imaging probes to date. The three research objectives stated above are then described before

providing final conclusions and perspectives. The detailed structure of the Thesis is as following:

Chapter 2 – Biomedical applications

The novel optical elastography probes developed in this Thesis, have been designed with two main biomedical applications in mind: the intraoperative detection of tumour margins in breast-conserving surgery and the assessment of pathological burn scars. These two clinical applications are presented in detail in this Chapter. The prevalence, risk factors and mortality of these applications are presented as well as the existing clinical assessment techniques to provide the reader with a comprehensive overview of the current state of each application and the existing limitations that can be overcome with the implementation of novel optical elastography probes.

Chapter 3 – Optical elastography

This Chapter presents the field of elastography, detailing several key studies in ultrasound elastography and magnetic resonance elastography before introducing optical elastography and the techniques of OCE, Brillouin microscopy and optical palpation. The mechanical model used in elastography, based on the principles of continuum mechanics, is described. An explanation of the stress and strain tensors is provided followed by an analysis of the simplifying assumptions used within elastography to reduce the complexity of the constitutive equation which describes elastic moduli. The Chapter concludes with an explanation of how the mechanical model is implemented in the optical elastography techniques described in this Thesis to generate images of mechanical contrast.

Chapter 4 – Optical coherence elastography

The principles of OCE are presented here along with an explanation of how displacement can be measured using OCT with a focus on compression OCE, due to its relevance within this Thesis. In addition, this Chapter also gives an in-depth description of QME and optical palpation techniques.

Chapter 5 – Validation of optical elastography techniques

Clinical validation of optical elastography is presented in this Chapter, showcasing the potential diagnostic value of these techniques. The first half of this Chapter describes the diagnostic accuracy of QME for detecting tumour in freshly excised breast specimens. The second half of the Chapter presents the diagnostic accuracy of optical palpation from the same set of breast specimens. This Chapter confirms the clinical validity of both QME and optical palpation and suggests the value in developed imaging probes using both these techniques.

Chapter 6 – Current state of optical coherence elastography probes

In this Chapter, an overview of the current state of OCE probes is presented. A framework is developed for comparing these probes, focusing specifically on optical imaging, loading mechanisms, image acquisition and signal processing methods.

Chapter 7 – Finger-mounted quantitative micro-elastography

In this Chapter, the development of a finger-mounted QME probe is presented. This probe represents a miniaturised optical imaging device and mimics the existing clinical practice of manual palpation. The results presented in this Chapter demonstrate that QME can be adapted to small imaging probes and that mechanical contrast can be accurately detected by a simplified 1-D M-mode scanning probe without the need for costly and bulky scanning mirrors or mechanical actuators. In addition, a methodology for acquiring 2-D elastograms is described which uses the natural motion of the finger to compress as well as scan the tissue, akin to manual palpation.

Chapter 8 – Camera-based optical palpation

In this Chapter, a new novel optical elastography technique is presented. The results demonstrate that optical palpation can be performed using a cost-effective digital camera, while still providing similar spatial resolution and mechanical contrast to conventional OCT-based optical palpation. This Chapter provides a detailed explanation of the working principle of camera-based optical palpation as well as validation of experimental results against FEA simulations for silicone phantoms and histopathology for breast tissue specimens.

Chapter 9 – Smartphone-based optical palpation: towards tactile imaging of skin for telehealth applications

In this Chapter, CBOP is adapted to a smartphone to enable wireless, remote optical palpation for telehealth applications. This development represents the first implementation of smartphone-based elastography and expands optical elastography from a predominantly laboratory-based technique to broader clinical applications, namely, the characterisation of pathological burn scars.

Chapter 10 – Conclusions and perspectives

The final Chapter in this Thesis summarises the developments and limitations presented previously and how this work can impact the field of optical elastography in the future.

CHAPTER 2

BIOMEDICAL APPLICATIONS

Optical elastography has been widely applied to biomedical applications, *e.g.*, ophthalmology, oncology and cell mechanics. Optical elastography utilises the principle that disease often alters the mechanical properties of tissue to detect and localise disease pathways based on mechanical contrast. In the context of this Thesis, optical elastography has been developed mainly for applications in the intraoperative assessment of tumour margins in breast-conserving surgery and pathological burn scars. This Chapter provides a comprehensive overview of both applications, focusing on the current problems and existing techniques that are used to assess breast tumour margins and to characterise pathological burn scars.

2.1 BREAST CANCER

Breast cancer is the most common type of cancer in women and affects approximately one in eight females over the course of an 85-year lifespan. It is responsible for 11.7% of all newly diagnosed cancers and in 2020, there were 2.3 million new diagnoses globally [30]. Recently, global incidence of breast cancer has been steadily increasing by 1-3% each year, for a number of reasons, including increased obesity and reduced physical activity. In addition, increased screening procedures are likely to have resulted in many previously unidentified cases being detected [31]. In Australia, it is estimated that there will be 20,825 newly diagnosed cases of breast cancer in 2021, at a rate of 57 diagnoses each day [32]. Figure 2.1 shows that breast cancer was the most commonly diagnosed cancer amongst the Australian population during 2020.

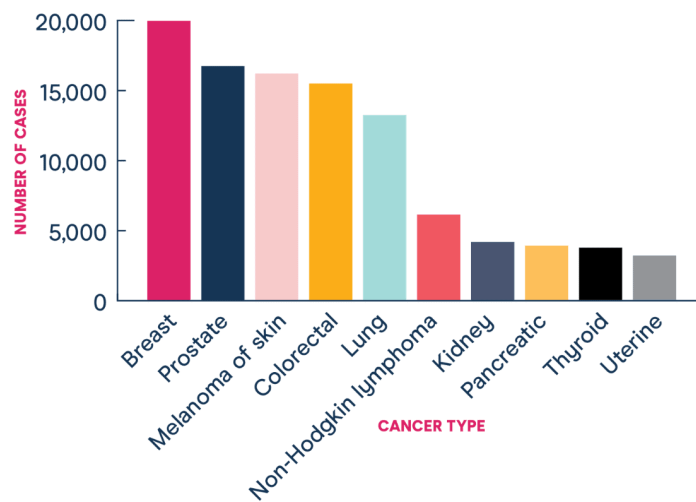


Figure 2.1: Chart showing the most commonly diagnosed cancers in Australia during 2020. Copyright © 2021 National Breast Cancer Foundation.

The most common risk factors associated with breast cancer include, age, geographical location, endogenous and exogenous female hormone exposure, lifestyle factors, family history and inherited genetic mutations [33]. Age is widely considered to be the most significant risk factor as the incidence of breast cancer doubles almost every 10 years from adulthood until menopause, when the rate of increase in incidence reduces significantly [34]. As a result, breast cancer incidence is highest in women aged over 50, with ~80% of all breast cancer diagnoses occurring in this age range [33]. Breast cancer incidence is also higher in developed countries. Regions of Northern America, Europe (excluding Eastern Europe) and Australia/New Zealand have a significantly higher incidence rate than Central African and South Central Asian countries which have the lowest incidence [35].

The higher incidence of breast cancer in developed countries is linked to the higher prevalence of known risk factors such as early age at menarche (first menstruation), nulliparity (having never been pregnant), advanced maternal age and late menopause. These factors are all related to the hormonal environment to which the breast is exposed, from menarche to menopause. It is believed that the higher parity and earlier age at first pregnancy may be related to the reduced incidence of breast cancer in developing countries, possibly due to the longer duration of breast-feeding which is hypothesised to reduce the risk of developing breast cancer [31]. In contrast, exogenous hormones such as oral contraceptives and hormone replacement therapies have been shown to increase the risk of developing breast cancer, however these cancers are rarely clinically advanced at presentation and have reduced mortality rates [36,37].

Lifestyle factors and obesity are associated with increased prevalence of breast cancer. Large weight gains after the age of 18 have been shown to increase the risk by 2% of developing breast cancer per unit of body mass index [38]. In addition, obesity in

postmenopausal women also linked with increased risks [39]. Likewise, excessive alcohol consumption has been linked to heightened risks and it is estimated that 4% of breast cancers in developed countries are due to alcohol consumption [40]. Family history is another important risk factor as the risk of developing breast cancer is doubled in women who have a first degree relative who developed breast cancer before the age of 50 [34]. Additionally, genetic factors such as germline mutations to the BRCA genes contribute to an increased risk, with 72% and 69% of BRCA1 and BRCA2 mutation carriers likely to develop breast cancer by the age of 80, respectively [41].

Breast cancer is the leading cause of cancer-related deaths in over one hundred countries and was responsible for 626,679 deaths, worldwide in 2018 [35]. While the incidence of breast cancer is relatively high, the 5-year survivability of early-stage cancers is 99%, however, this decreases with more advanced stage cancers at presentation to 84% for regional cancers and as low as 23% for late-stage cancers [42]. In Australia, breast cancer mortality reduced by 2.4% across all age groups between 1991-2006, suggesting that modern therapeutics, coupled with early diagnoses through mammographic screening were effective. Similar trends have been observed throughout other developed nations [42].

Breast screening is carried out to assess whether a patient has breast cancer with an aim to detect early-stage cancers, on account of the link between early diagnosis and increased survivability. Mammographic screening is the most effective tool for early-stage detection, often detecting the presence of breast cancer before symptoms present in a physical examination. Breast screening can be classified as either an organised population-based screening or opportunistic screening. During the former, a governing body usually organises for screening to be carried out periodically on a targeted group. Opportunistic screening, in contrast, is offered to patients without breast cancer symptoms who have presented to physicians for unrelated reasons [42].

There was a significant increase in the number of countries conducting screening programmes in the 1980s and 1990s, predominantly amongst developed countries. Most programmes were targeted towards women aged between 50-69 years old with two years between each screening. National participation in these programs varies from less than 20% in Turkey, the Slovakia and Japan to 80% in the United States, the Netherlands and Finland. In Australia, breast screening has been widely adopted and is attributed to reductions in mortality rates between 21-28% [42].

2.1.1 BREAST CANCER PHYSIOLOGY

The female breast, as shown in Fig. 2.2, can be considered as two main parts on a macroscopic level; glandular tissue which is responsible for milk production; and the

additional constituents that make up the breast such as adipose tissue, fascia (connective tissue) and muscles. The glandular tissue consists of 15-20 lobes which are located radially around the nipple. The lobes each consist of smaller lobules which are responsible for milk production and storage. The transport of milk occurs via a network of ducts connecting the lobules to the nipple [43]. As women age, the percentage of glandular tissue reduces and is replaced with adipose tissue [44].

The breast also comprises a network of nerves, blood vessels and lymphatic vessels. The blood vessels supply the breast tissue with nutrients to facilitate function, while the nerves provide sensation. The lymphatic vessels circulate lymph fluid through the lymph nodes as part of the immune system. These vessels also provide a pathway for cancer to spread throughout the body. The sentinel lymph node describes the first node to which cancer is most likely to have spread [45]. In the breast it is located in the armpit area (axilla) and is responsible for seventy-five percent of lymph drainage from breast tissue [46]. The presence of cancer cells in the lymph nodes is a strong indicator of metastasis, therefore, it is common to excise this node during surgery to study the spread of the disease and assess the potential for local recurrence [47].

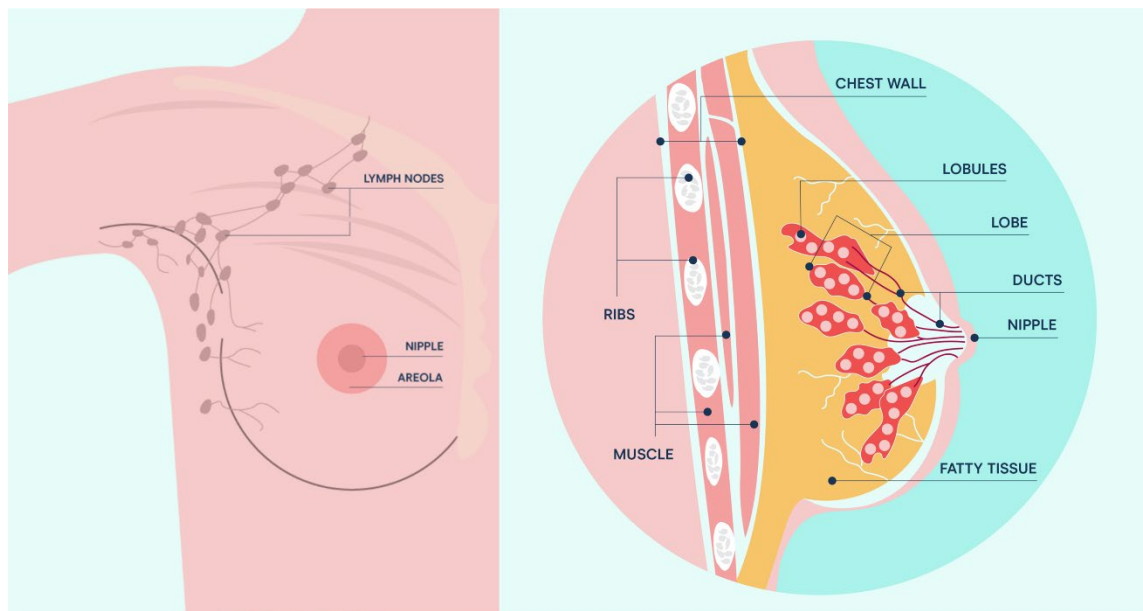


Figure 2.2: Anatomy of the female breast. National Breast Cancer Foundation © 2021.

Breast cancer stage is classified according to how advanced the cancer is and is described by a number from 0 through IV. Stage 0 cancers are at the earliest stage and are non-invasive meaning that they have not spread to other parts of the breast and are confined to either a duct or gland. Stage I describes early-stage invasive cancers, where the cancer has begun to infiltrate the surrounding regions. Stage II broadly refers to the early stage of invasion into other parts of the breast and body. Stages III and IV refer to the late stages of breast cancer

where the cancer cells have either advanced locally or metastasised to other parts of the body [48]. Most stages of breast cancer consist of classifying subcategories which are described in greater detail in Table 2.1.

Table 2.1: Classification of breast cancer stages. Adapted from [49]

Breast cancer stage	Size of cancer	Cancer cells present	
		Lymph nodes	Other parts of the body
0	Size not used for stage 0	No	No
I	<2 cm	No	No
	<2 cm	Yes*	No
IIA	2–5 cm	No	No
	No cancer found in breast	Yes*	No
IIB	2–5 cm	Yes*	No
	>5 cm	No	No
IIIA	<2 cm	Yes†	No
	2–5 cm	Yes†	No
	>5 cm	Yes*	No
	>5 cm	Yes†	No
IIIB	No cancer found in breast	Yes†	No
	Any size but the cancer has spread to nearby muscles and skin	Any (Can be yes or no)	No
IIIC	Any size	Yes‡	No
IV	Any size	Any	Yes
		(Can be yes or no)	

* Breast cancer cells have been found in one to three lymph nodes in the armpit.

† Breast cancer cells have been found in 4–9 lymph nodes in the armpit, and the lymph nodes are also enlarged, and/or attached to each other or to nearby tissue; or 1 or more lymph nodes under the breastbone, but not in any lymph nodes in the armpit.

‡ Breast cancer cells have been found in 10 or more lymph nodes in the armpit; or 1 or more lymph nodes above or below the collarbone; or 1 or more lymph nodes under the breastbone and 1 or more lymph nodes in the armpit.

Precursor lesions

Precursor lesions are cancer cells that remain contained within the basement membrane and are not invasive. Precursor lesions are the earliest stage at which cancer can be detected (Stage 0), and if left untreated, can develop into invasive carcinomas [50].

Ductal carcinoma *in situ* (DCIS) is a proliferation of neoplastic luminal cells that are contained within the ducts of the breast and accounts for approximately 25% of all newly diagnosed breast cancers. While DCIS is contained within the basement membrane, cells can spread beyond the ductal basement membrane into the surrounding parenchyma becoming an invasive carcinoma [51]. Women with a history of DCIS are four times more likely to develop invasive carcinomas than those of the same age without [52]. Despite being classified as precursory, DCIS is considered to be a Stage 0 breast cancer. As a result, treatment for DCIS often reflects that of more advanced carcinomas and involves surgical excision and/or radiotherapy [51].

Lobular carcinoma *in situ* (LCIS) is a proliferation of neoplastic cells in the terminal ductal lobular units of the breast. It is commonly detected in premenopausal women and like DCIS, the cells can penetrate the basement membrane and become invasive. Although the chance of LCIS developing into invasive carcinoma is low, it is considered to be both a precursor

and a risk factor as women who have a history of LCIS are almost ten times more likely to develop breast carcinoma than those without [53,54]. Unlike DCIS, surgery is not necessary for treating LCIS, however, in the past, mastectomies were recommended due to the risk factor for invasive carcinomas [54].

Invasive breast carcinomas

Invasive breast carcinomas are cancers which have begun to spread into the surrounding breast tissue. They are typically classified as early, locally advanced, or advanced (metastatic). Most breast cancers are only detected once they have become invasive. The two most common invasive breast carcinomas are invasive ductal carcinoma (IDC) (80% of diagnosed breast carcinomas) and invasive lobular carcinoma (ILC) (10% of diagnosed breast carcinomas) which originate in the ducts and lobules, respectively. Less common invasive carcinomas include inflammatory breast cancer, Paget's disease of the nipple, medullary carcinoma, and mucinous carcinoma [55].

IDC is categorised as a group of heterogeneous carcinomas which exhibit varied morphologies [56]. IDC has no distinctive visual features on the macroscopic scale and tumour sizes can also vary greatly, however, IDC is generally stiff and can be palpated. DCIS is a pre-cursor lesion for IDC, and Fig. 2.3 illustrates the progression from a normal duct to IDC. ILC is also macroscopically ill-defined and usually affects older women. ILC is challenging to identify via conventional mammography imaging. Ultrasound and magnetic resonance imaging (MRI) are better modalities to detect the presence of ILC. LCIS is a precursor to ILC [57].

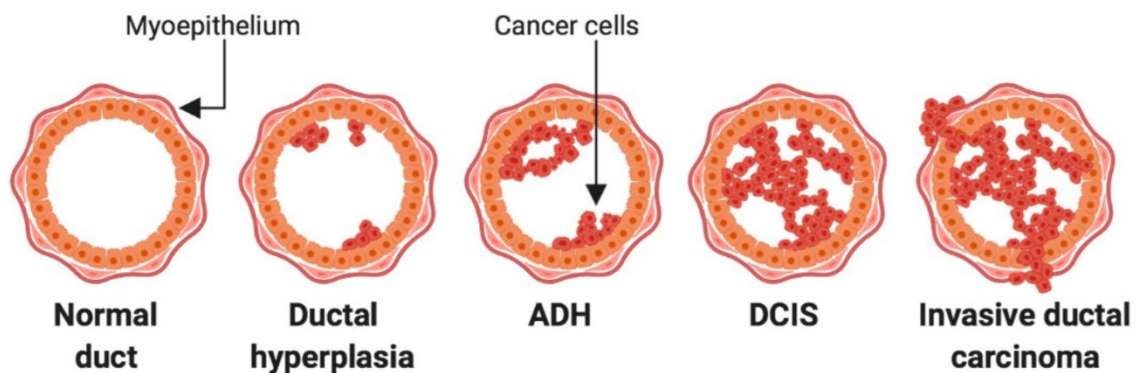


Figure 2.3: Stages of breast cancer development. Atypical ductal hyperplasia (ADH), ductal carcinoma *in situ* (DCIS).

Benign lesions

Benign lesions describe a number of abnormal growths in the breast that are non-cancerous and more commonly diagnosed by mammogram than cancerous tumours [58]. The symptoms of benign lesions often mimic those of cancer and include pain, swelling,

tenderness in the breast, palpable lumps, skin irritation, redness and discharge from the nipple. While all benign lesions are non-cancerous, some lesions, such as atypical hyperplasia, increase the risk of a patient developing breast cancer in the future [59]. Benign breast lesions are therefore classified into three categories based on the likelihood of tumour proliferation in the future: non-proliferative, proliferative without atypia, and proliferative lesions with atypia [60].

2.1.2 BREAST CANCER SURGERIES

Following a diagnosis of breast cancer, the most common first-line treatment involves surgical excision of the tumour. There are two surgical options available to women; mastectomy and breast-conserving surgery (BCS), both of which may be accompanied by radiotherapy and/or chemotherapy to further reduce the risk of local recurrence [61]. The following Sections will provide a brief overview of mastectomy and BCS procedures, highlighting the key benefits and current challenges faced.

Mastectomy

A mastectomy procedure, as illustrated in Fig. 2.4(a), involves the surgical removal of either one or both breasts. Mastectomy is accompanied by the removal of one or more axillary lymph nodes to assess whether the cancer has spread beyond the breast, and if further treatment is required. In relation to breast cancer, mastectomies are often recommended for women with a high tumour-to-breast ratio, multiple tumours, or locally advanced and inflammatory tumours [58]. It has been shown that younger women (under the age of 40), those with more aggressive tumours, and those who live further away from their treatment centres more often opt for mastectomies rather than BCS. Some women who have been diagnosed with breast cancer in one breast may also opt to have the other breast removed in a procedure known as contralateral prophylactic mastectomy (CPM) or bilateral mastectomy. CPM greatly reduces the risk of recurrence, however, it has not been shown to improve the long-term survival rates for women and presents additional surgical complications [62,63]. Prophylactic mastectomy may also be performed for women at high-risk of developing breast cancer such as BRCA1 and BRCA2 gene mutation carriers [58]. Following mastectomy procedures, some women may opt for breast reconstructive surgery, however, the risk of complications is twice as high for women undergoing mastectomy and breast reconstruction than for women undergoing BCS and radiation therapy [58].

Breast-conserving surgery

BCS, often referred to as lumpectomy or partial mastectomy, is the most common form of treatment for early-stage breast cancers. During BCS, the surgeon aims to remove only the

cancerous tissue along with a surrounding margin of healthy tissue, as shown in Fig. 2.4(b). Similar to mastectomies, the surgeon may also perform a biopsy of the sentinel node or axillary node clearance to assess whether the cancer has spread beyond the breast [58]. While the amount of breast tissue excised will depend on the size of the tumour, BCS preserves more of the shape and appearance of the breast than a mastectomy procedure. BCS is traditionally followed-up with a round of radiotherapy to reduce the chance of local recurrence. The combination of BCS and radiotherapy is commonly referred to as breast-conserving therapy (BCT) and has demonstrated similar long-term survival rates to those following mastectomy [64,65].

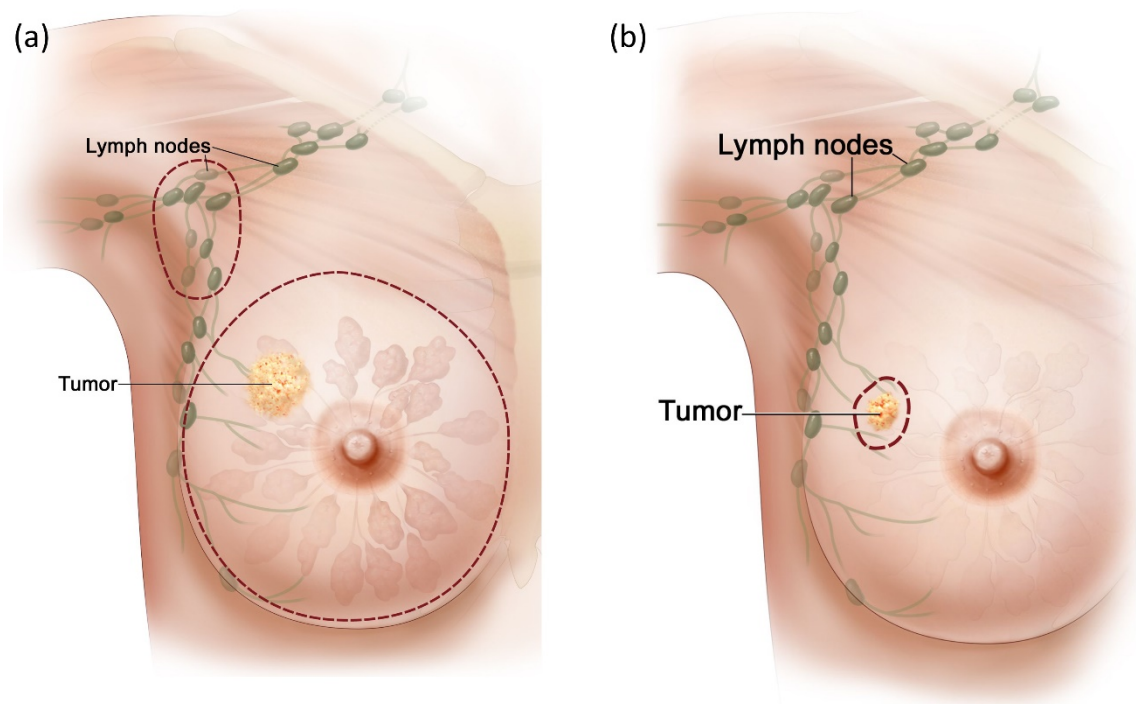


Figure 2.4: Breast cancer surgical treatments. (a) Mastectomy and (b) breast-conserving surgery where the red dashed lines indicate the region to be removed. For the National Cancer Institute © 2012 Terese Winslow LLC, U.S. Govt. has certain rights.

Following BCS, the status of the excised surgical margin is assessed by a pathologist to determine the likelihood of residual tumour in the patient. Positive/close surgical margins are those that contain cancerous tissue either close to or at the excised boundary, in contrast to negative margins which contain no cancerous tissue within the margin (Fig. 2.5). The definition of a surgical margin is somewhat clouded as it differs vastly between different hospitals, with some institutes adopting no ink on tumour (effectively > 0 mm) up to 5 mm at others [66]. Despite this ambiguity, positive surgical margins following BCS are highly suggestive of residual tumour in the cavity with studies finding residual tumour in up to 50% of all BCS procedures containing a positive margin [67,68]. This is of note as margin status is the strongest determinant of local recurrence [69].

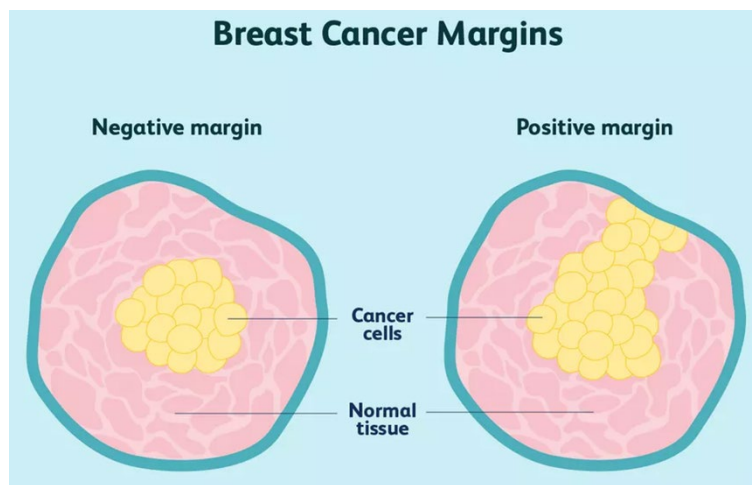


Figure 2.5: Illustration of breast cancer margins. Adapted from <https://www.verywellhealth.com/how-surgical-margins-affect-breast-cancer-decisions-430114>.

Intraoperative assessment of tumour margins in breast-conserving surgery is predominantly performed by manual palpation of the suspected region [70], however, this approach has a low sensitivity and struggles to detect small instances of tumour [71]. Therefore, detailed assessments of surgical margins are carried out via histopathological analysis, a process which takes several days to complete, meaning that if a positive margin is identified, the patient will have to undergo an additional surgical procedure to re-excise the tumour with re-excision rates reported in literature varying from 20-60% [72–74]. This additional procedure leads to additional financial costs, psychological stress and delays in follow-up therapy [75–77].

2.1.3 INTRAOPERATIVE TUMOUR MARGIN ASSESSMENT TOOLS

The high re-excision rate for patients undergoing BCS suggests that surgeons currently lack the tools necessary to reliably identify surgical margins of breast cancer specimens intraoperatively. This clinical need has resulted in a number of intraoperative tumour margin assessment tools being developed, however clinical acceptance rates remain relatively low, suggesting none of these proposed techniques satisfy all of the clinical requirements of a margin assessment tool for BCS. The following Section will describe several of these techniques, outlining each working principle, potential benefits, and the limitations preventing translation to routine use within intraoperative tumour margin assessment.

Frozen section analysis

Frozen section analysis (FSA) is a similar process to standard histopathological analysis, albeit, performed over a much shorter timeframe to allow intraoperative interpretation. During FSA, the excised specimen is orientated by a pathologist at the time of the surgery according to the surgical sutures, before being inked. The tissue is then sectioned, and slices

are visually assessed by the pathologist for malignancies [78]. Slices which contain suspicious regions of tissue are mounted onto a chuck and coated in optimal cutting temperature compound which creates a matrix for the specimen to be embedded within, before being immersed in liquid nitrogen for 10-15 seconds. The tissue block is then sectioned using a cryostat and sections are placed on glass slides and stained using a rapid hematoxylin and eosin staining procedure. Following the staining process, a coverslip is placed over the slide. The pathologist then assesses the slide and informs the surgeon on the state of the margin and whether further excision is required [79]. This process is shown in Fig. 2.6.

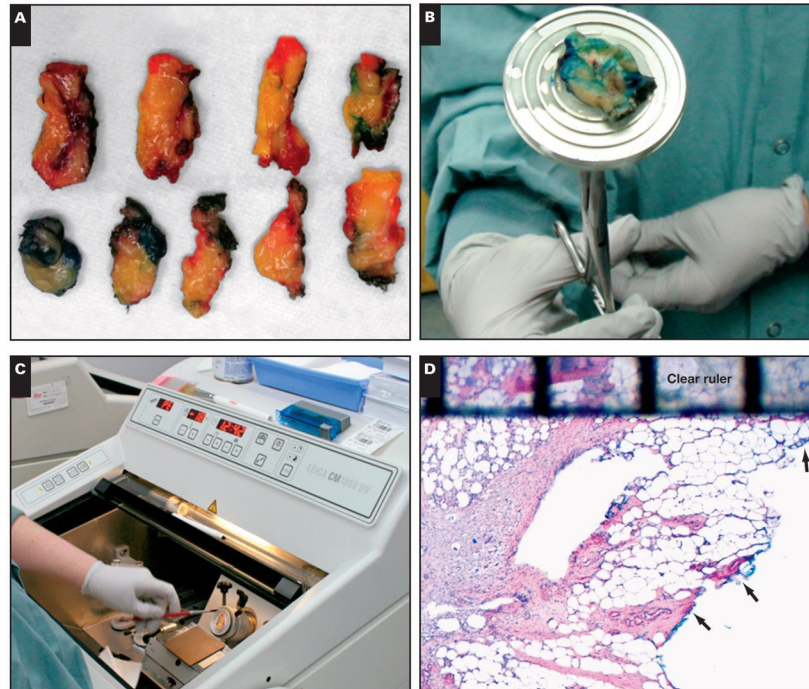


Figure 2.6: Frozen section analysis procedure for tumour margin assessment. (a) Sectioned breast specimen. (b) Frozen tissue section mounted on a chuck. (c) Tissue section cut using a cryostat. (d) Example of frozen section slide. Reproduced from [79].

The use of FSA for the intraoperative detection of breast cancer margins following BCS has demonstrated improved outcomes for patients, with one study by Jorns *et al.* reported a reduction in re-excision rates from 48.9% to 14.1% over one year [79]. Additionally, FSA mimics standard histopathological processes and therefore, does not introduce new processes to be adopted by surgeons and pathologists [80]. Nine different studies into the diagnostic accuracy of FSA reported a pooled sensitivity of 86% and specificity of 96% [80].

Despite these benefits, FSA has not been widely adopted for breast margin assessment. This is largely due to the time taken to perform FSA intraoperatively, typically prolonging the surgery by 25-30 minutes [78,81]. The time taken during FSA also limits the number of slides that can be prepared, effectively sub-sampling the excised tissue specimen and potentially excluding malignancy from assessment which could lead to an incorrect diagnosis [79,82]. The tissue freezing process can also introduce artifacts in FSA which, as a

result, requires a highly experienced pathologist to be present during the surgery to assess the slides. This places a significant burden on personnel which is not feasible for small clinical centres and costly for large ones [80].

Imprint cytology

Imprint cytology, also commonly referred to as ‘touch prep’ cytology, is a simple technique to assess the presence of tumour on a surgical margin. Similarly, to FSA, the tissue is orientated according to the surgical sutures on the excised specimen. The freshly excised tissue is pressed against a glass slide where the tumour cells will adhere to the glass but other tissue cells such as adipose tissue will not (Fig. 2.7(a)). The glass slide can then be either chemically fixed or air-dried, before being stained with hematoxylin and eosin prior to analysis by a cytopathologist, a pathologist specialising in the study of cytology [83]. Representative slides produced by imprint cytology are presented in Figs. 2.7(b) and (c).

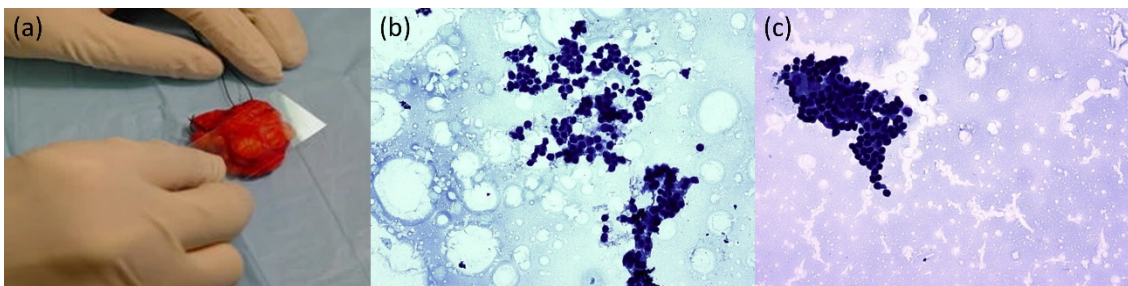


Figure 2.7: Imprint cytology for tumour margin assessment. (a) Photograph showing imprint cytology as the slide is pressed against the cut surface. Adapted from [84]. Representative images of (b) epithelial hyperplasia cells and (c) malignant cells. Reproduced from [85].

The process of imprint cytology takes approximately 15-20 minutes to complete and is relatively cost-effective [81,86]. In addition, it keeps the excised tissue intact for full histopathological analysis to be completed later, an advantage over FSA. A meta-analysis of eleven studies which used imprint cytology for breast margin detection, reported pooled sensitivity of 91% and specificity of 95%, outperforming FSA [80].

Imprint cytology, however, is only able to determine the presence of tumour on an excised surface, it is therefore unable to provide information as to the depth of the tumour, relative to the surgical margin. Therefore, this technique is not feasible for margins thicker than 0 mm. Additionally, like FSA, imprint cytology requires a pathologist to perform the procedure, in particular, a cytopathologist, which places even more demand on the personnel required to perform this technique [81].

Intraoperative specimen radiography

Intraoperative specimen radiography uses X-ray imaging to assess the surgical margins of excised breast tissue. Localisation of the tumour is performed by either hook wire or iodine-

125 titanium seed. Following excision, the surgeon orientates the tumour in an intraoperative radiography cabinet according to the surgical sutures and acquires digital images of multiple views (Fig. 2.8). The imaging is performed instantly, allowing the surgeon to review the images to confirm the completeness of the resection. Where necessary, radiologists are contacted to assist with image interpretation [87,88].

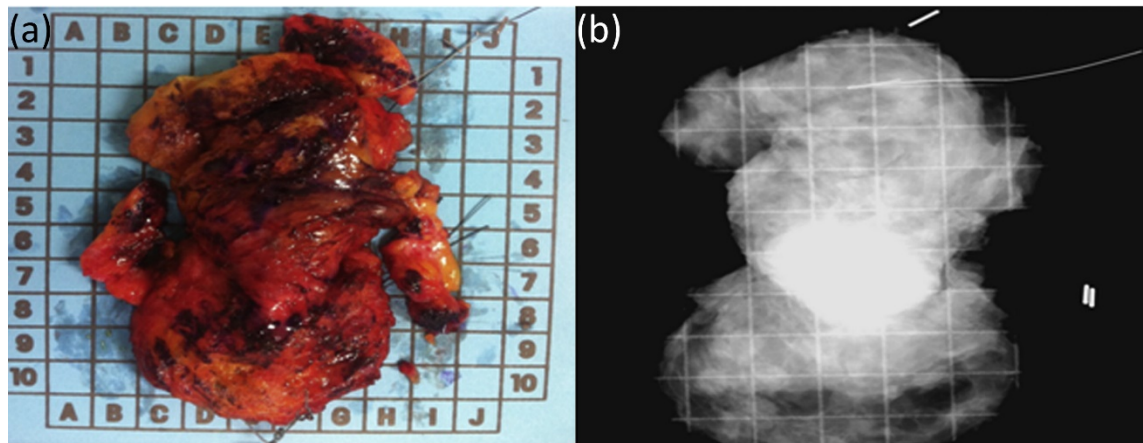


Figure 2.8: Intraoperative specimen radiography of freshly excised breast specimen. (a) Photograph of excised breast specimen and (b) intraoperative radiograph showing the presence of invasive ductal carcinoma. Adapted from [89].

The key benefit of intraoperative specimen radiography is the speed with which images can be generated and interpreted by the surgeon. Being able to perform intraoperative specimen radiography inside the surgical theatre reduces travel time between hospital departments. A study by Kaufman *et al.*, demonstrated that intraoperative specimen radiography takes an average of 1.1 minutes to complete [90]. In addition, generating images which can be readily interpreted by the surgeon removes the need for additional personnel. According to a meta-analysis of nine studies on intraoperative specimen radiography, the pooled sensitivity is 53% and specificity is 84% [80].

The low sensitivity for intraoperative specimen radiography is potentially caused by similar X-ray absorption in dense benign tissue and breast lesions. As a result, intraoperative specimen radiography struggles to provide contrast between dense tissue and tumour, particularly for *in situ* tumours [91]. Intraoperative specimen radiography is a projection-based technique, providing 2-D maps of X-ray absorption and therefore, cannot provide depth-sectioning of the imaged specimen. These factors combined explain why a recent multicentre study into the impact of intraoperative specimen radiography found no evidence that it reduced BCS re-excision rates [92]. Furthermore, intraoperative radiography systems are bulky, and need to be contained on a trolley which takes up a large amount of floorspace and contributes to crowding within the surgical theatre.

Intraoperative ultrasonography

Intraoperative ultrasound is routinely used in surgical applications such as abdominal laparoscopy [93] and as such is readily available in many surgical theatres. While its use in intraoperative tumour margin assessment is not as widespread as in other applications, intraoperative ultrasound is one of the more promising intraoperative tumour margin assessment techniques [94,95]. During inspection of the surgical margin, a handheld ultrasound scanner is used to create a 3-D map of the excised tissue based on the back-reflected ultrasonic waves. The surgeon and occasionally a sonographer interpret the images to determine the tumour distance from the surgical margin and whether a further shaving of the cavity wall is required [96].

Intraoperative ultrasound can depth-section the excised tissue which is crucial for the accurate assessment of surgical margins and offers improved contrast of non-calcified tumours, in contrast to intraoperative specimen radiography. In addition, its widespread use in other applications means that surgeons are often familiar with the technology and interpretation of the images, reducing the need for additional personnel during the surgery. Intraoperative ultrasound extends the surgery by 3-6 minutes, which is significantly lower than other techniques such as frozen section and imprint cytology. Despite these benefits, the diagnostic accuracy of intraoperative ultrasound is relatively low. St John *et al.* reported a pooled sensitivity of 59% and specificity of 81% taken from four independent studies into the diagnostic accuracy of intraoperative ultrasound for breast margin assessment [80].

While ultrasound offers improved imaging on non-calcified tumours, it provides limited contrast in calcifications, which are common in DCIS [97]. Ultrasound is also limited to spatial resolutions of 100s μm which further reduces the diagnostic capability of this technique [98].

Ultrasound elastography (USE), an extension of ultrasound imaging that maps the mechanical properties of soft tissue, has also been applied to breast cancer applications [99–101]. The addition of elastography in these assessments provides additional mechanical contrast compared to standard ultrasound imaging to differentiate between malignant and benign tissues. In particular, two USE techniques have seen widespread use in the diagnosis of breast cancer; strain elastography, which differentiates tissues based on the relative deformation under an applied load, and shear wave elastography, which induces an acoustic radiation force to quantify the tissue mechanical properties [102]. However, despite being widely used in breast cancer diagnoses, the limited spatial resolution of ultrasound elastography ($\sim 1\text{--}2\text{ mm}$) [103] has restricted its use as an intraoperative margin assessment

technique. The concepts and applications of ultrasound elastography are further detailed in Chapter 3.

Optical coherence tomography

OCT is one of the emerging intraoperative tumour margin assessment techniques and utilises low coherence interferometry to reconstruct tissue micro-architecture from back-reflected broad bandwidth light. This technique is often described as an optical analogue to ultrasound, which offers micro-scale spatial resolutions at a penetration depth of up to 2 mm. Intraoperative tumour margin assessment using OCT is performed using a handheld probe on the lumpectomy specimen following the initial excision which allows surgeons to scan different locations on the tissue surface, as shown in Figs. 2.9(a) and (b). Visual and tactile assessment of the specimen was performed to determine suspicious regions for OCT imaging, which can be seen in Figs. 2.9(c-d) [104].

OCT offers several distinct advantages that make it a potential candidate for intraoperative tumour margin assessment such as providing real-time reconstructions of the imaged tissue, allowing surgeons to make immediate decisions on whether to take additional cavity shavings. It is also able to image the tissue over large fields-of-view which enable large tissue specimens to be imaged. While still in the relative stages as an intraoperative tumour margin assessment tool, the diagnostic accuracy of OCT has been reported in a study of 229 lumpectomy specimens by Zysk *et al.*, with sensitivity and specificity of 55-65 and 68-70%, respectively, depending on the criteria used to classify a positive margin [104]. A separate reader study of 139 margins imaged from 71 lumpectomy patients demonstrated a sensitivity and specificity of 69% and 79%, respectively [105]. The low diagnostic accuracy of OCT is possibly due to its inability to reliably differentiate tumour from benign stroma. In addition, imaging artifacts caused by blood and thermal effects (due to cauterisation) can confound the interpretation of OCT images.

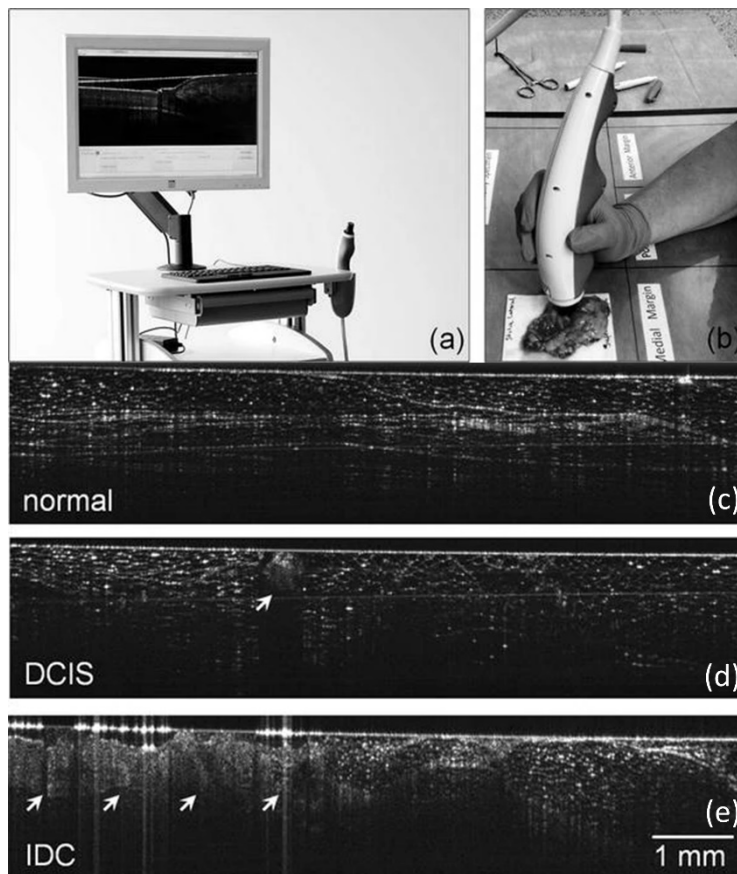


Figure 2.9: Intraoperative OCT for breast cancer margin imaging. (a) OCT system with (b) handheld probe. Acquired OCT images of (a) normal, (b) DCIS and (c) IDC tissue. Adapted from [104].

Quantitative micro-elastography

OCT utilises the optical properties of tissue to assess for tumour, however, cancerous tissue also exhibits unique mechanical properties from the surrounding tissue. This is the underlying principle leveraged by quantitative micro-elastography (QME) in the detection of residual tumour. QME is an optical elastography technique and uses the same principles of low coherence interferometry as OCT, while also detecting the relative changes in phase caused by small displacements to the imaged tissue under applications from some external load. This tissue displacement allows for the measurement of tissue strain. Quantification of the tissue mechanical properties is achieved by the implementation of a compliant silicone layer to detect the stress acting on the sample, allowing for sample elasticity to be estimated as the ratio of stress to strain [106]. By providing measures of tissue elasticity, QME is able to provide a higher contrast between tissue types than other optical elastography techniques that utilise strain only. In addition, QME, by utilising OCT is able to provide two contrast mechanisms of optical and mechanical contrast.

QME is still in its relative infancy as an intraoperative assessment of tumour margins in breast-conserving surgery. Most current studies are focused on small sample size technical demonstrations. Despite the lack of extensive studies to date, preliminary studies are

promising, with one reader study of 154 images from 71 BCS patients demonstrating 92.9% sensitivity and 96.4% specificity [105]. This study showed a marked improvement over the use of OCT alone, suggesting that QME may be suitable as an intraoperative tumour margin assessment technique. A limitation of this study is that it was not performed intraoperatively, rather the tissue specimens were scanned following the surgery. For QME to be considered for intraoperative assessment of tumour margins in breast-conserving surgery in the future, there needs to more published studies focused on intraoperative assessment.

2.2 BURN SCARS

Injuries resulting from burns represent a significant problem to public health. The World Health Organization (WHO), estimate that there are 180,000 deaths resulting from burn wounds each year, with low- and middle-income countries most at risk [107]. In Australia, the burn injury incidence rate is 24 in 100,000 which makes up 1.1% of all hospitalised injury cases. Men are more likely to develop burn injuries, making up almost two-thirds of all burn-related hospitalisations. Additionally, people living in remote areas are five times more likely to present to a hospital with burn-related injuries than people living in major cities, which can result in delays to treatment due to the increased distance from primary care centres [108]. A study performed by Gangemi *et al.* from 703 burns patients reported that 77% of all patients were diagnosed with some form of pathological scarring with pathological scarring at 57% of all burn sites [109].

Burn injuries often heal naturally without complications, however, pathological scarring can develop in some patients. One of the main risk factors of pathological scarring is skin type, as patients with dark skin tones (skin types 4-6 on the Fitzpatrick scale) are more likely to develop raised keloid scarring compared to lighter skin tones (skin types 1-3 on the Fitzpatrick scale) [109]. Other genetic risk factors include age and gender, with younger patients and women both more likely to develop pathological scarring [109,110].

In addition to genetic risk factors, the initial burn can also lead to the development of pathological scarring, depending on the severity. Higher degree burns which damage deeper layers of the skin are more likely to result in pathological scarring. There is also a correlation between the total body surface area (TBSA) burned and the scar pathology and burns located on the limbs, more likely to form pathological scarring than on the head or abdomen [109]. Other factors such as time to healing can also influence scar formation [110].

The mortality rate for severe burn injuries is 1.4-18% and varies between countries. Recent trends have shown decreasing burn mortality rates in developed countries (being replaced by increasing morbidity rates), due to the development of improved burn wound

treatments [111]. However, low-income countries continue to be most affected by burn wounds with burn mortality rates in children seven times higher than high-income countries [112].

The mortality rate is affected by the severity of the burn and increases significantly if TBSA involved is above 20%. Age is also correlated with mortality with rates as high as 13–39% in elderly populations [111].

2.2.1 BURN WOUND REPAIR PROCESS

Burns are classified according to the severity of the burn and how deep it has penetrated the skin as illustrated in Fig. 2.10. The four categories are described as:

- **First-degree (superficial) burns.** First-degree burns affect the outermost layer of skin (epidermis), resulting in a red, painful and dry burn site, rarely resulting in long-term tissue damage.
- **Second-degree (partial thickness) burns.** Second-degree burns penetrate through the epidermis and partially into the dermis. These burns appear red and blistered and may become swollen and painful.
- **Third-degree (full thickness) burns.** Third-degree burns damage the epidermis, and dermis, penetrating to the innermost layer of the skin (subcutaneous). These scars appear either white or black.
- **Fourth-degree burns.** Fourth-degree burns penetrate entirely through the skin and damage underlying tissue such as muscle, tendons and bones. These burns destroy the nerve ending in the burn site leaving the patient without sensation in the affected area.

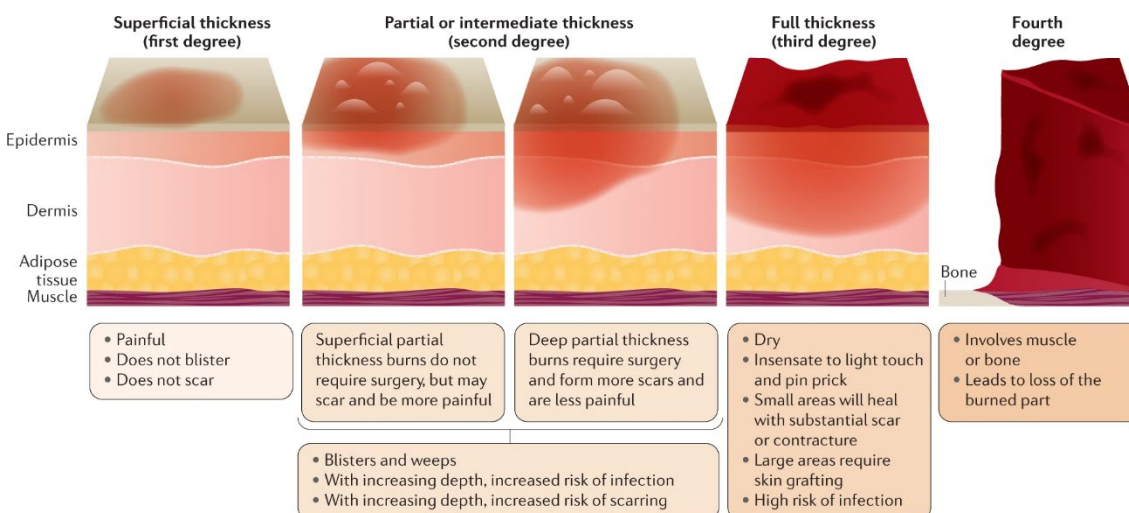


Figure 2.10: Classification of burn severity. Reproduced from [113].

The severity of the burn determines the rate at which the body recovers from the burn with higher degree burns taking longer to repair. In the case of fourth-degree burns, the tissue is heavily damaged and typically requires multiple skin grafts, due to the lack of soft tissue for graft support, or amputation. In the case of lower degree burns, the wound repair begins immediately following the initial injury and follows the same four phases of the natural healing process: haemostasis, inflammation, proliferation, and remodelling, which are described below (Fig. 2.11).

Haemostasis phase

Haemostasis occurs immediately following an injury and is the body's response to two problems that occur during injury; excessive blood loss and damage to the protective barrier of the epidermis [114]. During haemostasis, vasoconstriction occurs, which is the tightening of the blood vessels which prevents further blood loss. A blood clot also forms at the wound to further restrict blood loss and to prevent bacteria from entering the open wound and creating infection. A protein in the clot called fibrin creates cross-links on top of the skin [114].

Inflammatory phase

The inflammatory stage begins after the wound has clotted and involves macrophages (white blood cells) travelling to the wound to combat any bacteria that may have entered the body in a process called phagocytosis [114]. In addition to fighting infection, macrophages produce growth factors which trigger the healing process. In order for the macrophages to travel to the wound, the previously constricted blood vessels must expand, in a process known as vasodilation.

Proliferation phase

Fibroblasts enter the wound during the proliferation phase to produce collagen, a fibrous protein. This generates a connective skin tissue which replaces the fibrin matrix that was formed during haemostasis. Epidermal cells begin to proliferate, reforming the outermost layer of the skin, while the dermis retracts, closing the wound [114].

Remodelling/ maturation phase

Finally, the wound matures as collagen is rearranged. During this final stage, which can continue for years, fibroblasts regulate the process of breaking down the wound matrix and synthesis of a new ECM. This increases the tensile strength of the scar, up to ~80% of the unwounded tissue. Occasionally, during the remodelling, an imbalance will occur, disrupting

the matrix degradation and synthesis processes. This can lead to abnormal scar formation, such as hypertrophic or keloid scars [115].



Figure 2.11: The four stages of wound repair; haemostasis; inflammation; proliferation; and remodelling. Adapted from [116].

2.2.2 PATHOLOGICAL BURN SCARS

Pathological scarring is the result of an abnormal wound repair process. It describes a number of processes which result in functional as well as aesthetic issues for the patient such as increased pain and itch, restricted motion and increased risk of cancer [117,118]. These factors combined with the poor cosmesis of burn scars impact patient quality of life. It is considered to be triggered by prolonged inflammation and mechanical strain on the wound during the healing process, leading to overzealous collagen deposition and a palpable increase in scar stiffness [119]. As a result, wound healing time is used as a prognostic indicator for pathological scar formation, which necessitates frequent assessment of the scar over time. A brief summation of the most common pathological scars is presented below.

Atrophic scarring

Burn injuries rarely result in atrophic scars compared to other pathologies and are often generalised along with hypertrophic scars [120]. Atrophic scarring, however, is markedly different in its formation as it is caused by an absence of underlying structures which support the skin such as fat or muscle. Atrophic scars exhibit a deficit of elastic fibres compared to normal skin tissue, appearing sunken or recessed in the skin, giving them a pitted appearance, which leaves patients with poor cosmesis (Fig. 2.12(b)) [121].

Hypertrophic scarring

Hypertrophic scarring is the most common type of pathological scar formation following burn injuries and has been reported in 30-90% of burns patients [122]. It has been described as “the greatest unmet challenge after burn injury” [123]. Hypertrophic scars typically present as elevated, firm, and red as well as being itchy and tender (Fig. 2.12(f)). These scars cause pain, itch and poor cosmesis. They are restricted to the site of the original wound and do not recur following surgical excision [113]. Hypertrophic scarring typically reduces over time [107].

Hypertrophic scars form during the wound healing process in response to an imbalance of the deposition and degradation of ECM proteins. This can be caused by either overproduction of collagen, proteoglycans and fibronectin by fibroblasts or insufficient degradation and remodelling of the ECM [124]. Hypertrophic scars occur when the wound healing process is delayed, resulting in the pathological characteristics of hypertrophic scars, such as increased vascularisation, hypercellularity and increased collagen deposition, which is distributed parallel to the epidermal surface, resulting in an elevated stiffness [123,124].

Keloid scarring

Keloids are similar to hypertrophic scars in that they are characterised by excessive growth at the scar site, however, they are substantially larger than hypertrophic scars and can grow beyond the initial scar site. Another key distinction between the two scar types is hypertrophic scars will begin to develop around four weeks after the injury and continue to grow over several months before regressing. Keloids, in contrast, take longer to appear but will continue growing indefinitely [125,126]. Keloids are stiff, raised, and lumpy and can cause itch and pain, as well as poor cosmesis. While not life-threatening, keloid scars can grow across joints, restricting movement of the patient (Fig. 2.12(g)).

Keloid scars exhibit increased fibroblast density and increased fibroblast proliferation rates. Collagen fibres in keloids are larger, thicker, and wavier than those found in normal or even hypertrophic scars and are randomly distributed. Keloid pathogenesis remains an area of research, however, several hypotheses have been proposed to explain how they form. These include Altered Growth Factor Milieu, Growth Factor Differences, Extracellular Matrix Differences, Collagen Turnover, Tension, Genetic Immune and Sebum Reaction [127].

Scar contractures

Scar contractures form in response to excessive scarring and ongoing contraction and are a common pathological outcome following burns [128,129]. A study by Oosterwijk *et al.* showed that the prevalence of contracture following hospitalisation was 38–54%, decreasing over time post burn injury [130]. Scar contractures limit the patient's the range of motion (ROM) by restricting the full extension of joints (Fig. 2.12(e)). This is a debilitating issue and limits performing activities of daily living, affects physical health, and diminishes a patient's quality of life. In addition, overuse of unaffected joints can occur to compensate for joints affected by contractures.

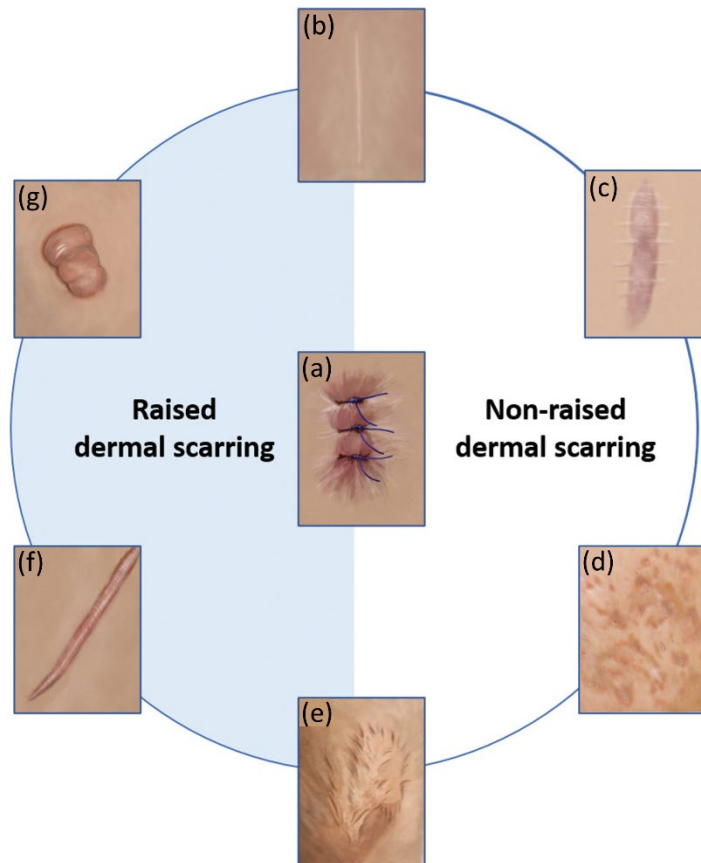


Figure 2.12: Illustration of different types of skin scars. Scars resulting from (a) the initial wound can form into (b) normal (fine-line) scars, (c) stretched scars, (d) atrophic scars, (e) contracted scars, (f) hypertrophic scars or (g) keloid scars. Adapted from [131].

2.2.3 BURN SCAR TREATMENT AND MANAGEMENT

There are a number of treatments available to burns patients to reduce the severity of scarring which reflects the broad variations in how burn scars form. The most common treatment methods include corticosteroid injections, silicone sheeting, pressure garments, massage therapy and pulsed dye laser treatment. A treatment plan typically involves a number of these techniques being used in conjunction with one another to provide the best outcomes.

Pressure garments in the form of elastic stockings apply 15-25 mmHg of pressure to the maturing scar (Fig. 2.13). These garments are required to be worn for 23 hr each day for up to twelve months, following wound closure [132]. However, there is limited evidence to suggest that pressure garments are effective at reducing scar severity and they are required to be worn for long periods of time and can cause discomfort to patients. Similarly, silicone sheeting is another non-invasive therapy which applies silicone sheets to the closed wound for 12-24 hours each day over several months. While this is believed to increase the scar temperature, hydration and oxygen tension in order to soften and flatten the scar, there is also a lack of evidence into the efficacy of this treatment [133]. Massage therapy is also widely used as it improves blood flow and lymphatic drainage. In addition massaging the scar

stimulates movement of the muscle fibres which enable smoother motion in the affected region [134]. Intralesional corticosteroid injections, while painful, are capable of suppressing inflammation and mitosis to increase the vasoconstriction in the scar. This form of treatment has been shown to be effective in flattening 50-100% of keloid scar with 9-50% recurrence rate [133]. Corticosteroid treatments typically involve 2-3 injections a month apart, however, the treatment can continue for over six months if needed, and are most effective on newer scars [133]. Finally, the use of pulsed dye lasers is relatively recent and involves the application of a short-pulsed 585 nm pulsed dye laser to reduce redness, itch and improve scar texture. Preliminary studies have shown promise [135], however, further clinical studies are required to determine the true efficacy of pulsed dye laser use in scar treatment [133].



Figure 2.13: Example of compression garment worn by patient with severe burn scars on their left hand. Reproduced from [136].

2.2.4 BURN SCAR ASSESSMENT TOOLS

The risk of pathological scar formation is of concern when treating scars and increases with time taken to heal the scar. Available therapies can modify and reduce the severity of pathological scarring with early interventions proving most effective. As a result, accurate diagnosis and assessment of the scar is crucial to providing the highest level of post-burn treatment and tailored therapeutic strategies.

Clinical assessment of burn scars is largely performed using subjective scar assessments. These scar assessments provide scales to rate certain characteristics of the scar, however, due to their subjectivity, are best used to assess changes in the scar over time rather than objectively compare one with another. The most commonly used scar assessment scale is the Vancouver Scar Scale (VSS), which was developed in 1990 by Sullivan. The VSS rates four variables: vascularity, height/thickness, pliability, and pigmentation. Despite this assessment being widely used to rate the effect of treatments on burns scars, it is dependent solely on the observer's rating. In contrast, the Patient and Observer Scar Assessment Scale (POSAS) incorporates the patient's opinion of the scar into the rating as well as the observer's, to

Table 2.3: POSAS Patient scale.

Parameter	1 = no, not at all					yes, very much = 10				
	1	2	3	4	5	6	7	8	9	10
Has the scar been painful the past few weeks?	<input type="radio"/>	<input type="radio"/>	<input type="radio"/>	<input type="radio"/>	<input type="radio"/>	<input type="radio"/>	<input type="radio"/>	<input type="radio"/>	<input type="radio"/>	<input type="radio"/>
Has the scar been itching the past few weeks?	<input type="radio"/>	<input type="radio"/>	<input type="radio"/>	<input type="radio"/>	<input type="radio"/>	<input type="radio"/>	<input type="radio"/>	<input type="radio"/>	<input type="radio"/>	<input type="radio"/>
	1 = no, as normal skin					yes, very different = 10				
Is the scar colour different from normal skin at present?	<input type="radio"/>	<input type="radio"/>	<input type="radio"/>	<input type="radio"/>	<input type="radio"/>	<input type="radio"/>	<input type="radio"/>	<input type="radio"/>	<input type="radio"/>	<input type="radio"/>
Is the stiffness of the scar different from normal skin at present?	<input type="radio"/>	<input type="radio"/>	<input type="radio"/>	<input type="radio"/>	<input type="radio"/>	<input type="radio"/>	<input type="radio"/>	<input type="radio"/>	<input type="radio"/>	<input type="radio"/>
Is the thickness of the scar different from normal skin at present?	<input type="radio"/>	<input type="radio"/>	<input type="radio"/>	<input type="radio"/>	<input type="radio"/>	<input type="radio"/>	<input type="radio"/>	<input type="radio"/>	<input type="radio"/>	<input type="radio"/>
Is the scar more irregular than normal skin at present?	<input type="radio"/>	<input type="radio"/>	<input type="radio"/>	<input type="radio"/>	<input type="radio"/>	<input type="radio"/>	<input type="radio"/>	<input type="radio"/>	<input type="radio"/>	<input type="radio"/>
	1 = as normal skin					very different = 10				
What is your overall opinion of the scar compared to normal skin?	<input type="radio"/>	<input type="radio"/>	<input type="radio"/>	<input type="radio"/>	<input type="radio"/>	<input type="radio"/>	<input type="radio"/>	<input type="radio"/>	<input type="radio"/>	<input type="radio"/>

The subjectivity in these scar scales means ratings can vary between assessors, particularly with different levels of experience, hence why objective scar assessment scales have recently been developed. Objective scar scales seek to quantify the scar characteristics, removing potential bias in the assessment of scar severity. The broad number of scar parameters such as colour, vascularity, pliability, and height/thickness have resulted in a large number of different objective tools being developed. In general, these scar assessment tools are designed to each quantify a single parameter of the scar, therefore, in the following Section, these tools are classified into four groups: colour, geometry, mechanical properties and, physiology.

Colour

Colour is difficult to quantify as it is heavily influenced by a number of external factors such as skin thickness, reflections and lighting conditions as well as the camera settings. The colour in scars is composed of three components: brown melanin pigment, red oxyhemoglobin in cutaneous vasculature, and yellow/orange bile and carotene pigments [138]. Scar colour is mainly assessed using either tristimulus colourimetry or narrow-band spectrophotometry, which are both based on reflectance spectroscopy.

Tristimulus reflectance colourimetry measures the back-reflected light from the scar using three filtered sensors to represent colour in the same way the human eye would perceive it. Colour is represented by the parameters L^* (lightness), a^* (portion of red or green) and b^* (portion of yellow or blue). Several commercial tristimulus devices have been developed such as the Minolta Chromameter (Minolta Camera Co., Osaka, Japan) and the LabScan XE (Hunter Associates Laboratory Inc., Reston, USA). These devices have shown a moderate to good correlation between a^* values, which represents pigmentation, and the vascularity of scars when validated against the vascularisation score of the POSAS. Additionally, there is moderate correlation between b^* , which represents pigmentation, and

the pigmentation score of the VSS, however, there was no correlation between b^* and the pigmentation score of the POSAS due to POSAS scoring hypopigmented and hyperpigmented similarly [139]. The clinical feasibility of these devices is somewhat limited due to the associated size and cost.

Narrow-band spectrophotometry also measures the vascularisation and pigmentation through detecting relative differences in absorption of red and green light by haemoglobin and melanin, respectively. Haemoglobin gives blood its red appearance as it reflects light in this bandwidth and absorbs green light, whereas melanin appears brown, due to its absorption of all wavelengths. Narrow-band spectrophotometry devices have shown strong correlation with the POSAS scores for vascularisation and moderate correlation with pigmentation scores, highlighting a problem with measuring colour as pigmentation is often masked when the scar is highly vascularised [139]. The clinical feasibility of narrow-band spectrophotometers is also limited by the cumbersome size of the devices and relatively high-cost.

Geometry

Scar geometry (height/thickness, surface area, roughness, etc.) forms another important aspect of scar assessment which is difficult to classify subjectively. Scar height is a key indicator in the formation of hypertrophic and keloid scars, however, scar assessment scales determine this as the amount of scar raised above the surface, which is inaccurate as the portion of the scar below the surface is not considered. The scar assessment tools mentioned below, therefore, aim to provide objectivity in their measurements as well as fully characterise the scar geometry [140].

Ultrasound has been routinely used to measure the histological thickness of scar tissue, based on its depth-scanning capability [141,142]. While ultrasound devices have only shown moderate correlation with tissue depth measured using VSS, this is likely due to the different parameters measured. Ultrasound devices measure the histological thickness which extends below the surface of the scar, whereas scar assessment scales like the VSS measure clinical thickness only. Commercial ultrasound scanners are available for scar assessments, including the DermaLab (Cortex Technology, Hadsund, Denmark), offer subcutaneous ultrasound imaging in a compact form-factor, making it suitable for routine clinical use. The feasibility is furthered by the DermaLab's modularity, which enables different configurations to measure up to nine different scar parameters.

Measuring the scar surface area, known as planimetry, allows clinicians to determine scar contraction over time [143]. This is most effective during the early stages of scar development as the boundaries become harder to delineate as the scar matures. Planimetry

is mainly performed by tracing the margins on a clear plastic film or by photographing the scar. Photography of the scar is simple and readily available, however, requires certain conditions to be effective. Firstly, the scar must be relatively flat as measurements are less reliable on curved surfaces [144]. Additionally, the camera settings, distance from patient and lighting conditions must be standardised to produce repeatable and comparable images [145].

Mechanical properties

Mechanical properties are a key determinant of scar pathology, as pathological scars such as hypertrophic or keloid scars will exhibit an elevated stiffness. As a result, there are several different techniques available for measuring skin mechanical properties. Skin elasticity measuring probes such as the Cutometer and Dermalab elasticity probe (Figs. 2.14(a) and (b)) are non-invasive tools which measure the stiffness of skin by means of suction. Negative pressure is created inside these devices which draws the skin into the probe aperture. A light source is directed across the aperture to determine how far the tissue has been drawn, with softer (less scarred) tissue being drawn further into the aperture than stiffer (more scarred) tissue (Figs. 2.14(c) and (d)) [145]. The cutometer has proved highly effective in the assessment of burn scar stiffness, however, it provides an average stiffness measurement over the aperture, effectively limiting the resolution to the size of the aperture. This can present challenges for mapping the local mechanical properties of scar tissue.

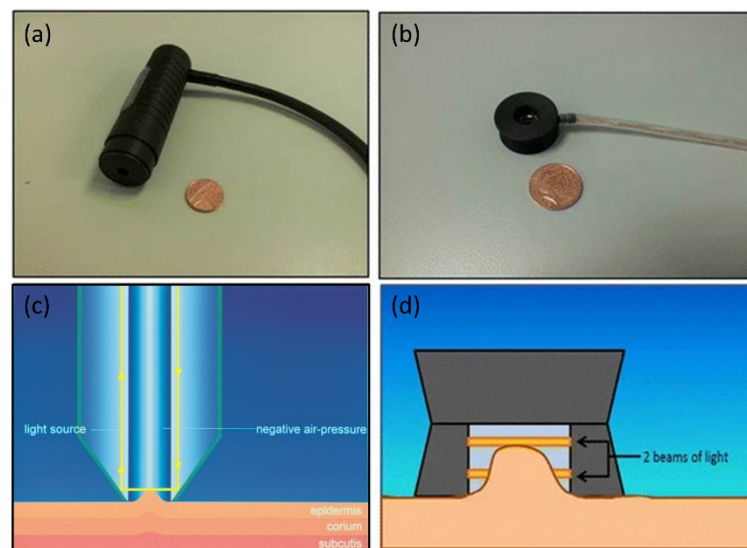


Figure 2.14: Devices for measuring scar mechanical properties. Photographs of (a) Cutometer and (b) Dermalab elasticity probes and the respective working principles shown in (c) and (d). Adapted from [145].

Tonometry is another tool for the measurement of scar mechanical properties and calculates the force required to deform the tissue a given amount. Tissue tonometers are weight-loaded devices which drive a blunt piston into the tissue and report the measured deformation, which is proportional to the tissue mechanical properties. Tissue tonometry

has been shown to be a valid and reliable tool for measuring burn scars [146], however, has similar limitations to the Cutometer in that the measurements of tissue deformation are taken over an averaged area.

In addition to the previously mentioned techniques, ultrasound elastography is emerging as a means for detecting scar mechanical properties. Ultrasound elastography generates an acoustic radiation force (ARF) in the tissue. The resulting displacement from the ARF produces shear waves which propagate away from the origin. Shear modulus, which is proportional to the elastic modulus for incompressible isotropic materials, can be estimated from the shear wave speed which is detected using multiple imaging beams. Preliminary studies have shown ultrasound elastography can reliably discriminate between pathological scars and healthy tissue, as shown in Fig. 2.15 [147–149]. The ability to localise the scar mechanical properties in depth coupled with measurements of scar geometry using ultrasound alone, enhance the clinical feasibility of ultrasound elastography for objective scar assessment. Despite the promise shown, ultrasound elastography still requires further studies to validate the calculation of shear modulus from shear velocity in burn scars [148]. Additionally, ultrasound resolution is on the order of one millimetre, which may be insufficient for detecting small instances of scar pathology or accurately mapping how the scar contracts over time.

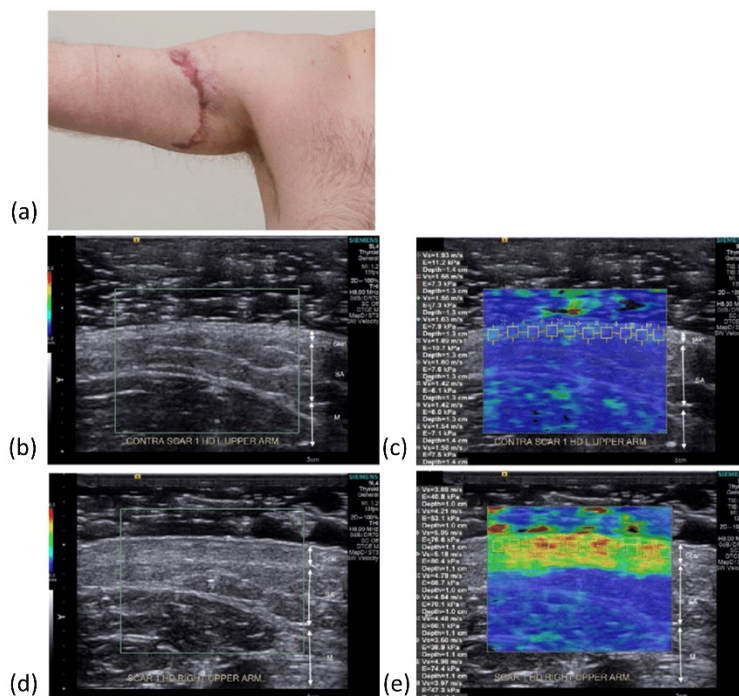


Figure 2.15: Ultrasound elastography of a 14-month-old burn scar on the arm of a 23-year-old male patient. (a) Photograph of scar. (b) Contralateral ultrasound image of healthy tissue and (c) corresponding elastogram with an average shear modulus of 7.9 kPa. (d) Ultrasound image of burn scar and (e) corresponding elastogram with a higher shear modulus of 61.0 kPa. Adapted from [149].

Physiology

Transcutaneous oximetry is a non-invasive means of measuring tissue oxygenation levels below the surface of the skin. Oxygen is carried in the blood stream and can therefore provide an indication of the blood flow to the scar [150]. Transcutaneous oxygen pressure can be measured using electrodes on the surface of the skin which warm the surrounding tissue promoting blood flow. In pathological scars, such as hypertrophic scars, the partial pressure of oxygen is lower than that of healthy skin and can therefore be used as an indicator for scar pathology.

Another physiological indicator of pathological scarring is the transepidermal water content. Transepidermal water loss (TEWL) can be measured by either open or closed evaporimeters and is proportional to the moisture in the skin [151]. As scar sites tend to have a lower moisture content than healthy skin, TEWL can be an effective tool for scar classification. Several commercial devices have been developed to measure TEWL in scars, however, these techniques which measure skin water content are highly susceptible to environmental factors and can become confounded by humidity [152].

CHAPTER 3

OPTICAL ELASTOGRAPHY

In this Chapter, the field of elastography is introduced and the three main elastography techniques are described, namely, ultrasound elastography, magnetic resonance elastography, and optical elastography. As optical elastography is the main focus of this Thesis, the most prominent of these techniques are presented before describing a mechanical model derived from continuum mechanics which is widely used to relate measured deformation to elasticity in elastography. The Chapter concludes by presenting how this mechanical model is implemented for the optical elastography techniques developed within this Thesis.

3.1 ELASTOGRAPHY

The mechanical properties of tissue serve as biophysical indicators of pathology. From whole organs down to the cellular scale, the mechanical properties influence tissue function and play a vital role in the onset and advancement of disease [1]. Over the last three decades, elastography has been established to non-invasively map these mechanical properties in tissue. Elastography techniques can generally be described by the imaging modality used to measure tissue displacement, the mechanism used to impart deformation to the sample, and the mechanical model used to relate measured deformation to a mechanical property. Initially, elastography techniques utilised ultrasound or magnetic resonance imaging (MRI) to measure displacement and these modalities are, therefore, the most prominent, providing the capability to image over large fields of view (in the centimetre range) with millimetre-scale resolution [153]. More recently, the maturation of optical imaging modalities, such as optical coherence tomography (OCT), has enabled elastography techniques to be developed with imaging resolutions an order of magnitude greater than either ultrasound elastography (USE) or magnetic resonance elastography (MRE), providing images of mechanical properties, termed elastograms, on the intermediate scale between cells and organs, albeit, at lower imaging depths, typically 1-2 mm in the case of OCT-based elastography (OCE) [22,154]. OCE, therefore, fills the gap between techniques that image mechanical properties on the cellular-scale, such as atomic force microscopy and micropipette aspiration, and existing elastography techniques which image on the macro-scale. This development

holds potential for an improved understanding, diagnosis, and management of disease onset [155].

3.1.1 ULTRASOUND ELASTOGRAPHY

The first application of ultrasound imaging to medicine is attributed to Professor Ian Donald [156,157], who was the first to incorporate ultrasound imaging into the field of obstetrics and gynaecology in 1958 at the University of Glasgow [158]. Ultrasound imaging has since been widely adopted for a range of clinical applications, due to its ease-of-use, real-time diagnostic capability, portability and relatively low cost [159]. By 1988, sonoelasticity imaging, an early USE technique, was being developed to map tissue displacement using an actuator to generate standing waves in the tissue which were measured by ultrasound using Doppler detection [160,161]. This method determined the vibrational amplitude using Fourier-Bessel analysis, where the amplitude was indicative of relative tissue stiffness, however, later studies found that the implementation of an additional actuator could produce a shift in the interference pattern resulting in crawling waves which can be used to determine local shear wave velocity and the tissue stiffness [162]. Several years later, in 1991, Ophir *et al.* proposed another variant called strain elastography in which a compressive load was applied to the tissue and the resultant 'local' strain was mapped at in location within the imaging field of view [163]. Following this breakthrough, further technical developments saw the image quality of ultrasound strain elastography improve to the point where it was applied to the detection of malignancies in breast and prostate cancer [164]. Ultrasound strain elastography has since become widely utilised with many devices commercially available. In the late 1990s [165], USE underwent another major development as shear wave elastography begin to be implemented, allowing for direct quantification of shear and elastic moduli by tracking the propagation of shear waves in tissue [164]. This quantification, coupled with high elastogram quality has resulted in shear wave elastography becoming widely adopted in recent years, particularly in the diagnosis of liver disease [166–168].

The two main USE techniques described above produce either images of local tissue strain (strain elastography) or of shear wave velocity (shear wave elastography). Strain elastography captures images before and after the application of a compressive load and does not monitor any dynamic processes in the tissue. As such, this method of loading is often referred to as static or quasi-static. Following the acquisition of both the unloaded and loaded images, the relative axial displacement is determined by either cross-correlation methods or Doppler analysis [169]. The change in axial displacement with depth provides a measure of tissue local strain, where softer features, such as adipose tissue, undergo more strain than stiffer features such as tumour. In contrast to strain elastography, shear wave elastography

tracks the propagation of shear waves over time and is thus considered a dynamic loading technique. While the velocity of acoustic (longitudinal) waves in tissue is too high to be readily detected (1450-1550 m/s) using ultrasonic methods, shear (transverse) waves, instead travel much slower (1-10 m/s) and can therefore be tracked using ultrasound. The measured shear wave velocity is higher in stiffer tissues than in softer tissues, and can be related to the tissue Young's modulus, E , by $E = 3\rho V^2$, where ρ is the material density (often assumed to be 1) and V is the shear wave velocity [164]. This relation makes several assumptions about the tissue structure, namely that it is homogeneous and isotropic, which are discussed in more depth in Section 3.3.

USE has been widely developed to image disease in the liver [166], breast [170], thyroid [171], lymph nodes [172] and prostate [173]. The nature of the disease in these applications determines which method of USE is most suitable. For example, diffuse organ disease is best evaluated using shear wave elastography, as it is quantitative and can provide a measure of tissue stiffness in lieu of contrasting features [164]. Shear wave elastography has, therefore, been implemented in applications such as the classification of liver fibrosis stages (Fig. 3.1), where advanced fibrosis correlates with an increased stiffness [166,167,174]. During USE of the liver, the patient is positioned in such a way as to open the intercostal spaces, improving the acoustic window to the liver [169]. It is common to image the right liver lobe to avoid cardiac motion from confounding the measurement. USE of the liver has shown a high diagnostic accuracy in assessing for patients with chronic hepatitis C, where measured liver stiffness values corresponded well with fibrosis stages. However, the accuracy of USE is lower with early stages as there is some overlap between the elasticity values, resulting in incorrect classification. In a meta-analysis of 40 USE studies, the pooled sensitivity and specificity were 83% and 89% for patients with cirrhosis and 79% and 78% for patients with significant fibrosis [175].

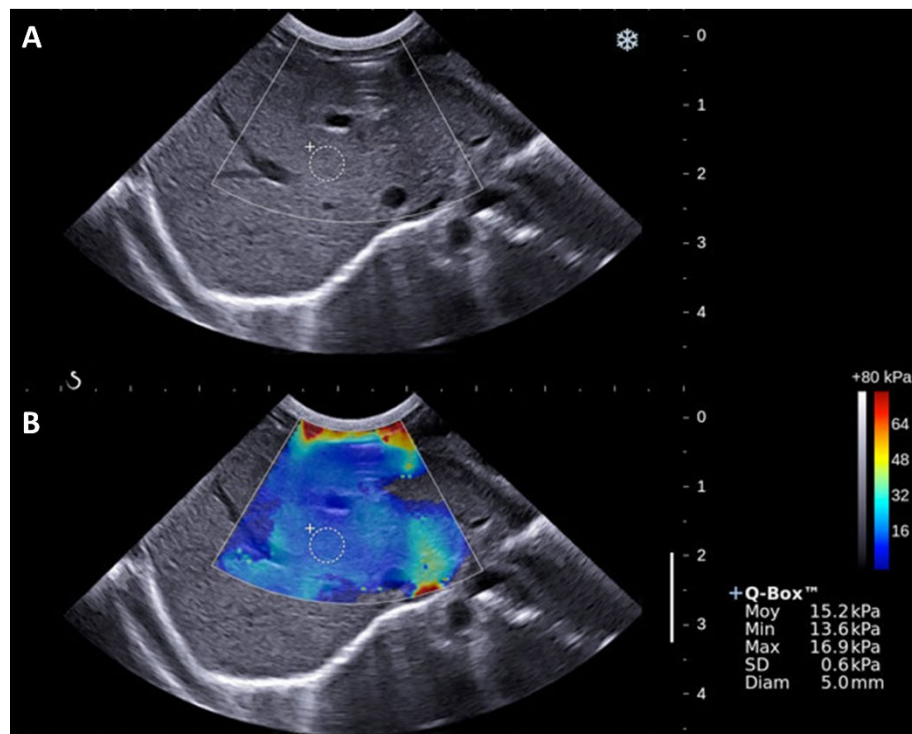


Figure 3.1: Shear wave USE of liver fibrosis on 21-day-old child. (a) Greyscale image and (b) overlaid tissue elasticity colourmap showing increased stiffness at the top of the region of interest. Adapted from <https://www.supersonicimagine.com/Aixplorerer-MACH2/GENERAL-IMAGING/PEDIATRICS>.

In contrast to shear wave elastography, strain elastography is best suited for imaging focal lesions, such as tumours which appear stiffer than their surrounding regions, and is capable of generating elastograms at greater depths than shear wave elastography (~ 6 cm) [164]. The measurement of malignant breast masses was the first clinical application elastography was applied towards [176] and remains one of the main application areas of strain elastography. Even in these early studies using strain elastography, breast cancers were clearly distinguishable by an apparent increase in stiffness, as well as appearing larger in the elastogram than the accompanying sonogram, as shown in Fig. 3.2. The unique combinations of lesion size and stiffness were used to clearly distinguish from surrounding regions of benign tissue. Follow-up studies have confirmed these findings and demonstrated high diagnostic accuracy in the detection of cancerous lesions from benign tissue with area under the receiver operating characteristic curves ranging from 0.89-0.95 [177–179]. The continual development of USE techniques towards breast cancer applications led to the emergence of semi-quantitative methods, such as comparing strain ratios between suspected regions of disease and surrounding tissue [180]. A meta-analysis of nine published studies into the diagnostic accuracy of USE strain ratios reported a pooled sensitivity and specificity of 88% and 83% for differentiating malignant from benign breast lesions. The same meta-analysis also reported the accuracy from three studies which reporting the tumour size, with sensitivity and specificity of 98% and 72%, respectively [181].

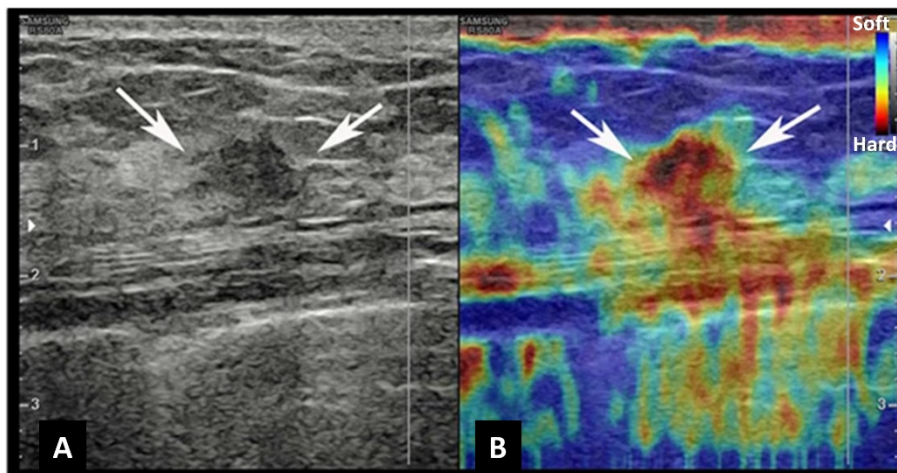


Figure 3.2: Representative image of strain USE performed on breast tissue. (a) Greyscale ultrasound image of suspicious lesion within the breast and (b) corresponding strain elastogram showing a region of elevated stiffness within the lesion. Adapted from [182].

3.1.2 MAGNETIC RESONANCE ELASTOGRAPHY

MRI was first proposed for clinical applications by Professor Raymond Damadian in 1971 [183] and has become prominent in medical diagnostics since, particularly in neurology [184], oncology [185] and hepatology [186]. In 1995, magnetic resonance elastography (MRE) was first proposed by researchers at the Mayo clinic. In this initial study, measurements of the shear modulus of gel materials were obtained by applying a harmonic mechanical excitation via a mechanical actuator and using MRI to track the propagating shear waves [12]. Early clinical studies utilised MRE to assess liver fibrosis. Following these initial demonstrations MRE was adopted as a non-invasive technique to quantitatively image the mechanical properties of tissue in liver, muscle, brain, lung, spleen, kidneys and pancreas [187]. The broad range of clinical applications, coupled with the existing availability of MRI systems, lead to the wide-spread adoption of MRE in healthcare clinics, which has been routinely used since 2010. Currently, more than 90% of commercial MRI systems are capable of performing elastography [188], emphasising the benefits that mechanical contrast can provide in addition to conventional MRI.

MRE is an elastography technique which quantitatively assesses the shear modulus in response to applied mechanical waves. During MRE, shear waves in the 50-500 Hz range are induced using an external driver which is synchronised with the magnetic resonance pulse sequence and positioned close to the scanned region. Modified phase-contrast MRI captures the resulting tissue displacement due to the shear wave propagation and uses this to spatially map the local shear modulus of the tissue, which is proportional to the tissue stiffness and therefore, provides contrast between health and potentially diseased regions [189,190].

Similar to USE, one of the main application areas for MRE is the evaluation of liver fibrosis due to its ability to non-invasively assess for disease based on increases in liver

stiffness (Fig. 3.3). A recent meta-analysis of the diagnostic accuracy of MRE in the staging of liver fibrosis in non-alcoholic fatty liver disease reported findings from twelve separate studies, involving 910 patients [191]. The pooled sensitivity and specificity for each stage were reported to be 77% and 90% for $F \geq 1$ (mild liver fibrosis), 87% and 86% for $F \geq 2$ (significant liver fibrosis), 89% and 84% for $F \geq 3$ (severe liver fibrosis) and 94% and 75% for $F \geq 4$ (early cirrhosis). These results suggest that MRE has a relatively high diagnostic accuracy in the diagnosis of hepatic fibrosis staging in patients suffering from non-alcoholic fatty liver disease [191].

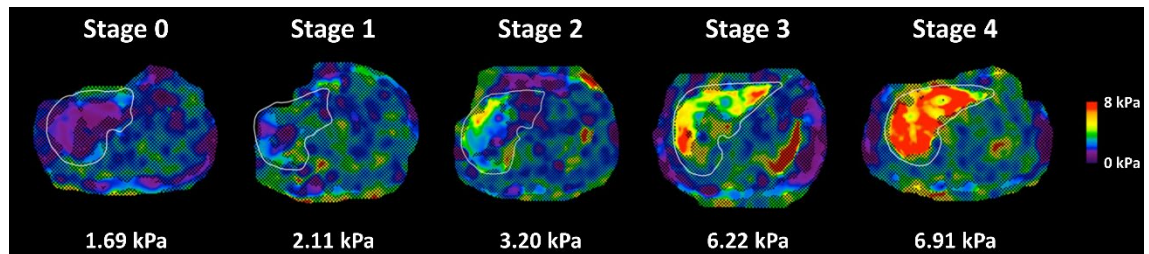


Figure 3.3: Stiffness maps obtained using MRE of five patients with non-alcoholic fatty liver disease at different stages of liver fibrosis. Histologically validated assessments of fibrosis stage are displayed above each image with the mean MRE stiffness values displayed below, showing an increase in liver stiffness with advanced liver fibrosis. Adapted from [192].

MRE has also been demonstrated to evaluate malignancies in the brain, with several studies analysing the mechanical contrast between regions of white and grey matter. These studies have reported shear moduli ranging from 2.5-15.2 kPa for white matter and 2.8-12.9 kPa for grey matter, respectively. While there is significant overlap in the measured shear moduli of white and grey matter, in general the data suggest that white matter is stiffer than grey matter *in vivo* [193–195]. In addition to measurements of shear moduli, MRE has been performed to study the potential relationship between changes in brain viscoelasticity and the onset of neurodegenerative diseases such as Alzheimer’s disease [196] and multiple sclerosis [197]. MRE has also been used to evaluate the stiffness of brain tumours prior to surgical excision with the goal of informing surgeons as to the difficulty of the procedure. Figure 3.4 shows the anatomic, wave propagation and elastograms for a stiff (which is typically harder to excise) and soft brain tumour. In a study of six patients with brain tumours, the shear stiffness measured by MRE was compared to the surgeon’s intraoperative evaluation of the tumour stiffness and found 100% agreement between the two assessments [195]. Another study of 12 patients also found good agreement between elasticity measurements and surgical assessment, however, greater correlation was found when comparing the ratio of tumour elasticity to surrounding brain tissue [198]. Finally, intra-tumour heterogeneity in fifteen meningioma patients was evaluated using a higher resolution MRE protocol than the previous two studies, with a 67% correlation to the

intraoperative measurements, however, higher accuracy may be possible if excluding highly vascular and smaller lesions [199].

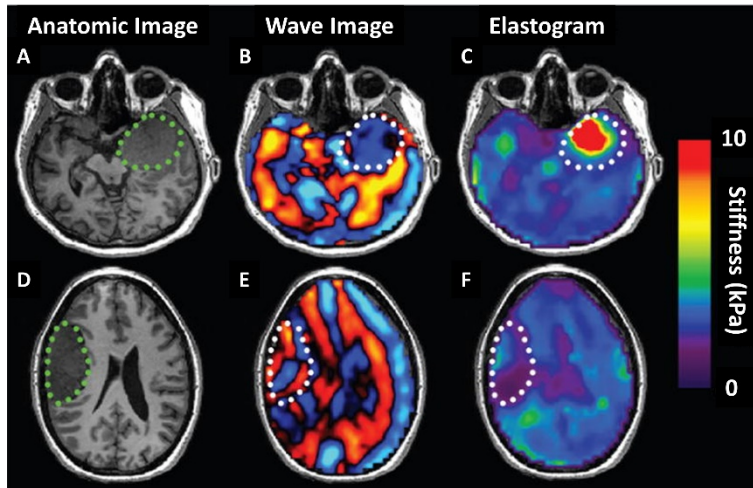


Figure 3.4: MRE images of two patients with meningiomas. (a) Anatomic image, (b) wave propagation image and (c) elastogram of patient with a stiff meningioma, which is outlined in each of the images. (d) Anatomic image, (e) wave propagation image and (f) elastogram of patient with soft meningioma. Mechanical contrast is clearly visible between the tumours and their surrounding regions. Note that the shear wavelength is longer in the stiff meningioma and shorter in the soft meningioma, relative to the surrounding parenchyma. Adapted from [198].

3.2 OPTICAL ELASTOGRAPHY

Compared to USE and MRE, optical elastography is at a relatively early stage of development. It is capable of imaging at an intermediate length scale between that of cells and organs [155], providing insight and understanding of disease progression on this scale. The use of optics provides a combination of milli- to micrometre-scale resolution, high displacement sensitivity, and rapid acquisition times [155]. Optical elastography itself is a broad field, describing a number of different imaging techniques based on techniques such as OCT [18,21,200,201], Brillouin microscopy [23,202], laser speckle imaging [24], and digital holography [25]. The following Sections provide a brief overview of the most prevalent optical elastography techniques of OCE and Brillouin microscopy. In addition, optical palpation, a more recent implementation, and a main focus of this Thesis, will be described. Further details for both OCE and optical palpation are provided in Chapter 4.

3.2.1 OPTICAL COHERENCE ELASTOGRAPHY

Elastography using OCT was first demonstrated in 1998 in a seminal paper by Schmitt that outlined the main principles and limitations of this technique [18]. This study used OCT to image a sample under bulk compression and measured the local sample displacement by computing the correlation between cross-sectional scans at the same spatial location. Maps of local displacement, termed elastograms, were produced from which local strain was calculated, highlighting the benefits of using OCE to detect mechanical contrast in soft

tissue [21]. Despite promising initial demonstrations, the field of OCE began to lose momentum due to limitations imposed by the technology at the time. The time-domain OCT systems used in OCE were unable to provide sufficient acquisition speeds or displacement sensitivity necessary to generate high-quality 3-D images [155]. The development of Fourier-domain OCT [203], signalled somewhat of a renaissance for OCE, producing significant improvements in acquisition speed and sensitivity, and providing the basis for most contemporary OCE systems.

OCE is one of the functional extensions of OCT, which also include Doppler OCT, polarisation-sensitive OCT (PS-OCT), and attenuation imaging [204,205]. These techniques are defined as so due to the additional functional information they provide in addition to the structural geometry imaged with OCT. OCE utilises OCT to image the mechanical deformation in a sample, in response to an applied load, which is generally classified as either compressive, harmonic, or transient. It is capable of providing micro-scale mechanical resolution of tissue specimens and has been widely applied to applications in oncology [105,206,207] and ophthalmology [208–210]. In contrast, Doppler OCT measures the Doppler shift in backscattered light to estimate fluid flow such as blood flow [211], PS-OCT recovers the polarisation information of backscattered light to reveal changes in birefringence caused by disease [212], and attenuation imaging provides additional contrast between healthy and diseased tissue by measuring the extinction of the OCT signal with depth [213]. As this Thesis is focused on optical elastography, the discussion of functional OCT technologies is limited to OCE, which is explored in greater detail in Chapter 4, whereas additional descriptions of functional OCT extensions can be found in the following reviews [204,205].

3.2.2 BRILLOUIN MICROSCOPY

Initially reported in 1922 [214], Brillouin scattering is described as the intrinsic inelastic scattering of light via gigahertz-frequency acoustic waves in materials [202]. This scattering process produces a frequency shift, ν_B , given as $\nu_B = (2\nu_0 n/c)V \sin(\theta/2)$ [202], where ν_0 is the illumination frequency, c is the speed of light, n is the local refractive index, θ is the angle between the incident and scattered light, and V is the acoustic velocity, which is related to the longitudinal modulus, M by $M = \rho V^2$, where ρ is the density. Note that the real portion of M defines the ratio of stress to strain for uniaxial deformation. Brillouin spectroscopy has been demonstrated on liquids since the 1960s, however, its potential as a diagnostic imaging technique wasn't realised until the development of higher-performance imaging spectrometers capable of sub-gigahertz spectral resolution [23,155]. This was first demonstrated by Scarcelli and Yun in 2008 [202] and prompted a number of successive

studies in Brillouin microscopy [215–218]. As an optical technique, Brillouin microscopy leverages high numerical aperture lenses to provide high spatial resolution - 1.5 micron axially and 0.3 micron laterally [215]. The additional benefits of being non-contact and requiring no external excitation make it particularly advantageous for applications in cell mechanics [219] and ophthalmology [220–222], which require minimal forces on the sample to avoid damage and discomfort. Figure 3.5(a) shows Brillouin microscopy images of a single mouse cell and Fig. 3.5(b) shows Brillouin microscopy applied to *in vivo* ophthalmic applications to detect mechanical heterogeneity in a patient with keratoconus.

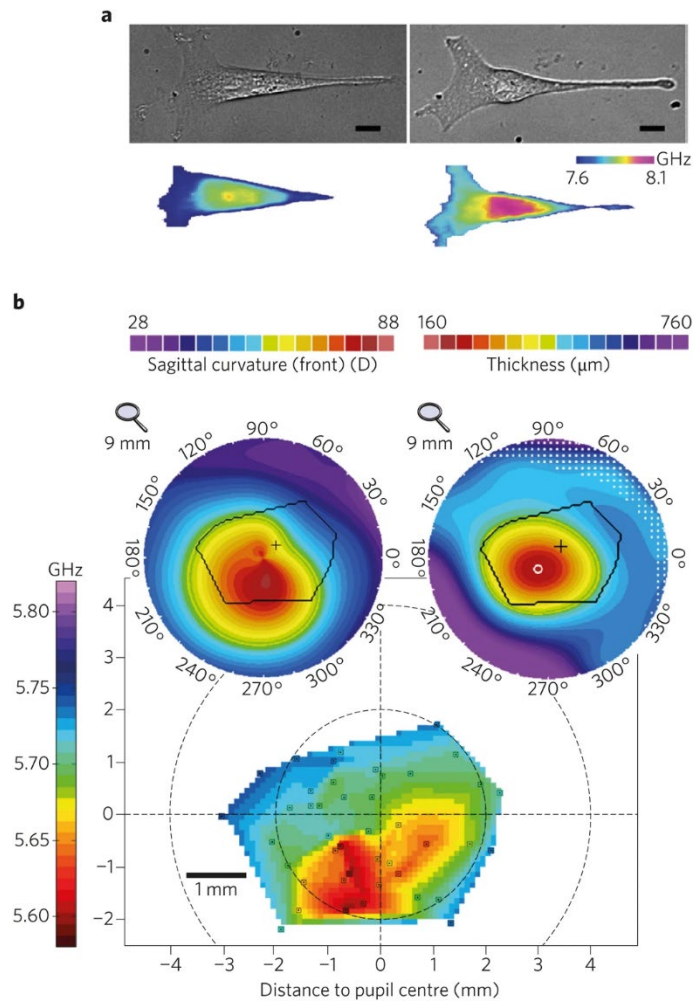


Figure 3.5: Brillouin microscopy in cell mechanics and ophthalmology applications. (a) Co-registered phase-contrast microscopy (upper panels) and Brillouin microscopy (lower panels) of an NIH 3T3 mouse fibroblast cell before and after hyperosmotic shock [219]. The colour bar represents the Brillouin frequency shift in GHz with an increased frequency shift following hyperosmotic shock. Scale bars 10 μm . (b) *In vivo* Brillouin microscopy of the cornea in a 40-year old keratoconus patient (bottom). Colour bar represents the Brillouin frequency shift in GHz. The keratoconic cornea exhibits large spatial variations in Brillouin shift compared to a healthy cornea [222]. Insets (top) show the respective sagittal curvature (D) and pachymetry (thickness) maps with Brillouin-scanned areas outlined. + signs in the insets represent the pupil centre.

The estimation of longitudinal modulus is dependent on prior knowledge of the sample density and refractive index which are not typically known in *in vivo* applications resulting in an element of uncertainty. Similar problems are present in both shear wave OCE and all axial displacement OCE measurements, which require prior knowledge of sample density and

refractive index respectively [155]. An additional challenge faced by Brillouin microscopy involves relating the measured longitudinal modulus to mechanical parameters such as Young's modulus which are more commonly used in other mechanical imaging techniques of atomic force microscopy and OCE. Longitudinal modulus, M , Young's modulus, E , and Poisson's ratio, ν , are elastic moduli that can be represented by the Lamé constants (λ and μ), as such, longitudinal modulus can be related to Young's modulus in terms of Poisson's ratio by $M = E(1 - \nu)/[(1 + \nu)(1 - 2\nu)]$ [155]. For incompressible materials, ν is approaches 0.5 and M becomes infinitely larger than E . Soft biological tissue is considered to be nearly incompressible with ν of 0.499 and higher. As a result, M can be several orders of magnitude greater than E [220]. The relationship between M and E , however, is not constant, possibly due to variations in ν with increasing E , or due to viscoelasticity affecting the phonons at the gigahertz frequencies used in Brillouin microscopy. Accurately quantifying the relationship between M and E , therefore, represents an important step in the development of Brillouin microscopy towards tissue and cellular mechanics. One of the potential challenges limiting the adoption of Brillouin in *in vivo* applications is the long acquisition times, with single axial line scans typically taking several seconds and full 3-D volumes taking ~ 20 min [222]. Nonlinear stimulated [218,223] and impulsive Brillouin [224] modalities represent promising solutions to decrease the acquisition times, however, further developments are still required.

3.2.3 OPTICAL PALPATION

Optical palpation is a relatively new technique, initially proposed by Kennedy *et al.* in 2014 [225], which utilises a pre-characterised compliant silicone layer to determine stress at the tissue surface under compression. The layer is placed on the tissue, and both are compressed between two rigid plates. The axial strain in the layer is determined by an optical imaging modality and is then related to axial stress using the pre-characterised stress-strain response of the layer. Initial demonstrations of optical palpation used OCT as the imaging modality [225,226], however, more recently techniques have been developed to instead utilise a digital camera [227], which can significantly reduce the cost and complexity of the imaging system and is more readily adapted into compact handheld probes.

While classified as an optical elastography technique, optical palpation is analogous in many ways to tactile imaging, a family of imaging techniques that generate 2-D maps of mechanical contrast by employing arrays of electronic sensors, called taxels, to detect a mechanical response through physical contact [228]. Originally developed for applications in robotics to replicate the sense of touch [229], tactile imaging has since been applied to

medical applications including vaginal [230] and breast imaging [231,232]. However, due to the physical spacing of the taxels in tactile imaging there exists a trade-off between the spatial resolution and field-of-view. Due to the cost and physical size, arrays tend to utilise 50 to 100 taxels, which provide spatial resolutions on the order of 1–2 mm. While resolutions as high as 2.7 μm have been achieved using piezoelectric nanowire LEDs, the aforementioned trade-off is evident as this system is only capable of a 100–200 μm field-of-view [233]. Despite optical palpation also using contact to infer sample stress, utilising high-resolution OCT systems or cameras instead enables high spatial resolutions over broad (>10 mm) fields-of-view, making it advantageous over tactile imaging, in applications which require high-resolution spatial mapping.

OCT-based optical palpation

OCT-based optical palpation was developed as a tactile imaging technique capable of mapping the surface stress with high spatial resolution. It has since been demonstrated in applications of oncology [226] and dermatology [234] where it is able to detect mechanical contrast in the sample through spatially varying strain (and therefore stress) in the compliant layer. While it can be used as a stand-alone imaging technique, OCT-based optical palpation can also be used in conjunction with OCE (this is the basis of QME) to increase the mechanical contrast without requiring any additional set-up other than the compliant layer placed between the sample and imaging window. Additionally, unlike other optical elastography techniques, optical palpation is capable of providing mechanical contrast without the need to detect an optical signal from within the sample, which is useful in clinical applications where the OCT signal is obscured such as in the presence of blood during surgery [225]. A more detailed description of OCT-based optical palpation is provided in Chapter 4.

Camera-based optical palpation

Camera-based optical palpation (CBOP) is a recently proposed optical palpation technique that utilises a digital camera and porous silicone layer to generate two dimensional (2-D) elastograms [227]. This technique evolved from OCT-based optical palpation, however, the OCT system, which can be bulky and expensive, is replaced with a low-cost compact camera. CBOP measures the changing optical transmission through the porous layers under compression and determines the corresponding axial stress from an optical transmission-stress characterisation curve for the porous material. A comprehensive explanation of the fundamental principles, potential applications and perspectives of CBOP are presented in

Chapter 8. In addition, a portable variant of this technique, smartphone-based optical palpation is presented in Chapter 9.

3.3 CONTINUUM MECHANICS MODEL OF TISSUE DEFORMATION

For all materials, there exists a relationship between the intrinsic mechanical properties, an applied force, and the resulting deformation which is defined by a mechanical model. Provided the mechanical model is known, knowledge of any two of these parameters enables the third to be derived. This is the underlying principle for elastography, which aims to measure the applied force and resulting deformation to determine the sample mechanical properties. In this Section, the continuum mechanics model used in elastography is presented.

3.3.1 DEFORMATION

Continuum mechanics considers a body as a homogeneous and continuous material such that an infinitesimally small element possesses the same physical properties as the whole body. The surface of the body is considered to be closed with the same number of particles at any time point. To describe the deformation of particles within a body under an applied load, we consider a continuum solid body C , in three-dimensional (3-D) space, illustrated in Fig. 3.6. The coordinates of any position in this body can be expressed as the vector, $\mathbf{x} = \sum_{i=1}^3 x_i \mathbf{e}_i$, where \mathbf{e}_i is the coordinate vector. The initial configuration of the body is known as the *reference* or *undeformed configuration* and any position on this undeformed configuration can be expressed as $\mathbf{X} = \kappa_0(C)$, where κ_0 is a function which maps the body to some real space [235]. Following the application of a load, the body will deform. We define the position within the *deformed configuration* as $\mathbf{x} = \kappa_t(C)$, where κ_t maps the position of the deformed body at some time t . The deformation between the undeformed and deformed configurations is described by $\mathbf{x} = \chi(\mathbf{X}, t)$, where χ maps the positions in the undeformed configuration to the deformed configuration. We consider deformation as the relative displacement of the same point in the two configurations and describe the displacement field as $\mathbf{u}(\mathbf{X}, t) = \mathbf{b}_t + \chi(\mathbf{X}, t) - \mathbf{X}$, where \mathbf{b}_t denotes the solid body motion or translation at time t [236].

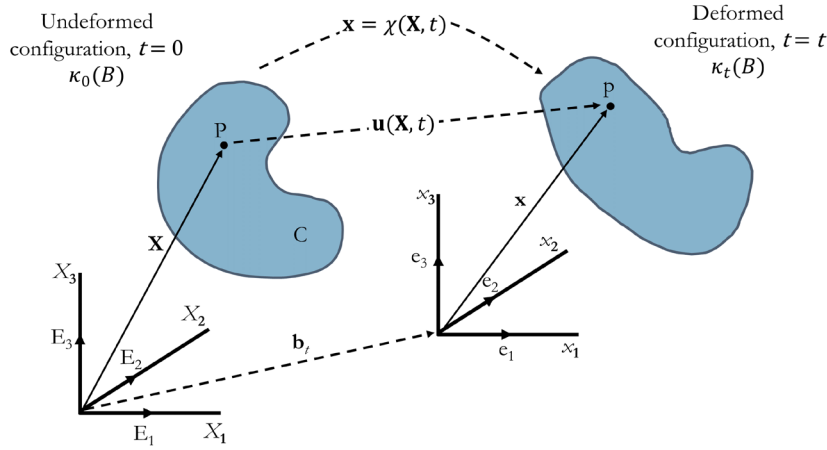


Figure 3.6: Diagram of deformation.

3.3.2 INFINITESIMAL STRESS AND STRAIN

One of the most common assumptions in elastography is that the sample behaves as a linear elastic solid, that is the deformation (or strain) in the sample is infinitely small. Here, the forces and resulting deformations are described using the infinitesimal stress and strain tensors. The stress tensor is a generic representation of the state of stress inside some constrained volume such as tissue. When an external force is applied to tissue, stresses will be generated throughout the volume in response to the force to remain in equilibrium. In analysing the stress, we consider a volume under the application of an arbitrary number of external forces $\mathbf{F}_1 \dots \mathbf{F}_n$, as illustrated in Fig. 3.7(a). To analyse the stress at an arbitrary point P , we separate the volume into two portions (I and II) along the plane S which passes through P , with a normal vector, \mathbf{n} . We assume that portion I is in equilibrium under the application of external forces \mathbf{F}_1 and \mathbf{F}_2 and the internally generated forces distributed over plane, S which represent the resulting action of portion II on portion I. The stress acting on some small area, ΔA , containing P , is determined by first considering the forces acting over this area by a resultant force $\Delta \mathbf{F}$ which is perpendicular to the plane S . According to Cauchy's stress principle, as the area, ΔA , reduces and approaches to 0, the ratio $\Delta \mathbf{F}/\Delta A$ can instead be represented as $d\mathbf{F}/dA$, defined as the surface traction or the stress vector, $\mathbf{T}^{(\mathbf{n})} = T_i^{(\mathbf{n})} \mathbf{e}_i$ at the point P with each component given as [235]:

$$T_i^{(\mathbf{n})} = \lim_{\Delta A \rightarrow 0} \frac{\Delta F_i}{\Delta A} = \frac{dF_i}{dA}. \quad (3.1)$$

The internal forces distributed throughout the entire volume can be represented accordingly via a Cauchy traction field $\mathbf{T}(\mathbf{n}, \mathbf{x}, t)$. As traction is dependent on the orientation of the plane, S , \mathbf{n} can therefore be decomposed into two components, normal stress:

$$\sigma_n = \lim_{\Delta A \rightarrow 0} \frac{\Delta F_n}{\Delta A} = \frac{dF_n}{dA}, \tag{3.2}$$

and tangential shear stress:

$$\tau = \lim_{\Delta A \rightarrow 0} \frac{\Delta F_s}{\Delta A} = \frac{dF_s}{dA}, \tag{3.3}$$

where \mathbf{s} can be two perpendicular vectors along the surface of plane S . Both normal and tangential stress are defined by a force over a surface area in units of Pascals, or alternatively N/m^2 . According to Cauchy's stress theorem, knowing the stress vectors in three mutually perpendicular planes allows for the stress vector to be determined on any plane passing through that same point and that there exists a second-order tensor field $\boldsymbol{\sigma}(\mathbf{x}, t)$, independent of \mathbf{n} [235]:

$$\mathbf{T}^{(n)} = \mathbf{n} \cdot \boldsymbol{\sigma} \quad \text{or} \quad T_j^{(n)} = \sigma_{ij} n_i. \tag{3.4}$$

The stress tensor can be represented in terms of its normal and shear stresses as shown in the following equation and illustrated in Fig. 3.7(a)(i):

$$\boldsymbol{\sigma} = \begin{bmatrix} \mathbf{T}^{(x)} \\ \mathbf{T}^{(y)} \\ \mathbf{T}^{(z)} \end{bmatrix} \equiv \sigma_{ij} = \begin{bmatrix} \sigma_{xx} & \sigma_{xy} & \sigma_{xz} \\ \sigma_{yx} & \sigma_{yy} & \sigma_{yz} \\ \sigma_{zx} & \sigma_{zy} & \sigma_{zz} \end{bmatrix} \equiv \begin{bmatrix} \sigma_{xx} & \tau_{xy} & \tau_{xz} \\ \tau_{yx} & \sigma_{yy} & \tau_{yz} \\ \tau_{zx} & \tau_{zy} & \sigma_{zz} \end{bmatrix}. \tag{3.5}$$

The individual components of stress in Eq. (3.5) are indicated on the cube faces in Fig. 3.7(a)(ii) using two subscripts. The first subscripts describe the direction of the normal relative to the plane; the second describes the direction the stress. In this description, the on-diagonal components of $\boldsymbol{\sigma}$ describe the normal stresses and the off-diagonal components, denoted by τ , describe the shear stresses.

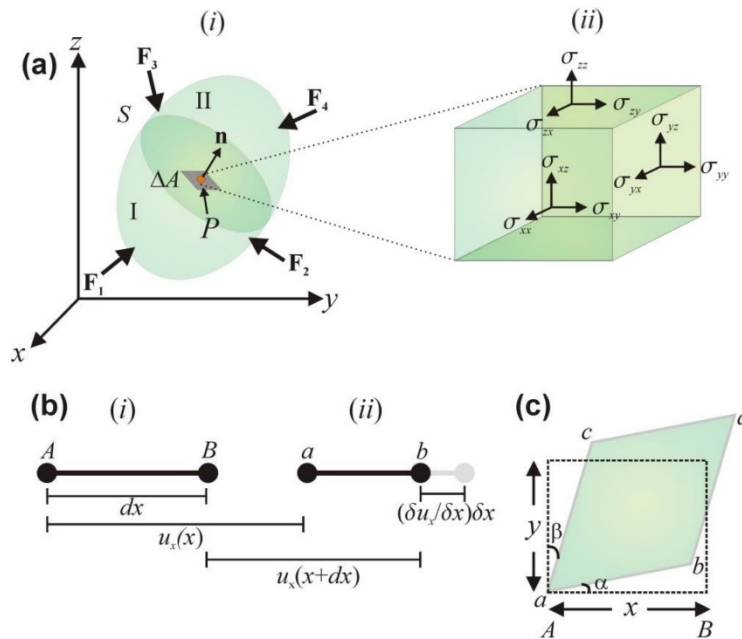


Figure 3.7: Stress and strain. (a) (i) Stress tensor components acting at the point P in a deformable body, (ii) represented by an infinitesimally small unit cube, under an applied load. (b) Normal strain along the x -axis of the cube in (a) (i) before and (ii) after deformation. (c) Shear strain in the xy -plane of the cube in (a) after deformation. Adapted from [154].

The strain tensor describes each component of the resulting deformation under the effect of an applied force. For example, we consider the strain along the x -axis of the cube shown in Fig. 3.7a(ii). Figure 3.7(b) illustrates the x -axis before (i) and after (ii) deformation in response to a compression load. The resulting displacement of point A is described as u_x and the initial length along the x -axis $|AB|$ is given by dx . After deformation, the length $|ab|$ is given as $dx + \frac{\partial u_x}{\partial x} dx$. The normal strain along this axis is, therefore, defined as the contraction of the initial dimensions:

$$\varepsilon_{xx} = \frac{|ab| - |AB|}{|AB|} = \frac{\partial u_x}{\partial x}. \quad (3.6)$$

This definition is also true for the normal strains in both the y - and z -axes; ε_{yy} and ε_{zz} are defined as $\partial u_y / \partial y$ and $\partial u_z / \partial z$, respectively. In elastography, strain defined in Eq. (3.6) is commonly referred to as local strain and is dimensionless [11]. While the definitions provided here focus on compression as it is most relevant to elastography, in general, this model is also used to describe tensile loading. Convention dictates that tensile strains are positive while compressive strains are negative. Therefore, the strain described in Fig. 3.7(b) would be negative as the quantity $\partial u_x / \partial x$ is negative.

Similar to the definitions for stress, strain can also be decomposed into normal and shear components. The xy -plane of the cube in Fig. 3.7(a) is represented in Fig. 3.7(c). Following deformation, the resulting area $\partial x \partial y$ appears as a parallelogram. Shear strain can be defined according to the change in angle between two axes that were previously perpendicular to one another. The shear strain, ε_{xy} , is given by $\alpha + \beta$, shown in Fig. 3.7(c). For small displacements gradients, $\tan(\alpha) \approx \alpha = \partial u_y / \partial x$ and $\tan(\beta) \approx \beta = \partial u_x / \partial y$, where u_y defines the displacement in the y -axis at point A. The shear strain, ε_{xy} , can therefore be defined as $(\partial u_y / \partial x + \partial u_x / \partial y)$. Interchanging both the x and y , and u_x and u_y , demonstrate that $\varepsilon_{xy} = \varepsilon_{yx}$. The shear strain components in the xy -plane can similarly be extended to describe the shear stresses in the xz - and yz -planes. Therefore, the infinitesimal strain tensor can be expressed as:

$$\varepsilon = \begin{bmatrix} \varepsilon_{xx} & \varepsilon_{xy} & \varepsilon_{xz} \\ \varepsilon_{yx} & \varepsilon_{yy} & \varepsilon_{yz} \\ \varepsilon_{zx} & \varepsilon_{zy} & \varepsilon_{zz} \end{bmatrix} = \begin{bmatrix} \frac{\partial u_x}{\partial x} & 0.5 \left(\frac{\partial u_x}{\partial y} + \frac{\partial u_y}{\partial x} \right) & 0.5 \left(\frac{\partial u_x}{\partial z} + \frac{\partial u_z}{\partial x} \right) \\ 0.5 \left(\frac{\partial u_y}{\partial x} + \frac{\partial u_x}{\partial y} \right) & \frac{\partial u_y}{\partial y} & 0.5 \left(\frac{\partial u_y}{\partial z} + \frac{\partial u_z}{\partial y} \right) \\ 0.5 \left(\frac{\partial u_z}{\partial x} + \frac{\partial u_x}{\partial z} \right) & 0.5 \left(\frac{\partial u_z}{\partial y} + \frac{\partial u_y}{\partial z} \right) & \frac{\partial u_z}{\partial z} \end{bmatrix}, \quad (3.7)$$

where the on-diagonal components describe the normal strains and the off-diagonal components describe the shear strains. It is worth noting that the shear components are scaled by 0.5 due to the symmetry between the shear strains within a plane *i.e.* $\varepsilon_{xy} = \varepsilon_{yx}$, $\varepsilon_{zx} = \varepsilon_{xz}$, and $\varepsilon_{yz} = \varepsilon_{zy}$.

3.3.3 GOVERNING EQUATIONS

The stress and strain tensors defined above provide information on the forces and deformation within a body under an applied load, however, the relationship between these two parameters specifies the mechanical properties of the sample and is defined by a set of governing equations. The first equation is derived from Newton's First Law of Motion and states that linear momentum is conserved. This can be expressed as:

$$\rho \ddot{\mathbf{u}} = \nabla \cdot \boldsymbol{\sigma} + \rho \mathbf{b}, \quad (3.8)$$

where ρ is the material density, $\ddot{\mathbf{u}}$ is the acceleration, and \mathbf{b} is the body force. The body forces in this definition refer to external forces on the body such as gravity. It can be seen from Eq. (3.8) that the rate of change of momentum must be balanced by the combination of the internal forces ($\nabla \cdot \boldsymbol{\sigma}$) and external forces ($\rho \mathbf{b}$).

The second equation is a generalisation of Hooke's Law and relates the stress and strain tensors in a linear elastic solid via a fourth-order elasticity tensor, C_{ijkl} , according to:

$$\sigma_{ij} = C_{ijkl} \varepsilon_{kl}. \quad (3.9)$$

C_{ijkl} , consists of 81 elements in a 9×9 matrix, however, due to the conservation of linear momentum, the stress tensor is symmetric ($\sigma_{ij} = \sigma_{ji}$) which reduces the number of elements in σ_{ij} to 6. Likewise, the strain tensor is also symmetric ($\varepsilon_{ij} = \varepsilon_{ji}$), reducing the number of elements in ε_{ij} to 6. This means that C_{ijkl} can be represented by a 6×6 matrix with 36 elements:

$$\begin{bmatrix} \sigma_{xx} = \sigma_1 \\ \sigma_{yy} = \sigma_2 \\ \sigma_{zz} = \sigma_3 \\ \sigma_{xy} = \sigma_4 \\ \sigma_{xz} = \sigma_5 \\ \sigma_{yz} = \sigma_6 \end{bmatrix} = \begin{bmatrix} C_{11} & C_{12} & C_{13} & C_{14} & C_{15} & C_{16} \\ C_{21} & C_{22} & C_{23} & C_{24} & C_{25} & C_{26} \\ C_{31} & C_{32} & C_{33} & C_{34} & C_{35} & C_{36} \\ C_{41} & C_{42} & C_{43} & C_{44} & C_{45} & C_{46} \\ C_{51} & C_{52} & C_{53} & C_{54} & C_{55} & C_{56} \\ C_{61} & C_{62} & C_{63} & C_{64} & C_{65} & C_{66} \end{bmatrix} \begin{bmatrix} \varepsilon_{xx} = \varepsilon_1 \\ \varepsilon_{yy} = \varepsilon_2 \\ \varepsilon_{zz} = \varepsilon_3 \\ \varepsilon_{xy} = \varepsilon_4 \\ \varepsilon_{xz} = \varepsilon_5 \\ \varepsilon_{yz} = \varepsilon_6 \end{bmatrix}. \quad (3.10)$$

In practice, it is not feasible to fully characterise the 36 elastic elements in the elasticity tensor, and so a number of simplifying assumptions are often made in elastography to reduce the complexity of this problem [20,237]. These assumptions are applied widely in elastography and are used throughout the work presented in this Thesis. The key simplifying assumption is that the material behaves as an elastically isotropic material, that is the mechanical properties of a point in the material are the same in all directions, regardless of the frame of reference. This assumption imparts maximum symmetry on the elasticity tensor, effectively reducing the number of elements to 2 [235]:

$$\begin{bmatrix} \sigma_1 \\ \sigma_2 \\ \sigma_3 \\ \sigma_4 \\ \sigma_5 \\ \sigma_6 \end{bmatrix} = \begin{bmatrix} C_{11} & C_{12} & C_{12} & 0 & 0 & 0 \\ 0 & C_{11} & C_{12} & 0 & 0 & 0 \\ 0 & 0 & C_{11} & 0 & 0 & 0 \\ 0 & 0 & 0 & C_{11} - C_{12} & 0 & 0 \\ 0 & 0 & 0 & 0 & C_{11} - C_{12} & 0 \\ 0 & 0 & 0 & 0 & 0 & C_{11} - C_{12} \end{bmatrix} \begin{bmatrix} \varepsilon_1 \\ \varepsilon_2 \\ \varepsilon_3 \\ \varepsilon_4 \\ \varepsilon_5 \\ \varepsilon_6 \end{bmatrix}. \quad (3.11)$$

Eq. (3.11) can be written in terms of the Lamé-constants, λ and μ :

$$\begin{bmatrix} \sigma_{11} \\ \sigma_{22} \\ \sigma_{33} \\ \sigma_{12} \\ \sigma_{13} \\ \sigma_{23} \end{bmatrix} = \begin{bmatrix} \lambda + 2\mu & \lambda & \lambda & 0 & 0 & 0 \\ 0 & \lambda + 2\mu & \lambda & 0 & 0 & 0 \\ 0 & 0 & \lambda + 2\mu & 0 & 0 & 0 \\ 0 & 0 & 0 & 2\mu & 0 & 0 \\ 0 & 0 & 0 & 0 & 2\mu & 0 \\ 0 & 0 & 0 & 0 & 0 & 2\mu \end{bmatrix} \begin{bmatrix} \varepsilon_{11} \\ \varepsilon_{22} \\ \varepsilon_{33} \\ \varepsilon_{12} \\ \varepsilon_{13} \\ \varepsilon_{23} \end{bmatrix}, \quad (3.12)$$

which can be represented more concisely as:

$$\sigma_{ij} = \lambda \varepsilon_{kk} \delta_{ij} + 2\mu \varepsilon_{ij}, \quad (3.13)$$

where δ_{ij} is the Kronecker delta which has the values of 1 when $i = j$, and 0 when $i \neq j$. In this expression, stress and strain are related by just two independent mechanical properties, λ and μ . It is also common in elastography to assume that the material is homogeneous such that the mechanical properties of a material are uniform throughout the body. Under this assumption, λ and μ remain constant, *i.e.*, $\nabla \lambda$ and $\nabla \mu \rightarrow \mathbf{0}$. Combining Eqs.(3.8) and (3.13) and ignoring the effect of body forces produces *Navier's equation*:

$$(\lambda + \mu) \nabla (\nabla \cdot \mathbf{u}) + \mu \nabla^2 \mathbf{u} = \rho \ddot{\mathbf{u}}. \quad (3.14)$$

Although the assumptions necessary to derive Eq. (3.14) are invariably violated in heterogenous tissues, they are adequate to accurately characterise tissue mechanical

properties in many cases. However, care must be taken to ensure the particular way in which the assumptions are violated is understood in each case.

3.3.4 ELASTIC MODULI

The constitutive equation completely describes the relationship between the stress and strain components in terms of the Lamé constants. Applying certain assumptions about the behaviour of stress and strain in a material allows several elastic moduli to be derived from some linear combination of the Lamé constants. As these moduli are related by the Lamé constants, for an isotropic material, characterisation of two moduli is sufficient to fully define the remaining ones.

Young's modulus (E) describes the stiffness of a material in either uniaxial tension or compression. It is defined as the slope of the stress-strain curve for a material and has the same units as stress, *i.e.*, Pascals, as strain is dimensionless [238]:

$$E = \frac{\sigma_z}{\varepsilon_z}. \quad (3.15)$$

In terms of Lamé constants, Young's modulus is expressed as $E = \mu(3\lambda + 2\mu)/(\lambda + \mu)$.

Poisson's ratio (ν) describes the ratio of axial to lateral strain in a material under an applied load and provides a measure of the material compressibility. For a material under compression in the z -axis, Poisson's ratio can be expressed as [238]:

$$\nu = -\frac{\varepsilon_x}{\varepsilon_z} = -\frac{\varepsilon_y}{\varepsilon_z}. \quad (3.16)$$

Poisson's ratio is a unitless measure and soft tissues typically exhibit a Poisson's ratio of $0 < \nu < 0.5$. Materials with a Poisson's ratio of 0.5 completely conserve their volume under compression and are termed incompressible. Soft biological tissues have reported Poisson's ratios from 0.45-0.49 [1] and are therefore often assumed to be incompressible. Poisson's ratio is expressed using Lamé constants as $\nu = \lambda/2(\lambda + \mu)$.

Shear modulus (G) defines the relationship between shear stress and shear strain for a load applied parallel to a plane. For example, shear modulus in the xy -plane can be expressed as [238]:

$$G = \frac{\sigma_{xy}}{\varepsilon_{xy}}. \quad (3.17)$$

The Lamé-constant μ defines the shear modulus and similarly to Young's modulus is given in terms of Pascals. As shear modulus is one of the Lamé constants, a relationship between Young's modulus, shear modulus and Poisson's ratio can be expressed as $G = E/2(1 + \nu)$.

Bulk modulus (K) is a measure of how a material resists uniform compression, defined as the ratio of hydrostatic pressure to change in volume [238]:

$$K = -\frac{\sigma}{\Delta V/V}. \quad (3.18)$$

The stress components in the bulk modulus are uniform, such that $\sigma = \sigma_x = \sigma_y = \sigma_z$ and is given in units of Pascals. In terms of Lamé constants, bulk modulus is given as $K = (3\lambda + 2\mu)/3$.

Longitudinal modulus (M) describes the ratio of axial stress to axial strain, however, unlike Young's modulus, all other strain components are considered to be 0. Longitudinal modulus is predominantly used to describe pressure waves and is commonly referred to as *P-wave modulus*, defined as:

$$M = \frac{\sigma_x}{\varepsilon_x} = \rho_x V_p^2, \quad (3.19)$$

where V_p is the velocity of the propagating pressure wave and ρ_x is the material density. The longitudinal modulus for isotropic materials is defined by the Lamé constants as $M = \lambda + 2\mu$ and uses units of Pascals.

3.3.5 FIRST-ORDER APPROXIMATIONS IN ELASTOGRAPHY

In general, elastography, seeks to derive one or more of the elastic moduli from a tissue sample to infer information about its disease state. However, it can prove challenging to experimentally determine the elastic moduli defined in the previous Section. This is especially true when analysing heterogeneous samples and utilising intricate loading schemes. As such, for a linear elastic and isotropic material, we describe deformation using Navier's equation, Eq. (3.14). While several simplifying assumptions have been applied to derive this equation, it is still difficult to derive elastic moduli in practical elastography applications. Therefore, several additional assumptions related to the sample deformation are applied, termed *first-order approximations*. Elastography techniques can be classified as either *static* or *dynamic*, depending on which approximations are used and how the sample is loaded.

Static or quasi-static elastography is the term used to describe techniques which apply deformation over a long enough time scale that the effect of inertia is negligible (*i.e.*, $\rho \dot{\mathbf{u}} = 0$). These techniques also assume that the sample is incompressible, such that the divergence, $\nabla \cdot \mathbf{u}$, is approximately zero, which reduce Navier's equation (Eq. (3.14)) to the Laplace equation [153]:

$$\nabla^2 \mathbf{u} = 0. \quad (3.20)$$

The solutions to Laplace's equation determined by the extrema of displacement, \mathbf{u} at the boundaries of the sample [153]. If we assume the simplest case of a homogeneous material under uniaxial compression in z , then the solution for displacement, $\mathbf{u}_z(z)$, is linearly proportional to z and the strain, ε_z , which is the derivative of displacement, is therefore

constant. In the case of a mechanically heterogeneous sample, the strain would vary in such a way that the size and direction of the variation is proportional to the elastic moduli of the contrasting feature. To derive elastic moduli of the sample directly, it is common to assume that the stress throughout the sample is uniaxial. This approach was adopted in the early demonstrations of USE by Ophir *et al.* [163] and in OCE by Schmitt [18] where strain provided a qualitative measure of tissue stiffness, however, more recent techniques have enabled the measurement of Young's modulus by implementing methods for determining the surface stress in addition to sample strain [106,239,240].

Dynamic elastography techniques typically apply a point load in the sample via high frequency loading and track the propagating shear wave to infer the sample mechanical properties. These techniques can be further classified depending on the type of mechanical wave measured. One of the most common dynamic elastography methods is shear wave elastography, which causes the sample to deform orthogonal to the direction of the propagating wave, while preserving the material volume ($\nabla \cdot \mathbf{u} = 0$). Navier's equation, therefore, reduces to the shear wave equation:

$$\nabla^2 \mathbf{u} = \frac{1}{c_s^2} \ddot{\mathbf{u}}, \quad (3.21)$$

where the shear wave speed, c_s , is given as:

$$c_s = \sqrt{\frac{\mu}{\rho}}. \quad (3.22)$$

Therefore, shear modulus can be determined by tracking the propagation speed, making some assumptions regarding the material density and ignoring any boundary effects.

Harmonic loading is another dynamic technique which applies a continuous sinusoidal load to generate standing waves within the sample. The spatial frequency of the standing wave can be used to determine the wave propagation speed and indirectly infer the material shear modulus. This method of loading allows for imaging over a longer timeframe, however, is highly dependent on the boundary conditions and is only suitable for applications where the boundary is well-defined.

3.4 OTHER MECHANICAL PROPERTIES

It is often convenient to model the mechanical response of tissue as a linearly elastic isotropic solid, despite soft biological tissue rarely behaving this way. In fact, most tissues exhibit some degree of viscoelasticity, poroelasticity, anisotropy, and nonlinear elasticity. While the mechanical model introduced in Section 3.3 does not describe the effects of these mechanical properties, and they are considered negligible in most elastography techniques, they can

provide additional mechanical contrast [241–243]. Here, we will briefly provide descriptions of these concepts for completeness and to provide some insight into potential sources of error arising from the simplified mechanical model.

Viscoelasticity describes the combination of both elastic and viscous behaviour, such that the application of an external force causes a temporal response in the deformation of viscoelastic materials. When a body undergoes a strain which is maintained constant, and the induced stresses decrease with time the body is said to be undergoing *stress relaxation*. Likewise, if the body is suddenly stressed, and the stress is maintained constant, but the deformation of the body changes with time, then the body is said to be undergoing *creep*. Finally, *hysteresis* is a phenomenon where a body exhibits a different stress-strain curve when loaded, compared to unloaded. These three phenomena collectively describe viscoelasticity [1]. When elastography imaging is performed over a relatively long acquisition time, such as the acquisition of a 3-D volume, the effects of viscoelasticity can manifest as localised differences in mechanical contrast, between spatial regions acquired at the start of the acquisition and at the end.

Poroelastic materials are biphasic materials containing an elastic matrix and an interconnected network of fluid-filled pores or voids. *Poroelasticity* describes the interaction between solid deformation and fluid flow inside a material as deformation of the body will impact the behaviour of the fluid, and vice-versa [244].

Anisotropy is the property of materials which exhibit different mechanical properties, depending on the orientation of the measurement. For example, tendons are a biological material that exhibit high degrees of anisotropy due to the linear arrangement of fibres. When imaging anisotropic materials, different mechanical properties will be observed, depending on its orientation [245].

Nonlinear elasticity has been defined using two different definitions, depending on the field of study. In continuum mechanics, nonlinear elasticity describes large deformations such that the infinitesimal strain theory no longer holds. Nonlinear elasticity in biology, however, describes materials which exhibit varying mechanical properties depending on the amount of loading applied. The two definitions effectively describe the concept of nonlinear elasticity from the theoretical and experimental perspectives, respectively [236]. As the mechanical properties of nonlinear elastic materials are dependent on the loading applied, the error induced by using a linear-elastic model increases with applied strain. Therefore, elastography methods typically apply low strains (<10%) to the sample where the stress-strain response is approximately linear, minimising the error in the measurement [20].

3.5 TISSUE ELASTICITY

The mechanical properties of tissue is governed by its constituent materials and how they are arranged [246]. In Fig. 3.8, a range of Young's moduli are given for many different tissue constituents, structures and organs [20]. It can be seen from these values that tissue exhibits varying Young's moduli from 10 Pa to 1 GPa, providing a broad range of mechanical contrast detectable by elastography techniques.

Tissues are composite materials, composed of constituents which are broadly classified as cellular (*e.g.*, blood, adipose tissue and epithelial cells); polymer (*e.g.*, collagen); elastomer (*e.g.*, elastin); and ceramic (*e.g.*, dentin) [20,246]. The Young's modulus of tissue is proportional to the density of these material constituents, with a higher density producing a higher Young's modulus [247].

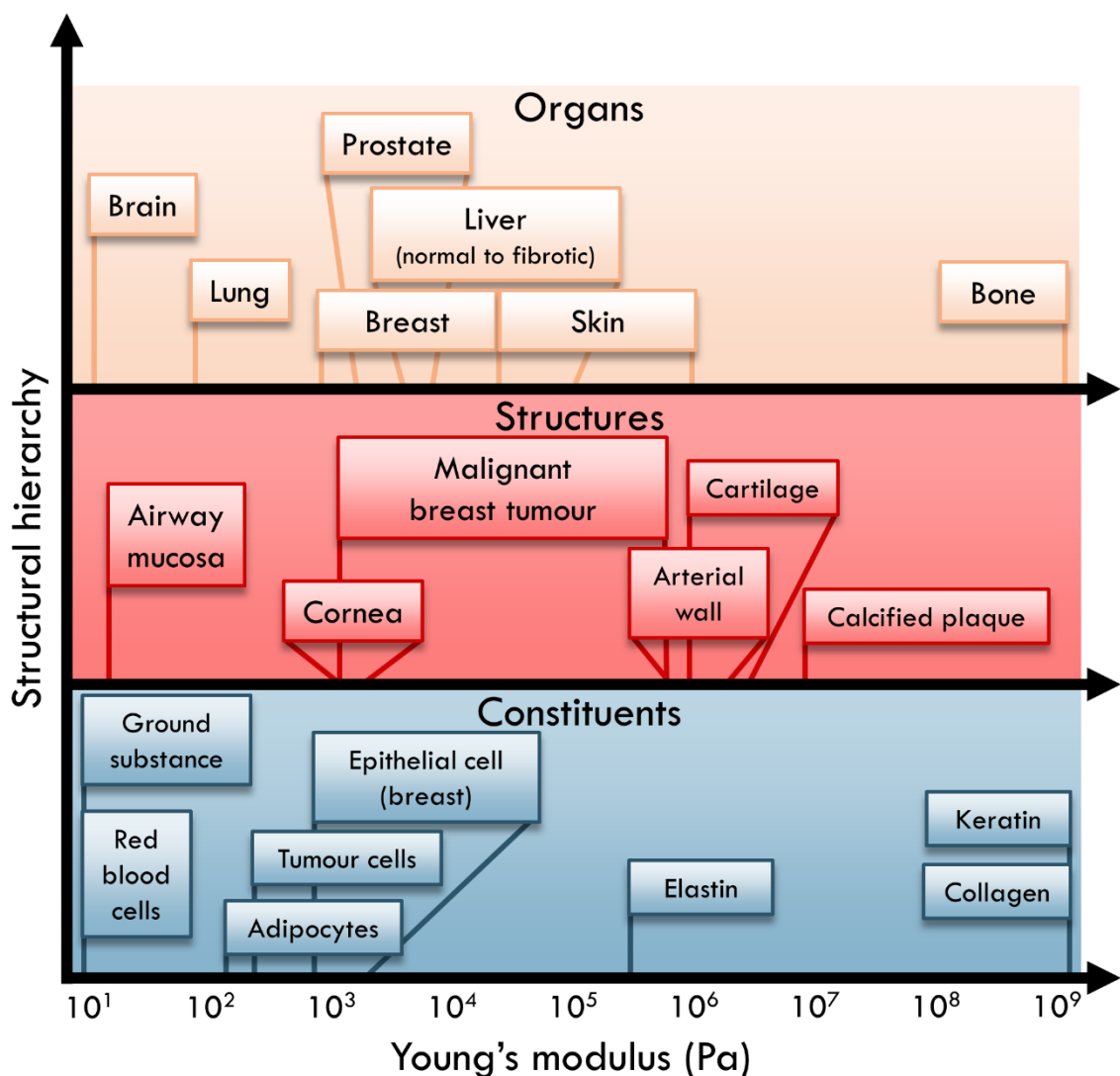


Figure 3.8: Reported values and ranges of Young's modulus for selected tissues and tissue constituents. Adapted from [20].

The constituents of biological tissue are hierarchically arranged and exhibit varying mechanical properties at different length scales from the molecular level through to whole

organs. This structural arrangement is linked to tissue function, *e.g.*, tendon is able to efficiently transfer loads between muscle and bone due to its arrangement in bundles of parallel fibres. Atomic force microscopy has been used to study the effects of length scale on tissue mechanical properties with one study observing a 100-fold increase in Young's modulus of porcine articular cartilage from the nanoscale (~ 20 kPa) to the microscale (~ 2.6 MPa) [248]. This study highlights the structure- and scale-dependent nature of tissue mechanical properties.

The onset of disease affects tissue at each level of the structural hierarchy, resulting in changes to the mechanical properties from the nano- to the macro-scale. In analysing the mechanical properties of individual cells and the surrounding extracellular matrix, studies have shown an inextricable relationship between disease progression and cellular biomechanics [249,250]. One study looking at the relative mechanical properties of cancerous and benign mesothelial cells reported Young's moduli of 0.53 kPa and 1.97 kPa, respectively [251]. Interestingly, disease causes a softening of individual cells, however, at the macroscopic scale, disease is often characterised by an increase in mechanical properties, forming the basis for diagnostic techniques such as manual palpation and elastography. These elastography techniques have reported Young's moduli of ~ 100 s kPa for macroscopic cancerous tissue [159,252], with the increase attributed to elevated collagen production stiffening the stroma that surrounds the tumour cells [253].

3.6 MECHANICAL MODEL FOR OPTICAL ELASTOGRAPHY TECHNIQUES IN THIS THESIS

Having described the continuum mechanics model used for elastography in the previous Sections of this Chapter, we will now briefly consider how this model is applied to the two optical elastography techniques developed and used in this Thesis, namely, quantitative micro-elastography (QME) and optical palpation. Both are compressive elastography techniques which seek to measure the local sample elasticity and surface stress, respectively [106,225]. In QME, tangent modulus (which is the same as Young's modulus in a linear elastic material, and thus is also defined as E), is measured by detecting the local axial stress, σ_{zz} , through a compliant layer and the local axial strain, ϵ_{zz} , through phase-sensitive detection of the sample displacement using OCT under a quasi-static load. This technique assumes that the stress and strain tensors consist of just one component each in the axial direction and that the sample is a homogeneous, linear-elastic, isotropic material. As such, tangent modulus is represented by the generalised Hooke's law [106]:

$$E = \frac{\sigma_{zz}}{\varepsilon_{zz}}. \quad (3.23)$$

Optical palpation in contrast, only measures the 2-D surface stress, σ_{zz} , to provide mechanical contrast, while making the same assumptions about the sample and the uniaxial application of stress. The mechanical contrast, therefore, proportional to the underlying elasticity from features within the sample [225]:

$$E \propto \sigma_{zz}. \quad (3.24)$$

To avoid violating the assumptions that underpin Eqs. 3.23 and 3.24, elastography techniques such as those described in this Thesis limit the applied strain to the linear elastic region of the stress-strain curve. For biological tissue such as breast tissue, this has been reported to be less than 20% strain [254].

CHAPTER 4

OPTICAL COHERENCE ELASTOGRAPHY

Optical coherence elastography (OCE) is a prominent optical elastography technique that has shown promise in the assessment of multiple diseases based on their distinct mechanical properties. In this Thesis, the diagnostic potential of OCE has motivated the development of novel imaging probes as well as the development of a new optical elastography technique. In this Chapter, a comprehensive background of OCE is provided, first describing the fundamentals of optical coherence tomography (OCT), before detailing how displacement is measured in OCE and the different loading techniques implemented. Finally, this Chapter concludes with a description of the two OCE variants, quantitative micro-elastography (QME) and optical palpation, explored in this Thesis.

4.1 OPTICAL COHERENCE TOMOGRAPHY

As outlined in the Introduction, optical elastography produces maps of mechanical contrast by measuring the deformation induced in a sample by a mechanical load using an optical imaging modality. In OCE, the underlying imaging modality is OCT, a non-invasive optical imaging technique that generates volumetric data of tissue microstructure by measuring the interference between the localised back-reflection of light from within the sample and from the reference mirror. OCT has predominantly been applied to clinical applications in areas such as ophthalmology [255–257], cardiology [258–260] and endoscopy [261,262], where its depth-sectioning capability provides diagnostic information about the tissue micro-structure.

In OCT, low-coherence light is directed through a low numerical aperture (NA) lens into the sample, where it is backscattered at the boundaries of tissue with different refractive indices [263]. OCT measures the time-of-flight of the backscattered light, similarly to how ultrasound measures the echo delays of sound waves, however, due to the speed of light, the delays are too short to be measured directly. Instead, low coherence interferometry is used to measure the time-of-flight [264,265]. This involves splitting the broadband light from the source into two optical paths, known as the sample path and the reference path. The light backscattered from the sample path is interfered with the light reflected (typically from a mirror) in the reference path to produce an interference pattern, which is recorded on a

detector [263,264]. The relative delay between the reflected light in the two paths is encoded in the detected interference pattern. Importantly, constructive interference necessary to achieve OCT imaging only occurs when the optical path lengths, that is the distance travelled by the light in the sample and reference paths, respectively, is matched to within the coherence length of the light source ($\sim 10 \mu\text{m}$). In biological tissues, where there are typically many scattering interfaces, scanning the reference mirror in time-domain OCT (TD-OCT) or analysing the interference spectrum in Fourier-domain OCT (FD-OCT) allows for a one-dimensional (1-D) depth-resolved scan of the sample reflectivity, where the intensity of the scan is used to visualise the sample microstructure. This is known as an *A-scan* and takes its name from the conventions used in ultrasound [266].

In OCT, A-scans (Fig. 4.1(a)) can be acquired at different spatial locations by scanning the beam along an axis orthogonal to the OCT beam (denoted as the z -axis), to generate two-dimensional (2-D) scans, termed *B-scans* in the xz -plane (Fig. 4.1(b)). Acquiring multiple B-scans at different spatial locations along the third axis produces three-dimensional (3-D) volumes, termed *C-scans* (Fig. 4.1(c)) [267]. These volumes can then be sectioned to provide different orientations of the sample such as *en face* (Fig. 4.1(d)) views at different depths [266].

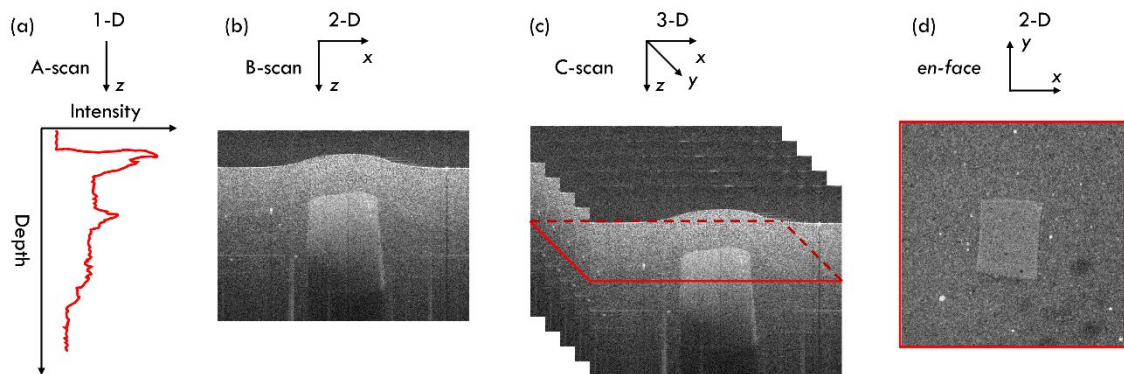


Figure 4.1: Conventional OCT scan modes. (a) A-scan, (b) B-scan, (c) C-scan and (d) *en face* images of a structured silicone inclusion phantom.

The first demonstration of OCT by Huang *et al.* in 1991 [264] utilised TD-OCT configurations where A-scans are acquired by temporally shifting the position of the reference mirror (varying the reference arm optical path length) to reconstruct a reflectivity profile in depth, *i.e.* an A-scan (Fig. 4.2). The second generation of OCT systems saw the implementation of FD-OCT where the spectral interference frequencies were used to generate A-scans. While initially proposed by Fercher *et al.* in 1995 [268], FD-OCT became prominent in 2003 after several independent studies demonstrated the improved image acquisition speed and sensitivity afforded by this configuration [203,269,270]. In contrast to TD-OCT, the reference mirror in FD-OCT is fixed and the A-scans are generated from the analysis of the interference spectrum. FD-OCT can be further categorised into two

techniques based on differences in the light source and how the interference pattern is detected; spectral-domain OCT (SD-OCT) which uses a continuous bandwidth light source and a spectrometer to measure the interference spectrum on a line-scan camera and was the first of the FD-OCT techniques to be developed [270–273]; and swept-source OCT (SS-OCT), where a tuneable light source rapidly sweeps across a broad bandwidth as a function of time and the interference pattern is detected by a single photodiode [269,274–276]. A diagram of an SD-OCT system is shown in Fig. 4.3

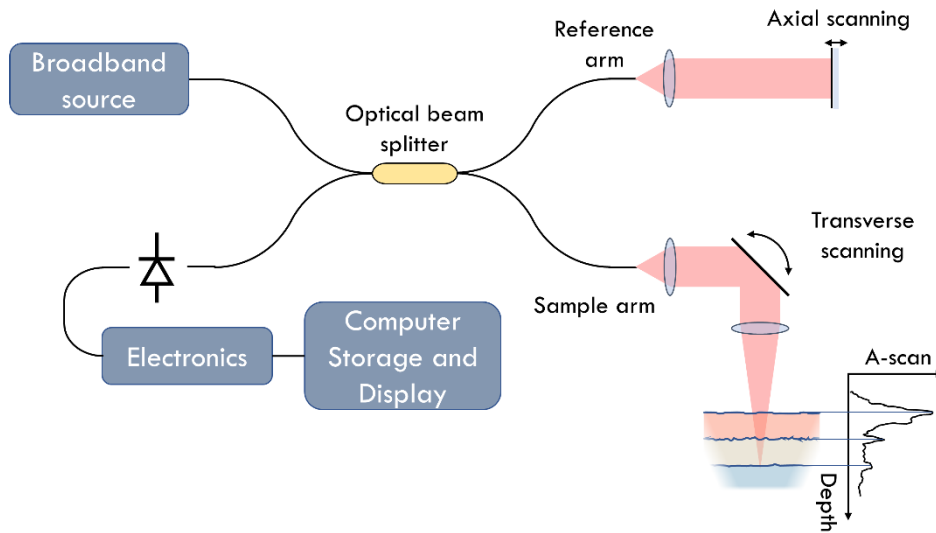


Figure 4.2: Diagram of a TD-OCT system showing a reference arm with an axially scanning mirror.

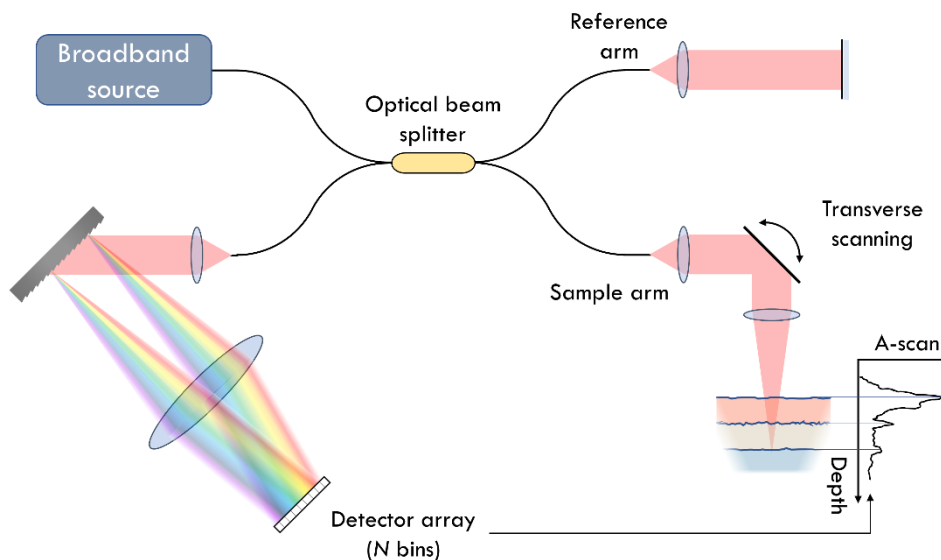


Figure 4.3: Diagram of an SD-OCT system showing a reference arm with a stationary mirror and the combined interference spectrum being separated into the individual frequency components by a spectrometer.

4.1.1 OCT IMAGING PARAMETERS

Resolution is one of the key imaging parameters of OCT and describes the smallest resolvable separation between two point objects. In OCT, there are two resolution components: axial resolution which is defined by the light source, and lateral resolution

which is defined by the objective lens in the sample arm. It is important to note that these resolution components are largely decoupled (although, if the NA of the lens is high enough it will impact the axial resolution) [266]. For a Gaussian spectrum, axial resolution, δ_z , is often defined as the full-width-at-half-maximum (FWHM) of the OCT for a single scatterer, given as [266]:

$$\delta_z = \frac{2 \ln 2}{\pi} \frac{\lambda_0^2}{n \Delta\lambda}, \quad (4.1)$$

where λ_0 is the central wavelength of the light source, $\Delta\lambda$ is the optical bandwidth and n is the refractive index of the sample. The lateral resolution is given as [266,277]:

$$\delta_x = \sqrt{2 \ln 2} \frac{\lambda_0}{\pi NA}, \quad (4.2)$$

where NA is the numerical aperture of the objective lens and defines how lateral resolution is dependent on the focusing power of the objective lens. While a higher numerical aperture lens would provide tighter focusing and improved lateral resolution, it would also reduce the depth of focus, DOF_z , defined as the axial distance along the beam between locations where the cross-sectional beam area is twice as large as the beam waist, given as [277]:

$$DOF_z = \frac{n \lambda_0}{2 \pi NA^2}. \quad (4.3)$$

Therefore, there exists a trade-off in OCT between lateral resolution and depth of focus. The lateral field of view, FOV_x , for OCT systems is typically 10-15 mm and is limited by the ability to telecentrically (constant, non-angular FOV) scan the beam across the sample. The lateral field of view is defined by [266]:

$$FOV_x = \frac{f \tan \theta}{2} \quad (4.4)$$

where f is the focal length of the objective lens and θ is two times the angular deviation in the scanning mirror [266]. The key imaging OCT parameters described above are shown in Fig. 4.4.

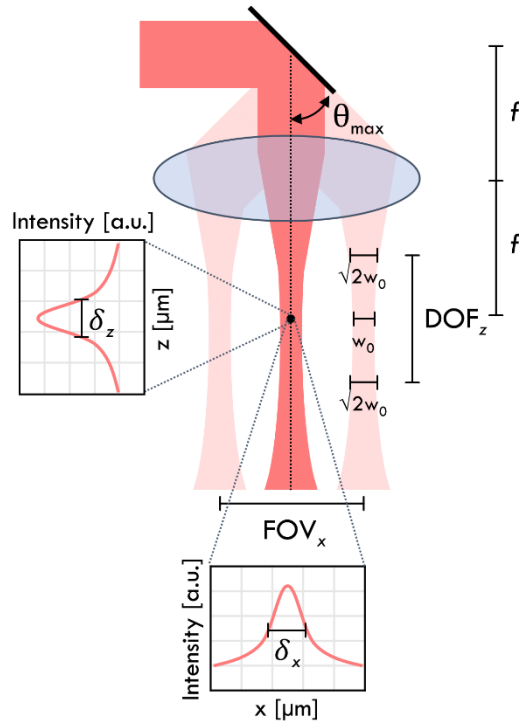


Figure 4.4: Diagram of OCT imaging parameters for a Gaussian beam. θ_{max} maximum angle of scanning mirror; w_0 beam waist; DOF_z axial depth of field; f focal length; FOV_x lateral field of view; δ_z axial resolution; and δ_x lateral resolution. Adapted from [278].

The OCT signal is susceptible to several noise sources including electrical noise, thermal noise, quantisation noise and mechanical noise. In OCT, signal-to-noise ratio (SNR) is a measure desired signal relative to the background noise and is defined as the ratio of OCT signal intensity to the intensity of the noise sources,

$$OCT_{SNR} = \frac{\langle S \rangle^2}{\sigma_n^2}, \quad (4.5)$$

where S is the amplitude of the OCT signal and σ_n is the standard deviation of the noise. Due to the potentially large variations in SNR within a single image, it is frequently presented on a logarithmic scale in units of decibels (dB) [278],

$$OCT_{SNR_{dB}} = 10 \log_{10} OCT_{SNR} = 20 \log_{10} \frac{\langle S \rangle}{\sigma_n}. \quad (4.6)$$

Sensitivity in OCT is defined as the smallest signal measurable by the system. The sensitivity of OCT devices, Σ , is defined as reciprocal of the minimal sample arm reflectivity, $R_{s,min}$, for an OCT SNR of 1 [203],

$$\Sigma = \frac{1}{R_{s,min}}. \quad (4.7)$$

Therefore, a smaller $R_{s,min}$ will produce a higher sensitivity. Sensitivity can also be defined as the maximum OCT SNR produced by imaging a perfect reflector [269]. Sensitivity, like

SNR, is described in units of dB, relative to the system noise [278]. In practice, the sensitivity can be determined by dividing the measured SNR of the sample by the noise floor [203].

The optimal central wavelength for OCT systems is another important parameter and is largely dependent on the sample and application. Longer wavelengths are less susceptible to optical scattering and can penetrate further into the tissue sample, however, absorption of light by water is dependent on the wavelength. Most OCT systems, therefore, employ light sources with wavelengths centred around 800-1300 nm, as this overlaps with the *optical diagnostic window* (650-1360 nm), maximising the penetration depth of the incident light in tissue [263,279]. This typically provides imaging of 1-2 mm in depth, depending on the sample optical properties [263,264,277].

4.2 OPTICAL COHERENCE ELASTOGRAPHY

4.2.1 MEASUREMENT OF DISPLACEMENT WITH OCT

In OCE, mechanical properties are estimated from the resulting sample displacement under an applied load using an appropriate mechanical model. In initial studies, displacement was estimated between OCT B-scans by cross-correlation approaches [18,280,281]. These methods tracked the small granular features that arise in coherent imaging techniques, termed speckle [282]. Speckle arises from interference between light backscattered from sub-resolution particles within each resolution element of the OCT system. Speckle is temporally invariant in a stationary sample, however, under an applied load, the speckle pattern will displace and can be described by the *frozen-speckle model* [283]. This model assumes that the speckle pattern does not change with displacement and the relative displacement between two speckle patterns can be tracked, often by cross-correlation, in 1-D, 2-D and 3-D [284,285]. Speckle tracking methods are limited, however, as the spatial resolution in the elastogram is degraded compared to the OCT resolution due to the size of the window needed to perform the cross-correlation (~ 4 -5 times the OCT resolution). Additionally, the dynamic range for displacement using speckle-tracking is limited by the size of speckle at the lower end and the decorrelation of speckle in response to sample displacements above $\sim 0.5 \times$ the OCT resolution at the upper limit [20,283,286].

Phase-sensitive detection has also been implemented in OCE [287–289]. Its emergence in OCE coincided with the implementation of FD-OCT systems as they enabled the complex form (providing access to both intensity and phase) of the depth-resolved signal to be readily obtained. This method compares the difference in depth-resolved phase between two successive OCT scans in an unloaded and loaded state. The displacement between the OCT scans results in a corresponding phase shift, $\Delta\phi$ [287]. Phase-sensitive detection allows for

axial tissue displacement to be estimated on a scale set by the optical wavelength, rather than the axial resolution. The displacement in the axial direction is related to the phase difference by [288–290]:

$$u_z = \frac{\Delta\phi \lambda_0}{4 \pi n} \quad (4.8)$$

where λ_0 is the central wavelength of the light source and n is the refractive index of the sample. The sensitivity of this method, that is the smallest detectable change in phase difference, $\sigma_{\Delta\phi}$, is determined by the OCT SNR, defined in Eq. (4.6). Assuming the SNR is sufficiently high ($|S| \gg |\sigma_n|$), then the standard deviation of a measured phase, ϕ , can be described as

$\sigma_\phi^2 = \frac{1}{2} \left(\frac{|\sigma_n|}{|S|} \right) = \frac{1}{2} (\text{SNR})^{-1}$. Therefore, the standard deviation between two measured phases, $\Delta\phi$, can be described according to [291]:

$$\sigma_{\Delta\phi} = \sqrt{2\sigma_\phi^2} = \frac{1}{\sqrt{\text{OCT}_{\text{SNR}}}} \quad (4.9)$$

4.2.2 OCE LOADING METHODS

A key aspect in OCE is the loading method which induces deformation in the sample. The loading method determines what mechanical model must be used to estimate a mechanical property from measured deformation. Here, we introduce the three main loading methods commonly used in the OCE techniques, namely, compression, harmonic, and transient loading.

Compression

Compressive loading was the loading mechanism used in many initial OCE demonstrations [18] and remains prominent in contemporary OCE techniques. This method of mechanical loading is applied in a quasi-static and step-wise manner at relatively low frequency (<50 Hz) to avoid the generation of propagating elastic waves in the sample [155]. Compressive loading induces a local strain in the tissue, defined as the gradient of axial displacement with depth, which is mapped into an elastogram (Fig. 4.5(a)) [20]. While strain is a relative quantity, under the simplified mechanical model for elastography in Chapter 3, stress applied by compressive loading is assumed to be uniform throughout the sample, therefore, the axial component of strain is considered inversely proportional to the elastic modulus.

Compression loading is a relatively simple and practical loading method which enables rapid acquisition over a large field of view as the entire area of interest is loaded simultaneously: 3-D volumes have been acquired using compressive loading in as little as

5 seconds [201]. While strain provides maps of mechanical contrast, these values are qualitative. To address this limitation, a variant of compression OCE has been proposed in which a transparent, compliant silicone layer is placed between the imaging window and tissue, and the layer thickness under compression is measured to provide an estimate of axial stress at each spatial location in the elastogram [106]. This stress measurement is effectively the basis of optical palpation and will be discussed further in Section 4.3.2. By measuring both stress and strain, the elastic modulus, can be estimated, quantifying the sample mechanical properties and increasing the contrast in elastograms by as much as 100 times [155]. This is known as QME [106] and is described in greater depth in Section 4.3.1. Compression OCE is the main loading mechanism used in this Thesis as the low complexity of the technique makes it easier to implement in optical elastography probes.

Harmonic

OCE is also performed using dynamic loading mechanisms. One method applies a continuous single-tone sinusoidal excitation at a single frequency to induce harmonic tissue motion. Harmonic loading may be applied in a localised area or, similarly to compression OCE, across the entire sample in the field of view. In the presence of reflective boundaries and under steady-state conditions, harmonic excitation can lead to the generation of standing waves at the resonant frequencies of the sample as shown in Fig. 4.5(b). The resonant frequency is determined by sweeping the excitation through a range of frequencies and is related to the elastic modulus of the sample [292]. Harmonic OCE is unique in that it is dependent on the boundary effects that are typically avoided in other OCE loading methods. This type of loading is, therefore, beneficial when imaging tissue such as the eye [293] or eardrum [294], when the mechanical boundaries are well defined. The challenge, however, is when the boundary conditions are not well defined as the measured resonance is a function of both the sample's structure and boundaries, as well as its mechanical properties, and it is challenging to decouple these mechanical parameters [155]. Another method, termed spectroscopic OCE, applies harmonic loading over a range of frequencies to generate local vibration in the sample. By measuring the vibrational amplitude, the viscoelastic properties can be inferred [295].

Transient

Dynamic loading can also be applied by a local transient (pulsed) load which generates a propagating wave in the sample. In this context, transient loading refers to the lateral propagation of waves in the sample, however, axially transient OCE has also been performed whereby the transient response is measured along the axis of loading [296]. Transient OCE

has been implemented using several different configurations such as contacting indenters, acoustic radiation force (ARF), focused air jets and pulsed lasers [20–22]. The Young's modulus in transient OCE is estimated from the phase velocity of the propagating wave, as detected by OCT (Fig. 4.5(c)) [297]. Under the simplifying assumptions of uniform density, mechanical homogeneity and a known Poisson's ratio, the square root of the elastic modulus is proportional to the measured phase velocity [20–22]. Acoustic wave propagation and, hence, the corresponding elastic modulus, is influenced by the sample geometry and the excitation method used. The nature of propagation differs with depth and in the presence of layers and are thus described differently: waves at or close to the tissue surface are described as surface acoustic or Rayleigh waves [297]; wave propagation in thick tissues are described as shear waves; and wave propagation along a layered medium are described as Lamb or Rayleigh–Lamb waves [154]. The acoustic waves in transient OCE rapidly attenuate and disperse [298], which limits the fields of view. Alternatively, the loading can be repeated at various locations at the expense of significant delays to image acquisition. It is, therefore, challenging to implement transient OCE techniques in many *in vivo* applications which are typically time sensitive. Recently, high-speed Fourier-domain mode-locked lasers have been applied to SS-OCT systems, demonstrating rapid acquisition rates of ~ 1.5 MHz, which represents a possible solution to this problem [299,300].

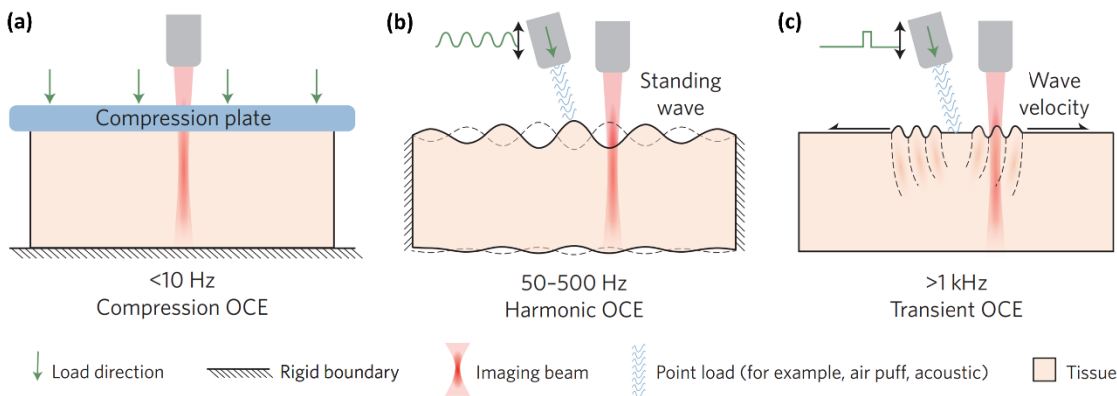


Figure 4.5: Diagrams of common OCE loading methods with representative values for the mechanical frequencies. (a) Compression OCE, (b) harmonic OCE and (c) Transient OCE. Adapted from [155].

4.3 OPTICAL ELASTOGRAPHY TECHNIQUES IN THIS THESIS

Since it was first proposed, optical elastography has undergone many technological developments to optimise the diagnostic capability in different biological applications. By leveraging the particular advantages of different imaging systems, loading mechanisms and displacement measurement algorithms, a vast array of optical elastography methods have emerged. In the following Section, two such methods which are applied in this Thesis will

be described. These methods each utilise the mechanical model presented in Chapter 3 to produce estimates of tissue mechanical properties.

4.3.1 QUANTITATIVE MICRO-ELASTOGRAPHY

QME is a variant of compression OCE that provides quantification by estimating the elasticity of a sample [106]. It is defined as the ratio of stress, the force per unit area, to strain, the subsequent change in length. The following Sections will describe how these parameters are measured in QME.

Strain estimation

QME, in common with most compression OCE techniques, estimate strain to provide mechanical contrast between different features in a sample. In many demonstrations of compression OCE, the applied stress throughout the sample is assumed to be uniform and the measured bulk strain, ϵ_b , therefore acts as a surrogate for elasticity, as $E = \sigma/\epsilon_b$ [1,2]. However, the bulk strain refers to just a single measurement of axial strain and is not depth-resolved. As OCE is focused on providing depth-resolved information of the sample mechanical properties, local strain, ϵ_l , is a better definition [1–3,20]:

$$\epsilon_l = \frac{\Delta u_z}{\Delta z} \quad (4.10)$$

where Δu_z is the change in axial displacement measured over an axial depth range Δz , which defines axial resolution of the local strain. It can be seen from Eq. (4.10), that if Δz is the same length as the unloaded sample, l_0 , then the local and bulk strain will be equivalent, assuming uniaxial loading. The goal of strain estimation in OCE is to utilise the measured local displacement to derive the local strain in Eq. (4.10). Strain can be computed from displacement using several different methods which can affect the accuracy of the strain estimation. One simple method for strain estimation involves taking the finite differences of the axial displacement. This method was first proposed for ultrasound elastography [163], and was later applied to OCE [18]. The finite difference strain estimation determines strain, ϵ_i^f , as the difference in local axial strain, divided by the difference in depth, over a window of over m points [287]:

$$\epsilon_i^f = \frac{u_{i+m-1} - u_i}{z_{i+m-1} - z_i} = \frac{\Delta u_z}{\Delta z} \quad (4.11)$$

where u_i is the local axial displacement at the i^{th} location, z_i is the depth at the i^{th} location and $\Delta z = m\delta z$. While this is a relatively straightforward strain estimation approach, differentiation of the displacement is a noisy process, resulting in a low-quality strain estimation [287]. Alternatively, strain can be estimated by determining the gradient of

displacement over a window of multiple points, whilst considering the variance of the displacement measurements (which are dependent on the OCT SNR). This is often achieved using linear regression methods such as weighted least squares (WLS) strain estimation which assigns a weighting to each displacement measurement based on the corresponding OCT SNR and determines the gradient of the displacement over the window by minimising the variance between the displacement measurements and the linear fit. In WLS strain estimation, the linear fit for displacement, \hat{u}_z , in depth, z is given as [287]:

$$\hat{u}_z = \varepsilon_{zz}Z + c, \quad (4.12)$$

where ε_{zz} is normal axial strain, c is an error constant, and the fitting is performed over the range $z_i \leq z \leq z_i + \Delta z$. For a given set of displacements and at corresponding depths within this range, strain is estimated by minimising the sum of squared differences, R , between the i^{th} measured displacement, u_{z_i} , and the displacement determined by the linear fit in Eq. (4.12), \hat{u}_z , *i.e.*, by minimising the following [287]:

$$R = \sum_{z_i \in \Delta z} w_i [u_{z_i} - \varepsilon_{zz}z_i - c]^2, \quad (4.13)$$

where the weighting variable for each pixel, $w_i = 1/\sigma_{u_{z_i}}^2$, is related to the OCT SNR by combining Eqs. (4.8) and (4.9). The analytical expression for WLS strain is defined as [287]:

$$\varepsilon_{zz}^w = \frac{\sum w_i \sum w_i z_i u_{z_i} - \sum w_i z_i \sum w_i u_{z_i}}{\sum w_i \sum w_i z_i^2 - (\sum w_i z_i)^2} \quad (4.14)$$

Applying Eq. (4.14) to each pixel in the OCT FOV obtains a spatially resolved strain elastogram. To provide 2-D and 3-D strain elastograms, the strain calculation is performed over a rolling window of points. Typically, the size of this window is selected to be $\sim 10\times$ the OCT axial resolution to ensure sufficient pixels containing high OCT SNR are included, which degrades the strain resolution proportionally [301]. This method has shown a ~ 12 dB improvement in strain SNR over finite differences approaches [287]. It can be seen in Fig. 4.6, that for a homogeneous sample (blue line) the axial displacement is linearly proportional with depth and the corresponding strain is therefore uniform. For a heterogeneous sample (*i.e.*, a stiff embedded inclusion), the change in displacement with depth varies between materials with different mechanical properties, and the measured strain in soft materials is greater than that in stiff materials. This difference in measured strain provides a contrast mechanism for OCE to differentiate between different tissue types.

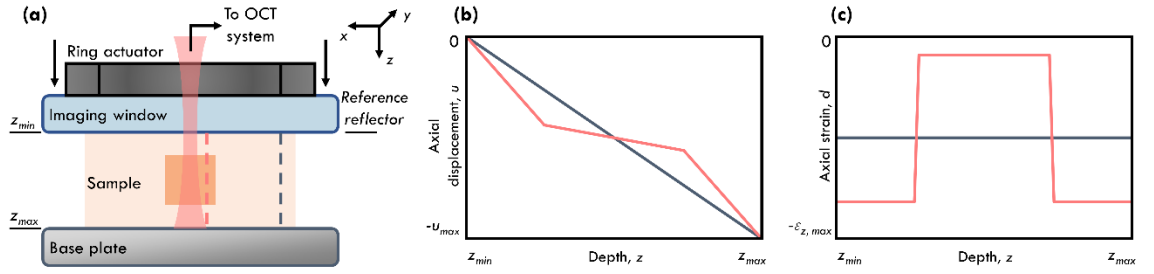


Figure 4.6: Diagram of displacement and strain measured in compression OCE. (a) Compression OCE set-up featuring a ring actuator, imaging window, base plate, and heterogeneous sample containing a relatively stiff inclusion. (b) Illustrations of the axial displacement profiles through the inclusion (red) and through a homogeneous portion (blue) of the sample are shown and (c) the corresponding axial strain profiles. The stiffer inclusion undergoes less strain than the surrounding regions of homogeneous sample.

Stress estimation

In QME, a clear compliant layer is placed on the sample surface (Fig. 4.7(a)(i)), and both are compressed against a rigid base plate under an applied strain (Fig. 4.7(a)(ii)). The OCT images in Figs. 4.7(b) and (c) show the initial layer thickness $l_0(x, y)$ and the loaded layer thickness $l(x, y)$, respectively. Once strained (often referred to as preloaded), a microscale actuation is applied to the layer and sample to induce a small local displacement. This displacement is detected using phase-sensitive OCT as described in Section 4.2.1. Stress is estimated by first determining the bulk axial strain, $\epsilon_{layer_b}(x, y)$, at each lateral location in the layer which defines the position along the layer stress-strain curve, $E[\epsilon_{layer_b}(x, y)]$. The local axial strain in the layer is determined from the actuator driven displacement as $\epsilon_{layer_l}(x, y) = u_z(x, y)/l(x, y)$, where $u_z(x, y)$ is the axial displacement taken at the layer-sample interface [106]. The change in axial stress is given as:

$$\sigma_{layer}(x, y) = E'[\epsilon_{layer_b}(x, y)] \cdot \epsilon_{layer_l}(x, y), \quad (4.16)$$

where $E' = d\sigma/d\epsilon$ is the tangent modulus of the stress-strain curve, analogous to elasticity, shown in Fig. 4.7(d).

Elasticity

According to the assumptions in the simplified mechanical model, elasticity can be represented by the ratio of axial stress to axial strain. In QME, the stress is assumed to be uniaxial, that is the stress measured in the layer is the same as the stress in the sample [106]. The local strain in the sample $\epsilon_{sample_l}(x, y, z)$ is determined from the sample displacement (Fig. 4.7(f)), allowing for sample elasticity, $E_{sample}(x, y, z)$ to be calculated by:

$$E_{sample}(x, y, z) = \frac{\sigma_{layer}(x, y)}{\epsilon_{sample_l}(x, y, z)}, \quad (4.17)$$

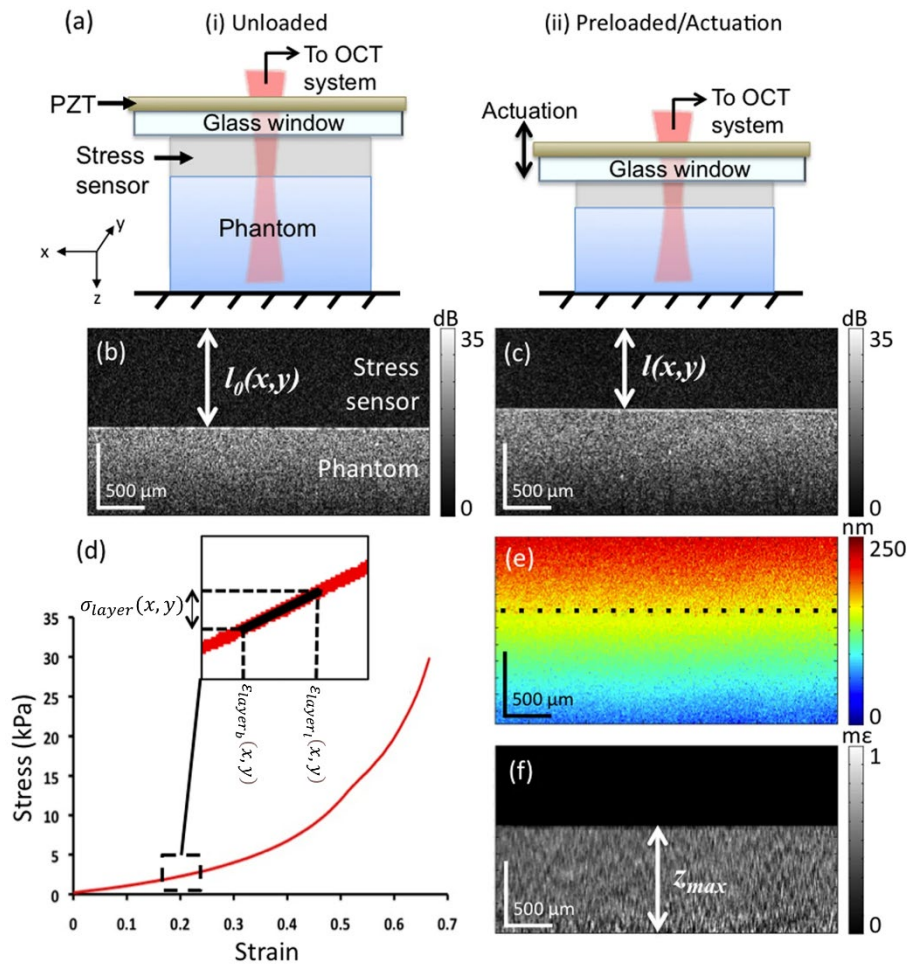


Figure 4.7: Methodology for QME. (a)(i) A silicone compliant layer is placed on the sample surface before (b) undergoing a preload. The corresponding OCT images for the (b) unloaded and (c) loaded set-up shown the change in layer thickness with preload. (d) The pre-characterised stress-strain curve for the layer material is used to determine the stress on the layer from the corresponding strain induced, which is assumed to act uniformly with depth into the sample. (e) The local displacement is induced in the sample due to the microscale actuation is measured by phase-sensitive detection and (f) the resulting sample strain is shown. Adapted from [106].

The assumption of uniaxial stress which underpins QME has previously been validated using finite element analysis in a study that confirmed that the stress field was approximately uniform with depth in layered structures and structured tissue-mimicking inclusion phantoms [302]. QME, therefore, can provide accurate depth-resolved measurements of tissue mechanical properties on the micro-scale, as shown in Fig. 4.8. The unique benefits of this technique make it an appealing option in many diagnostic imaging techniques where disease can be classified based on its mechanical properties. This is evident from a recent study of 71 breast-conserving surgery (BCS) specimens in which 142 margins were assessed using QME, demonstrating a sensitivity of 92.9% and specificity of 96.4% [105]. This study is described in detail in Chapter 5.

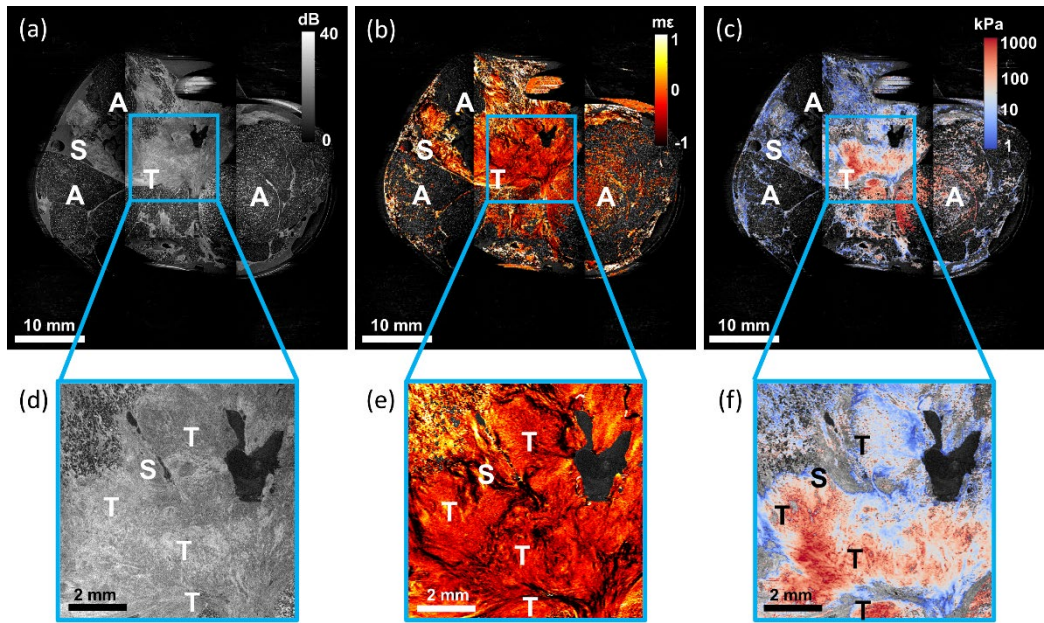


Figure 4.8: OCT, strain OCE and QME of a freshly excised mastectomy specimen containing invasive ductal carcinoma. (a) OCT, (b) strain OCE and (c) QME are shown over a broad 45×45 mm field of view. Magnified *en face* views are shown in (d), (e) and (f) where regions of invasive tumour and stroma are present. It is clear from (f) that QME produces a higher contrast than OCT (d) and strain OCE (e) for the same sample. A, adipose tissue; T, invasive tumour; NC, non-contact; S, uninvolved stroma. Adapted from [303].

4.3.2 OCT-BASED OPTICAL PALPATION

Optical palpation is a relatively new optical elastography approach, first presented in 2014 [225]. This technique generates stress images, based on the principle that a sample under compression will exhibit stress at its surface. The surface stress is indicative of the underlying elasticity of structures in the sample and mapping this stress provides mechanical contrast in a sample.

Optical palpation, like QME, uses OCT to measure the axial deformation of a clear compliant silicone layer to estimate the surface stress as shown in Fig. 4.9. The layer thickness, l_0 , is known prior to testing and the stress-strain relationship of the silicone is characterised. As compression is applied, the layer, which is placed between the sample and imaging window, deforms. OCT captures the deformed layer thickness, $l(x, y)$, at each lateral location, which allows for the strain to be calculated:

$$\varepsilon_{layer_b}(x, y) = \frac{\Delta l(x, y)}{l_0} = \frac{l_0 - l(x, y)}{l_0}. \quad (4.18)$$

In OCT-based optical palpation, the sample undergoes a compressive strain of 15–25% to ensure sufficient contact between the specimen, layer, and imaging window. While this strain is beyond the typical linear elastic region for a material, it is low enough to minimise the impact of nonlinear elasticity on the measured stress.

In contrast to QME, there is no need for additional micro-scale actuation as $\varepsilon_{layer_b}(x, y)$ is calculated from the bulk deformation of the layer. Stress at each lateral location,

$\sigma_{layer}(x, y)$, is then determined using the characterised stress-strain relationship, E_{layer} , as a look-up table according to the following:

$$\sigma_{layer}(x, y) = E_{layer} \cdot \varepsilon_{layer_b}(x, y). \quad (4.19)$$

There are two key assumptions that underpin the concept of optical palpation; firstly, that the stress field within the sample is uniform and uniaxial; and secondly, that friction between the layer interfaces is negligible [225].

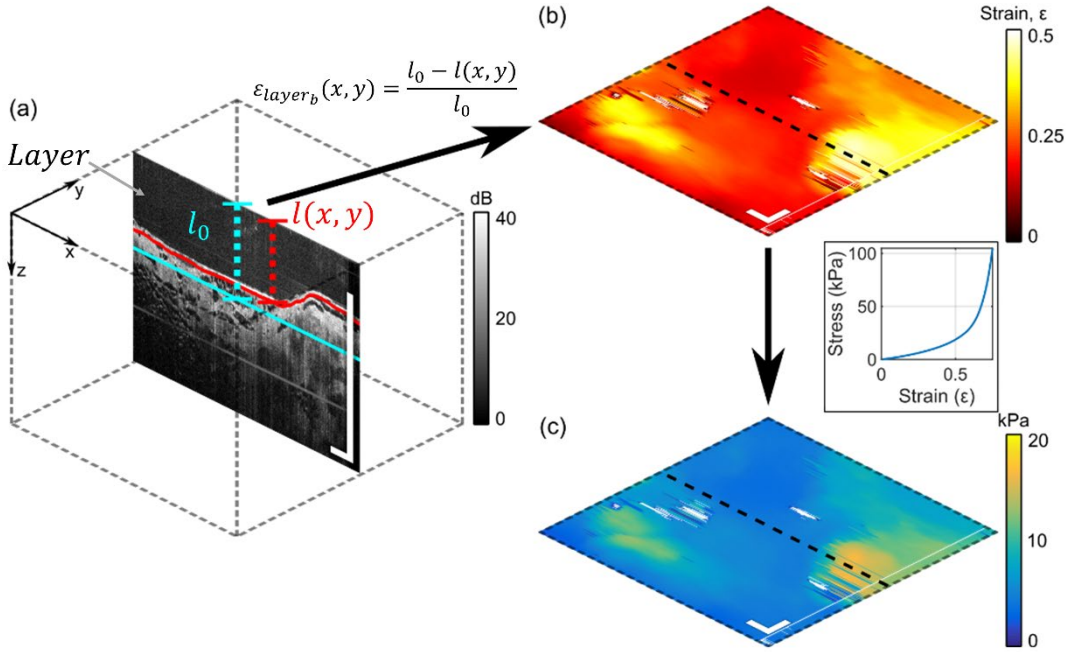


Figure 4.9: Optical palpation working principle. Before imaging, a silicone layer with initial (relaxed) thickness l_0 is placed on the tissue and bulk compression is applied. For each OCT B-scan in a 3-D volume (a), the layer/tissue interface is detected, allowing the final (compressed) layer thickness $l(x, y)$ to be measured and the *en face* map of layer strain (b) to be computed. This is then mapped to stress, presented in the optical palpogram (c), using the pre-characterised layer stress-strain curve. Scale bars = 1 mm. Reproduced from [304].

The clinical feasibility of optical palpation has been demonstrated in several studies, particularly for applications in breast surgery [226,304,305] and dermatology [234]. In one study, optical palpation was able to distinguish between adipose tissue, uninvolved dense tissue and invasive tumour in 34 freshly excised breast tissue specimens based on the mechanical contrast generated (Fig. 4.10) [226]. In a larger study, 71 BCS specimens were imaged using optical palpation, generating 142 margins for assessment. Sensitivity and specificity were calculated by comparing the performance of an automated classifier to the true margin status as determined by co-registration with histology. The sensitivity (83.3%) and specificity (86.2%) represent a higher diagnostic accuracy than was achieved using OCT on the same data set (sensitivity and specificity of 69.0% and 79.0%, respectively), demonstrating the potential clinical value of this technique [304]. This study is described in detail in Chapter 5.

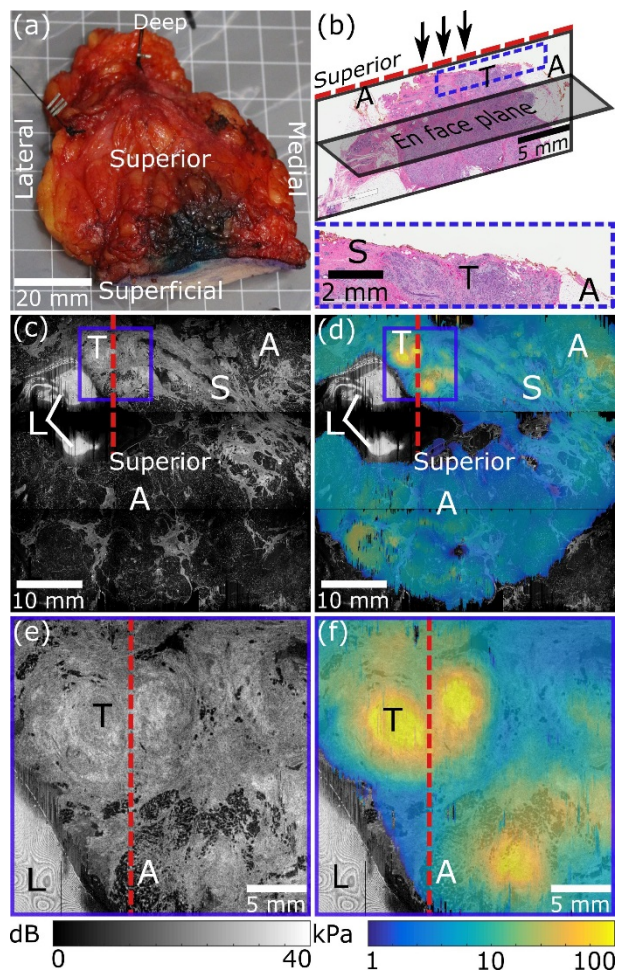


Figure 4.10: Optical palpation of breast-conserving surgery specimen with a margin involved by invasive tumour. (a) Photograph of the specimen. (b) Histology. Wide-field *en face* (c) OCT image and (d) optical palpogram. Magnified *en face* (e) OCT image and (f) optical palpogram. A, Adipose tissue; L, Layer artifact; S, Stroma; T, Invasive tumour. The direction of OCT beam indicated by black arrows in (b). Digital micrograph in the plane orthogonal to *en face* images, the approximate location indicated by the red dashed line in (c)-(f). Reproduced from [226].

CHAPTER 5

CLINICAL VALIDATION OF OPTICAL ELASTOGRAPHY

5.1 PREFACE

Optical coherence elastography (OCE) is a promising technique for the detection and classification of disease based on contrasting mechanical properties, however, much of the work to date has focused on initial proof-of-principle studies. To translate OCE from laboratory-based demonstrations to clinical implementations requires demonstrations of clinical efficacy and the development of novel imaging probes, designed specifically towards the intended clinical application.

In this Chapter, clinical validation of two OCE techniques, quantitative micro-elastography (QME) and optical palpation, is demonstrated. The diagnostic accuracy for detecting tumour margin in breast-conserving surgery (BCS) patients is presented for both techniques. The Chapter consists of two co-authored publications.

The first publication assesses the diagnostic accuracy of QME, reporting a sensitivity and specificity of 92.9% and 96.4%, respectively. Kelsey M. Kennedy, Renate Zilkens, Wes M. Allen, Ken Y. Foo, Qi Fang, Lixin Chin, Rowan W. Sanderson, James Anstie, Philip Wijesinghe, Andrea Curatolo, Hsien Ern I. Tan, Narelle Morin, Bindu Kunjuraman, Chris Yeomans, Synn Lynn Chin, Helen DeJong, Katharine Giles, Benjamin F. Dessauvague, Bruce Latham, Christobel M. Saunders, Lixin Chin, and Brendan F. Kennedy, “*Diagnostic accuracy of quantitative micro-elastography for margin assessment in breast-conserving surgery*,” *Cancer Research*, 80(8): p. 17731783, 2020.

The second publication assesses the diagnostic accuracy of optical palpation, demonstrating sensitivity and specificity of 83.3% and 86.2%, respectively. Ken Y. Foo, Kelsey M. Kennedy, Renate Zilkens, Wes M. Allen, Qi Fang, Rowan W. Sanderson, James Anstie, Benjamin F. Dessauvague, Bruce Latham, Christobel M. Saunders, Lixin Chin, and Brendan F. Kennedy, “*Optical palpation for tumour margin assessment in breast-conserving surgery*,” *Biomedical Optics Express*, 12(3): p. 1666-1682, 2021.

This Chapter highlights the efficacy of OCE techniques in assessing tumour in BCS patients and suggests based on the high diagnostic accuracy of both QME and optical palpation, that these techniques could be translated towards clinical applications.

5.2 DIAGNOSTIC ACCURACY OF QUANTITATIVE MICRO-ELASTOGRAPHY FOR MARGIN ASSESSMENT IN BREAST-CONSERVING SURGERY

Kelsey M. Kennedy,¹ Renate Zilkens,^{1,2} Wes M. Allen,^{1,3} Ken Y. Foo,^{1,3} Qi Fang,^{1,3} Lixin Chin,^{1,3} Rowan W. Sanderson,^{1,3} James Anstie,^{1,3} Philip Wijesinghe,^{1,3} Andrea Curatolo,^{1,3} Hsern Ern I. Tan,² Narelle Morin,⁴ Bindu Kunjuraman,⁵ Chris Yeomans,⁶ Synn Lynn Chin,⁵ Helen DeJong,¹ Katharine Giles,⁷ Benjamin F. Dessauvage,^{2,6} Bruce Latham,⁶ Christobel M. Saunders^{2,5,8} and Brendan F. Kennedy^{1,3}

Cancer Research, 80(8): p. 1773-1783, 2020.

Abstract: Inadequate margins in breast-conserving surgery (BCS) are associated with an increased likelihood of local recurrence of breast cancer. Currently, approximately 20% of BCS patients require repeat surgery due to inadequate margins at the initial operation. Implementation of an accurate, intraoperative margin assessment tool may reduce this re-excision rate. This study determined, for the first time, the diagnostic accuracy of QME, an optical coherence tomography (OCT)-based elastography technique that produces images of tissue microscale elasticity, for detecting tumour within 1 mm of the margins of BCS specimens. Simultaneous OCT and QME were performed on the margins of intact, freshly excised specimens from 83 patients undergoing BCS and on dissected specimens from 7 patients undergoing mastectomy. The resulting three-dimensional images ($45 \times 45 \times 1$ mm) were coregistered with postoperative histology to determine tissue types present in each scan. Data from 12 BCS patients and the 7 mastectomy patients served to build a set of images for reader training. One hundred and fifty-four subimages ($10 \times 10 \times 1$ mm) from the remaining 71 BCS patients were

¹ BRITeLab, Harry Perkins Institute of Medical Research, QEII Medical Centre, Nedlands and Centre for Medical Research, The University of Western Australia, Perth, Western Australia, 6009, Australia

² School of Medicine, The University of Western Australia, Perth, Australia.

³ Department of Electrical, Electronic & Computer Engineering, School of Engineering, The University of Western Australia, Perth, Australia.

⁴ Sonowest, Perth, Australia.

⁵ Breast Centre, Fiona Stanley Hospital, Murdoch, Australia.

⁶ PathWest, Fiona Stanley Hospital, Murdoch, Australia.

⁷ OncoRes Medical, Perth, Australia.

⁸ Breast Clinic, Royal Perth Hospital, Perth, Australia.

included in a blinded reader study, which resulted in 69.0% sensitivity and 79.0% specificity using OCT images, versus 92.9% sensitivity and 96.4% specificity using elasticity images. The quantitative nature of QME also facilitated development of an automated reader, which resulted in 100.0% sensitivity and 97.7% specificity. These results demonstrate high accuracy of QME for detecting tumour within 1 mm of the margin and the potential for this technique to improve outcomes in BCS.

©2020 American Association for Cancer Research.

5.2.1 INTRODUCTION

Success of breast-conserving surgery (BCS) is characterised by clear margins and a good cosmetic outcome for the patient. However, approximately 20% of cases require repeat surgery due to inadequate margins [306–308]. Re-excision surgery causes substantial physical, psychologic, and financial burdens for patients, with higher risk of complications [309], worse cosmesis, and additional costs, on average, of >\$10,000 per patient [310]. Intraoperative detection of tumour at the margins would allow more complete resection of malignant tissue in the first operation, provide the surgeon with confidence that no residual cancer remains in the breast, and reduce the number of re-excision surgeries.

Several techniques are currently used for intraoperative margin assessment. Intraoperative pathologic assessment can be performed using frozen section analysis and imprint cytology [311], but these techniques are resource-intensive, sample only a small percentage of the surgical margins, and have limited efficacy, especially for ductal carcinoma *in situ* (DCIS; ref. [312]), and, thus, have not been widely adopted [313]. Another available technique, intraoperative specimen radiography (IOSR), provides an X-ray image of the excised specimen. IOSR can show that the main lesion has been removed, which is particularly useful for nonpalpable tumours that are localised using preoperative wire insertion [314] or radioactive seed placement [315]. However, IOSR accurately predicts margin status in only 48% of cases [316] and has been shown not to reduce re-excision rates [316,317]. Intraoperative ultrasound guidance of excision has been shown in a small number of studies to reduce re-excision rates by more than half for invasive cancers [318,319], but ultrasound is operator-dependent and has limited reliability for visualising *in situ* or multifocal cancers [320,321].

To address the shortcomings of existing techniques, a range of margin assessment tools have been proposed, relying on various contrast mechanisms to detect cancer. One commercially available technique uses radiofrequency spectroscopy to measure the dielectric properties of tissue, implemented in a handheld probe (MarginProbe, Dune Medical

Devices). The technique shows high accuracy for margin assessment in homogeneous, *ex vivo* tissues (*e.g.*, if the probe is placed over a large region of tumour, >6 mm diameter) but has lower accuracy (70% sensitivity and 70% specificity) when multiple tissue types are present in the interrogated region [322]. In a randomised trial with 596 patients, use of MarginProbe on excised specimens reduced re-excision rate from 25.8% to 19.8% but suffered from low specificity with a 53.6% false positive rate [323].

Fluorescent modalities that utilise molecular contrast to intraoperatively highlight cancer are also under development, potentially enabling surgeons to visualise tumour in the cavity, as well as in the excised lump [324–327]. A small number of proof-of-principle studies in humans have been reported [324,325,327], but the efficacy of these techniques for reducing re-excision rates in BCS has not been determined. In addition, they typically rely on preoperative, systemic administration of exogenous dyes, requiring extensive dosing and tumour uptake studies, and creating potential barriers to clinical translation [324]. Another optical technique, surface-enhanced Raman scattering [328], has recently been proposed, using targeted nanoparticles for multiplexed imaging of cancer biomarkers. A preliminary study on *ex vivo* tissues dissected from mastectomy and lumpectomy specimens showed promising sensitivity (89.3%) and specificity (92.1%) for cancer detection, and the technique is conducive to personalised biomarker imaging based on tumour-specific molecular profiles. However, it is restricted to surface imaging, and, while many institutions have adopted a “no tumour on ink” criterion for invasive cancers, larger margins are typically desired for *in situ* cancers [306]. Label-free optical techniques have also been proposed, including diffuse reflectance spectroscopy/hyperspectral imaging [329,330], autofluorescence lifetime imaging, and Raman spectroscopy [331]. However, diffuse techniques can suffer from low spatial resolution (~ 5 mm; ref. [329]), while autofluorescence and Raman techniques typically have low scanning speeds (12–24 minutes/margin; ref. [331]), making clinical translation more challenging.

OCT is a promising optical technique capable of three-dimensional (3D), high-speed, high-resolution imaging without need for exogenous contrast agents. OCT may be described as an optical analogue to ultrasound. It uses interferometry to effectively measure “time of flight” of light in tissue, creating an image based on the amount of back-scattered light, with microscopic resolution (2–10 μm) up to 1 to 2 mm in depth. These imaging specifications match well with the clinical requirements of margin assessment in BCS. Preliminary studies have reported high sensitivity (80–94%) and specificity (87–93%) for detecting cancer, primarily in mastectomy tissues [332–334]. However, these mastectomy samples were typically dissected to expose a bulk of dense, high-grade tumour for imaging. The image contrast in this scenario may not translate to margin assessment in BCS, in which typically

lower-grade tumours must be detected at the edge of intact specimens or, for detecting residual tumour, directly within the surgical cavity. The largest study to date that used OCT to assess margins in BCS specimens reported sensitivity of 55% to 65% and specificity of 68% to 70% [335]. One reason for this relatively low accuracy may be the limited ability of OCT to distinguish between tumour and surrounding normal stroma [336–338]. Stronger contrast between tissue types is expected to aid surgeon decision-making in the intraoperative setting [339,340].

Beyond its distinct molecular and optical properties, breast cancer also exhibits distinct mechanical properties [100,254,341]. At the cellular scale, atomic force microscopy has revealed unique mechanical signatures within the breast tumour microenvironment caused by the mix of cellular proliferation and desmoplastic stroma [341]. At the macro-scale, surgeons rely on mechanical changes as they manually palpate the tissue, feeling for the boundaries of the typically stiff lesion. However, palpation is a subjective tool, and a large proportion of breast lesions are considered “impalpable,” that is, too small or soft to detect through touch [342]. Elastography is a technique that creates images of the mechanical properties of tissue, complementing palpation by visualising mechanical changes in 2D or 3D. Elastography based on ultrasound has been developed for a number of applications, including preoperative diagnosis of breast lesions [100,343], but has not been applied to intraoperative margin assessment, mainly due to its relatively low spatial resolution. In an emerging technique, OCT elastography is used to measure tissue deformation under an applied load, offering 3D maps of mechanical properties with microscale resolution [344]. OCT elastography techniques can be classified according to the mechanical loading mechanism used, with compression and shear wave being the most prominent [344]. Although early compression OCT elastography studies produced maps of tissue deformation (strain; refs. [336,345]), which is an indirect and qualitative measure of elasticity, introduction of a stress sensing technique to map the local stress in 2D at the tissue surface, has enabled QME, providing 3D maps of local elasticity, under the assumption of uniaxial stress [346]. Preliminary QME data in mastectomy specimens showed that elasticity images provide additional contrast between tumour and normal tissue compared to OCT and strain, and the technique has been extended to incorporate a wide-field scanning mechanism that enables entire margins of BCS specimens to be imaged within an intraoperative timeframe [347]. To build on these promising feasibility studies and to determine the clinical potential of QME for intraoperative margin assessment, it must be established whether clinicians can interpret QME images to accurately identify close or positive tumour margins in BCS specimens. To this end, the goal of this study is to conduct, for the first time, a blinded reader study, with postoperative histology as the gold standard, to determine the diagnostic accuracy (sensitivity

and specificity) of QME, compared with OCT alone, for detecting tumour within 1 mm of the margins of freshly excised specimens from patients undergoing BCS.

5.2.2 PATIENTS AND METHODS

Patient recruitment and imaging

All study procedures were performed after approval by the ethics board of the South Metropolitan Area Health Service in Western Australia. Ninety patients were recruited for this study after informed written consent was obtained: 83 patients (with no prior excision) undergoing BCS for treatment of breast cancer and 7 patients undergoing mastectomy for treatment of breast cancer. Samples from the 7 mastectomy patients and 12 of the BCS patients were used to create a set of pilot data for training readers. Data from the remaining 71 BCS patients were included in the blinded reader study. Table 5.1 summarises the disease characteristics of all BCS patients.

For patients undergoing BCS, following surgery, the fresh, intact specimens were transferred to the pathology department at Fiona Stanley Hospital. Pathologists at this institution dictated that tissue should be placed in fixative (formalin) within 1 hour of receiving the specimen from surgery, to avoid any tissue degradation that might influence histological processing. Between excision and imaging, specimens were kept in air at room temperature, and the surface was kept hydrated by applying droplets of saline. Specimen orientation was maintained using clips and sutures, per standards at this institution. In most cases (8/12 pilot cases and 68/71 cases for the reader study), two margins were imaged. In the remaining cases, one margin was imaged due to delays in scanning the specimen within the allotted time. No more than two margins per specimen were scanned as, in addition to imaging, sufficient time was needed to transfer the specimen from pathology, select a margin for scanning and orientate the specimen in the imaging system. Margins for scanning were chosen based on consultation with pathologists, observation of the intraoperative specimen radiography (when available), and surgical notes indicating if extra cavity shavings were performed intraoperatively. The “closest tumour margin” distances reported in Table 5.1 were determined by postoperative histology and include superficial and deep margins (considering radial margins only, which are most clinically relevant, the rate of tumour margins <1 mm in the reader study was 21%). For patients undergoing mastectomy, nondiagnostic tissue was dissected by a pathologist to create samples of approximately $5 \times 5 \times 0.5$ cm, which were also imaged within approximately 1 hour of excision.

Table 5.1: BCS patient and clinical specimen characteristics

	Pilot study (12 patients)		Reader study (71 patients)	
	Number	Percentage	Number	Percentage
Age, y				
Mean	60		59	
SD	9		11	
Range	44–74		26–76	
≤65	8	67%	48	68%
>65	4	33%	23	32%
Surgical diagnosis*				
Ductal carcinoma <i>in situ</i>	6	50%	44	62%
Invasive ductal carcinoma	8	67%	43	61%
Invasive lobular carcinoma	2	17%	8	11%
Invasive mucinous carcinoma	1	8%	3	4%
Mixed invasive ductal lobular carcinoma	0	0%	2	3%
Invasive micropapillary carcinoma	0	0%	1	<1%
Invasive apocrine carcinoma	0	0%	1	<1%
Invasive solid papillary carcinoma	0	0%	2	3%
No tumour [†]	0	0%	3	4%
Palpability				
Palpable	7	58%	45	63%
Impalpable	5	42%	26	37%
Total lesion size (greatest dimension)				
<1 cm	1	8%	15	21%
1–2 cm	5	42%	27	38%
>2 cm	6	50%	26	37%
No tumour	0	0%	3	4%
Closest tumour margin[‡]				
<1 mm [¶]	7	58%	32	45%
1–3 mm	4	33%	25	35%
>3 mm	1	8%	11	15%
Not applicable (no tumour)	0	0%	3	4%

* Multiple tumour types may occur in a given patient, such that diagnosis percentages add to >100%.

[†] Tumour was excised in original core biopsy.

[‡] Includes deep and superficial margins in addition to radial margins.

[¶] Thirteen (18%) of BCS specimens in the reader study had positive margins (*i.e.*, tumour on ink).

Imaging was performed on a benchtop, wide-field QME system [347]. Briefly, the system is based on a Telesto II spectral-domain OCT system (TEL220C1, Thorlabs). It uses a superluminescent diode light source with a central wavelength of 1300 nm and a bandwidth of >170 nm, illuminating the sample with 2.5 mW of power (a low power level that is safe for users). The measured axial and lateral resolutions in air are 5.5 μm and 13 μm ,

respectively. The system captures one-dimensional axial scans (A-scans) in 14 μ s, and the beam is raster scanned to build a 3D image measuring $16 \times 16 \times 3.5$ mm in 55 seconds. Wide-field images are generated by translating the specimen relative to the OCT scan head between 3D acquisitions, as described previously [345,347]. Nine subvolumes are acquired with 1-mm overlap in the lateral plane, resulting in a $45 \times 45 \times 3.5$ mm image captured in under 9 minutes. The partially overlapping subvolumes are stitched to form mosaicked wide-field images, presented in the *en face* plane. The measured displacement sensitivity of the OCT system is 1.4 nm at an OCT signal-to-noise ratio of 40 dB, acquired under clinical testing conditions in the pathology laboratory (*i.e.*, without a vibration isolation table).

A compliant silicone layer is placed between the specimen and imaging window to ensure contact between the uneven specimen surface and window, as well as to estimate stress for quantification of elasticity [346]. After establishing contact, microscale displacement (up to 9.5 μ m) was applied to the specimen surface using a piezoelectric actuator. Images were processed to determine stress, strain, and elasticity, and elasticity was overlaid on the solid regions of the OCT images for visualisation, using an algorithm described previously [345]. OCT data are displayed in grayscale from 0 to 40 dB, and elasticity data are displayed in colour on a logarithmic scale from 3.63 to 363 kPa.

5.2.1 HISTOPATHOLOGY AND COREGISTRATION WITH IMAGING DATA

Following imaging, specimens were fixed in formalin and submitted for standard histopathologic processing. Specimens were inked for orientation and sliced in “bread-loaf” fashion from lateral-to-medial, superficial-to-deep, or superior-to-inferior margins to generate histologic sections at each plane. This sectioning protocol resulted in histology typically being performed in a plane orthogonal to the *en face* plane in which QME images are displayed. The positions of the histology sections were coregistered with images by cross-referencing the blocking diagram and photographs taken of the specimen during scanning. Pathologists (BFD, BL) determined tissue types present in the histology images. Engineers and pathologists worked together to confirm co-registration by cross-checking tissue features present in the histology images with similar features present in the OCT images, using the depth cross-section (B-scan) view of OCT to match the histology plane where needed, as described in [345].

To focus the histologic analysis, and to facilitate the subsequent reader study, 3D regions of interest (ROI), $10 \times 10 \times 1$ mm, were selected from the wide-field ($45 \times 45 \times 1$ mm) scans. At least one ROI was selected on every margin scanned in this study. ROIs were then included in the reader study if they met the following criteria: good physical contact with the specimen; tissue not extensively damaged by thermal effects (due to cauterisation during

resection) as assessed by histopathology; and availability of a reliable histology match for the ROI. Considering that histology slices are typically taken approximately every 3 mm, 1 to 3 sections were available for a given ROI. ROIs were designated as “positive” for cancer if the pathologist identified any tumour within 1 mm of the margin in the histology sections corresponding to the ROI, similar to designation of “positive” margins in other diagnostic accuracy studies in BCS specimens [331,335]. In each case, the ROI was selected before the histology was analysed by the pathologist. As such, the researchers selecting the ROI did not know the outcome of the corresponding histology. Note: The clinical standard at the hospital where the study was performed is 1 to 2 mm for invasive ductal carcinoma and 2 mm for DCIS.

5.2.2 READER STUDY AND STATISTICAL ANALYSIS

The reader study was designed to have three main outcomes: diagnostic accuracy (sensitivity and specificity) of OCT, QME, and OCT plus QME. Seven readers [2 surgeons, 2 engineers, 1 medical sonographer, 1 pathology scientist (equivalent to a pathology assistant) and 1 medical resident], blinded to the histologic results, participated in the study. First, readers were trained to read OCT images in a 1.5-hour session. They then completed a reading of all ROIs (OCT alone, using criteria in Fig. 5.1(a)) within 10 days of training and had access to the training images during reading. Two weeks following the OCT training, readers were trained to read QME images in another 1.5-hour session. They then completed a reading of all ROIs once more, this time viewing OCT and QME side-by-side, from which accuracy was calculated for QME (using criterion in Fig. 5.1(b)) and OCT plus QME (using criterion in Fig. 5.1(c)). To remove potential bias due to reader memory, the order and orientation of ROIs were randomised between readings. In both readings, readers viewed the ROIs ($10 \times 10 \times 1$ mm, presented as a stack of *en face* images displayed every $20 \mu\text{m}$ up to 1 mm in depth) using the open source software ImageJ (v1.52a; ref. [348]), which allowed scrolling through depth to visualise the volume. Readers completed their evaluation using a custom-built interface in which they followed a set of criteria for the presence of cancer in each image type and selected “cancer” or “not cancer” as the endpoint (Fig. 5.1).

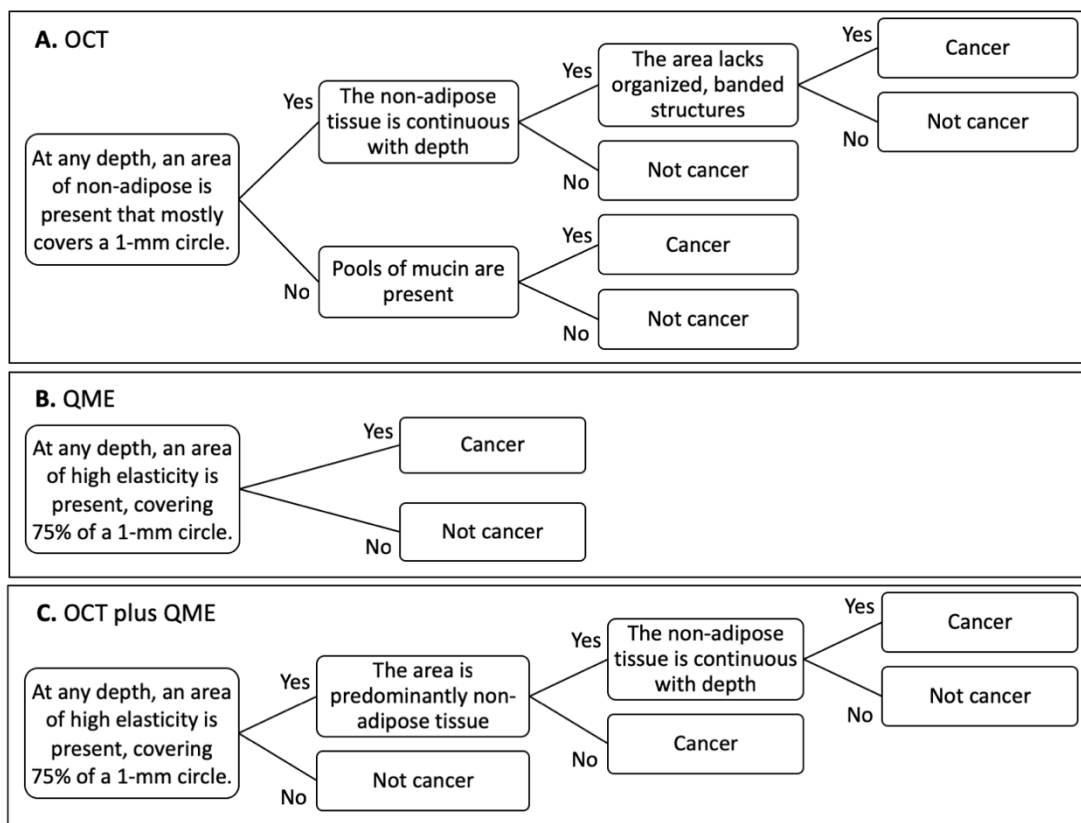


Figure 5.1: Reader criteria for determining presence of cancer. Criteria for cancer using OCT images (a), QME images (b), OCT and QME combined (c).

Criteria for cancer in OCT images (Fig. 5.1(a)) were determined on the basis of three main observations from prior OCT studies of breast tissues [333,337,345,349,350] and pilot study data. First, it has been established that adipose tissue is easily distinguished from other tissues in breast based on its “honeycomb” structure in OCT. Therefore, readers were trained to first identify solid features >1 mm in diameter. If the ROI was made up of all adipose tissue or adipose tissue with only small (<1 mm), isolated solid features, it was considered “not cancer”. Second, it was found in preliminary OCT studies on BCS specimens [345] and in this study that cancer near the margin tends to have continuity with depth, uninterrupted by regions of adipose tissue. Thus, if readers found a region of solid tissue, they were to scroll through the 3D image, checking if the feature extended down into the specimen. Finally, a criterion was added to help distinguish benign stroma from regions of cancer. In benign stroma, a striated or banded pattern is observed in OCT, likely due to the organisation of the underlying collagen. Cancer tends to disrupt this organisation and result in heterogeneous patterns in OCT [336,351]. One special case is mucinous carcinoma (present in four recruited patients), in which tumour cells produce pools of a liquid substance known as mucin. Mucinous pools result in regions of low signal in OCT images, appearing similar to adipose tissue, but can often be identified by the outline of the pool, which has higher OCT signal.

Thus, readers evaluated OCT images for the presence of these structures, even if at first it appeared that the tissue was adipose tissue (bottom path, Fig. 5.1(a)).

In QME images, readers were trained to look for areas of high elasticity, based on studies across spatial scales showing that cancer and its associated stroma are stiffer than benign tissues [254,341,347]. To avoid mistaking small, isolated patches of stiff stroma for cancer, the region of high elasticity had to cover at least 75% of a 1-mm diameter circle (Fig. 5.1(b)). This diameter was chosen empirically based on analysis of how tumour presented in QME images both in previous studies [346,347] and in the training data. The user interface enabled readers to calculate this precisely by dragging their cursor to any location in the ROI. High elasticity was defined as >26.3 kPa, based on analysis of prior and current study data and is denoted by a black line on the colour scale of all presented QME images. To assess OCT + QME in combination, readers were again directed to assess continuity with depth and ensure that the region was solid tissue, in addition to the elasticity criterion (Fig. 5.1(c)). Mucinous carcinoma presented a special scenario (second step in Fig. 5.1(c)): if an area had high elasticity but appeared in the OCT to lack “solid tissue,” this was likely a mucinous carcinoma, and, as such, results in “cancer” in the decision tree. This was based on our observation that even these liquid-dominant tumours resulted in high elasticity, likely due to interstitial fluid pressure within the tissue.

Finally, the QME criterion, facilitated by its quantitative nature, was implemented into a preliminary automated algorithm. This involved thresholding the elasticity values in the QME images at every depth to generate binary images (with ones representing pixels with an elasticity >26.3 kPa), then convolving these binary images with a 1 mm diameter circular kernel. The values at each pixel in the kernel were normalised such that the result of the convolution equalled the percentage of the circle covered by high elasticity. If, for a given ROI, the convolution produced a value $\geq 75\%$ at any location in the ROI, that ROI was interpreted as containing cancer. As such, this algorithm was equivalent to the QME reader criteria shown in Fig. 5.1(b). This algorithm was implemented on a standard desktop computer using MATLAB (Mathworks, R2016a), and took approximately one minute to read all ROIs.

Following the readings, the sensitivity, specificity, positive predictive value (PPV), negative predictive value (NPV), and accuracy were calculated for each reader. 95% confidence intervals were estimated using the score interval for a binomial case (“Wald” interval; ref. [352]). Aggregates were computed by taking the sum of the individual results of the seven readers (the totals of true positive, false positive, true negative, and false negative counts), and computing the sensitivity, specificity, PPV, NPV, accuracy, and confidence intervals on these summed totals. The performance of QME and OCT plus QME were

compared against OCT alone using McNemar test [353] for statistical significance. Interreader agreement was quantified using the Fleiss' Kappa metric [354].

5.2.3 RESULTS

OCT and QME images of malignant and benign breast tissues at the margin

Intact BCS specimens from 71 patients were scanned for the reader study, without any damage to the tissue nor disruption to typical histopathologic protocol. One hundred and seventy-four ROIs from the 71 patients were selected and coregistered with histology. Of these, 154 ROIs were included in the reader study. Table 5.2 summarises the tissue types and characteristics of the included ROIs. Reasons for exclusion were extensive thermal damage, as determined by postoperative histology ($n = 3$); inconclusive registration with histology sections ($n = 4$); insufficient contact between the specimen, silicone layer, and the imaging window ($n = 3$); imaging artifacts (*e.g.*, stray reflections or surgical clips precluded image interpretation, $n = 4$); insufficient elasticity data overlaid on solid tissue ($n = 2$); a rare form of mucinous DCIS (insufficient data to build decision criteria, $n = 2$); and the region of tumour within the ROI having a size <1 mm ($n = 2$). Of the 154 ROIs included in this study, 24 had cancer within 1 mm of the surface, corresponding to a prevalence of 15.6%. Most were made up of a mix of tissue types, including adipose tissue, stroma, and parenchymal tissues.

Table 5.2: Summary of regions of interest included in study.

ROI selection	Number	
Imaged margins	139	
ROIs coregistered with histology	174	
ROIs included in reader study	154	
Tissue types in included ROIs		Percentage (/154)
Cancer within 1 mm (positive ROI)	24	15.6%
Invasive (solid)	14	9.1%
Invasive (mucinous)	3	1.9%
DCIS	7	4.5%
Clear within 1 mm (negative ROI)	130	84.4%
Predominantly adipose tissue	38	24.7%
Adipose tissue with dense stroma	37	24.0%
Adipose tissue with ducts/vessels	24	15.6%
Adipose tissue with strands of connective tissue	19	12.3%
Dense stroma	12	7.8%

Figures 5.2–5.4 present ROIs from the reader study, representative of the various tissue types encountered in the study. In each case, *en face*, 10×10 mm OCT and QME images are displayed at a depth of 40 to 60 μm , along with the corresponding hematoxylin and eosin histology. The plane and orientation of the histology is indicated by the red dashed line in each set of images.

Figure 5.2 shows ROIs containing benign breast tissues: adipose tissue (Figs. 5.2(a)–(c)) and a mix of adipose tissue and stroma containing benign ducts (Figs. 5.2(d)–(f)). The OCT in Fig. 5.2(a) depicts the honeycomb structure typical of adipose tissue. Thin strands of connective tissue are present throughout this ROI, and QME shows that the elasticity in these regions tends to be low (Fig. 5.2(b)). Six of seven readers called this benign using OCT alone, compared to all readers using QME combined with OCT. A larger region of benign stroma is shown at the margin in Fig. 5.2(d), and 5.3(d) analysis reveals that this structure lacks continuity, with intermittent adipose tissue present with depth, similar to the pattern in the histology image (Fig. 5.2(f)). However, using OCT alone, three readers incorrectly assessed this as cancer. In QME (Fig. 5.2(e)), this stroma exhibits mostly low elasticity. Very small pockets of high elasticity are seen at a few points throughout the stroma, but only features with more widespread elasticity were considered suspicious for cancer. All seven readers correctly called this benign using QME and QME plus OCT.

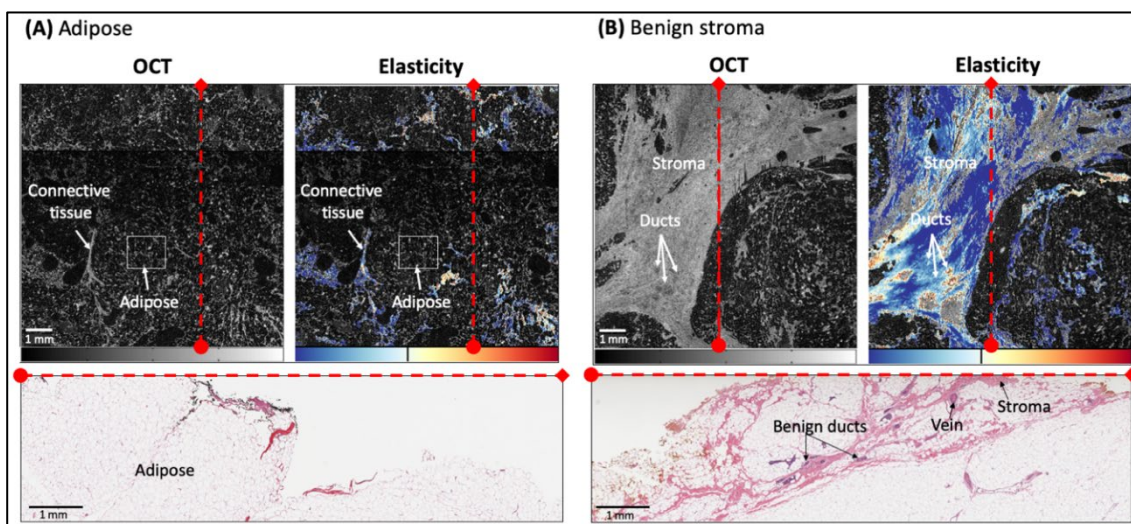


Figure 5.2: Examples images of benign breast tissues. OCT, QME, and H&E histology of (a) adipose tissue with thin strands of stroma and (b) a large region of benign stroma and adipose tissues. Colour bars: OCT 0–40 dB; Elasticity 3.63–363 kPa.

Figure 5.3 shows positive ROIs from two BCS cases, each containing invasive ductal carcinoma on the margin. In Fig. 5.3(c), the histology image reveals invasive ductal carcinoma grade 3 with high cellular density, surrounded by adipose tissue. Correspondingly, the OCT (Fig. 5.3(a)) captured a region of solid tissue with a nodular appearance (no indication of striated, organised collagen) that matches the location of tumour in the

histology image. In QME (Fig. 5.3(b)), this region shows elevated elasticity, due to the much higher cellular density in the tumour compared with the surrounding adipose tissue. This detected region of tumour is approximately 2 mm across, making up <math><0.2\%</math> of the total surface area of this particular margin, demonstrating the high resolution of the technique. All seven readers evaluated this ROI correctly using OCT, QME, and the combination. The histology image in Fig. 5.3(f) shows invasive ductal carcinoma grade III surrounded by a mix of stroma and adipose tissue. A mix of adipose tissue and solid tissue is also present in the OCT image (Fig. 5.3(d)), and QME reveals a portion of the solid tissue to have high elasticity (Fig. 5.3(e)). 3D analysis of the images shows that the region with high elasticity is also continuous with depth (*i.e.*, adipose tissue is not revealed underneath). On the basis of OCT alone, one of the seven readers called this as a false negative, mistaking it for benign, whereas all seven readers evaluated this as cancer using QME alone or alongside OCT.

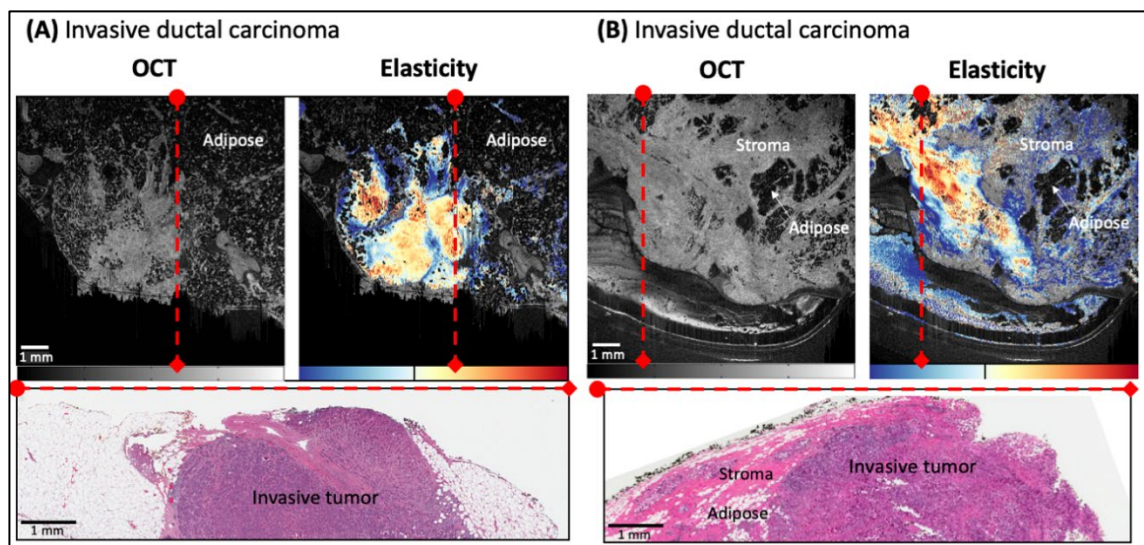


Figure 5.3: Example images of invasive ductal carcinoma. OCT, QME, and H&E histology of (a) highly cellular invasive ductal carcinoma on the margin and (b) invasive ductal carcinoma on the margin surrounded by adipose tissue and stroma tissues. Colour bars: OCT 0-40 dB; Elasticity 3.63-363 kPa.

Figure 5.4 shows ROIs containing two malignant tissue types: DCIS (Figs. 5.4(a)–(c)) and mucinous carcinoma (Figs. 5.4(d)–(f)), which were designated “impalpable” preoperatively and required hookwire guidance for lesion excision. Despite being palpable on a macroscale, changes in mechanical properties on a microscale are detectable by QME for these tissue types [346]. Figures 5.4(a)–(c) shows an example of DCIS within 0.15 mm of the margin; the histology image (Fig. 5.4(c)) shows the involved duct surrounded by dense, benign stroma. The OCT (Fig. 5.4(a)) shows no apparent contrast between this duct and the surrounding stroma, but the QME (Fig. 5.4(b)) highlights high elasticity corresponding to the region of DCIS. This elevated elasticity corresponds to the dense, proliferating cells within the duct, as well as a fibrotic stromal response [355] immediately surrounding the duct. Throughout the stroma in the rest of the ROI, there are small, localised areas of

elevated elasticity, but most do not meet the size criterion for cancer defined in this study. Six of seven readers evaluated this correctly using OCT alone, as the structure shows continuity with depth, and all readers evaluated it correctly using QME. In Fig. 5.4(d)–(f), a region of benign stroma and adipose tissue neighbours a region of mucinous carcinoma on the margin. In OCT (Fig. 5.4(d)), the region corresponding to the mucinous tumour is difficult to distinguish from the surrounding adipose tissue, and one reader designated this as benign. However, in QME (Fig. 5.4(e)) the tumour exhibits elevated elasticity, and all readers correctly classified this ROI as cancerous when QME was available.

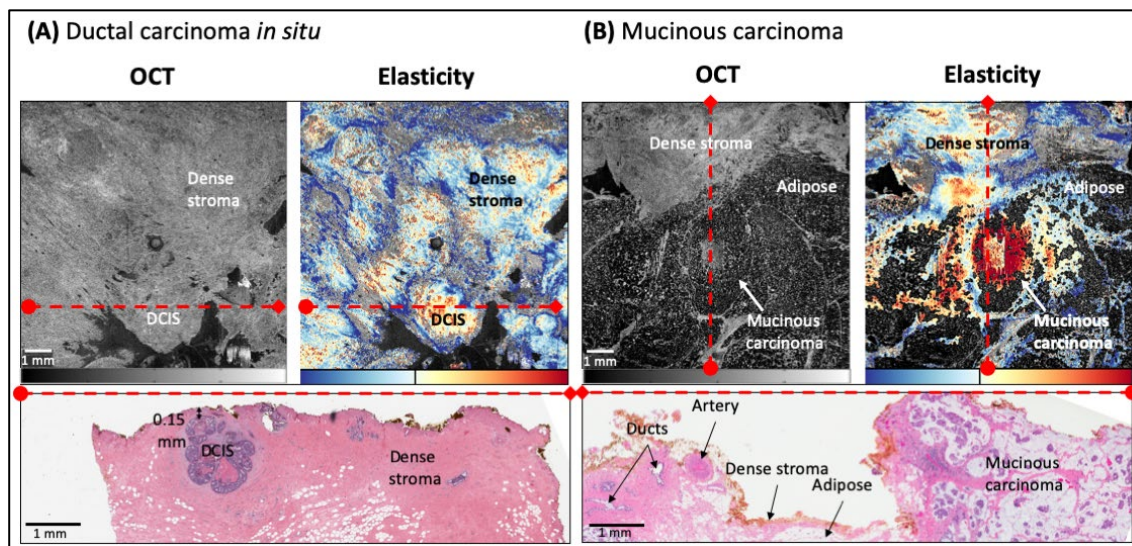


Figure 5.4: Example images of ductal carcinoma in situ (DCIS) and mucinous carcinoma. OCT, QME, and H&E histology of (a) DCIS 0.15 mm from the margin and (b) invasive mucinous carcinoma present on the margin. Colour bars: OCT 0–40 dB; Elasticity 3.63–363 kPa.

Blinded reader study results in higher accuracy using QME over OCT alone

Table 5.3 summarises the results of the reader study. Readers completed evaluation of the 154 OCT plus QME ROIs in an average of 4 hours, or approximately 90 seconds per ROI. Interreader agreement was nearly perfect for QME and OCT plus QME, and moderate for OCT alone, according to a standard interpretation of the Fleiss' Kappa index for interrater agreement. Reported ranges for sensitivity and specificity in Table 5.3 indicate 95% confidence intervals. On the basis of the aggregate results, the sensitivity, specificity, and accuracy of OCT for detecting cancer within 1 mm of the margin were 69.0%, 79.0%, and 77.5%, respectively. Using QME, sensitivity, specificity, and accuracy were 92.9%, 96.4%, and 95.8%, respectively. Using combined OCT and QME criteria, sensitivity, specificity, and accuracy were 80.4%, 99.5%, and 96.5%, respectively. Sensitivity was significantly ($P < 0.05$) improved using QME over OCT alone for 6 of the 7 readers, and specificity was significantly improved using QME over OCT alone for all 7 readers.

Table 5.3: Reader study results.

OCT					
Reader	Sensitivity	Specificity	PPV	NPV	Acc
Eng 1	62.5 ± 19.4%	85.4 ± 6.1%	44%	93%	82%
Eng 2	70.8 ± 18.2%	86.9 ± 5.8%	50%	94%	84%
Surg 1	62.5 ± 19.4%	74.6 ± 7.5%	31%	92%	73%
Surg 2	66.7 ± 18.9%	72.3 ± 7.7%	31%	92%	71%
Path	66.7 ± 18.9%	83.8 ± 6.3%	43%	93%	81%
Res	79.2 ± 16.2%	74.6 ± 7.5%	37%	95%	75%
Radiol	75.0 ± 17.3%	75.4 ± 7.4%	36%	94%	75%
Agg	69.0 ± 7.0%	79.0 ± 2.6%	38%	93%	78%
QME					
Reader	Sensitivity	Specificity	PPV	NPV	Acc
Eng 1	100.0 ± 0.0%	97.7 ± 2.6%	89%	100%	98%
Eng 2	100.0 ± 0.0%	97.7 ± 2.6%	89%	100%	98%
Surg 1	75.0 ± 17.3%	88.5 ± 5.5%	55%	95%	86%
Surg 2	95.8 ± 8.0%	97.7 ± 2.6%	88%	99%	97%
Path	95.8 ± 8.0%	97.7 ± 2.6%	88%	99%	97%
Res	87.5 ± 13.2%	97.7 ± 2.6%	88%	98%	96%
Radiol	95.8 ± 8.0%	97.7 ± 2.6%	88%	99%	97%
Agg	92.9 ± 3.9%	96.4 ± 1.2%	84%	99%	96%
Automated Reader	100.0 ± 0.0%	97.7 ± 2.6%	89%	100%	98%
OCT + QME					
Reader	Sensitivity	Specificity	PPV	NPV	Acc
Eng 1	87.5 ± 13.2%	100 ± 0.0%	100%	98%	98%
Eng 2	87.5 ± 13.2%	100 ± 0.0%	100%	98%	98%
Surg 1	70.8 ± 18.2%	96.9 ± 3.0%	81%	95%	93%
Surg 2	95.8 ± 8.0%	100 ± 0.0%	100%	99%	99%
Path	70.8 ± 18.2%	100 ± 0.0%	100%	95%	96%
Res	66.7 ± 18.9%	99.2 ± 1.5%	94%	94%	94%
Radiol	83.3 ± 14.9%	100 ± 0.0%	100%	97%	97%
Agg	80.4 ± 6.0%	99.5 ± 0.5%	96%	97%	97%

Abbreviations: Acc, accuracy; Agg, aggregate; Eng, engineer; Surg, surgeon; Path, pathology scientist; Res, medical resident; Sonog, sonographer.

Also reported in Table 5.3, the automated reader for QME resulted in 100.0%, 97.7%, and 98.1% sensitivity, specificity, and accuracy, respectively.

5.2.4 DISCUSSION

This study is the first to determine the accuracy of QME, or any variant of optical elastography, for assessment of tumour margins in specimens excised during BCS. Prior to this study, recent investigations had demonstrated that QME has the potential to delineate tumour in breast tissue based on elevated elasticity on a micro-scale [346,347]. In these

studies, as in this one, the contrast between tumour and healthy tissue based on changes in elasticity was shown to be complementary to the structural contrast provided by the underlying modality, OCT. However, prior studies had not investigated the ability of QME to identify positive margins in specimens from BCS. This study has demonstrated high accuracy of QME (96%) compared with OCT (78%) for detecting cancer within 1 mm of the margin in BCS specimens. The measurements here, on intact BCS specimens immediately following surgery, are also of high clinical relevance, compared with prior OCT studies that relied primarily on dissected mastectomy specimens for testing novel margin assessment techniques [332,333,349].

The QME results here indicate that tissue elasticity is an accurate predictor of malignancy. This trend was consistent across multiple tumour types in this study (*e.g.*, solid and mucinous invasive carcinomas, and DCIS), although this must be confirmed with larger sample sizes of each tumour type. Future data collection will also continue to elucidate the sources of elevated elasticity in each tumour type, for example, deposition of stiff desmoplastic stroma, changes in collagen alignment, or interstitial fluid pressure. Better understanding of these mechanisms may foster even greater precision in the use of QME to detect various tumour types intraoperatively. This goal may be facilitated by implementing ultrahigh resolution QME to achieve cellular-scale elasticity resolution [356,357].

Perhaps counterintuitively, although combining OCT and QME improved overall accuracy compared with OCT alone, the sensitivity using the high elasticity criterion (93%) was greater than that using QME and OCT criteria together (80%). This may be due to variability in reader interpretation of the qualitative OCT criteria (interpretation of structures) versus little variability in interpretation of the quantitative QME criterion (elasticity threshold). In particular, analysis of reader notes revealed variability in whether readers considered features as “continuous” with depth based on OCT (Fig. 5.1(a)), which was requisite in this study for an ROI to be considered positive (the engineers who participated as readers had prior experience in reading OCT and elastography images, which may have contributed to their slightly superior reading performance). On the other hand, specificity of OCT and QME together (~100%) was greater than that of QME (96%) or OCT (79%) alone, indicating that the combination of information reduces false positives (*e.g.*, mistaking benign, fibrous stroma for cancer). To improve intraoperative margin assessment and ultimately reduce the need for costly repeat surgeries, high sensitivity is essential to ensuring that less cancer is missed (*i.e.*, minimising false negatives). High specificity, on the other hand, ensures that less benign tissue is unnecessarily removed, and, while important to avoid overtreatment of the cancer, could be considered secondary to the need for high sensitivity in margin assessment. QME showed the best overall performance on both sides, but future

studies will need to analyse the amount of repeat surgeries avoided versus extra volumes of tissue removed.

Although the accuracy of OCT reported here is similar to that reported in another study in BCS specimens [335], further refinement and quantification of OCT criteria may potentially increase accuracy in future studies. For instance, quantification of the rate of OCT signal attenuation with depth has shown potential for distinguishing benign and malignant regions [333,337], although it is not clear the extent to which this will improve accuracy. Our preliminary automation of QME reading could also be extended to incorporate both QME and OCT-based information into an algorithm utilising neural networks.

Although the spatial resolution of OCT and QME images is on the order of micrometres, which is comparable or superior to many existing intraoperative margin assessment techniques, readers were directed to ignore features smaller than approximately 1 mm. This set an effective “diagnostic resolution” of approximately 1 mm, and further study is needed to assess the accuracy of OCT and QME for smaller features, such as very early stage DCIS. However, at a more advanced stage, DCIS tends to result in dilation of ducts, and even small ducts can result in a fibrous stromal response in the surrounding tissue [355]; thus, QME is expected to be sensitive to the associated mechanical changes caused by these features. The resolution of the technique may also improve in the future using the inverse method to solve for elasticity [358,359], rather than rely on assumptions of stress uniformity with depth, as in our current method; however, computation times currently prohibit this from being implemented in clinically feasible timeframes.

Although the results presented here demonstrate the potential of QME for margin assessment in BCS, additional development is required to address the exclusion criteria described in the Results section. In particular, ROIs were excluded because of thermal damage, insufficient contact between the specimen, silicone layer and the imaging window, imaging artifacts and insufficient elasticity data overlaid on solid tissue. In the case of thermal damage, future studies could mitigate its presence in the images by using combined contrast from QME and OCT, including investigation of textural analysis, as well as colorimetric data from photographs simultaneously taken of the specimen, which often show black marks on the tissue surface that may correspond to thermal damage.

Two margins per specimen were imaged in this study, at a rate of approximately 9 minutes per margin. In some specimens, postoperative histology revealed cancer within 1 mm on margins that were not scanned, leading to a discrepancy in the overall prevalence of close margins reported in Table 5.1 (45%) and the prevalence of ROIs containing cancer (15.6%). To facilitate rapid intraoperative QME of all radial margins, which is desirable in the clinical scenario, higher acquisition speed has been achieved using a novel approach [360], and may

be further increased by implementation of high-speed OCT systems, an order of magnitude faster than that in this study [361]. In addition, reader evaluation of the images took 90 seconds on average, which is conducive to clinical timeframes. However, to enable entire margins to be analysed intraoperatively will require the development of image processing algorithms that facilitate more rapid image interpretation. Finally, a handheld probe is in development to allow QME assessment of tissues directly within the surgical cavity and to facilitate implementation into the clinical workflow [362].

In this study, analogously to previous studies [332,335], we selected ROIs ($n = 154$) on which the reader study was performed rather than performing the study on entire margins. Of utmost importance to our reader study is the ability to correspond reader ratings to a ground truth. Without ground truth histology correspondence to our images, we have no basis to classify regions as tumour or non tumour. As the histology protocol used at our hospital enabled histology matching on only a small subset of each margin, the ROI approach was required. As this study has demonstrated strong correspondence between high elasticity and corresponding co-registered tumour, a next step is to perform a reader study on entire margins.

In summary, QME, an emerging OCT elastography technique that probes tissue elasticity on the microscale, has demonstrated detection of close and positive margins in freshly excised specimens in BCS with 93% sensitivity and 96% specificity. The use of intrinsic tissue contrast without need for exogenous dyes and the optimal trade-off in speed, field of view, and resolution provided by QME make it a promising candidate for improving intraoperative guidance of BCS. More broadly, QME may be applicable in a range of surgical or preoperative biopsy guidance applications, particularly in cancers that are known to exhibit altered mechanical properties.

5.3 OPTICAL PALPATION FOR TUMOUR MARGIN ASSESSMENT IN BREAST-CONSERVING SURGERY

Ken Y. Foo,^{1,2} Kelsey M. Kennedy,¹ Renate Zilkens,^{1,3} Wes M. Allen,^{1,2} Qi Fang,^{1,2} Rowan W. Sanderson,^{1,2} James Anstie,^{1,2} Benjamin F. Dessauvague,^{3,4} Bruce Latham,^{4,5} Christobel M. Saunders,^{3,6,7} Lixin Chin,^{1,2} and Brendan F. Kennedy^{1,2,8}

Biomedical Optics Express, 12(3): p. 1666-1682, 2021.

Abstract: Intraoperative margin assessment is needed to reduce the re-excision rate of breast-conserving surgery. One possibility is optical palpation, a tactile imaging technique that maps stress (force applied across the tissue surface) as an indicator of tissue stiffness. Images (optical palpograms) are generated by compressing a transparent silicone layer on the tissue and measuring the layer deformation using OCT. This paper reports, for the first time, the diagnostic accuracy of optical palpation in identifying tumour within 1 mm of the excised specimen boundary using an automated classifier. Optical palpograms from 154 regions of interest (ROIs) from 71 excised tumour specimens were obtained. An automated classifier was constructed to predict the ROI margin status by first choosing a circle diameter, then searching for a location within the ROI where the circle was $\geq 75\%$ filled with high stress (indicating a positive margin). A range of circle diameters and stress thresholds, as well as the impact of filtering out non-dense tissue regions, were tested. Sensitivity and specificity were calculated by comparing the automated classifier results with the true margin status, determined from co-registered histology. 83.3% sensitivity and 86.2% specificity were achieved, compared to 69.0% sensitivity and 79.0% specificity obtained with OCT alone on the same dataset using human readers. Representative optical palpograms show that positive margins containing a range of cancer types tend to exhibit higher stress compared to negative margins. These results demonstrate the potential of optical palpation for margin assessment.

¹ BRITELab, Harry Perkins Institute of Medical Research, QEII Medical Centre, Nedlands and Centre for Medical Research, The University of Western Australia, Perth, Western Australia, 6009, Australia

² Department of Electrical, Electronic & Computer Engineering, School of Engineering, The University of Western Australia, Perth, Australia.

³ School of Medicine, The University of Western Australia, Perth, Australia.

⁴ PathWest, Fiona Stanley Hospital, Murdoch, Australia

⁵ School of Medicine, University of Notre Dame, Fremantle, Australia

⁶ Breast Centre, Fiona Stanley Hospital, Murdoch, Australia

⁷ Breast Clinic, Royal Perth Hospital, Perth, Australia

⁸ Australian Research Council Centre for Personalised Therapeutics Technologies, Perth, Australia

© 2021 Optical Society of America under the terms of the OSA Open Access Publishing Agreement

5.3.1 INTRODUCTION

Breast-conserving surgery (BCS) is one of the main treatments for early-stage breast cancer [363], however, 20–30% of patients must undergo more than one procedure due to positive margins on the excised specimen [364–369], which increases the risk to patient health [369–373], worsens cosmetic outcomes [369–374], and causes adverse socioeconomic effects [369,370,372,373]. Although histopathological intraoperative margin assessment techniques such as frozen section histology and imprint cytology can reduce re-excision rates by 9–36% [371,375,376], these techniques have not been widely adopted [377] due to the additional time (10–30 minutes) [378,379] and resources (*e.g.*, a specialised pathologist) [375] required and the broad range of reported sensitivities (59–100%), and specificities (71–100%) [371,378,379]. Another technique, specimen radiography, has had minimal impact on re-excision rates [376,379], in part due to the suboptimal diagnostic accuracy (33–66% sensitivity, 60–95% specificity) [371,378] and difficulties in detecting and interpreting calcifications [371,378,380]. More recently, a tool using radiofrequency spectroscopy (MarginProbe) has been approved for use in the USA, however, the reported sensitivity (70%) and specificity (70%) are relatively low [376,381]. Therefore, an effective intraoperative margin assessment tool is yet to be widely adopted.

Several optical imaging techniques, such as Raman spectroscopy, fluorescence imaging, and OCT, are currently being investigated to improve intraoperative margin assessment [381]. In particular, OCT generates images based on differences in the optical backscattering of tissues in real-time, without the use of contrast agents and with relatively high spatial resolution (5–10 μm) [381,382], however, benign fibroglandular tissue and tumour tissue can sometimes appear similar in OCT images [382–386]. Another family of techniques, tactile imaging, visualises the force applied across a sample surface (stress) as an indicator of tissue stiffness [231,387]. This relies on the same principle as manual palpation, in which the surgeon locates embedded lesions by applying a force to the tissue and feeling the resistance using their fingertip. Previous implementations of tactile imaging have utilised electronic sensors with the spatial resolution determined by the sensor spacing (typically ~ 1 mm) [388–394]. Our group has pioneered a novel form of tactile imaging, termed optical palpation [395], in which a uniform, transparent, silicone layer is compressed on the tissue surface and the resulting strain (*i.e.*, the relative deformation of the layer) is measured with OCT. Using the pre-characterised layer stress-strain curve, a two-dimensional (2-D) stress map (termed an optical palpogram) can be generated, with greater stress indicating stiff tissue

(*e.g.*, tumour) [386]. Surgeons may then be trained to identify cancer from these images, which may be facilitated by an appropriate choice of colormap (*e.g.*, a divergent colormap that provides contrast between stiff and soft regions) and applying the optical palpogram as a semi-transparent overlay over the OCT image to provide additional structural information. The spatial resolution of optical palpation has previously been shown to be 160–390 μm [386,395,396], which outperforms many previously developed tactile imaging techniques (0.8–2 mm) [388–394].

Optical palpation is expected to be particularly useful for breast cancer margin assessment because cancer alters the mechanical properties of tissue [397]. Surgeons currently utilise this to locate the tumour during surgery through manual palpation [378,398], however, this is subjective, and many breast lesions are clinically impalpable (*i.e.*, too small or soft to be felt) [399]. Although the fingertip reportedly has a spatial resolution of 1.5–2.5 mm [400] in ideal conditions, lesions up to 15 mm in size may be impalpable [399], due to surgical gloves degrading both spatial resolution and the ability to detect mechanical contrast in the tissue [401]. With the enhanced resolution and decreased subjectivity afforded by optical palpation, however, such impalpable lesions may potentially be identified. Optical palpation is related to quantitative micro-elastography (an OCT-based imaging technique that generates a three-dimensional (3-D) tissue stiffness map) [402], however, a significant advantage of optical palpation is the potential for alternative implementations using more cost-effective imaging systems, which would facilitate uptake by medical institutions, particularly in lower resource settings. For example, our group has recently demonstrated camera-based optical palpation, which uses a simple digital camera to measure the silicone layer deformation [227]. Additionally, as optical palpation does not rely on the detection of optical signals directly from the tissue, it may be more robust and practical for surgical deployment, as it is not affected by factors such as blood at the tissue surface that can inhibit other optical imaging techniques, such as OCT. Whilst we have previously shown that optical palpation can provide contrast between benign fibroglandular tissues and tumour tissues [386], the sensitivity and specificity has not yet been reported.

In this paper, the diagnostic accuracy of optical palpation is assessed. Seventy-one BCS specimens were imaged and 154 optical palpation regions of interest (ROIs) (130 benign, 24 containing tumour within 1 mm of the margin) from 142 margins were generated. We additionally propose a classification algorithm to differentiate benign and malignant ROIs. An ROI is classified as malignant if, at any location within the ROI, a circle centred on that location contains high stress over $\geq 75\%$ of its area. Sensitivity and specificity are calculated by comparing the predicted margin status from the automated classifier with the true margin status, as determined from co-registered histology. The performance of this automated

classifier is assessed and optimised, and the results indicate optical palpation shows promise for intraoperative margin assessment.

5.3.2 MATERIALS AND METHODS

Patient recruitment and dataset construction

Seventy-one female patients undergoing breast-conserving surgery at Fiona Stanley Hospital (Project No: FSH-2015-032) in Western Australia were included in this study. Ethics approval was granted by the Sir Charles Gairdner and Osborne Park Health Care Group Human Research Ethics Committee (Lead HREC No: 2007-152) with all participants providing informed consent. One fresh tissue specimen was scanned per patient, with on average two margins scanned per specimen. Of these 71 specimens, final pathology showed 32 (45%) had tumour within 1 mm of any margin, 36 (51%) had tumour ≥ 1 mm from any margin, and 3 (4%) did not have any tumour.

A dataset containing 154 10×10 mm² ROIs was selected from 139 imaged margins. 174 ROIs were initially selected from the imaged margins (prior to reviewing the post-operative histology), with preference for regions with good contact between the specimen, layer and imaging window; no extensive thermal damage from cauterisation during resection; and reliable histology available. After imaging, post-operative histology was obtained following the standard protocol at the institution, which involved fixing the specimen in formalin, inking to preserve orientation and slicing in a 'bread-loaf' manner to obtain histology slides in a plane orthogonal to the *en face* plane. These were co-registered with ROIs by consulting the specimen photographs and blocking diagrams (which indicated the corresponding tissue slice for each histology slide) and cross-checking features in histology with those in the OCT images, using the OCT depth cross section where needed. Following review of the histology with a pathologist, 20 ROIs were excluded for reasons including extensive thermal damage visible in the histology slides (3 ROIs), inconclusive histology slide co-registration (4 ROIs), imaging artifacts (4 ROIs), insufficient contact (3 ROIs), insufficient stress data in solid tissue regions (2 ROIs), tumour < 1 mm in size (2 ROIs), and presence of mucinous ductal carcinoma *in situ* (DCIS) (a rare form of cancer, for which insufficient samples were present) (2 ROIs). ROIs were assigned a true class of positive if any region with positive margins existed within the ROI, and a true class of negative otherwise. Positive margins are defined here as cancer < 1 mm from the surface as determined by pathologists from postoperative histology, which is the currently accepted surgical excision margin required at the clinical practice that we obtained specimens from and consistent with similar BCS diagnostic accuracy studies [403,404]. The pathologists were blinded to any optical palpation information. The final dataset of 154 ROIs (24 positives, 130 negatives) was also used in a

recent reader study assessing the diagnostic accuracies of OCT and quantitative micro-elastography [384], thus enabling direct comparison between these modalities and optical palpation.

Imaging protocol and system

A Thorlabs Telesto II spectral-domain OCT system in common-path configuration with a superluminescent diode source (1300 nm centre wavelength, 220 nm full width at half maximum bandwidth) was used for tissue imaging. 3-D volumes (C-scans) were constructed by combining 2-D images (B-scans), which in turn consisted of a sequence of one-dimensional (1-D) scans in depth (A-scans). A Thorlabs LSM04 objective lens was used, providing measured axial and lateral resolutions (in air) of 5.5 μm and 13 μm respectively, and a field-of-view (in air) of $16 \times 16 \times 3.5 \text{ mm}^3$. Wide-field benchtop scanning was implemented by placing the sample on a pair of orthogonal translation stages, enabling up to a 3×3 grid of subvolumes to be acquired per sample for a total field-of-view of $\sim 45 \times 45 \text{ mm}^2$. Each subvolume comprised $808 \times 808 \times 1024$ pixels (x, y, z) after averaging. To apply compression, the sample was placed on a motorised laboratory jack and an imaging window (65 mm diameter) was fixed above the sample, such that raising the laboratory jack would press the sample against the imaging window. The imaging window was fixed parallel to the laboratory jack baseplate to minimise uneven compression from a tilted imaging window, since this could otherwise result in image misclassification. Further details on the imaging setup are provided in [385].

Prior to tissue imaging, a transparent, compliant silicone layer ($\sim 5 \text{ cm}$ diameter) with uniform thickness ($\sim 500 \mu\text{m}$) was manufactured from Wacker Elastosil P7676 (cross-linker catalyst mixing ratio 1:1). The mechanical characteristics (stress-strain curve) of the silicone were characterised using a uniaxial compression testing apparatus [395], and the undeformed layer thickness was measured with an OCT system. A new layer was used for each imaged margin. As the field-of-view was smaller than both the imaging window and the layer, conditions at the boundary of the imaging window and layer could be ignored, since only the central region was imaged.

Fresh BCS specimens ($\sim 1\text{--}4 \text{ cm}$ thick) acquired immediately after surgery and kept hydrated with saline were imaged. The specimens were not trimmed to reduce geometric irregularity prior to imaging. During imaging, the silicone layer was placed on the tissue and lubricated with silicone oil (Wacker AK50) on the surface facing the imaging window, and the specimen was placed on the laboratory jack. The laboratory jack was then raised to apply bulk compression ($\sim 10\text{--}30\%$ strain per specimen, 6.5% standard deviation) against the imaging window, which was fixed to an actuator to enable both quantitative micro-

elastography images and optical palpograms to be generated from the same data. No mechanism was used to constrain the specimen laterally, such that it was free to expand during compression. As the compression force was distributed over the relatively large area of the imaging window, the specimen did not slip substantially during compression, even after applying saline and silicone oil. Each margin was imaged within nine minutes, and specimens were returned for standard histopathological processing within an hour of collection from surgery.

To ensure optical palpograms obtained from different specimens can be meaningfully compared, we controlled the bulk compression to be largely consistent between specimens. In particular, this allows comparable optical palpograms to be obtained from specimens with different thicknesses. The applied range of bulk compression was chosen to maximise contact with the imaging window and generate good contrast in quantitative micro-elastography images, while accommodating for variations in specimen surface topology.

To generate optical palpograms, a map of layer strain (defined as the change in layer thickness divided by the undeformed thickness) across the compressed tissue surface is measured by identifying the layer/tissue interface in each averaged B-scan using an automatic algorithm based on the Canny edge detector in post-processing [395]. Using the stress-strain curve, the layer stress due to bulk compression is determined to generate optical palpograms. Converting layer strain to stress enables an intuitive physical interpretation for optical palpograms as the force applied at each location on the surface of the specimen; additionally, non-linearity in the stress-strain curve results in additional contrast between stiff and soft features when converted to stress. If negative stress occurs in a region (for example, because the local layer thickness increases after compression, or the edge detector fails), a stress of 0 kPa is recorded. This procedure is illustrated in Fig. 5.5.

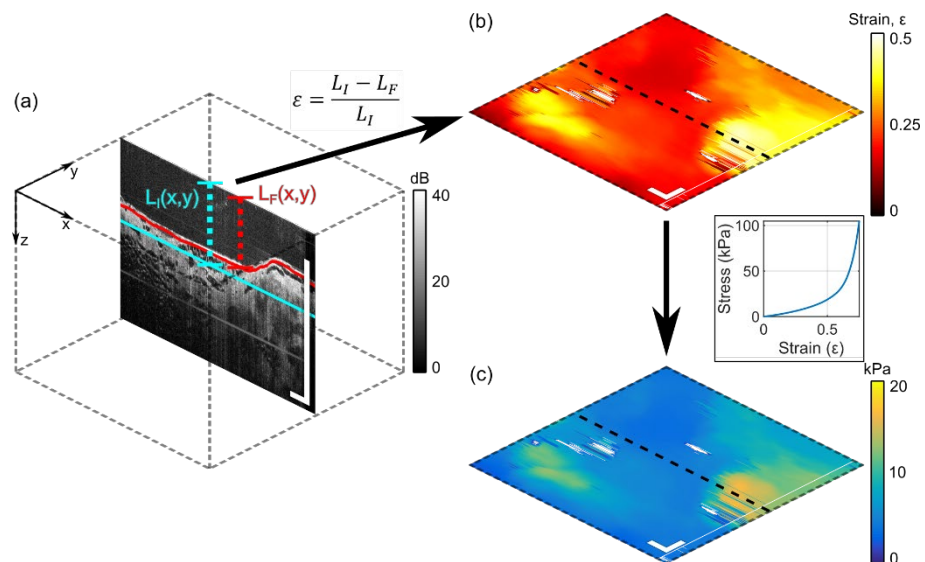


Figure 5.5: Optical palpation working principle. Before imaging, a silicone layer with initial (relaxed) thickness $L_I(x,y)$ is placed on the tissue and bulk compression is applied. For each OCT B-scan (a), the layer/tissue interface is detected, allowing the final (compressed) layer thickness $L_F(x,y)$ to be measured and the *en face* map of layer strain (b) to be computed. This is then mapped to stress, presented in the optical palpogram (c), using the pre-characterised layer stress-strain curve. Scale bars = 1 mm.

Data processing and analysis

To assess the sensitivity and specificity of optical palpation, a classifier algorithm was constructed to predict whether an ROI contained cancer in the margin based on the stress map, and the prediction was compared to the true margin status as determined by co-registered post-operative histology. Essentially, the classifier predicts an ROI is positive if a circle $\geq 75\%$ filled with high stress can be found anywhere in the ROI, for a given circle diameter and stress threshold. More concretely, the optical palpograms are first binarized by setting all pixels greater than or equal to the stress threshold to one, and all other values to zero. These images are then convolved with a circular kernel such that the output of the convolution indicates the fraction of the circle filled with “ones” at the corresponding location, and if any output is $\geq 75\%$, the ROI is predicted to be positive. A 75% threshold was chosen to match the criteria used for both manual and automated classification in a previous study assessing the accuracy of quantitative micro-elastography [384]. Two variants of this classifier were tested: the first is exactly the algorithm described above, whereas the second includes a prefiltering step in which stress outside regions of dense tissue (identified from an *en face* OCT image at a single plane $\sim 100 \mu\text{m}$ below the surface using an intensity-based segmentation algorithm detailed previously) [405] is filtered out (*i.e.*, set to 0 kPa). The main steps performed by the segmentation algorithm to generate a dense tissue mask from the OCT image were noise removal, intensity thresholding, removal of connected components in the binary image with < 200 pixels, and clean-up by applying morphological closing to fill in small holes. The removal of non-dense tissue regions from optical palpograms was motivated by the observation that false positives tend to occur due to high

surface stress in regions with adipose tissue at the surface (possibly due to tumour just outside the margin, as illustrated in Fig. 5.6), as well as artifactual high stress due to layer edge misdetection in regions of poor contact between the layer and tissue surface. Additionally, the layer edge detection algorithm was less reliable in adipose tissue compared to dense tissue, since the layer interface with adipose tissue often exhibited lower intensity in OCT than that with dense tissue; furthermore, the honeycomb texture of adipose tissue sometimes confused the edge detection algorithm. The classifier is illustrated by the flowchart in Fig. 5.7(a).

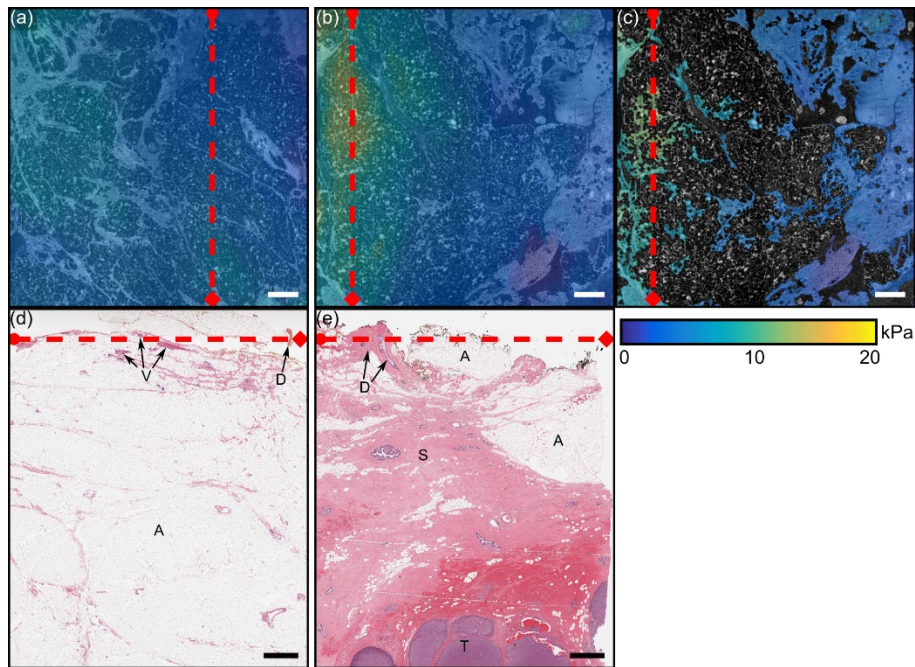


Figure 5.6: Optical palpation in adipose tissue. All optical palpograms are shown overlaid over the *en face* OCT image $\sim 100\ \mu\text{m}$ below the tissue surface. (a) Example of an ROI that is classified as a true negative whether or not non-dense tissue is removed. Histology for this ROI (d) shows mostly adipose tissue and no tumour below this ROI. (b) Example of an ROI that is classified as a false positive when non-dense tissue is not removed but becomes a true negative when non-dense tissue is removed. (c) Histology for this ROI (e) shows a large tumour is present $\sim 7.3\ \text{mm}$ from the tissue surface, with mostly adipose tissue close to the surface. Histology was taken in a plane orthogonal to the *en face* view at the location and orientation indicated by the dashed red lines. A, adipose tissue; S, stroma tissue; T, tumour tissue; D, ducts; V, vessels. Scale bars = 1 mm.

To optimise the classifier performance, a range of input parameters (circle diameter and stress threshold) were tested. The circle diameters ranged from 0.1 mm to 2 mm in increments of 0.1 mm. For each circle diameter, a receiver operating characteristic (ROC) curve was constructed by varying the stress threshold and plotting sensitivity against $(1 - \text{specificity})$. To determine the stress thresholds, for each circle diameter and each ROI, the maximum stress threshold below which the ROI would be classified positive was calculated. Choosing the stress thresholds in this way removes sampling error from the ROC curves, which would likely be present if a linearly spaced sequence of stress thresholds were used instead. The optimum circle diameter is obtained by maximising the area under the ROC curve (AUC), and the optimum stress threshold is obtained from the point on the optimum ROC curve that is closest to the top-left corner (which represents perfect

classification). The classifier optimisation procedure is summarised in the flowchart in Fig. 5.7(b).

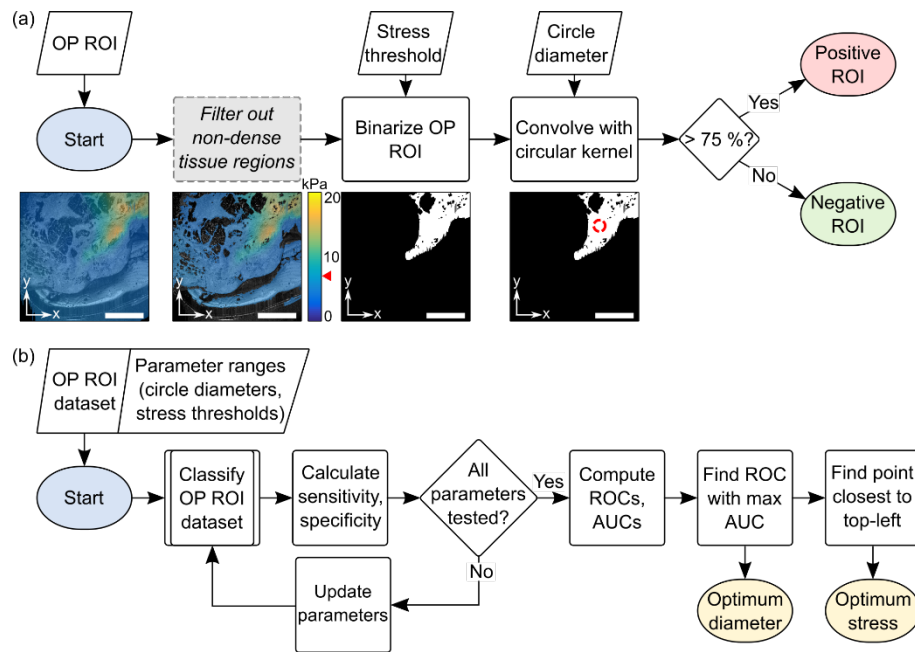


Figure 5.7: (a) Flowchart illustrating the classifier algorithm. The classifier was tested both with and without a prefiltering step to remove non-dense tissue regions (indicated by the grey dashed box). The progress of an example positive ROI through the classifier pipeline is shown below the flowchart. The stress threshold used in this example was 7.04 kPa (indicated by the red triangle on the colour scale), and the circle shown on the binary image has a diameter of 1.1 mm. (b) Flowchart illustrating the classifier parameter optimisation procedure used to determine the optimum circle diameter and stress threshold (and, hence, optimum sensitivity and specificity). OP, optical palpation. Scale bars = 3 mm.

To indicate the potential classifier performance on an independent dataset, leave-one-patient-out cross-validation was performed. Specifically, in a single iteration of cross-validation, all ROIs from a single patient are assigned to the validation set, and all remaining ROIs are assigned to the training set. The optimum classifier parameters are calculated by applying the previously described method to the training set, and the optimum classifier is then applied to the validation set. This is repeated 71 times, with the ROIs from each patient comprising the validation set exactly once. As each ROI is tested once, randomisation of the training and validation sets is not applicable. The final reported optimum circle diameter, stress threshold, sensitivity and specificity are the average of the results over all ROIs. All data processing and analysis was done using MATLAB R2016A.

Results

Figure 5.8 shows four representative optical palpograms for several tissue types. Each optical palpogram is presented as a semi-transparent overlay in dense tissue regions of the corresponding *en face* OCT image at ~ 100 μm depth. Figure 5.8(a) shows an example of a negative margin in a region of dense stroma (validated by histology in Fig. 5.8(c)), in which the stress appears relatively homogeneous and low. This is distinct to the stress above positive margins (Figs. 5.8(b), 5.8(e), and 5.8(f)), each of which exhibits regions of elevated

stress of varying degree and distribution, depending on the cancer type. For example, Fig. 5.8(b) shows a positive margin containing invasive ductal carcinoma (IDC) (validated by histology in Fig. 5.8(d)), which exhibits a large region of very high stress corresponding to the location of the tumour. By comparison, DCIS embedded in benign dense tissue (Fig. 5.8(e), with histology in Fig. 5.8(g)) corresponds to a much smaller region of moderately elevated stress. Although the contrast in DCIS appears lower than in IDC, with an appropriate choice of stress threshold and circle size, DCIS may nonetheless be identified in optical palpograms, demonstrating how this technique may be sensitive to even small tumours. The additional contrast gained by optical palpation over OCT in Fig. 5.8(e) has been quantified by measuring the OCT signal and stress in the tumour and benign regions, indicated by the regions along the red line between the black bars and white bars, respectively. Only dense tissue regions were included in this calculation, and values are reported as mean \pm standard deviation.

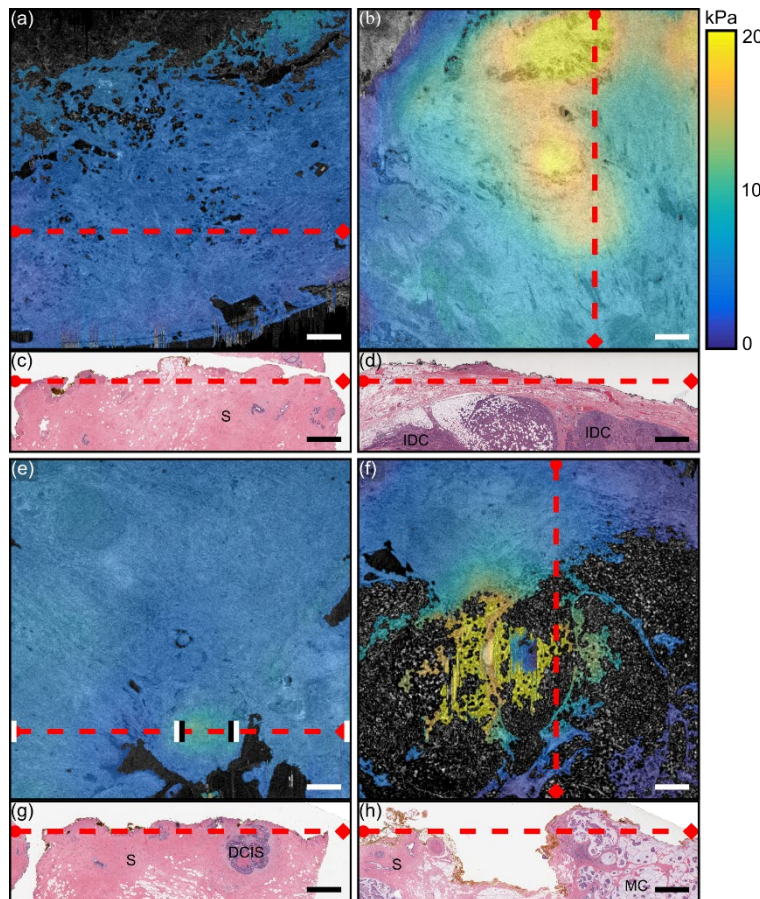


Figure 5.8: Examples of optical palpation images overlaid on dense tissue regions of *en face* OCT ~ 100 μm below the tissue surface for ROIs containing only benign stroma (a), IDC (b), DCIS (e), and mucinous carcinoma (f). Corresponding histology is shown in (c), (d), (g) and (h). Histology was taken in a plane orthogonal to the *en face* view at the location and orientation indicated by the dashed red lines. For (e), regions along the red line between the white bars indicate the regions used to measure the OCT signal and stress in benign dense tissue, and regions along the red line between the black bars indicate the regions used to measure the OCT signal and stress in tumour tissue. S, stroma; IDC, invasive ductal carcinoma; DCIS, ductal carcinoma *in situ*; MC, mucinous carcinoma. Scale bars = 1 mm.

In OCT, the signal in benign regions and tumour regions was 22.15 ± 4.95 dB and 20.62 ± 5.37 dB, respectively, indicating tumour and benign tissue are indistinguishable in OCT in this case. However, in the optical palpogram, the stress in benign regions and tumour regions was 4.15 ± 1.13 kPa and 8.99 ± 1.19 kPa, respectively, illustrating that optical palpation can provide contrast between tumour tissue and benign dense tissue regions. Finally, Fig. 5.8(f) shows an example of mucinous carcinoma. Here, high stress is visible in the region corresponding to the pools of mucin, which may be a result of fluid pressure caused by the mucin.

To demonstrate the relationship between tumour depth and stress, Fig. 5.9 shows boxplots describing the stress distribution above regions with tumour < 1 mm from the surface compared to stress above regions with tumour either ≥ 1 mm from the surface or absent. The stress above regions with tumour < 1 mm from the surface was obtained from positive ROIs. Since a typical positive ROI could contain regions where tumour was ≥ 1 mm from the surface, the stress corresponding to only regions with tumour < 1 mm from the surface was obtained by averaging the stress in a sliding 0.6 mm diameter circular window throughout the ROI, then taking the maximum of this average for each ROI. The window size was chosen to match the optimum circle diameter for the unfiltered optical palpograms (see Table 5.4). To ensure fair comparison with regions where tumour was ≥ 1 mm from the surface or absent, this procedure was also used to obtain the negative ROI stresses. From these boxplots, the median and interquartile range of the stress in regions with negative margins appears lower than that in regions with positive margins, although there is a large overlap over the extent of the boxplot whiskers (representing the range). The statistical significance between the two populations was assessed using the Wilcoxon rank-sum test (also known as the Mann-Whitney U test or Mann-Whitney-Wilcoxon test), which test the null hypothesis that two populations have equal medians. This was chosen instead of other common tests (*e.g.*, Student's t-test) because it does not assume the populations are normally distributed. The population medians were thus found to be different to a statistical significance of $P < 3.4 \times 10^{-7}$. Therefore, in this dataset, regions above tumour < 1 mm from the surface exhibited a statistically significantly higher stress than regions with tumour ≥ 1 mm from the surface or absent.

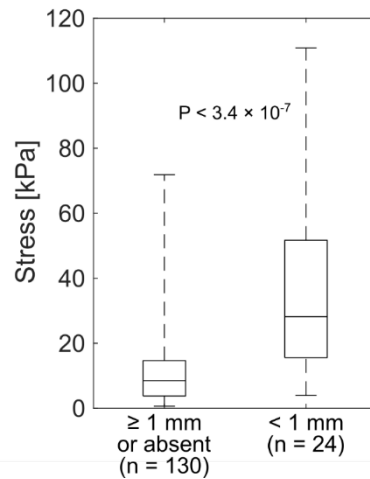


Figure 5.9: Boxplots showing the distribution of average stress in regions with tumour ≥ 1 mm from the surface or absent compared to regions with tumour < 1 mm from the surface. A statistically significant difference ($P < 3.4 \times 10^{-7}$) is observed between the two populations, using the Wilcoxon rank-sum test. For the box plots, centre line = median, box = interquartile range, whiskers = minimum and maximum.

The results of both classifier variants on the 154 ROIs using a range of circle diameters and stress thresholds are summarised by the AUC plots in Fig. 5.10(a) and the optimum ROC curves in Fig. 5.10(b). In each of the AUC plots, a global peak can be identified corresponding to the optimal diameter (indicated by the triangles). When only dense tissue regions are included in the optical palpograms, the AUC plateaus after ~ 0.7 mm, indicating circle size has little effect on the classifier performance after this point. In particular, although the optimum circle diameter increases from 0.6 mm to 1.1 mm after excluding non-dense tissue, similar performance (as indicated by the AUC) can be achieved with a circle size as small as 0.7 mm. The ROC plots show that excluding non-dense tissue regions enables the plot to more closely approach 100% sensitivity and specificity, indicating improved classifier performance. The optimum stress threshold, sensitivity, and specificity for each classifier variant is indicated by a cross marking the point closest to the top-left corner.

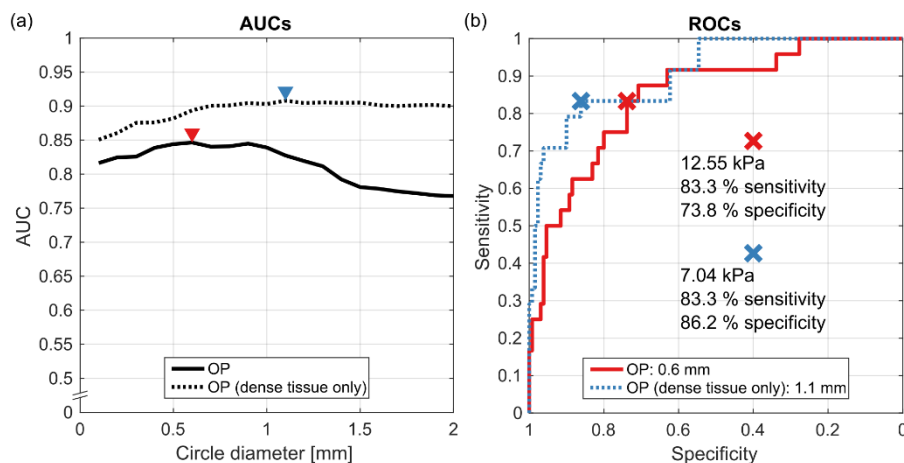


Figure 5.10: (a) AUC plots used to determine the optimum circle diameter. (b) ROC curves with maximum AUC used to determine the optimum stress threshold, sensitivity and specificity. The blue and red curves correspond to the optimum circle diameters identified from the AUC plots that are indicated by the blue and red triangles, respectively. OP, optical palpation.

The optimum sensitivities and specificities (and corresponding AUC, circle diameter and stress threshold) are summarised in Table 5.4. The optimum sensitivity and specificity of the basic optical palpation classifier are 83.3% and 73.8%, respectively, obtained using a circle diameter of 0.6 mm and stress threshold of 12.55 kPa. Pre-filtering non-dense tissue increases specificity to 86.2% by reducing false positives due to high stress in adipose tissue and artifactual high stress in non-contact regions. Filtering out these regions also increases the optimum circle diameter (1.1 mm compared to 0.6 mm) and reduces the optimum stress threshold (7.04 kPa compared to 12.55 kPa). However, since pre-filtering non-dense tissue regions causes classifier performance to plateau after ~ 0.7 mm (Fig. 5.10(a)), this variation in optimum classifier parameters may be a result of the classifier optimisation procedure, rather than a change in the optical palpograms. To provide some context for these results, the sensitivity and specificity of optical palpation with dense tissue regions filtered out are lower than those of quantitative micro-elastography (100.0% and 97.7%, respectively), but higher than those of OCT (69.0% and 79.0%, respectively), when tested on the same dataset. The diagnostic accuracy of OCT shown here is also similar to that reported by others in previous studies [404]. The method used to obtain the quantitative micro-elastography and OCT results has been described in detail previously [384]; briefly, quantitative micro-elastography images were classified by searching for regions where a 1 mm diameter circle was $\geq 75\%$ filled with elasticity above 26.3 kPa, whereas OCT images were classified by seven human readers based on criteria including the presence and organisation of solid tissue, the continuity of solid tissue with depth, and the presence of mucin. The lower accuracy of optical palpation compared to quantitative micro-elastography is expected, since quantitative micro-elastography generates more information than optical palpation (a 3-D map of tissue stiffness in quantitative micro-elastography images, compared to the 2-D map of layer stress in optical palpograms), albeit with more demanding costs (financial, hardware, software, and time), both during acquisition and processing. However, the benefit of the additional contrast provided by optical palpation compared to OCT is also reflected in the superior performance.

Table 5.4: Optimum diagnostic accuracies and classifier parameters.

	Sensitivity	Specificity	AUC	Circle diameter [mm]	Stress threshold [kPa]
Optical palpation	83.3%	73.8%	0.847	0.6	12.55
Optical palpation (dense tissue only)	83.3%	86.2%	0.908	1.1	7.04
Quantitative micro-elastography*	100.0%	97.7%		1.0	26.3 [†]
OCT (human reader study)*	69.0%	79.0%			
Leave-one-patient-out cross-validation					
Optical palpation	75.0%	74.6%		0.61 ± 0.05 [‡]	12.60 ± 0.53 [‡]
Optical palpation (dense tissue only)	75.0%	86.2%		1.12 ± 0.13 [‡]	7.04 ± 0.21 [‡]

* From [384].

[†] For quantitative micro-elastography, stress refers to the local tissue elasticity [402].[‡] Mean ± standard deviation.

Leave-one-patient-out cross-validation decreased sensitivity by 8.3% from 83.3% to 75.0% for both the basic and non-dense tissue excluded classifiers, which corresponds to an additional two of the 24 positive ROIs becoming false negatives. This occurs because the dataset contains only two examples of tumour exhibiting a small, concentrated region of high stress. When either of these ROIs are used for testing (*i.e.*, they are excluded from the training set), the circle diameter increases and stress threshold decreases, causing them to be misclassified (since the small region of high stress is not large enough to fill 75% of the increased circle diameter). Therefore, including more positive ROIs would likely improve the cross-validated sensitivity. However, cross-validation had practically no effect on the specificity, and the classifier parameter standard deviation is small, suggesting that application of this classifier, with the optimum parameters found here, to an independent dataset may yield a similar specificity to that achieved in this study. It should be noted that while the cross-validated results provide an indication of the classifier performance on an independent dataset, they do not indicate the diagnostic accuracy of applying the classifier with the stated parameters to the dataset in this study; this is indicated by the non-cross-validated results.

5.3.3 DISCUSSION

In this study, the diagnostic accuracy of optical palpation for detecting tumour < 1 mm from the tissue surface in 154 ROIs taken from BCS specimens was measured for the first time. A classifier based on simple thresholding and convolution was proposed and optimised for this ROI dataset, with leave-one-patient-out cross-validation performed to assess generalisability to an independent dataset. Two variants of this classifier were tested to evaluate whether the diagnostic accuracy could be improved by filtering non-dense tissue regions. 83.3% sensitivity and 86.2% specificity were achieved using a circle diameter of 1.1 mm and stress threshold of 7.04 kPa with non-dense tissue regions filtered. To support

these findings, representative images of optical palpograms in regions containing benign stroma, IDC, DCIS, and mucinous carcinoma were presented. Additionally, an analysis of the stress distribution showed that the stress above positive margins was higher than that above negative margins to a statistical significance of $P < 3.4 \times 10^{-7}$.

For the optimum classifier parameters (1.1 mm circle diameter, 7.04 kPa stress threshold, and non-dense tissue filtered out), there were four false negatives and 18 false positives. Of the false negatives, three contained DCIS and one contained mucinous carcinoma. One of the DCIS cases contained multiple small regions with high stress (> 7.04 kPa), however these were too small (~ 0.7 mm diameter) to be classified positive using a 1.1 mm circle diameter. This suggests DCIS and mucinous carcinoma may be more challenging to identify in optical palpograms compared to IDC (since all IDC ROIs were correctly classified), perhaps because regions of DCIS or mucinous carcinoma may often be smaller or softer than IDC. Of the false positives, 15 were classified positive due to regions > 1.1 mm in diameter with stress only slightly above the threshold (< 3 kPa above 7.04 kPa). This suggests specificity could be increased substantially by a small increase in stress threshold, although at the expense of sensitivity.

In this study, a fixed threshold of 75% was chosen for the minimum percentage of the circle required to be filled with high stress to result in a positive classification. This threshold was based on the criteria used in a previous study on the diagnostic accuracy of quantitative micro-elastography [384]. It is possible that changing this threshold criterion could affect the sensitivity and specificity. For example, requiring the circle to be 100% filled could bias the algorithm to classify ROIs as negative, since then a single pixel below the high stress threshold within the circle would cause a negative classification. This could potentially significantly degrade sensitivity, especially for cases using a large circle diameter, high stress threshold, or excluding non-dense tissue. Assessment of the impact of the circle percentage threshold on sensitivity and specificity could be a possible direction for future study.

The optical palpation technique presented in this manuscript is still at an early stage, and as such the results presented here demonstrate proof-of-principle rather than a clinical study. While this paper has presented an assessment of optical palpation on excised BCS specimens, one future research avenue of great interest towards clinical application would be implementing and assessing optical palpation *in vivo* directly in the surgical cavity. Current margin assessment techniques have so far only been applied to excised specimens (indeed, histopathological techniques would be impossible to perform on *in vivo* tissue). However, direct assessment of the cavity would enable surgeons to directly locate residual tumour, thus avoiding the problem of co-registering the excised specimen to the cavity. Therefore, future research may involve developing and assessing optical palpation for *in vivo* applications.

The straightforward and practical nature of optical palpation provides several notable benefits. Unlike some elastography techniques, optical palpation does not require an actuator [402,406], decreasing the cost of the system. The removal of a moving mechanical part and associated electronics may also increase system robustness and, in the case of *in vivo* surgical cavity imaging, simplify probe design. Additionally, optical palpation requires less data compared to other elastography techniques, as optical palpation requires only a single measurement at each location, while alternative elastography techniques (such as quantitative micro-elastography) require multiple measurements to calculate displacement [406]. This may enable faster acquisition and processing times, which may be particularly desirable due to intraoperative time constraints; alternatively, the sampling density or field-of-view may be increased while maintaining the same acquisition and processing times. Recently, our group have demonstrated optical palpation can be achieved without an OCT system using camera-based optical palpation [227], which uses a simple digital camera to measure the compression-dependent change in optical attenuation in a specially designed stress layer. This can generate optical palpograms with similar contrast and resolution to OCT-based optical palpation, while drastically reducing the cost of the system by a factor of ~ 100 compared to an OCT system (the camera and lens in total cost $\sim \$800$ USD), and also significantly reducing data size and acquisition and processing times (since only 2-D images are captured, rather than 3-D OCT data) [227]. Developing camera-based optical palpation handheld probes could allow surgeons to image suspicious locations in the cavity in seconds; furthermore, the conceptual similarity between optical palpation and the routine practice of manual palpation may help reduce the training needed to operate such probes and interpret optical palpograms.

It should be noted that optical palpation does not enable direct measurement of the distance between tumour and the tissue surface; rather, the deeper a stiff tumour is embedded, the less visible it will be in the optical palpogram. This effect helps explain why regions above positive margins exhibit higher stress than regions above negative margins (Fig. 5.9), as well as how the reasonably high diagnostic accuracy of optical palpation was achieved. Additionally, the diagnostic accuracy reported here will vary with the definition of a positive margin (defined here as tumour within 1 mm of the excised tissue surface); furthermore, the optimal circle diameter and stress threshold would likely change, since the size and intensity of an embedded inclusion in an optical palpogram depends on the inclusion depth. Since OCT was used as the underlying imaging modality, the OCT image may also be used to ascertain the distance of tumour from the surface, and thus, through combination with optical palpation, potentially increase diagnostic accuracy, however, this was not done in this paper (although OCT images from a single plane ~ 100 μm below the surface were

used for the non-dense tissue filter). Previous work in tactile imaging has also demonstrated “mechanical imaging”, in which a 3-D map localising stiff lesions in breast tissue is generated from a 2-D force sensor array output and an initial model of the tissue structure [387,407]. In future work, this technique may also be applied to optical palpation to enable the margin distance to be estimated without needing an OCT system.

Our results show that, for our dataset, including only dense tissue regions generally increased specificity whilst having little effect on sensitivity. One potential explanation for this may be that benign adipose tissue can be distinguished from dense tissue with high confidence in OCT images [408–410]; therefore, excluding regions with adipose tissue at the surface results in the exclusion of some regions with no tumour at the surface. If these regions correspond to negative margins, excluding these regions removes the chance of false positives occurring (thus increasing specificity); however, if they correspond to positive margins (for example, due to cancer < 1 mm from, but not touching, the tissue surface), the likelihood of false negatives increases (thus decreasing sensitivity). It should be noted that as there has been an increasing trend towards only classifying “tumour on ink” (*i.e.*, tumour touching the surface) as a positive margin for IDC [370], the reduced ability to detect tumour below the surface may not be too detrimental clinically (although a 2 mm margin is still recommended for DCIS) [411]. The improved performance for our classifier when only dense tissue is included indicates that, for our dataset, regions with adipose tissue at the surface are more likely to correspond to negative margins than positive margins. The improved performance after excluding non-dense tissue may also be partially attributed to the removal of artifacts in optical palpograms in which high stress was displayed in regions of non-contact (most often due to errors in the edge detection algorithm), further reducing the number of false positives detected. However, more data is needed to determine if the potential reduction in false positives achieved by excluding non-dense tissue outweighs the potential increase in false negatives across a larger dataset.

It should also be considered that optical palpation generates a map of layer stress, which increases with applied compression. By comparison, for ideal, linear elastic samples, techniques that measure tissue stiffness are independent of bulk compression, however, for hyperelastic samples (*e.g.*, breast tissue) [412] stiffness also increases with applied compression. Therefore, it is important to keep the applied bulk compression relatively constant between tissue samples. In this paper, bulk strain was maintained between ~ 10 – 30% , which was sufficiently uniform to enable comparison between different scans. Alternatively, a larger bulk strain may be used to increase the visibility of tumours embedded in deeper regions. Additionally, in this paper, stress was estimated from layer strain using a simple 1-D model that is described by the stress-strain curve, but does not account for the

effects of friction or lateral effects (*i.e.*, changes in the stress-strain curve at a given lateral location due to compression at an adjacent location). The use of this simple model therefore likely results in some error in the stress estimate, however, this was minimised experimentally by applying lubricant between the stress layer and the imaging window to reduce friction. In future work, an improved model utilising finite element analysis (termed “computational optical palpation”) may also be used to account for lateral effects, which has been shown to improve resolution [413].

One potential challenge facing optical palpation is the impact of surface topology variations on the resulting stress map. Highly variable surface topology may generate variations in the stress map, which may suggest the presence of a stiff inclusion that does not exist. To reduce this effect, we have designed the stress layer stiffness to match that of breast tumours. As a result, surface topology variations due to soft benign tissue do not cause significant deformation in the layer (thus not appearing in the optical palpogram), whereas stiff tumours still cause deformation in the stress layer and are thus visible. An experimental analysis of the effect of surface topology on the stress map in silicone phantoms has also showed that topology variations have little impact on stress compared to stiff features [396]. As a result, in this paper, surface topology variations did not seem to greatly affect the ability of optical palpation to detect stiff tumours, as demonstrated by the reasonably high diagnostic accuracy.

In conclusion, the diagnostic accuracy of optical palpation for identifying positive margins was found to be 83.3% sensitivity and 86.2% specificity using a dataset containing 154 ROIs taken from BCS specimens. This result was achieved using a classifier that searched for 0.6 mm diameter circular regions in optical palpograms with non-dense tissue filtered that were $\geq 75\%$ filled with stress above 7.04 kPa. These results demonstrate the potential of optical palpation as a tumour margin assessment tool for BCS.

Acknowledgements

The authors acknowledge the facilities and scientific and technical assistance of the Australian Microscopy & Microanalysis Research Facility at the Centre for Microscopy, Characterisation and Analysis, the University of Western Australia, a facility funded by the University, State and Commonwealth Governments. This work was supported by research grants from the Australian Research Council and the Department of Health, Western Australia; a research contract with OncoRes Medical; and the Herta Massarik PhD Scholarship for Breast Cancer Research from the University of Western Australia.

CHAPTER 6

OPTICAL COHERENCE ELASTOGRAPHY IMAGING PROBES

6.1 PREFACE

As described previously, the translation of an imaging technique towards clinical applications requires clinical validation and the development of imaging. In Chapter 5, the clinical efficacy of optical coherence elastography (OCE) in the assessment of tumour in breast-conserving surgery (BCS) patients is presented, showing a high diagnostic accuracy. These promising results suggest that OCE can be translated into routine use in BCS provided a suitable imaging probe, capable of meeting the challenges of clinical applications can be designed. In this Chapter we review a number of the more prominent OCE imaging probes to date. In particular focusing on how the needs of the clinical applications shape the design of OCE imaging probes. This Chapter provides the reader with a comprehensive overview of existing OCE probes and provides insight into the design considerations necessary to the fabrication of new OCE imaging probes for specific clinical applications. In addition, the core OCE concepts of optical design, mechanical loading and acquisition protocols are presented in the context of these applications namely, ophthalmology, oncology, and dermatology.

This Chapter is an adaption of a first-authored book chapter, Rowan W. Sanderson, Qi Fang, Andrea Curatolo, and Brendan F. Kennedy, “*Optical coherence elastography imaging probes*,” in Brendan F. Kennedy (Ed.), *Optical Coherence Elastography: Imaging Tissue Mechanics on the Micro-Scale*, AIP, (to be published October 2021), which is intended for a wide audience and provides the reader with descriptions of the core concepts and applications of OCE.

This Chapter includes a discussion of finger-mounted quantitative micro-elastography (QME) in the broader context of OCE imaging probes. An in-depth description of finger-mounted QME is presented in Chapter 7.

6.2 OCE IMAGING PROBES

Rowan W. Sanderson^{1,2}, Qi Fang^{1,2}, Andrea Curatolo^{1,2,3} and Brendan F. Kennedy^{1,2}

Book Chapter in Optical Coherence Elastography: Imaging Tissue Mechanics on the Micro-Scale, AIP Publishing, (to be published October 2021).

Abstract: Imaging probes for OCE are undergoing development to enable its practical implementation in a number of applications. The specific challenges posed by each application defines the technical requirements for each probe, leading to the development of a range of bench-top, handheld, and endoscopic probes. In addition, a number of more compact OCE imaging probes have been proposed, including finger-mounted and needle-based probes. In this Chapter, we describe each of these probes in detail within the context of the relevant applications they are proposed for. An analysis of each probe is provided, with particular focus on optical design, mechanical loading, and image acquisition protocol.

6.2.1 INTRODUCTION

The main applications of OCE are ophthalmology [208,414,415], oncology [106,206], tissue engineering [416] and mechanobiology [417]. While OCE has shown significant potential in these applications, so far, most studies have focused on proof-of-principle studies in engineering laboratory-based settings. To move beyond the laboratory and into routine use requires the development of sample-system interfaces, *i.e.*, imaging probes, that provide access to the specific region of interest in a form factor that is practical and convenient for the intended user, *e.g.*, a physician or biologist. In this Chapter, we will review the progress made to date in the development of OCE imaging probes towards deployment in the various applications described.

It is instructive to consider that, in common with the development of many imaging techniques, the development of OCE can broadly be defined by the following distinct stages that encompass technology readiness levels 1-7 [418]:

1. Initial proof-of-concept implementation.
2. Technique refinement and characterisation.
3. Feasibility studies in a laboratory environment.

¹ BRITelab, Harry Perkins Institute of Medical Research, QEII Medical Centre, Nedlands and Centre for Medical Research, The University of Western Australia, Perth, Western Australia, 6009, Australia

² Department of Electrical, Electronic & Computer Engineering, School of Engineering, The University of Western Australia, Crawley, Western Australia, 6009, Australia

³ Image-guided Devices for Ophthalmic Care Laboratory (IDoc), International Centre for Translational Eye Research, ul. Skierniewicka 10A, 01-230 Warsaw, Poland and Institute of Physical Chemistry, Polish Academy of Sciences, ul. Kasprzaka 44/52, Warsaw, Poland

4. Clinical and scientific validation in the intended operational environment for a given application.
5. System commercialisation.

As indicated above, invariably, the design and development of OCE imaging probes are determined by the specific requirements set by different applications. For some applications, systems designed for use in the laboratory require minimal additional development and largely involve the refinement of proof-of-concept systems to make them accessible to the non-OCE expert, *e.g.*, in areas such as tissue engineering and cell biology, bench-top setups may already be an adequate interface. In other cases, particularly in clinical applications, bench-top probes often cannot easily access the region of interest, *e.g.*, *in vivo* imaging of arteries or intraoperative detection of residual tumour in a surgical cavity.

In this Chapter, we will explore OCE imaging probes proposed so far, summarised in Table 6.1, that form sample-system interfaces to bridge the gap between studies in controlled environments and those in the intended operational environments. We classify these probes into four groups, namely, bench-top probes, handheld probes, endoscopic probes, and other compact imaging probes, and list the main applications that have been proposed for each group. We describe the technical aspects of each probe in terms of optical design, mechanical loading, and acquisition protocol, and describe how each probe is designed to suit particular applications.

Table 6.1: Summary of OCE imaging probes and relevant applications.

	Probe	Application area
Bench-top probes	Lan <i>et al.</i> [419]	Ophthalmology
	Lan and Twa [420]	Ophthalmology
	De Stefano <i>et al.</i> [421]	Ophthalmology
	Zvietcovich <i>et al.</i> [210]	Ophthalmology
	Ramier <i>et al.</i> [422]	Ophthalmology
	Nair <i>et al.</i> [209]	Ophthalmology
	Kling [423]	Ophthalmology
	Liu <i>et al.</i> [424]	Dermatology
Handheld probes	Li <i>et al.</i> [206]	Oncology
	Kennedy <i>et al.</i> [425]	Oncology
	Fang <i>et al.</i> [28]	Oncology
	Fang <i>et al.</i> [426]	Oncology
	Bartolini <i>et al.</i> [427]	Dermatology
	Parmar <i>et al.</i> [428]	Dermatology
Endoscopic probes	Liu <i>et al.</i> [429]	Oncology
	Qu <i>et al.</i> [430]	Cardiology
	Bu <i>et al.</i> [431]	Pulmonology
	Robertson <i>et al.</i> [432]	Pulmonology
	Qi <i>et al.</i> [433]	Cardiology
	Nakamura <i>et al.</i> [434]	Endoscopy
	Karpiouk <i>et al.</i> [435]	Cardiology
Other compact probes	Fang <i>et al.</i> [436]	Oncology
	Kennedy <i>et al.</i> [437]	Oncology
	Kennedy <i>et al.</i> [438]	Oncology
	Latus <i>et al.</i> [439]	None specified
	Sanderson <i>et al.</i> [440]	Oncology

6.2.2 BENCH-TOP IMAGING PROBES

Bench-top OCE imaging probes are those with the largest form factor and, as mentioned above, invariably require the least technical development to translate laboratory-based OCE systems to routine use in the intended operational environment. These probes are suitable for those applications where straightforward access to the tissue is possible, *e.g.*, for imaging the eye, excised specimens, and the skin. Bench-top OCE imaging probes typically provide a larger field of view (FOV), as well as higher lateral resolution, imaging speed and sensitivity than more compact probes at the expense of a larger form factor.

Bench-top OCE probes, such as those shown in Figure 6.1, have been developed for applications in ophthalmology for *in vivo* assessment of corneal biomechanics, *e.g.*, for assessing the effect of ultraviolet (UV) crosslinking of corneal collagen to treat keratoconus and in oncology for tumour margin assessment of excised human breast tissue [106,303,425,441,442]. More preliminary bench-top probes have been proposed in other applications, *e.g.*, in dermatology for *in vivo* assessment of systemic sclerosis [424]. One of the main challenges in common with all OCE imaging probes is in achieving a mechanical loading mechanism aligned with the optical axis of the optical coherence tomography (OCT) system without obscuring the imaging FOV. The key design choices to overcome this

challenge are dependent on both clinical application and the OCE technique used. Specifically in ophthalmology, the eye, being a delicate organ, is highly sensitive to direct contact and large forces cannot typically be applied, hence non-contact, transient loading is preferred, whereas in oncology, excised specimens can be larger than 5×5 cm and therefore require a large FOV and loading area, most readily achieved using compressive loading. In the rest of this Section, we classify bench-top probes into two groups based on their clinical application in ophthalmology and oncology, respectively.

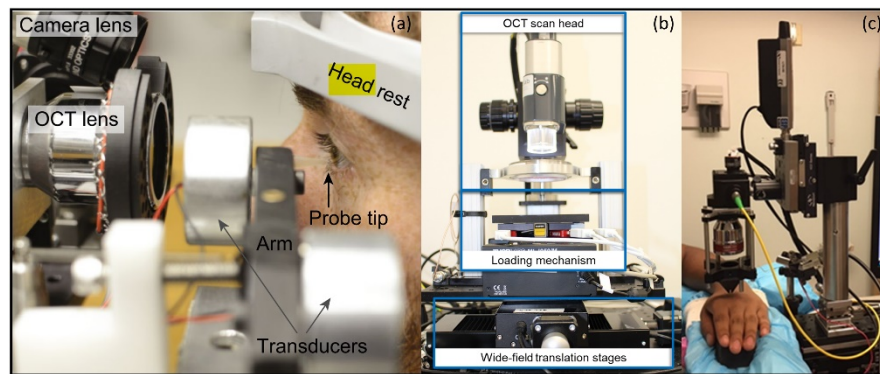


Figure 6.1: Examples of bench-top OCE imaging probes for applications in (a) ophthalmology [422], (b) oncology (adapted with permission from [303] © The Optical Society) and (c) dermatology (adapted from [424]).

6.2.2.1 OPHTHALMIC BENCH-TOP PROBES

Optical design

In the majority of ophthalmic applications of OCE, analogously to ophthalmic OCT, spectral domain OCT systems with central wavelength at ~ 800 nm are used, providing A-scan acquisition rates ~ 100 kHz [209,419,423,443]. More recently, several studies have demonstrated the use of swept-source OCT systems, employing Fourier-domain mode-locked (FDML) lasers, with central wavelengths ~ 1000 nm or ~ 1300 nm providing much higher acquisition speeds (> 1 MHz [299,300]).

Common-path interferometry is often incorporated into ophthalmic bench-top probes, as sharing the reference and sample arms along a single optical path reduces susceptibility to phase fluctuations caused by using OCT systems in clinical settings, *e.g.*, due to vibrations and thermal variations, thus providing nanometer-scale displacement sensitivity close to that attainable in the laboratory [444]. Originally proposed by Kennedy *et al.* for applications in oncology [445], common-path OCE imaging probes have since been developed for ophthalmic applications [209,419,443]. However, in some bench-top OCE imaging probes [210,421,423], it is more practical to implement dual-arm interferometers rather than common-path interferometers as it is more straightforward to optimise the reference arm signal, resulting in high OCT SNR, and they are often less spatially confined, allowing easier implementation of unobstructed mechanical loading mechanisms [444].

The majority of ophthalmic OCT scan systems are telecentric, employing large (one- or two-inch aperture) f-theta objective lenses and galvanometric mirror scanners as shown in Fig. 6.2(a). However, such design is often not compatible with mechanical loading mechanisms centred and collinear with the optical axis, as required to load tissues like the cornea. For this reason, novel optical scan probe designs have been developed. In particular, Lan and Twa [420] modified a Schwarzschild lens system, which was initially proposed for use in astronomical telescopes [446], to design an OCE scan objective, illustrated in Fig. 6.2(c). The Schwarzschild scan objective effectively creates a partial aperture along the optical axis to allow for placement of the mechanical loading mechanism required to generate mechanical waves close or on the corneal apex (optical axis), whilst preserving the ability to perform OCT scanning to measure propagation of the mechanical waves. In applications where transient mechanical loading is applied and capturing the resulting travelling wave is desired, one could opt to use a resonant scanner instead of a galvanometric scanner for the mirror steering the scanning optical beam along the fast axis [300].

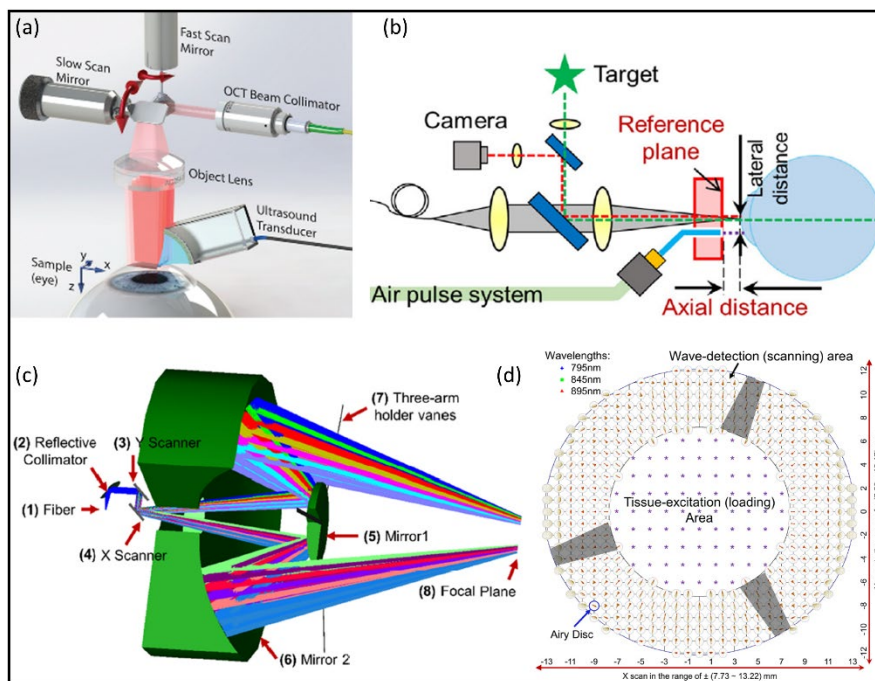


Figure 6.2: Schematic diagrams of bench-top OCE imaging probes for use in ophthalmology. (a) Telecentric f-theta scanning system with galvanometer mirrors. Adapted from [447]. (b) Schematic of an *in vivo* clinical corneal biomechanics bench-top OCE imaging probe, with micro air-puff system, fixation target and pupil camera, along with a representative corneal surface displacement profile. Reproduced from [443]. (c) Design of a Schwarzschild scan objective for ophthalmic OCE and (d) demonstration of the loading and scanning areas, as well as the spot diagrams at the focal plane. The purple stars show the possible loading locations. The distance between two spots is 1 mm in the x - and y -directions. The shadow areas are due to the obscuration of the mirror mount [420]. (c) and (d) adapted with permission from [420] © The Optical Society.

A challenge for *in vivo* ophthalmic imaging is eye motion which can lead to imaging artifacts that can cause errors in the measurement of tissue deformation. Such unwanted patient motion is also an issue in OCT systems for which a number of mitigation strategies have been developed. These strategies can be leveraged in bench-top OCE imaging probes

to expedite development. For example, motion artefact can be substantially reduced using a chin and headrest [422]. In some cases, a bite plate with a disposable single-use cover is used to stabilise the skull and minimise head motion [421]. In addition, clinical OCE imaging probes often include a visual fixation target and a pupil camera to ensure eye centration and stability, whilst also enabling potential residual eye motion to be monitored [419,443]. To achieve this, dichroic mirrors and beam splitters must be added in the OCT beam path.

Mechanical loading

The eye is sensitive to externally applied forces which can cause discomfort for the patient and involuntary eye movements that distort images. Non-contact loading methods such as micro air-puff [419,443,448–450] (Fig. 6.3(a)) and acoustic micro-tapping via an air-coupled ultrasound (ACUS) transducer [443,445,447] (Figs. 6.3(b) and (c)) have been developed to overcome this challenge. In general, these mechanical loading mechanisms are introduced at an angle with respect to the OCT scan objective to avoid obstruction to the OCT beam path. As a consequence, tissue loading cannot be made centred and collinear with the imaging axis and the corneal apex, thereby increasing the complexity of the image reconstruction and the accuracy of the elasticity estimation.

Another mechanical loading mechanism that could minimise patient discomfort uses ambient pressure modulation in an eye cup/chamber [423]. In an innovative solution that eliminates any patient discomfort, the natural arterial pressure in the eye is used as the mechanical loading mechanism, reducing the need to apply an external mechanical load [209].

While non-contact loading is most common in ophthalmic OCE, preliminary contact-based techniques have also been demonstrated [421,422]. De Stefano *et al.* have utilised lower compressive forces than those used in other compression OCE techniques (*e.g.*, when preloading surgical specimens), in conjunction with a topical anaesthetic to reduce patient discomfort (Figs. 6.3(d) and (e)) [421]. Meanwhile, Ramier *et al.* [422] have developed a separate contact loading method, utilising a 2 mm-diameter spring-loaded probe tip to provide contact forces of ~ 0.02 N, vibrating over ~ 1 s with a frequency linearly modulated between 2 kHz and 16 kHz. Contact is made at different off-centre positions on the eye, on the cornea, limbus, and sclera (Fig. 6.1(a)).

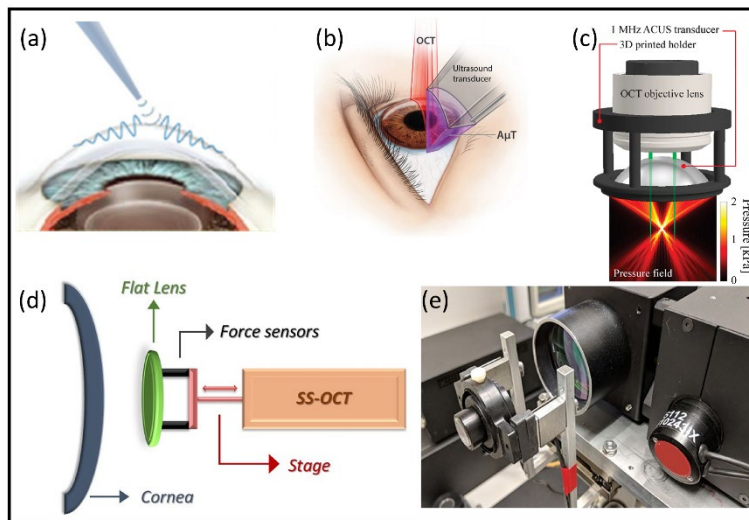


Figure 6.3: Photograph and schematic diagrams of ophthalmic bench-top OCE imaging probes. (a) Schematic diagram of a non-contact micro air-puff probe. Adapted from [449], DOI: 10.1088/1612-2011/10/7/075605 © Astro Ltd. Reproduced by permission of IOP Publishing. All rights reserved. (b) Schematic diagram of non-contact transient loading using focused ultrasound to generate elastic shear waves in the cornea. Adapted from [451]. (c) Schematic and design of acoustic micro-tapping setup and a novel spherically focused confocal ACUS probe [210] © The Optical Society. (d) Schematic and (e) picture of a contact compression OCE clinical probe, with a focus on the optics and loading stage, including galvanometer scanning mirrors, scan lens, transparent flat lens, force sensors, and translational stage. (d) and (e) reproduced from [421].

Acquisition protocol

The majority of ophthalmic bench-top OCE imaging probes have utilised phase-sensitive detection, where the shift in phase between an unloaded and loaded sample is proportional to the tissue displacement [208,445]. De Stefano *et al.* [421] proposed an alternative displacement measurement technique based on speckle tracking, where the cross-correlation between consecutive 2-D OCT images under different loading conditions was computed, allowing the deformation to be measured in two spatial dimensions. In this technique, the cross-correlation was computed between a window in the first image and several windows close to the origin in the second image, and the highest correlation was attributed to the corresponding displacement. This procedure was performed iteratively for a range of windows throughout the entire imaging FOV.

Transient loading mechanisms are widely used in ophthalmic OCE techniques, resulting in the propagation of elastic waves in the cornea with velocities typically in the range 1-15 m/s [447,452]. To provide OCE measurements with high spatial resolution requires sufficiently high A-scan acquisition rates, typically above 50 kHz for a wave travelling > 5 m/s [208]. Early studies using OCT systems with A-scan acquisitions of ~ 30 kHz were restricted to using M-mode scanning to accurately sample wave propagation [449]. In these implementations, consecutive A-scans were acquired at the same spatial location, restricting the ability to generate high speed 2-D elastograms. More recently, acquisition protocols enabled by high speed OCT systems, have been developed, *e.g.*, those based on FDML lasers provided A-scan acquisition rates of 1.5 MHz [299] and 1.6 MHz [300], with wavelengths

centred around ~ 1300 nm. This enables wave propagation to be measured in B-M mode configurations, where the wave motion at each pixel in a cross-sectional plane is measured between consecutive B-scans at rates of up to 16 kHz using a resonant scanner. This configuration has provided real-time 2-D OCE acquisition while providing nanometer-scale displacement sensitivity [300].

6.2.2.2 ONCOLOGICAL BENCH-TOP PROBES

Optical design

OCT systems with a central wavelength of ~ 1300 nm are typically used in oncological OCE imaging probes to provide the largest imaging depth in dense tissues [303,453]. These applications mainly use compression OCE, whereby *ex vivo* tissue samples are compressed using a flat plate connected to a mechanical actuator. As the tissue has been excised from the patient, contact methods which apply higher forces (typically several Newtons) than those used in ophthalmology are suitable and provide uniform compression over a large FOV. Furthermore, surgical specimens often have large variations in surface topographies which can be challenging to image with OCT due to the relatively shallow imaging depth (typically 2-3 mm). Compression loading has the added benefit, from an OCT imaging perspective, of removing fluctuations in surface height making imaging more straightforward. Oncological OCE imaging probes also employ relatively low NA telecentric objective lenses to achieve sufficient depth of field at high lateral resolutions (~ 15 μm in air) while also reducing scan distortion and field aberrations [206,303].

Analogously to ophthalmic OCE imaging probes, a key design consideration for oncological OCE imaging probes is the need to align the mechanical loading mechanism along the same axis as the OCT imaging beam. For compression OCE techniques, Kennedy *et al.* [454] proposed, initially for dermatology applications, a ring actuator with a 15 mm aperture. A circular glass window attached to the actuator provides a common-path reference reflection to minimise noise in clinical environments, whilst also acting as the compression plate used to deform the sample. This approach was then modified for use in scanning human breast specimens [441,445]. In these implementations, the common-path reference reflection was taken from the glass-tissue interface, leading to variations in the reference signal that reduced OCT and, therefore, OCE image quality [454]. Subsequent studies utilised a silicone compliant layer to measure stress (discussed further in the following Section), which also provided a more consistent reflection from the glass-layer interface [106].

Mechanical loading

Compression loading is widely used in oncological OCE imaging probes as it allows for large FOVs to be acquired more rapidly than with other loading mechanisms, as only two OCT measurements are required at each spatial location. To accommodate for relatively large surgical specimens, Allen *et al.* developed a wide-field imaging system with a 65 mm-diameter aperture PZT actuator, capable of scanning over a $\sim 50 \times 50$ mm *en face* FOV [441]. This design uses step loading between B-scans to facilitate wide-field volumetric scanning of tissue with B-scan acquisition speeds of ~ 50 Hz. Initial implementations using ring actuators made direct contact between the glass window and tissue surface, allowing for the measurement of strain [441,442,445,455–457]. Quantification of tissue mechanical properties, *i.e.*, by measuring tissue elasticity, was later achieved with the introduction of a compliant layer, of silicone or agar, in contact with the tissue of interest, which, importantly, allows for comparison between different tissue samples [106,303,425]. The introduction of the layer also ensures more uniform contact is made with the surface of the tissue as it is able to conform to the tissue geometry, providing a more uniform loading on the tissue and removing artifacts present in initial strain imaging techniques.

While many demonstrations utilise step-wise loading of the tissue via a piezoelectric actuator, Sovetsky *et al.* proposed a ramp loading mechanism and continuous measurement of OCT B-scans at the same lateral position. A main objective was to enable the generation of 2-D elastograms where the elasticity is presented under the same preload conditions, enabling the effect of nonlinearity to be minimised [458]. Whilst ramp loading can be used to account for potential variations in elasticity within B-scans, it may not be compatible with volumetric scanning as the start and end of the scans would be under very different bulk compression. This would result in variations in measured elasticity because of the nonlinear elasticity of tissue and would also distort the OCT image, as the start and end of the scan would be acquired from different regions of the sample (because of higher deformation towards the end of the scan). In addition, it would be challenging to implement this approach in timeframes compatible with intraoperative volumetric acquisition, although this could potentially be achieved using high-speed OCT systems with A-scan acquisition rates > 1 MHz.

Acquisition protocol

Phase-sensitive detection is the most common method for measuring tissue displacement in oncological probes. In the case of tumour margin assessment in breast-conserving surgery, volumetric imaging is particularly advantageous as it allows large regions of the sample to be assessed. However, the specimen size often exceeds the FOV of the scan lens. To address

this, multiple, partially overlapping sub-volumes can be acquired and then stitched together to create a mosaicked image with much larger FOV. This has been demonstrated by Allen *et al.* [441], by implementing the wide-field ring actuator, described previously, in conjunction with two linear translation stages to reposition the sample in the x - and y -axes relative to the OCT scan head. This design demonstrated the largest OCE FOV to date, acquiring $\sim 50 \times 50 \times 2 \text{ mm}^3$ volumes in approximately 10 minutes. While this is within the accepted acquisition time for intraoperative assessment (typically 10-15 minutes added), faster acquisition rates would allow all surfaces of the specimen to be imaged, providing a more complete analysis of the tumour margins. Undersampling in the lateral direction is one potential route to reduce the acquisition time, however, this can degrade image quality, whereas implementation of higher acquisition speed OCT systems can also facilitate shorter acquisition times. Another approach, currently only practical for quasi-static mechanical loading, is the C-M approach, where two full C-scan volumes are recorded before and after the stimulus is applied, as shown by Kennedy *et al.* [201].

In addition to the time required to acquire data, an important consideration is the time required to process and visualise the data, as intraoperative interpretation is ultimately required in oncological applications. Kirk *et al.* demonstrated near video-rate visualisation of elastograms, processing 21 cross-sectional elastograms per second by implementing phase-sensitive compression OCE using a GPU to process the sample strain [459]. As this work was performed in 2014, more modern GPUs are likely to greatly increase the processing speed.

6.2.3 HANDHELD IMAGING PROBES

A main objective in translating OCE into a handheld format is to put the technology directly in the hands of physicians, enabling them to access tissue *in vivo* in a practical manner. For example, as described in Section 6.2.2.2, for tumour margin assessment in breast-conserving surgery, bench-top OCE imaging probes can be used to detect tumour in the margins of *ex vivo* tissue specimens, however, this is a poor surrogate for determining if there is residual tumour in the surgical cavity: the surgeon's primary requirement. As handheld probes are manoeuvrable and have a smaller form factor, they provide the opportunity to directly assess the surgical cavity to more definitively determine if there is residual tumour following surgical excision, as well as maintaining the capability to scan the specimen. In dermatology, for applications such as burn scar assessment and diagnosis of skin lesions, handheld probes can facilitate *in vivo* scanning of the entire body as the manoeuvrable nature of these probes enables scanning of hard-to-reach locations on the body. In addition, handheld probes can

potentially be easily operated by physicians, which may help to facilitate eventual widespread adoption of OCE techniques.

Despite the compact nature of handheld OCE imaging probes, they are typically still large enough to accommodate similar optical and mechanical components to bench-top systems, such as scanning mirrors and piezoelectric actuators. This can lead to more efficient development of these probes compared to, for example, endoscopic probes where entirely new mechanical loading mechanisms are often required. So far, handheld OCE imaging probes have mainly been designed for clinical applications in breast-conserving surgery [28,429] (Fig. 6.4(a)) and in dermatology [427,428] (Figs. 6.4(b)-(d)), but also have potential in other applications, such as in brain tumour resection [460,461]. A primary consideration for handheld OCE imaging probes is often the requirement to develop scanning regimes that overcome the effects of both user motion, caused by involuntary hand motion, and patient motion, resulting from, for example, the beating heart. This has resulted in handheld probe designs employing novel scan patterns to facilitate the rapid acquisition of B- and/or C-scans without substantial distortion caused by motion artifacts [28,426].

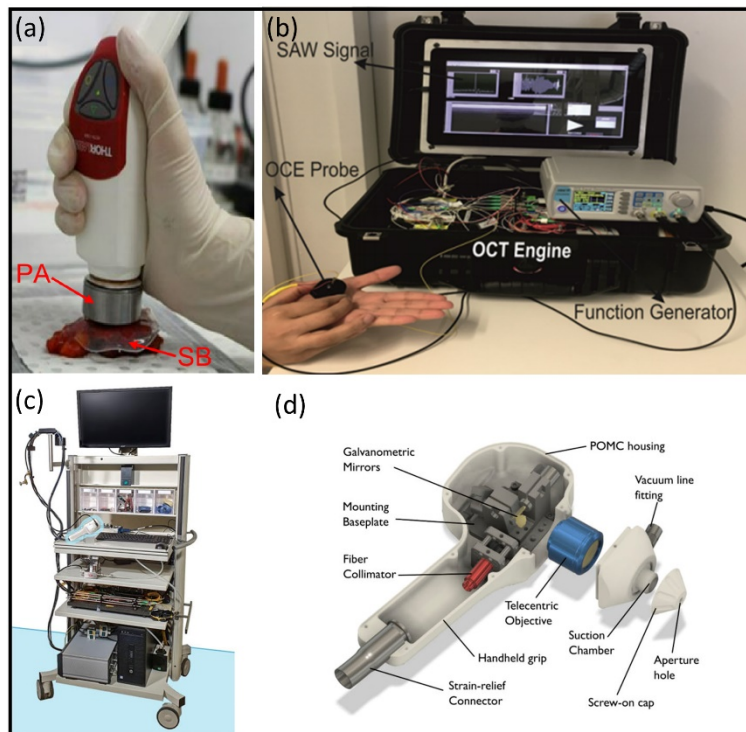


Figure 6.4: Overview of handheld OCE imaging probes. (a) Photograph of ring actuator-driven handheld probe scanning excised breast tissue for tumour margin assessment. Adapted with permission from [28] © The Optical Society. (b) Photograph of portable probe and OCT system for assessment of systemic sclerosis. Adapted from [428]. (c) Photograph of system set-up and (d) enlarged 3D design of negative pressure probe designed for assessment of skin mechanical properties. Reproduced from [427].

In summary, a number of handheld OCE imaging probes have been developed in recent years and whilst they still largely remain in technical development, it is anticipated that their continued development will lead to more OCE applications in the intended operational

environment. In this Section, we describe the development of handheld OCE imaging probes so far, summarised in Table 6.2.

Table 6.2: Summary of handheld OCE imaging probes.

Handheld Probe	Optical Configuration	Scanning Mirrors	Loading Method	Imaging Dimensions
Fang <i>et al.</i> [28]	Common-path	MEMS	Quasi-static compression	3-D
Fang <i>et al.</i> [426]	Common-path	MEMS	Compression	3-D
Bartolini <i>et al.</i> [427]	Dual-arm	Galvanometers	Suction	3-D
Parmar <i>et al.</i> [428]	Common-path	None	Transient loading	1-D
Liu <i>et al.</i> [429]	Common-path	None	Compression	1-D

Optical design

Handheld OCE imaging probes in oncology and dermatology applications typically utilise an OCT system comprising a source with central wavelength close to 1300 nm and an axial resolution of ~ 5 -10 mm, similar to conventional bench-top OCT systems [426,427,429]. Common-path interferometry is often used, where a fixed partial reflector is positioned in the sample arm and serves as a reference reflector [28,426,428,429]. As described in Section 6.2.2, common-path OCE provides handheld probes with increased phase stability in the presence of user and sample motion [444], directly translating to higher sensitivity and mechanical contrast. This is particularly important for handheld probes as the portable nature of these devices makes them more susceptible to motion artifacts than bench-top probes which are mounted and, therefore, inherently more stable. In addition, common-path OCE imaging probes allow for interferometer designs with fewer components facilitating the development of more compact devices.

Conventional OCT scan heads typically use galvanometers to drive the scanning mirrors, however, some handheld probes instead adopt microelectromechanical system (MEMS)-based mirrors which are significantly smaller. Additionally, in MEMS implementations, a single mirror can readily scan on two axes, thereby reducing the size, complexity and the scan field distortion associated with a two-mirror scan system [28,426]. However, the scanning speed of these mirrors is limited by the relatively low mechanical resonance frequency of MEMS devices (~ 100 -1000 Hz). As imaging at lower scanning speeds will result in higher levels of motion artifact, novel image acquisition strategies must be implemented to reduce their effect. To meet the requirements of relatively compact form factors, handheld OCE imaging probes also adopt smaller lenses, resulting in field curvature artifacts and elevated optical aberrations compared to bench-top systems.

Mechanical loading

The majority of handheld probes demonstrated so far implement compression-based loading mechanisms, enabling relatively fast scanning of large volumes of tissue compared with other OCE techniques. In addition, contact methods serve to stabilise the probe against the sample, helping to mitigate the effects of motion artifacts. However, the mechanical model used to quantify mechanical properties in compression OCE assumes the contact area is infinitely large and provides a bulk compression to the tissue. The validity of these compression models reduces as the probe diameter decreases, *i.e.*, as the deformation approximates a point indentation. Despite the reduced size of the handheld probes, Fang *et al.* demonstrated that for a 20 mm-diameter contact these assumptions remained valid when comparing against the measured elasticity of uniaxial compression tests [28]. This handheld probe used a quasi-static compression method, where, analogously to bench-top implementations described in Section 6.2.2.2, a micro-scale actuation is supplied by a ring actuator to enable collinear excitation and loading [28]. Both the ring actuator and the distal end of the probe are threaded, allowing for straightforward attachment of the loading mechanism to the probe. This design more closely resembles bench-top OCE imaging probes [18,462], however, the piezoelectric stacks in the actuator can be bulky and increase the size of the probe. This is of particular concern in surgical procedures such as breast-conserving surgery where surgical cavities are often only several centimetres wide. To begin to address this, Fang *et al.* demonstrated in a separate study a hand motion-induced loading method whereby bidirectional manual compression is applied directly by the user to deform the sample with a quasi-ramp [426]. A similar manual loading mechanism has also been demonstrated using a probe with a < 2 mm-diameter tip. In this approach, the measured Doppler phase shift was used to estimate the resulting axial velocity [429,463]. Given the very small diameter probe tip, this design necessitated the use of an indentation model, instead of a compressive model to accurately estimate elasticity [463].

In contrast to compression methods, Parmar *et al.* demonstrated a portable handheld OCE device which utilises a piezoelectric transducer to excite surface acoustic waves (SAWs) in the tissue [428]. This approach represents a fully portable system in which the OCE imaging probe and associated components (light source, function generator, etc.) are contained in a transportable case. The compact size of the probe is achieved by omitting scanning mirrors, utilising M-mode OCT imaging to detect the speed of SAWs at a single location. This design is potentially suitable for the classification of diseases that manifest over relatively large areas such as systemic sclerosis [464] which require reliable and repeatable classification of skin elasticity rather than localised mapping of mechanical properties [428].

However, the feasibility of such an approach is dependent on a relatively uniform stiffness of the diseased tissue to avoid sampling errors. Bartolini *et al.* also proposed an OCE imaging probe for dermatology. In this approach, the tensile deformation induced in tissue under suction is analysed [427]. The tissue is drawn into an aperture by negative pressure and the magnitude of deformation, which is indicative of the skin's mechanical properties, is measured using OCT. This approach resembles the Cutometer, a device used widely in dermatology to assess skin pliability [465]. This is an interesting approach, as incorporating elements from established clinical devices into the design of a new OCE imaging probe may improve the likelihood of clinical translation, as it may reduce development time and may lower the barrier to clinical acceptance.

Acquisition protocol

In bench-top OCE systems, conventional galvanometer-based scan patterns are used that employ a sawtooth waveform to scan the beam in the x -direction before rapidly repositioning the mirror after completion of a B-scan. As discussed above, a promising direction for handheld OCE imaging probes is the use of MEMS-based scanning that provides relatively large FOVs in a compact form factor, however, the relatively low MEMS resonance frequency limits the speed at which the mirror can reposition. This makes it challenging to achieve the sharp transitions required to generate sawtooth scan patterns. OCT acquisition in MEMS-based handheld probes have, therefore, been limited to relatively low B-scan rates, *e.g.*, 24 Hz in one demonstration that employed such raster scanning [28]. As a result, MEMS-based handheld OCE imaging probes may be susceptible to imaging artefacts caused by involuntary movement of the user and/or patient motion. One solution involves the implementation of a novel scan pattern that does not rely on the sharp transition present in raster scan patterns. Fang *et al.* demonstrated a custom scan pattern [28], illustrated in Fig. 6.5, that allowed B-scans to be acquired on both the rising and falling edge of the waveform (corresponding to the green and blue lines in Fig. 6.5(d)). The impact of the lower MEMS resonance frequency was limited by smoothing the turnaround point, enabling a B-scan rate of 215 Hz. Spatial correspondence between consecutively acquired B-scans was provided by flipping the x -axis of the B-scan acquired on the falling edge. However, slight variations between the acceleration and deceleration of the mirror meant that it was not possible to perform phase-sensitive detection by subtracting consecutive B-scans. For this reason, instead, the phase difference between consecutive “rising edge” B-scans and consecutive “falling edge” B-scans was calculated, as illustrated in Fig. 6.5(d). To create volumetric scans, it was necessary to interleave the lateral position on the slow scanning

axis (y) (Fig. 6.5(e)) [28]. This approach allowed volumetric scans ($6 \times 6 \times 2$ mm) to be acquired in < 4 seconds.

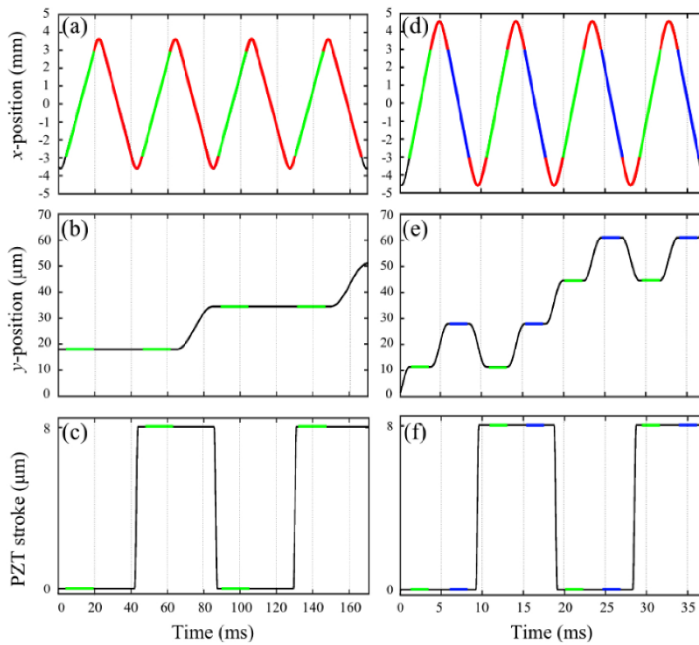


Figure 6.5: Standard unidirectional and custom bidirectional scan patterns. (a), (b) and (c) represent the x -position, y -position and PZT stroke in the standard scan pattern. The green lines and red curves indicate the B-scans and the regions when the MEMS returns to the starting point (fly-back), respectively. (d), (e) and (f) represent the x -position, y -position and PZT stroke in the custom scan pattern. The green and blue lines indicate B-scans in the positive and negative x -directions, respectively. The red curves in (d) indicate the sinusoidal turn-around regions between B-scans. Reproduced with permission from [28] © The Optical Society.

6.2.4 ENDOSCOPIC IMAGING PROBES

Development of endoscopic probes is of keen interest due to the large number of potential applications [466–468], particularly in cardiology and pulmonology, where scanning arteries and airways requires the development of probes with confined form factors. Extensive work has been performed to develop endoscopic OCT probes, *e.g.*, radial scanning has been achieved by either rotating the probe or installing a mirror in the probe tip, and these developments can be leveraged in the development of endoscopic OCE imaging probes. However, the tubular geometries imaged with these probes present challenges in incorporating the mechanical loading along the same radial access as the OCT beam and synchronising this with the OCT scanning. As a result, endoscopic OCE imaging probes have necessitated the development and implementation of several novel optical design and mechanical loading mechanisms. shows some examples of endoscopic OCE imaging probes specifically designed for different applications and Table 6.3 provides a summary of the main endoscopic OCE imaging probe designs proposed so far.

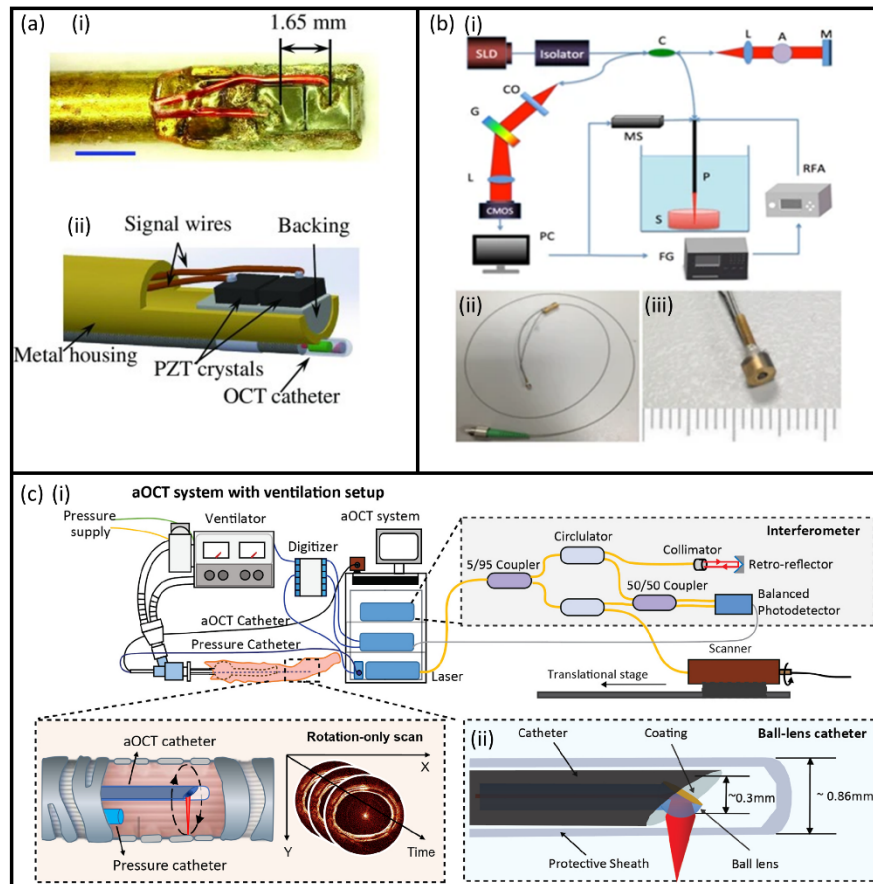


Figure 6.6: Examples of endoscopic OCE imaging probes. (a) Integrated acoustic radiation force (ARF) OCE imaging probe for cardiac tissue imaging. (i) Photograph of multitransducer ultrasound array (scale bar is 2 mm) and (ii) schematic of the assembled multitransducer ARF OCE imaging probe. Adapted with permission from [435]. (b) Endoscopic OCE imaging probe for imaging vascular lesions. (i) Overview of acoustic radiation force impulse (ARFI) OCE system set up. C: collimator, L: lens, A: attenuator, M: mirror, G: grating, MS: mechanical stage, RFA: radio frequency amplifier, P: probe, S: sample, FG: function generator. Photographs of (ii) probe design and (iii) probe head including a ring transducer and optical elements. Adapted from [430]. (c) Anatomical OCE imaging probe for airway imaging. Schematics of (i) anatomical OCE system with ventilation setup and (ii) the ball-lens structure at the tip of the anatomical OCE imaging probe. Adapted with permission from [431] © The Optical Society.

Table 6.3: Summary of several endoscopic OCE imaging probes.

Endoscopic Probe	Application Area	Beam Shape	Loading Method	Imaging Dimensions
Qu <i>et al.</i> [430]	Cardiology	Gaussian	ARF	2-D
Bu <i>et al.</i> [431]	Pulmonology	Gaussian	Passive loading	2-D
Robertson <i>et al.</i> [432]	Pulmonology	Gaussian	Passive loading	2-D
Qi <i>et al.</i> [433]	Cardiology	Gaussian	ARF	3-D
Nakamura <i>et al.</i> [434]	Endoscopy	Gaussian	ARF	2-D
Karpiouk <i>et al.</i> [435]	Cardiology	Gaussian	ARF	1-D
Fang <i>et al.</i> [436]	Oncology	Bessel	Quasi-static compression	3-D

Optical design

There are two main optical designs used in endoscopic OCE imaging probes: side-facing and forward-facing imaging probes. Schematics of these two designs are presented in Fig. 6.7. For most developments in cardiology and pulmonology, a side-facing optical design, often achieved by either fixing an angled reflector along the optical axis or polishing the fibre tip

down to a 45° angle, is chosen as the anatomical structure of arteries and airways are most easily imaged using this geometry. Side-facing probes allow for the construction of images perpendicular to the direction of the probe which is useful for imaging along narrow channels within the body. Side-facing designs are also more common in endoscopic probes which use transient loading based on ARF excitation as, to reduce the form factor, the optical fibre and ultrasound transducer are typically arranged side-by-side along the length of the probe rather than at the tip [435]. In contrast, a rigid, forward-facing probe proposed for micro-endoscopy of tumour in animal models was developed based on compression OCE. In this approach, displacement was applied from the proximal end of the probe which translated to axial compression at the interface between the probe and the tissue [436].

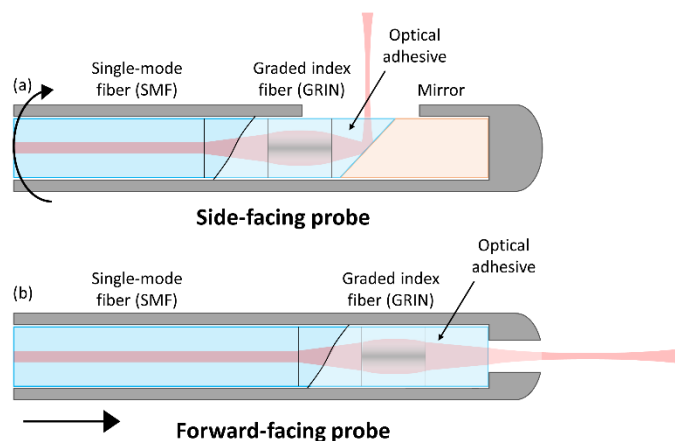


Figure 6.7: Schematic diagrams of optical designs used in (a) side-facing and (b) forward-facing endoscopic OCE imaging probes.

Most endoscopic OCE imaging probes utilise a graded-index (GRIN) lens design as the fibre optics are compact and can be implemented in a similar fashion to existing endoscopic probes. In this design, a length of single mode fibre (SMF) is spliced to a short (< 1 mm) length of GRIN fibre. However, this increases the number of optical interfaces (*i.e.*, single mode fibre to GRIN fibre and GRIN fibre to optical adhesive) which can result in autocorrelation artifacts and reduced sample power when operated in common-path. As a result, most endoscopic OCE imaging probes utilise a dual-arm rather than common-path configuration. Although a common-path configuration is more compact, dual-arm configurations provide more straightforward control of reference arm power, which can be important for optimising OCT image quality.

The size of most endoscopic OCE imaging probes ranges from 1-5 mm in diameter to enable manoeuvrability through the narrow passages of the arteries and airways [433–436]. As illustrated in Fig. 6.7, a length of GRIN fibre is often used to focus the optical beam into the tissue. This is due to the refractive index in GRIN fibres varying radially, causing the light to propagate sinusoidally through the fibre. The specific length of the GRIN fibre controls

the working distance and focal length of the beam. This design typically produces a lateral resolution of 15-20 μm [432,433]. In a rigid, forward-facing micro-endoscope design, Fang *et al.* implemented a more complex triplet GRIN lens design attached to an objective lens to provide a Bessel beam illumination to the sample, as opposed to a Gaussian beam illumination which most other probes employ [436]. The entire GRIN lens system had a length of 53 mm and allowed for an ultrahigh resolution endoscopic probe with a lateral resolution of 1.6 μm and an extended 80 μm depth-of-focus provided by the Bessel beam illumination. It should be noted that the complexity of this optical design would be difficult to replicate in the case of a radial scanning beam.

Mechanical loading

The mechanical loading mechanism required for endoscopic OCE imaging probes is typically distinct to that required in other OCE imaging probes as, in the endoscopic case, the scan head of the imaging probe is located deep inside tissue. This imposes restrictions on how the loading can be applied and requires the development of novel approaches. Here, we will review three loading methods used in endoscopic OCE imaging probes.

The most commonly used loading method in endoscopic OCE imaging probes so far is ARF, where compact ultrasound transducers, of diameter $\sim 1\text{-}2$ mm, are used. While these transducers do not provide the same loading force as larger modules, they impart sufficient displacement to enable phase-sensitive detection. A challenge in ARF-induced OCE is that acoustic coupling is required between the ultrasound transducer and the tissue, which may be difficult to ensure in clinical applications. One approach to overcome this challenge is to integrate the coupling solution inside a protective sheath, similar to catheters for intravascular imaging [435].

For small animal imaging, quasi-static compression using a rigid forward-facing endoscope as a compression plate has been proposed, which allows for the quantification of tissue elasticity using an implementation of QME [436]. In this approach, tissue displacement is supplied via microscale actuation from a piezoelectric actuator. Fang *et al.* presented two different system layouts to achieve quasi-static compression: one with the actuator positioned behind the sample and driving the sample directly, for imaging *ex vivo* samples; the other implementation, which used an actuator positioned along the shaft of the probe, is better suited for *in vivo* imaging, as it is easier to control the force necessary to deform the tissue. However, this implementation reduced the lateral resolution (from 1.5 μm to 1.6 μm) and the OCT depth-of-field (from 94 μm to 80 μm) [436].

The two loading methods outlined above are examples of external mechanical loading. Alternatively, passive loading is a third loading method which utilises natural physiological

motion of the tissue to induce deformation. This method has been explored by Robertson *et al.* who monitored the displacement caused by tidal breathing, known as *wall compliance*, in the airway wall (Fig. 6.8) [432]. This technique was later expanded on by Bu *et al.* to encompass changes in the physical structure of the airway in what is defined as *local compliance* [431]. While passive loading is not achievable in all clinical applications, in instances where it can be leveraged, it provides the advantage of minimising probe size, as no external mechanical loading mechanisms are needed. Compared to other endoscopic OCE imaging probes, a probe which uses tidal breathing, or some other passive loading methods could potentially be designed to be as small as the width of the optical fibre, which could open up new applications in imaging very narrow orifices in humans or animals. However, the amplitude and rate of loading in passive OCE techniques is difficult to control, making it challenging to generate reliable, high quality elastograms.

Acquisition protocol

In endoscopic OCE imaging probes, the tubular nature of vessels and airways requires implementation of a unique scan pattern to capture these structures. Often, radial scanning is performed, whereby the OCT beam is rotated inside the structure by an external mechanical motor. This allows for the reconstruction of radial 2-D cross-sectional images. This can be combined with a mechanical translation stage to ‘pullback’ the endoscopic probe to construct 3-D maps of tissue inside a cylindrical structure. As the rotational motor and translational stage are both situated external to the probe tip, additional measures must be taken to ensure that the rotation applied at one end is translated to the probe tip and not subject to nonuniform rotation distortion (NURD) [469]. One approach is to encase the endoscopic probe in a torque coil, a highly flexible metal sheathing which ensures precise torque response at high rotational speeds [430]. In clinical applications where the probe dimensions must be minimised, the torque coil is not suitable and a software-based approach could be implemented, such as that presented by Uribe-Patarroyo and Bouma [470]. This technique measures the true rotational speed of the OCT probe by analysing the statistical fluctuations of the speckle in the OCT image and performs real-time corrections. For applications not involving tubular structures, conventional raster scanning can be used to generate 2-D or 3-D maps of elasticity [436]. A comparison between images acquired using radial scanning and conventional raster scanning is shown in Fig. 6.8.

Wall compliance is broadly defined as the change in airway wall thickness (radius) as a function of pressure at each polar angle [431,432]. This measurement is, therefore, reliant on accurate determination of the origin from which the radius is calculated, which is typically taken as the OCE imaging probe tip. This method, however, is highly susceptible to motion

artifacts. To overcome this, Bu *et al.* proposed a method where the origin for the measurement of radius is defined as the geometric centroid of the wall in each frame (one full rotation of the OCE imaging probe) as this provides robust measurements in the presence of motion artifacts [431].

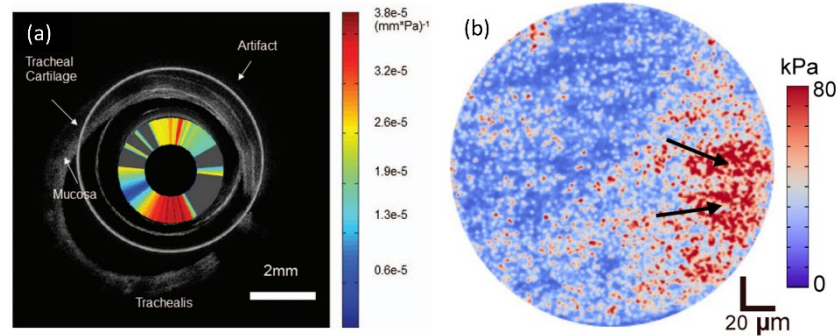


Figure 6.8: Comparison of typical 2-D mechanical contrast images produced by (a) a radially scanning endoscopic OCE imaging probe. Adapted from with permission from [432]. (b) A raster scanning endoscopic OCE imaging probe [436]. OCE measurement of wall compliance (inversely proportional to elasticity) produced by passive loading (colour scale) overlaid on the radial OCT image is shown in (a), whereas in (b) elasticity is shown. (b) Adapted with permission from [436] © The Optical Society.

6.2.5 OTHER COMPACT IMAGING PROBES

Clinical palpation is widely used to identify and localise tumour based on its elevated stiffness in comparison to surrounding tissues in a range of surgical procedures, including breast-conserving surgery [70] and removal of hepatic metastases [471]. While clinical palpation is routinely used to detect large tumours, it is inherently subjective and has an effective spatial resolution on the order of 1 mm, preventing the detection of small extensions of tumour. In the case of breast-conserving surgery, this contributes to 20-30% of patients requiring re-excision because of tumour missed during the initial surgery. QME has previously shown promise in the detection of tumour in *ex vivo* breast specimens, demonstrating improved accuracy compared to OCT alone and potential in reducing the re-excision rate [425]. Additionally, as discussed in Section 6.2.3, several handheld OCE imaging probes are in development to translate OCE into a smaller form factor. However, challenges shared by bench-top and handheld OCE imaging probes are that they only image up to ~ 1 mm below the tissue surface and provide less direct feedback to the surgeon when compared to clinical palpation. To separately address these challenges, compact OCE imaging probes, including needle probes [437,438] and a finger-mounted probe [440], have been proposed. More specifically, needle probes have the potential to image mechanical properties several centimetres below the tissue surface, significantly extending the depth at which OCE measurements can be acquired; the finger-mounted probe is promising to preserve the

dexterity afforded by clinical palpation and potentially provides a more practical means for intraoperative OCE.

Optical design

Compact OCE imaging probes demonstrated so far feature simplified optical designs owing to the limited spacing for components in the probe. Analogously to some endoscopic OCE imaging probes described in Section 6.2.4, these compact OCE imaging probes utilise a length of GRIN fibre (typically 270-800 μm) to focus the beam into the sample, spliced to a length of SMF and coupled to a fibre-based OCT system [437–440]. In demonstrations of needle OCE so far, these optical components have been encased in 20-22-gauge needles, using optical glue to fix them in place. The illumination beam can be forward-facing [437,438] or side-facing [439], depending on the requirements of the application. In addition, these probes have mainly been implemented using common-path configurations, where the reference reflection is provided by a small section of optical adhesive, cured at the probe tip. In the initial, and so far only, implementation of the finger-mounted probe, the optical components were sealed in a 3-D printed case which was mounted on the finger, as shown in Figs. 6.9(a) and (b). Due to the small form factor of these compact OCE imaging probes, the optical design excludes scanning mirrors, resulting in the acquisition of 1-D elasticity plots in most cases. In a side-facing probe (Figs. 6.9(c)-(e)), A-scans are acquired orthogonally to the axis of the probe which may be useful in clinical applications where the needle can only be inserted from restricted positions and angles.

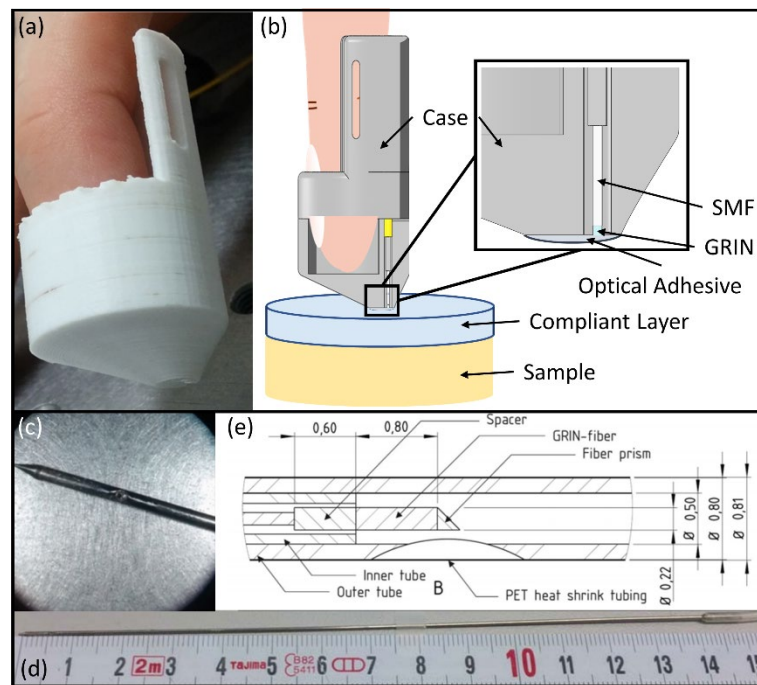


Figure 6.9: Compact OCE imaging probe optical designs. (a) Photograph and (b) schematic of finger-mounted probe with inset showing the fibre probe and optical adhesive. Adapted with permission from [440] © The Optical Society. (c) and (d) Photographs and (e) schematic of side-facing needle probe. Reproduced from [439].

Mechanical loading

To date, mechanical loading for compact OCE imaging probes has mainly been achieved by compressing the tissue using the probe tip. In the case of needle probes, as the mechanical deformation associated with a needle piercing tissue is very difficult to incorporate in a simple mechanical model that can be used in OCE, the piercing function of the needle was decoupled from the imaging function using a two-stage process [437,438]. First, a sharp guide needle of larger diameter than the imaging needle (an 18-gauge needle has been demonstrated so far) is inserted to the region of interest in the tissue. Then, the flat-tipped imaging needle (a 22-gauge needle has been demonstrated) is inserted through the guide needle to position the imaging needle at the region of interest. Next, the imaging needle is manually pushed past the tip of the guide needle to create a sub-surface indentation from which 1-D strain plots are generated. Advancing the probe further into the tissue produces larger displacements in the tissue along the beam axis which is measured in the successive OCT acquisitions using phase-sensitive detection [438].

In the finger-mounted probe, similar to clinical palpation, mechanical deformation is imparted to the tissue by applying pressure to the region of interest with the fingertip [440]. In the initial implementation, the probe is worn on the tip of the finger which is positioned orthogonally to the tissue surface. It may prove more practical to develop a side-facing probe to enable the detection of compression applied with the side of the fingertip rather than the front tip. In addition, the preliminary work utilised a compliant layer placed between the

tissue and the probe, and the compression was applied to both the layer and the tissue to enable the QME measurement. In future work, to make the QME measurement more viable in clinical applications, the layer needs to be affixed to the probe and the probe needs to be sterilised.

Another potential method of mechanical loading, incorporated in a side-facing needle OCE imaging probe [439], is via excitation of tissue from an external piezoelectric actuator. In this method, a sinusoidal burst is applied to a piezoelectric actuator which induces propagating shear waves in the sample. For a known tissue density, the shear wave velocity, which can be derived from the phase-sensitive detection, is directly related to the elastic modulus by assuming the Poisson's ratio of tissue is 0.5.

Acquisition protocol

So far, due to the compact nature of these probes, 1-D plots of strain or elasticity have mainly been generated, by acquiring A-scans at the same location. The forward facing needle OCE imaging probes presented by Kennedy *et al.* acquired A-scans at a rate of 5 kHz [437,438]. Phase difference was calculated between consecutive A-scans, where the relative displacement between A-scans varied based on the local mechanical properties of the sample (Fig. 6.10). Averaging was performed on every 1,000 A-scans to reduce the effect of mechanical noise on the measured phase. Strain was calculated as the derivative of the displacement with depth and is inversely proportional to elasticity of the imaged sample under the assumption of uniform stress along the axis of the acquired A-scan. In the case of the side-facing probe, A-scans were acquired at a rate of 5.5 kHz and phase difference was computed between consecutive A-scans [439]. The first maximum in the amplitude of the phase difference denoted the wave front of the generated shear wave with subsequent maxima due to detected reflections. Monitoring the time delay between the excitation of the shear wave and when it is detected by the probe allows for the determination of the shear wave propagation and, therefore, the elasticity. This technique is dependent on prior knowledge of the material density and has shown to be less sensitive in higher density samples where phase-wrapping often occurs, confounding the wave front detection.

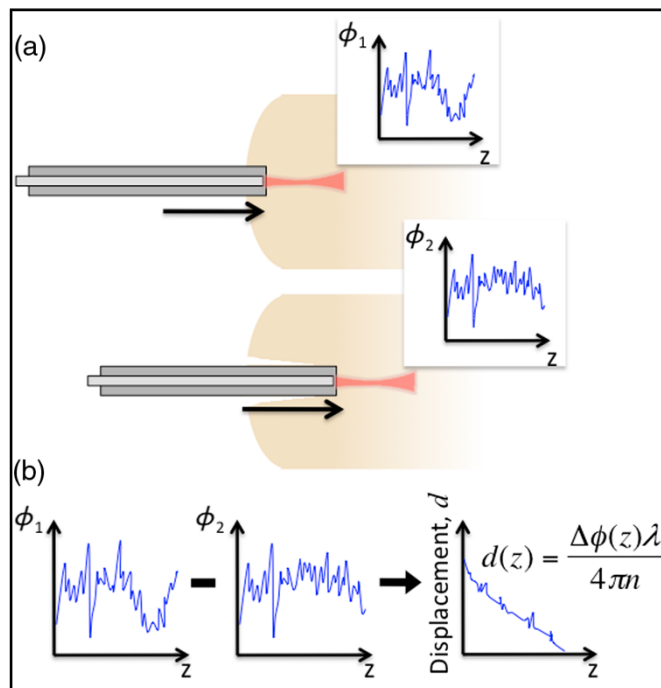


Figure 6.10: Method for the measurement of tissue displacement in forward-facing needle OCE imaging probes. (a) Measurements of the phase in the OCT A-scans are acquired at two incremental needle probe positions. (b) The phase difference between the two A-scans, $\Delta\phi = \phi_1 - \phi_2$, is linearly related to axial tissue displacement. Reproduced with permission from [438].

In the case of the finger-mounted probe, A-scans were acquired at 10 kHz and the phase difference was also calculated between consecutive A-scans. In addition to 1-D measurements at the same location as shown in Fig. 6.11, the finger-mounted probe can acquire 2-D images, shown in Figs. 6.11(d) and (e) by simultaneously moving the finger in the lateral direction while compressing the tissue in the axial direction. In signal processing, an adaptive filter compensates for the variation in axial compression rate imparted by the user, allowing for the calculation of elasticity based on uniform strain between successive A-scans. In this initial demonstration, the motion of the probe was not tracked as it moves across the sample, therefore, the precise spatial location of the A-scans is unknown. For this reason, the x -axis in Figs. 6.11(d) and (e) is given as time rather than spatial position. Incorporating motion-tracking, *i.e.*, using magnetic position sensors or speckle pattern analysis, into future designs would potentially enable the determination of the A-scan spatial location within the image, providing spatially accurate reconstructions of OCT and elasticity in 2-D.

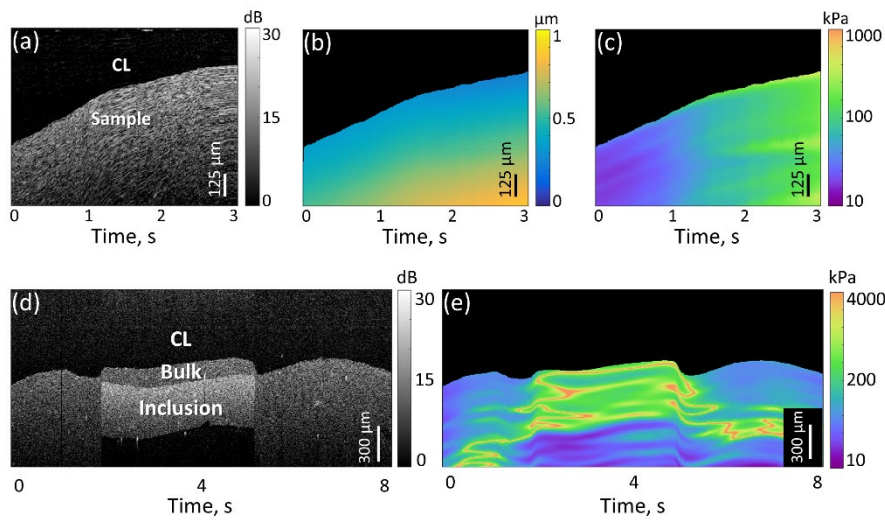


Figure 6.11: Images acquired by finger-mounted OCE imaging probe. 1-D acquisition of (a) OCT M-mode, (b) axial displacement, and (c) elasticity maps plotted over time. (d) 2-D-OCT scan over a stiff silicone inclusion embedded within a soft silicone bulk and (e) the corresponding 2-D elasticity map with the x-axis given in seconds. In (b), (c) and (e), the compliant layer (CL) is masked out. Adapted with permission from [440] © The Optical Society.

In common with all OCE techniques, in finger-mounted QME, friction between the probe tip and the tissue can limit the accuracy of the elasticity measurement, especially in the case of 2-D imaging using the finger-mounted probe. When high friction occurs at the probe tip or the tissue surface, it can create a shearing in the tissue, producing regions of compressive and tensile strain which are not along the imaging direction. This can generate artifacts in the resulting strain and elasticity measurements. Therefore, careful consideration must be given to the design of the probe tip and the contact conditions to ensure minimal surface friction.

6.2.6 CONCLUSIONS

The continued development of OCE imaging probes is vital if OCE is to be translated from a research-centric set of imaging techniques into a tool for diagnosis and assessment in a broad range of clinical and biological applications. In this Chapter, we have described a range of OCE imaging probes and how they have been engineered towards specific clinical applications in areas such as ophthalmology, oncology, and pulmonology. While most of these probes are still in the early stages of development and have yet to be demonstrated in their operational environment, they have the potential to offer unique medical imaging solutions based on three key design considerations; optical design; mechanical loading; and acquisition protocol. The development of these probes will undoubtedly benefit from the continued evolution of OCT and OCE methodology which will likely provide higher acquisition rates, smaller form factors and lower cost components. These improvements could facilitate the clinical adoption of OCE imaging probes while also expanding OCE to a broader range of applications.

CHAPTER 7

FINGER-MOUNTED QUANTITATIVE MICRO-ELASTOGRAPHY

7.1 PREFACE

In the previous Chapter we have reviewed the growing number of optical coherence elastography (OCE) probes developed towards clinical use and explored how the design of each probe is dictated by the unique requirements of the intended clinical application. In general, these probes seek to extend the sense of touch, which is widely used in medical diagnoses, by providing information on tissue mechanical properties, albeit, at higher resolutions and sensitivities.

The sense of touch is intuitive and allows for easy differentiation between materials of contrasting stiffnesses. Therefore, despite the improvements to modern diagnostics, many surgeons still rely predominantly on their sense of touch to discriminate between healthy and diseased tissue during surgical procedures. While the sensitivity and resolution are significantly lower than that of optical elastography techniques, the inherent benefits of manual palpation seemingly outweigh the benefits of most current implementations of intraoperative devices, precluding their use in surgery. For intraoperative breast cancer margin assessment, many of the proposed imaging tools are disruptive and would replace manual palpation altogether. Not only does this remove the diagnostic capability of manual palpation, which is effective for detecting larger tumours, but it also forces surgical teams to significantly change the existing clinical procedures and develop new skills which takes time.

In this Chapter we propose finger-mounted quantitative micro-elastography, a wearable optical coherence elastography probe which seeks to provide the diagnostic imaging capability of optical elastography while mimicking the existing clinical practise of manual palpation. This work represents a proof-of-principle for finger-mounted quantitative micro-elastography. This Chapter consists of a first-authored publication titled, Rowan W. Sanderson, Andrea Curatolo, Philip Wijesinghe, Lixin Chin, and Brendan F. Kennedy, “*Finger-mounted quantitative micro-elastography*,” *Biomedical Optics Express*, 10(4): p. 1760-1773, 2019., and an additional Section detailing preliminary results on freshly excised breast tissue.

7.2 FINGER-MOUNTED QUANTITATIVE MICRO-ELASTOGRAPHY

Rowan W. Sanderson,^{1,2} Andrea Curatolo,^{1,2,3} Philip Wijesinghe,^{1,2,4} Lixin Chin,^{1,2} and Brendan F. Kennedy^{1,2}

Biomedical Optics Express, 10(4): p. 1760-1773, 2019.

Abstract: We present a finger-mounted quantitative micro-elastography (QME) probe, capable of measuring the elasticity of biological tissue in a format that avails of the dexterity of the human finger. Finger-mounted QME represents the first demonstration of a wearable elastography probe. The approach realises optical coherence tomography-based elastography by focusing the optical beam into the sample via a single-mode fibre that is fused to a length of graded-index fibre. The fibre is rigidly affixed to a 3-D-printed thimble that is mounted on the finger. Analogous to manual palpation, the probe compresses the tissue through the force exerted by the finger. The resulting deformation is measured using optical coherence tomography. Elasticity is estimated as the ratio of local stress at the sample surface, measured using a compliant layer, to the local strain in the sample. We describe the probe fabrication method and the signal processing developed to achieve accurate elasticity measurements in the presence of motion artifact. We demonstrate the probe's performance in motion-mode scans performed on homogeneous, bi-layer and inclusion phantoms and its ability to measure a thermally-induced increase in elasticity in *ex vivo* muscle tissue. In addition, we demonstrate the ability to acquire 2-D images with the finger-mounted probe where lateral scanning is achieved by swiping the probe across the sample surface.

© 2019 Optical Society of America under the terms of the OSA Open Access Publishing Agreement

7.2.1 INTRODUCTION

For centuries, physicians have relied on the sense of touch to qualitatively assess disease based on changes in the mechanical properties of tissue, *i.e.*, manual palpation [472]. The sustained and widespread clinical use of manual palpation is largely attributed to the dexterity

¹ BRITelab, Harry Perkins Institute of Medical Research, QEII Medical Centre, Nedlands and Centre for Medical Research, The University of Western Australia, Perth, Western Australia, 6009, Australia

² Department of Electrical, Electronic & Computer Engineering, School of Engineering, The University of Western Australia, 35 Stirling Highway, Perth, Western Australia, 6009, Australia

³ Current address: Visual Optics and Biophotonics Group, Instituto de Óptica "Daza de Valdés", Consejo Superior de Investigaciones Científicas (IO, CSIC), C/Serrano, 121, Madrid 28006, Spain

⁴ Current address: SUPA, School of Physics and Astronomy, University of St. Andrews, KY16 9SS, UK

of hand motion and its ease of use [66,473]. However, the inherent subjectivity, lack of quantification and relatively low spatial resolution, limit the efficacy of manual palpation in correctly identifying diseased tissue [71]. One proposed solution is elastography, a family of imaging techniques developed over the past 30 years that map tissue elasticity by combining medical imaging with mechanical deformation [153]. Elastography was initially developed using ultrasound [163,165] and magnetic resonance imaging [12], and has been proposed for a range of clinical applications, particularly in hepatology [474,475] and oncology [99]. More recently, optical coherence tomography (OCT)-based elastography, OCE, has been developed to improve both the spatial resolution (to 10s–100s μm) and sensitivity (to nanometre-scale deformations) in comparison to other approaches, albeit to a relatively shallow imaging depth of ~ 1 mm in turbid tissue [22,155,285,288,298,476,477]. OCE is undergoing development in a range of fields, most prominently in ophthalmology [208], cardiology [478], and oncology [206,442]. As a photonics-based technique, OCE is amenable to miniaturisation into small form factor probes, such as needles and endoscopes [436,437,479]. Such probes have the potential to enhance the clinical applicability of OCE. Initially, OCE probes, such as needle OCE, were limited to measurements of strain, yielding qualitative assessments and providing low contrast in some instances [302]. For clinical applications, quantitative imaging can aid in the identification of diseased tissue, facilitate rapid interpretation of results and also enable more ready comparison of results obtained from different patients. More recently, to address this, there have been several demonstrations of quantitative OCE probes [436,463], however, in these demonstrations mechanical loading was applied using bulky mounted set-ups or by motorised stages that are impractical for routine use by clinicians.

Here, we propose a novel OCE probe, in which the sample arm of an OCE system is encased in a 3-D-printed thimble and worn on the finger. This technique represents the first finger-mounted, and indeed wearable, version of OCE. In addition, more broadly, there have been few demonstrations of a free-hand OCE probe without the need for supporting apparatus [480]. Our methodology is based on QME [106,303], a compression-based OCE technique that utilises phase-sensitive detection to estimate the elasticity of a sample by combining the surface stress, measured using a compliant layer, with the local axial strain measured throughout the OCT field-of-view. To realise finger-mounted QME, we extend on QME signal processing to generate accurate elasticity measurements in the presence of motion artifact induced by the finger.

Finger-mounted QME has the potential to preserve much of the dexterity and ease of use of manual palpation, whilst also providing the quantification, relatively high spatial resolution and depth-sectioning capability of OCE. This technique may increase the clinical

applicability of OCE, particularly in scenarios where the use of a relatively bulky handheld probe is not convenient, *e.g.*, in assessing if residual tumour is present in small cavities following excision of the main tumour mass in breast-conserving surgery. In this paper, we provide experimental validation of finger-mounted QME on homogeneous, bi-layer and inclusion phantoms and *ex vivo* muscle tissue. We demonstrate that finger-mounted QME is capable of measuring the elasticity of silicone phantoms to within 21% of the expected value (compared to 8% for a bench-top implementation of QME [106]), and that it can distinguish the change in mechanical properties between raw and cooked kangaroo muscle tissue. Furthermore, we demonstrate a method to perform 2-D scanning in finger-mounted QME by swiping the probe across the sample surface with a gentle, yet increasing, compression. The results presented in this paper highlight the potential of finger-mounted QME for development towards clinical applications that currently rely on manual palpation.

7.2.2 METHODS AND MATERIALS

Probe design

Finger-mounted QME comprises a fibre probe (illustrated in Figs. 7.1(a) and (b)) connected to a spectral-domain OCT system (TEL320, Thorlabs, USA) with a central wavelength of 1300 nm, a 3 dB-bandwidth of 170 nm, and a measured full-width-at-half-maximum (FWHM) axial resolution of 5.2 μm . The probe is configured as a common-path interferometer to maximise displacement sensitivity [10], which was measured to be 1.44 nm for an OCT signal-to-noise (SNR) of 40 dB [303]. The probe consists of a single mode fibre (SMF) spliced to a 270 μm length of graded-index (GRIN) fibre (Miniprobes, Australia) that focuses the beam into the sample. The fibre probe is embedded within a thin channel along the underside of a 3-D-printed thimble, as illustrated in Figs. 7.1(b), using an ultra-violet-curable optical adhesive (NOA68, Norland Products, USA). The adhesive also seals the fibre in place at the tip of the thimble (adhesive thickness, 70 μm) and provides the reference reflection in the common-path interferometer. In finger-mounted QME, A-scans are acquired at 10 kHz.

Two fibre probes were used in this study, manufactured to the same specifications; Probe 1 was used to generate the results presented in Figs. 7.2-7.4, and Probe 2 was used for Figs. 7.1, 7.5-7.7. The working distance of Probe 1 was 1.9 mm from the tip of the probe and the FWHM lateral resolution at the focus was measured to be 17.6 μm , whilst Probe 2 had a working distance of 1.6 mm and a measured FWHM lateral resolution at the focus of 12.5 μm . The usable imaging depth for these probes was ~ 800 μm , therefore the beam properties had minimal effect on the lateral resolution with depth. A beam profile of Probe 2 in both x - and y -directions is presented in Figs. 7.1(c). The beam profile was taken in the

plane orthogonal to the direction of the beam and the FWHM x - and y -diameters were measured along the major and minor beam axes, demonstrating a profile that closely resembles that of an equivalent ideal Gaussian beam. A small deviation from the ideal Gaussian beam profile can be observed in this figure. This is likely due to aberrations caused by the cured optical adhesive at the fibre tip.

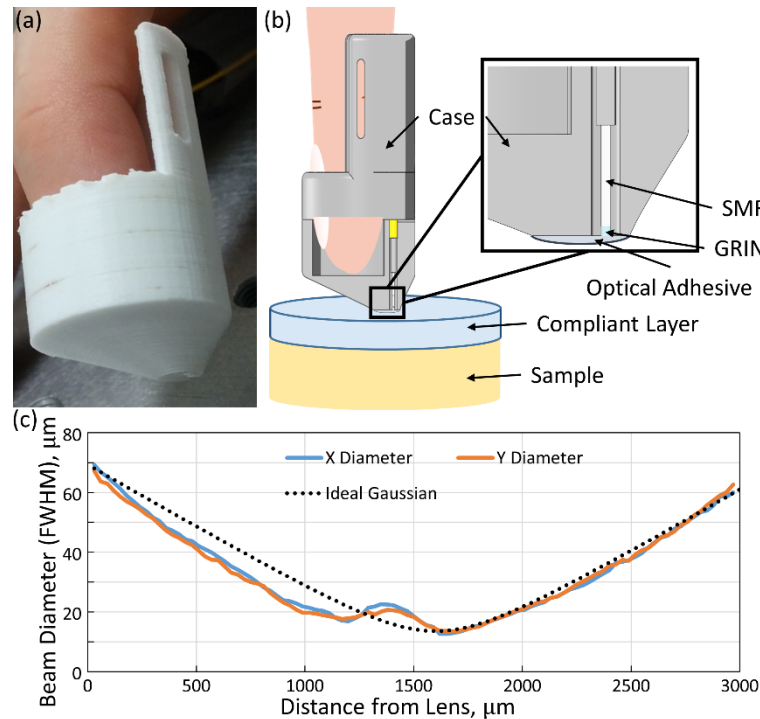


Figure 7.1: Finger-mounted QME probe (a) photograph, (b) schematic with inset showing the fibre probe and optical adhesive. (c) Beam profile of Probe 2 compared to an ideal Gaussian beam.

Phantom and compliant layer fabrication

Five cylindrical, homogeneous tissue-mimicking silicone phantoms, each with a radius and thickness of 5 mm and 2 mm were used as test targets to assess the probe's accuracy in measuring elasticity. The phantoms were fabricated by mixing a room-temperature-vulcanising silicone elastomer and curing agent together in addition to a non-crosslinking polydimethylsiloxane (PDMS) oil (Wacker, Germany) [481]. The mechanical properties of the phantoms were controlled by varying the elastomer type and mixing ratios. To generate optical scattering, $2 \text{ mg}\cdot\text{ml}^{-1}$ of titanium dioxide (TiO_2) powder (Sigma Aldrich, product 232033) was added to the phantoms. The phantoms were fabricated to have elastic moduli in a range found in soft tissues (6.5–160 kPa, measured at 10% absolute strain) and were characterised using a uniaxial compression device, which we considered to be the 'gold standard' for characterisation of mechanical properties. Hereon, we refer to the elastic moduli measured by the compression device as 'expected'. The measured and expected results of one such phantom are plotted against stress, rather than the conventional strain, in Fig. 7.2(e), for consistency with the general case of a sample of unknown thickness, where

the absolute strain is unknown. In addition to homogeneous phantoms, a bi-layer phantom was fabricated, with the distance from the nearest surface of the phantom to the boundary between the layers located within the OCT field of view, allowing us to conveniently assess the probe's ability to detect boundaries within samples. The top/bottom layers had elastic moduli of 24 kPa/160 kPa, contained $0.5 \text{ mg.ml}^{-1}/3 \text{ mg.ml}^{-1}$ of TiO_2 , and were 0.4 mm/3 mm thick, respectively. An inclusion phantom was also fabricated for the 2-D scans. In this phantom, a stiff inclusion was embedded within a softer bulk material. The elastic modulus of the bulk was 24 kPa and of the inclusion was 160 kPa, both measured at 10% strain. Optical contrast was provided by adding 0.5 mg.ml^{-1} to the bulk and 3 mg.ml^{-1} of TiO_2 to the inclusion. The inclusion had dimensions (length \times height) of $\sim 1 \text{ mm}$ and $\sim 0.5 \text{ mm}$, respectively. The compliant layers used to estimate stress in QME were also fabricated from this silicone. In the homogeneous scans, the compliant layer material matched that of the sample and for the bi-layer and 2-D scans, the compliant layers had an elastic modulus of 24 kPa at 10% strain. The compliant layers were all $\sim 500 \mu\text{m}$ thick and contained no scatterers to ensure that the OCT SNR in the sample was maximised.

Finger-mounted QME measurements

Finger-mounted QME is based on a technique previously implemented in a bench-top imaging system [106]. In this approach, phase-sensitive detection is used to measure both the stress at the sample surface and the depth-dependent strain in the sample and elasticity is quantified as the ratio of these parameters [106]. To measure stress, a compliant layer is placed on the surface of the sample. The layer is nonlinear-elastic, displaying an increasing effective elastic modulus with strain [106]. Using the known stress-strain characteristic of the layer, measuring the strain in the layer using OCT allows us to calculate the axial stress at the layer-sample interface [225]. The strain in the sample was measured from OCT data as the slope of axial displacement using a finite difference approach [287].

The probe is worn on the finger and is forward-facing, such that the light is incident orthogonally to the tissue surface, assuming that the finger is positioned perpendicular to the sample surface. To deform the sample, axial compression is applied by the finger to both the compliant layer and the sample. A-scans are acquired and assembled to form a motion-mode (M-mode) image, as shown in Fig. 7.2(a). Figure 7.2 (b) shows the axial displacement, u_z (estimated from the phase difference, $\Delta\phi$) between consecutive A-scans, according to, $u_z = \Delta\phi\lambda/4\pi n$, where λ is the central wavelength of the OCT light source and n is the material's refractive index [290].

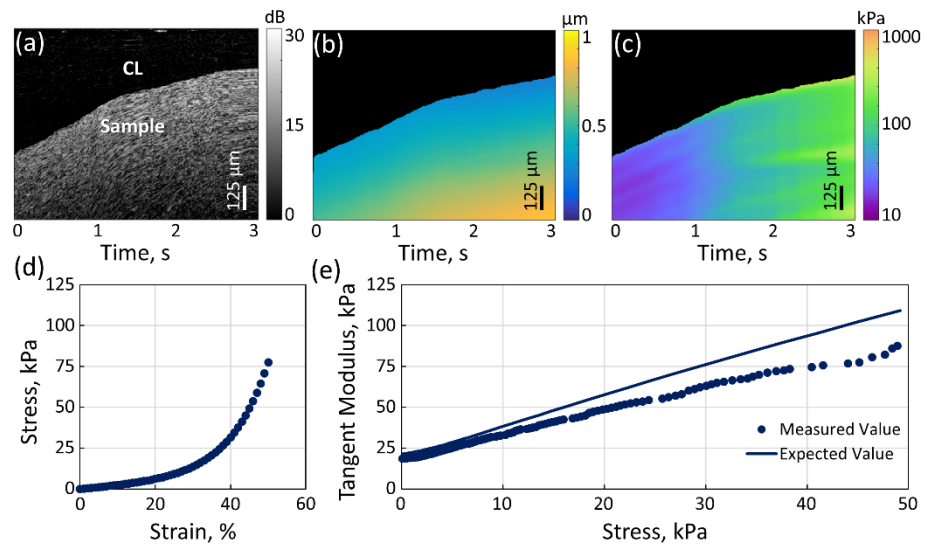


Figure 7.2: (a) OCT M-mode, (b) axial displacement, and (c) tangent modulus maps plotted over time. In (b) and (c), the compliant layer (CL) is masked in black. (d) Stress-strain curve of the compliant layer material and (e) tangent modulus plot measured with increasing stress in a phantom, evaluated from tangent modulus map shown in (c).

Key to the reconstruction of elasticity from finger-mounted QME data is the implementation of a number of filtering steps. The filtering performed on the displacement to reduce the effect of motion artifact is described in the following paragraph and is illustrated in Fig. 7.3. The layer-sample interface was determined for every A-scan using Canny-based edge detection [106]. Starting with the first A-scan, the axial displacement in the range 300–324 μm below this interface was cumulatively summed for every consecutive A-scan, until a threshold of 350 nm was reached. Analysing the axial displacement over this depth helped to reduce the impact of surface friction on the displacement whilst remaining in a region of high OCT SNR. If 350 nm was reached too quickly (<3 A-scans) or too slowly (>40 A-scans), the displacement data was assumed to be noisy, and the initial A-scan was discarded. This was repeated for all A-scans. 350 nm was empirically selected for the threshold as it allowed us to obtain a strong signal well above the displacement noise floor and prevent significant decorrelation effects. A block diagram describing the signal processing is shown in Fig. 7.3 (a). In the M-mode image in Fig. 7.3 (b), discarded A-scans are represented by vertical, cyan lines. Figure 7.3 (c) displays the filtered OCT image after the selected A-scans had been discarded and the remaining A-scans had been stitched together. After filtering, the displacement map was smoothed with a Gaussian filter ($\sigma_{\text{depth}} = 12 \mu\text{m}$ and $\sigma_{\text{time}} = 15 \text{ms}$), and then sub-sampled every one-hundredth A-scan (one every 10 ms), in order to increase processing speed without noticeable degradation in image quality (Fig. 7.2(b)). A second Gaussian filter was applied on the sub-sampled displacement to further reduce noise in the strain calculation ($\sigma_{\text{depth}} = 24 \mu\text{m}$ and $\sigma_{\text{time}} = 300 \text{ms}$). Strain was estimated as the gradient of the axial displacement with depth using a finite-difference approach [287]. This is termed ‘incremental strain’ as it describes the strain induced between

consecutive A-scans. This approach allowed us to accommodate for a variable range of compression applied by the finger which is of key importance in finger-mounted QME, given that the velocity of the finger is uncontrolled.

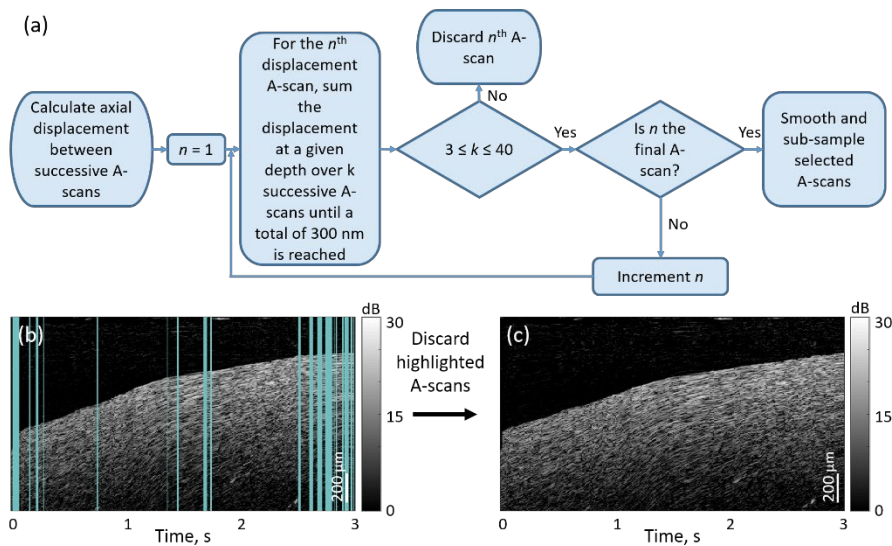


Figure 7.3: (a) Block diagram representation of the filtering scheme used to reduce hand motion artifacts. (b) M-mode scan illustrating discarded A-scans in cyan. (c) The filtered OCT image.

The absolute strain in the layer was determined by measuring the thickness of the layer from the layer-sample interface in the OCT scan. Tangent modulus (the gradient of the stress over strain, equivalent to the Young's modulus in linear-elastic materials) in the layer is estimated from the absolute strain using the pre-calibrated stress-strain curve of the silicone, which is represented in Fig. 7.2(d) [106]. The axial incremental stress at the layer-sample interface is then calculated as the product of the layer modulus and the layer incremental strain. The tangent modulus of the sample is estimated by dividing the axial incremental stress in the layer by the incremental strain in the sample (Fig. 7.2(c)), under the assumption that the stress is constant with depth. Tangent modulus represents the effective modulus of a material at a particular strain and we subsequently refer to it as 'elasticity'. In Fig. 7.2(c), the measured elasticity increases with time. This is expected as the silicone phantom is a nonlinear elastic material. In Fig. 7.2(e), the elasticity measured both with the probe and the uniaxial compression device are plotted as a function of stress and close correspondence is demonstrated.

7.2.3 RESULTS

Homogeneous silicone phantoms

Figure 7.4 shows a plot of the mean elasticity measured at 10% strain with the finger-mounted probe for five homogeneous silicone phantoms of varying elasticity against the expected elasticity (blue dots), measured using the uniaxial compression device. The red line

indicates the ideal outcome where the measured elasticity is equal to the expected elasticity and the error bars represent one standard deviation across five separate measurements of each silicone sample. As the elasticity of each silicone sample is different, the corresponding stress at 10% strain varies in each case. The stresses of these samples were measured to be 0.5, 1.9, 4.6, 7.6 and 16 kPa respectively, when using the finger-mounted probe. The results show a strong correspondence between the measured and expected elasticity with a mean absolute percent error (MAPE) of 13%. The mean elasticity measured for each silicone sample is within 21% of the expected elasticity (compared to 8% for bench-top QME) [106]. The increased error using the finger-mounted probe is likely due to the variability of hand motion and an increase in friction, which is explained further in the Discussion.

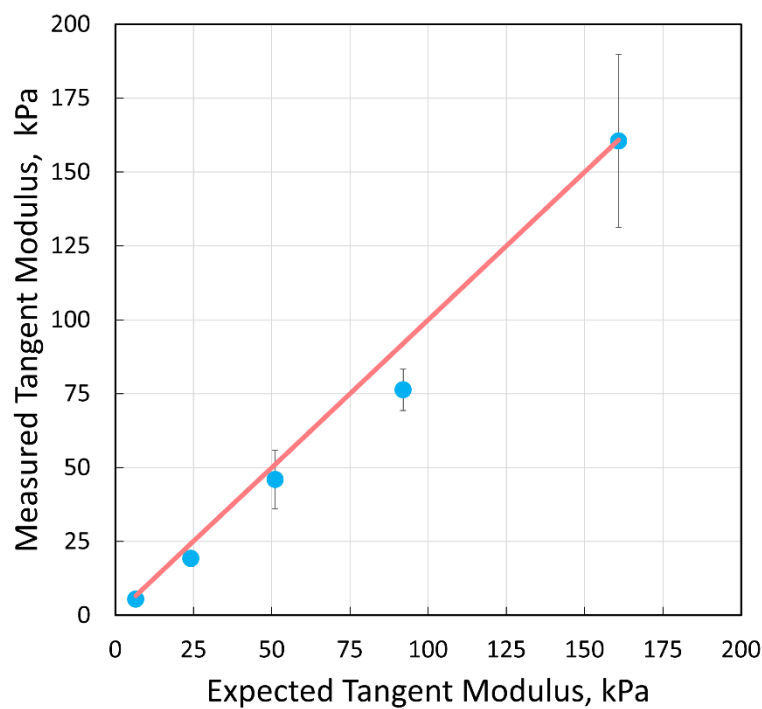


Figure 7.4: Mean tangent moduli measured in five homogeneous phantoms of varying elasticity compared to expected values measured with uniaxial compression. The error bars show one standard deviation.

Bi-layer silicone phantoms

In order to validate the ability to delineate two materials with varying mechanical properties in finger-mounted QME, measurements were performed on the bi-layer phantom. The M-mode OCT image is shown in Fig. 7.5(a). Figure 7.5(b) presents the corresponding OCT SNR, averaged over 50 A-scans, taken about the red line in Fig. 7.5(a). The individual layers can be distinguished by the change in signal intensity and attenuation. In Fig. 7.5(b), the boundary between the compliant layer and the top layer of the phantom is identified by the green diamond, whilst the yellow triangle indicates the boundary between the top (Layer 1) and bottom (Layer 2) layers of the phantom.

Figure 7.5(c) displays a map of the elasticity measured with the finger-mounted probe in the bi-layer phantom with the compliant layer masked out. In both layers, an increase in elasticity is observed with time. This is expected as the layer materials are nonlinear and therefore stiffen with increasing stress. The difference in elasticity between Layer 1 and Layer 2 is further illustrated in Fig. 7.5(d), which shows a plot of the elasticity over depth along the red line in Fig. 7.5(c), which corresponds to an applied stress of ~ 5 kPa. The boundary between layers measured using elasticity is consistent with the boundary determined from the corresponding OCT plot in Fig. 7.5(b). The elasticity in Layer 1 (between 400–600 μm) is noticeably lower than the elasticity in Layer 2 (beyond 600 μm in depth), as expected. The interface between the two layers is blurred because of the Gaussian smoothing applied to reduce noise. In Fig. 7.5(e), plots of the measured (dotted lines) and expected (solid lines) elasticity are presented over the applied stress from the corresponding regions of interests (ROI) shown in Fig. 7.5(c). The measured values in Fig. 7.5(e) are taken from the axially averaged elasticity within the ROI denoted by the blue (soft layer) and orange (stiff layer) dotted lines in Fig. 7.5(c). In this plot, close correspondence with the gold standard uniaxial compression device is observed.

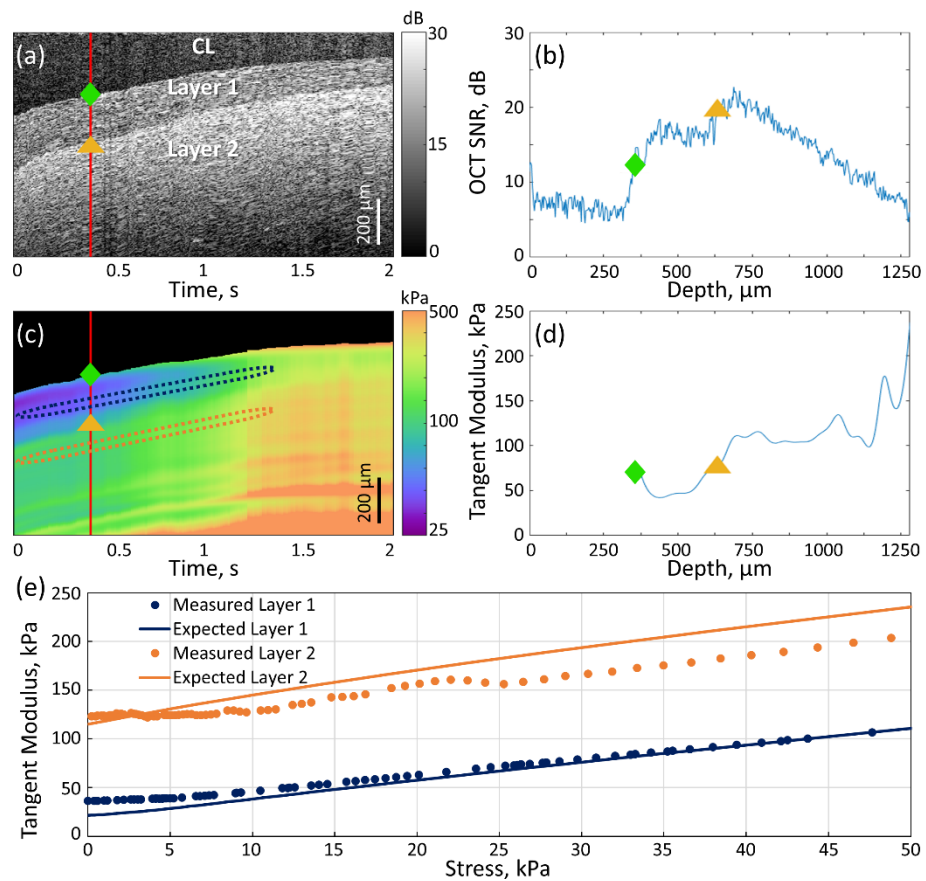


Figure 7.5: Finger-mounted QME on a bi-layer phantom. (a) M-mode OCT image showing the compliant layer (CL), soft layer (Layer 1) and stiff layer (Layer 2) and (b) OCT SNR with depth, average taken over 50 A-scans where the green diamond indicates the upper layer boundary and the yellow triangle indicates the lower. (c) Corresponding elastogram with ROIs overlaid (CL masked in black) and (d) tangent modulus vs depth with diamond and triangles representing the same boundaries as in (b). Both (b) and (d) were taken over the A-scan corresponding with the red lines in (a) and (c). (e) Measured tangent moduli of Layer 1 (blue) and Layer 2 (orange) layers plotted on the same axes as the respective expected measurements, acquired through uniaxial compression.

Compared to the compression test, the finger-mounted probe consistently overestimated the elasticity of Layer 1, but underestimated that of Layer 2, with a MAPE of 22% and 8%, respectively. Layer 2 exhibited increasing error with increasing stress. The cause of this error is explained further in the Discussion.

Kangaroo muscle

Finger-mounted QME was demonstrated on a 1 cm³ excised section of kangaroo muscle tissue. Scanning was first performed on the raw tissue. After scanning, the sample was cooked in boiling water in a vacuum-sealed bag for four minutes and re-scanned. Figures 7.6(a) and (c) show M-mode OCT and QME images, respectively, of the raw sample. Similarly, Figs. 7.6(b) and (d) show M-mode OCT and QME images, respectively, of the sample after cooking. Comparing Figs. 7.6(a) to (b) reveals that cooking the tissue resulted in an increase in the OCT SNR, which may be caused by a reduction in water content [482]. Similarly, Figs. 7.6(c) and (d) display a marked increase in elasticity after cooking. Figure 7.6(e) highlights the variation in elasticity between the raw (blue) and the cooked

(orange) samples as a function of stress, axially averaged over the regions indicated by the dotted blue and orange outlines in Figs. 7.6(c) and (d), respectively.

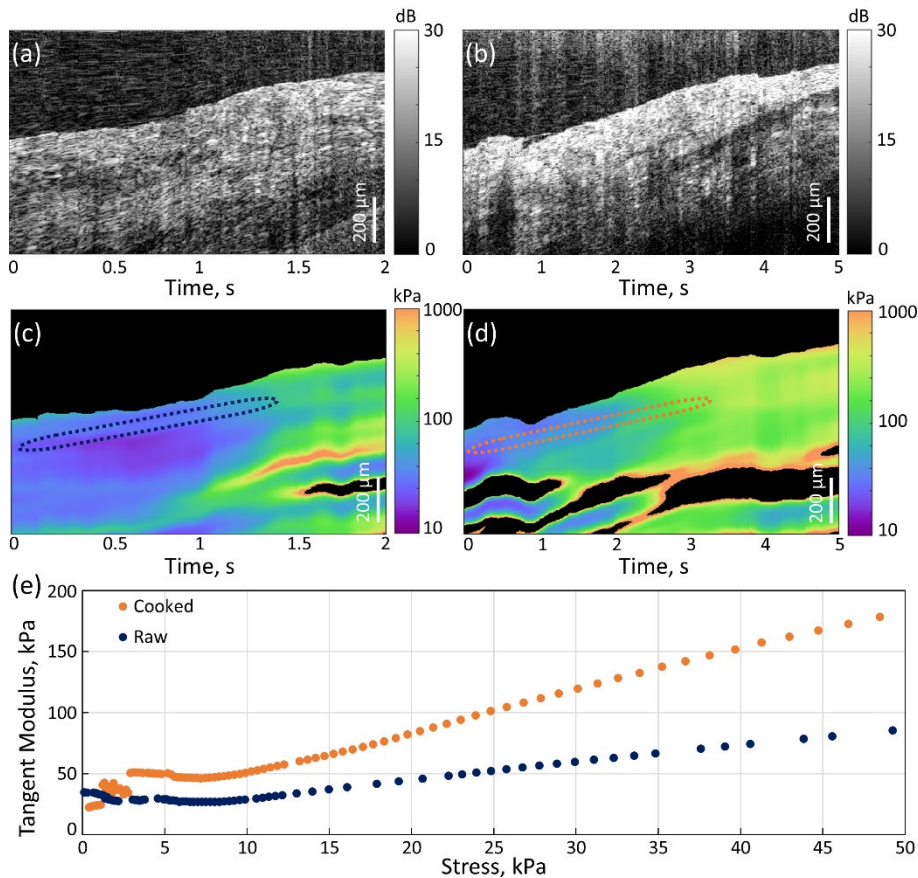


Figure 7.6: OCT M-mode scans of (a) raw kangaroo muscle and (b) the same region of tissue after being cooked for four minutes. The elastograms of (c) the raw and (d) the cooked muscle with ROIs represented by dotted lines (CL masked in black). (e) Tangent modulus measurements for the ROIs in the cooked and raw sample.

It can be seen in Fig. 7.6(e) that the difference in elasticity between the raw and cooked samples becomes more prominent at higher stresses. For example, at a stress of 10 kPa, the elasticity of the raw and cooked tissue was 29 kPa and 50 kPa, respectively, compared to 117 kPa and 203 kPa at a stress of 50 kPa. This change in mechanical properties was confirmed qualitatively during the experiment by manual palpation and is consistent with prior studies on muscle tissue from other species [483]. We can see in Fig. 7.6(e) that the measurements for the cooked sample in the stress range 0-3 kPa, show a lower elasticity than the raw sample. This discrepancy is likely due to the probe not being positioned exactly perpendicular to the surface, decoupling the direction of the applied force and the axis which is scanned, resulting in a lower measured elasticity. This phenomenon is noticeable in tissue scans due to the heterogeneous structure, however, it reduces with higher stresses. This is most likely because of the operator's finger naturally tending towards perpendicular in order to apply higher forces to the sample [484].

2-D scanning on a silicone inclusion phantom

In addition to M-mode scanning, as shown in Fig. 7.7, we also acquired preliminary 2-D scans with finger-mounted QME by swiping the finger across a silicone inclusion phantom whilst acquiring A-scans. A compliant layer was placed on the inclusion phantom and the probe was brought into contact with the layer. During scanning, the finger applied both a lateral and axial motion, resulting in a ramp compression to the compliant layer and phantom. The increasing axial compression is a function of lateral position and ensured sufficient incremental strain was applied between consecutive A-scans. The speed at which the finger was swept across the sample was determined empirically by observing the real-time OCT image. The scans presented in Fig. 7.7 were taken on the inclusion phantom described in Section 7.2.2. The contrast between the surrounding bulk and the embedded inclusion is visible in the OCT image shown in Fig. 7.7(a). It is worth noting that the total length of the scan was ~ 5 mm and the inclusion was 1 mm wide. Considering this, it is apparent from Fig. 7.7 that the scanning performed by the finger is non-uniform, highlighting the effect of varying speeds of lateral hand motion. This results in a difference between the perceived and true dimensions of the imaged features, suggesting that a mechanism to compensate for this non-uniform scanning is required. This issue is described in more detail in the Discussion.

In finger-mounted QME, we consider compressive strain to be negative, and tensile strain to be positive [485]. Furthermore, we assume that compression is uniform and uniaxial. This, however, does not always hold true as mechanical heterogeneity and complex surface topologies can introduce tensile strain as well as compressive strain [485]. This is evident in 2-D finger-mounted QME as the probe sweeps over the boundary between the bulk and inclusion, where regions of tensile strain were measured. To account for the presence of both compressive and tensile strain, Fig. 7.7(b) displays the magnitude of the elasticity, taken from both the positive (tensile) and negative (compressive) strains. The mean measured elasticity and standard deviation of this scan was 51 ± 4 kPa and 318 ± 67 kPa over 10–15% preload strain in the bulk and inclusion, respectively. These values are approximately twice the expected elasticity. While the contrast between the inclusion and bulk is apparent, there are regions of high elasticity that appear as orange lines in Fig. 7.7(b). The local boundary between tensile and compressive strain crosses zero, resulting in an asymptote in elasticity, corresponding to the orange lines. Due to the large smoothing kernels used in the processing code, this artifact also effects the surrounding regions of the bulk and inclusion, contributing to the overestimation of elasticity in these regions. This can be observed in the thin region of bulk above the inclusion. The mean measured elasticity in this region is 125 ± 12 kPa, ~ 2.5 times the measured elasticity in the rest of the bulk. Furthermore, the use of a logarithmic

scale reduces the contrast of this particular region relative to the inclusion, however, there is still sufficient contrast in the elasticity measurements to delineate the inclusion from the bulk.

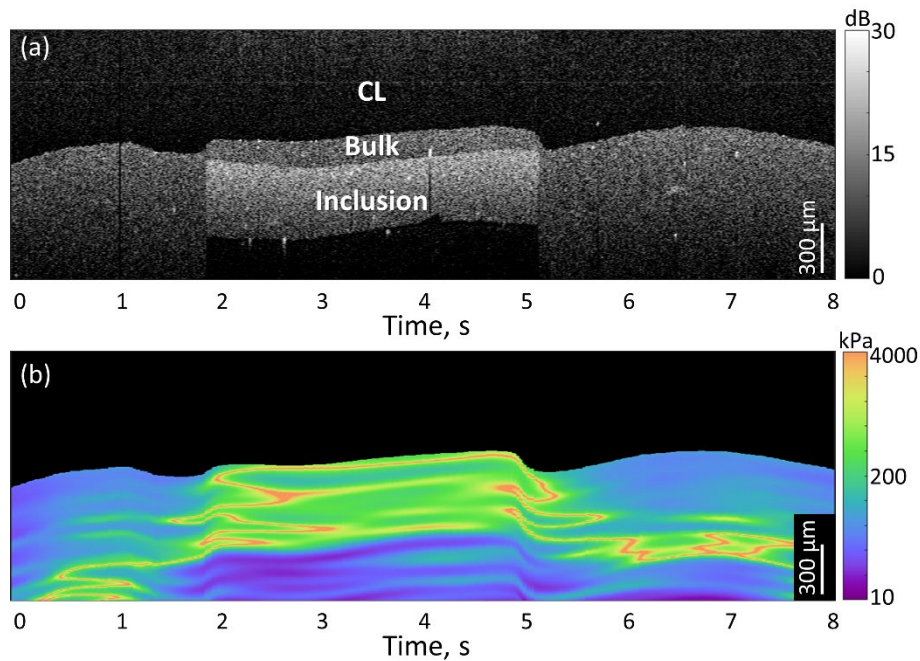


Figure 7.7: (a) 2-D-OCT scan over a stiff silicone inclusion embedded within a soft silicone bulk and (b) the corresponding 2-D elasticity map with the x-axis given in seconds (CL masked in black).

Silicone, like tissue, exhibits a nonlinear stress-strain relationship, however, for small changes in strain, this relationship can be approximated as linear. In 2-D scanning, we aim to limit the strain in the sample to 0–20% so that the measurements are taken from an approximately linear region of the stress-strain curve. This ensures that the elasticity measured in the bulk will be constant over the whole scan. Uniform elasticity in the surrounding bulk, allows 2-D scanning to detect features of interest such as the inclusion shown in Fig. 7.7(b), based on mechanical contrast. This presents an additional problem, however, as the incremental strain is now reduced, which in turn leads to lower strain SNR in finger-mounted QME and a reduction in signal quality. Despite these issues, Fig. 7.7 presents high contrast between the inclusion and surrounding bulk in both the OCT image and elastogram, demonstrating the potential of 2-D finger-mounted QME.

7.2.4 DISCUSSION

In this paper, we have presented finger-mounted QME, a technique that provides quantitative measurements of the mechanical properties of soft tissue using a wearable elastography probe. While previous OCE probes such as needle-based OCE aim to replace manual palpation, finger-mounted QME offers the unique advantage of complementing manual palpation with OCE imaging. In needle OCE, as the needle tip is distal to the hand and because the needle is rigid, the dexterity of manual palpation is inherently lost. Using this

probe, we have demonstrated the capability to measure elasticity in silicone phantoms and to delineate the mechanical properties of heterogeneous samples. Our approach utilises a compact implementation of QME, which has potential for use in confined spaces such as surgical cavities, with the trade-off of an additional 13% error compared to bench-top QME [106]. This represents a nominal increase in error as the mechanical contrast between healthy and diseased tissue is often significantly greater than this error. For example, invasive ductal carcinoma in breast tissue is up to seven times stiffer than adipose tissue [486], likewise, cirrhotic liver tissue is approximately twice as stiff as healthy liver tissue [487].

The error in the finger-mounted QME measurements is attributed largely to the frictional force between the compliant layer and the sample, which restricts lateral expansion of the compliant layer. As the silicone is incompressible, higher friction results in restricted deformation of the compliant layer for the same stress. Therefore, the absolute stress derived from the compliant layer is typically underestimated, leading to an underestimation of the elasticity of the sample [488], as can be seen in Fig. 7.2(e). In bench-top QME, PDMS oil is applied to both sides of the compliant layer to mitigate this friction on both the imaging window and the sample [106]. In finger-mounted QME, however, PDMS oil is only applied to the probe-compliant layer interface as PDMS oil between the sample and compliant layer, coupled with the indenter-like profile of the probe tip, will cause the compliant layer to slip during scanning. At higher stresses, the compliant layer will slip completely off the sample, therefore preventing the estimation of elasticity. Applying oil to only the probe-compliant layer interface, results in an increased error due to friction compared to the bench-top counterpart. This error is also seen in the measurement of Layer 2 for the bi-layer scans presented in Fig. 7.5, however, in the same scan Layer 1 was slightly overestimated. This overestimation may be due to a similar effect, where Layer 2 restricts the lateral expansion of the thinner top layer, resulting in a lower axial strain and a higher measured elasticity, which was prominent enough to dominate the effects of friction at the compliant layer-Layer 1 interface. Finger-mounted QME demonstrated a MAPE of 22% and 8% for the upper and lower layers respectively, which is similar to the 15% reported by benchtop QME [106]. This shows that despite the simplified optical design and hand-motion associated with the finger-mounted probe, this technique is still capable of reproducing elasticity measurements with high accuracy and providing high contrast between different materials.

One of the key challenges facing finger-mounted QME is the implementation of accurate 2-D and, eventually, 3-D scanning. In this paper, we have presented preliminary 2-D scans that serve as an example for the extension of the technique to 2-D. These results were acquired by swiping the finger along the tissue surface and using the finger motion as both the scanning and mechanical loading mechanism. A main issue with this approach is that the

reconstruction of OCT images and elastograms does not account for non-uniform velocities of the scanning finger. Without implementing a method to accurately track the motion of the probe, it is challenging to determine the location of A-scans within a 2-D scan, resulting in distortion of the apparent dimensions of sample features as seen in Fig. 7.7. This could be overcome by using a lateral scanning mechanism, such as compact microelectromechanical system (MEMS) scanning mirrors, already deployed in other OCT probes [489–492]. This, however, would add considerable bulk to the design, increasing the probe footprint and reducing dexterity. Alternatively, an external tracking system, such as a magnetic position sensor, could be used to determine the probe location during the scan [493]. However, the spatial and temporal resolution of magnetic tracking systems is low compared to OCT, and such a system would likely need to be complemented by additional sensors, such as accelerometers, or some form of image registration to infer the motion of the probe from the changes in the acquired images. Another option would be to exploit the decorrelation time of the speckle pattern to estimate velocity [470]. This approach has been employed to account for non-uniform rotation distortion (NURD) in endoscopic OCT applications [470], and could be modified to account for linear motion across the sample surface in finger-mounted QME.

Finger-mounted QME aims to improve diagnostic outcomes by complementing manual palpation with a quantitative assessment of disease. One area of potential application, is in breast-conserving surgery, which relies heavily on manual palpation to detect traces of tumour during surgery [71]. During this procedure, the surgeon strives to excise the tumour, in addition to a thin surrounding layer of healthy tissue [494,495]. Surgeons then often manually palpate the surgical cavity to determine if there is residual tumour in the patient [71]. However, in 20–30% of breast-conserving surgery patients, additional surgery is required as not all of the residual tumour was excised [496]. Finger-mounted QME scanning of the cavity walls could improve the detection of residual tumour. By looking for changes in the mechanical properties of cancerous tissue, our technique could potentially identify tumour that was not picked up by manual palpation. Finger-mounted QME also holds potential in applications relating to the intraoperative detection of hepatic metastases [497] and pancreatic insulinomas [498], both of which typically present as stiff lesions. As with BCS, surgeons performing these procedures rely on manual palpation to detect changes in the mechanical properties of tissue to guide them in locating the malignancies and finger-mounted QME has the potential to improve on this existing approach [497,498]. Finger-mounted QME is particularly well-suited to these applications as the compact design is ideal for confined spaces such as a surgical cavity and the acquisition rate used (10 kHz) enables finger-mounted QME to be performed within several seconds, comparable to the time scale

of some manual palpation techniques. Furthermore, OCT systems with acquisition times orders of magnitude faster than 10 kHz are readily available [499]. In this first demonstration of finger-mounted QME, we chose to use conservative acquisition times and to focus on the proof-of-principle. In future development, using faster acquisition times, combined with more rapid compression of the tissue with the finger, would allow measurements to be acquired in milliseconds.

The clinical suitability of finger-mounted QME could be enhanced by replacing the plastic thimble case with a surgical glove to ensure the probe can be used in sterile scenarios. Embedding the optical components in a glove would better preserve tactile sensation and could provide surgeons with improved dexterity over the rigid plastic case currently used. However, even the addition of a second set of gloves has shown reductions in hand sensitivity during surgery [500] and the addition of the optical fibre and associated components would more than likely incur a similar or greater reduction in sensitivity. As manual palpation is predominantly performed using the fingertips [473], positioning any components that would hinder sensitivity away from the fingertip would better preserve tactile sensitivity whilst still providing the surgeon with the benefits of QME.

7.2.5 CONCLUSIONS

This paper presented the first finger-mounted OCE probe. The probe features a forward-facing fibre probe in a compact implementation of QME. Demonstrations in 1D on silicone samples have shown that finger-mounted QME is capable of estimating the elasticity of materials within 21% of the expected value. Finger-mounted QME was also capable of measuring the thermally-induced changes in kangaroo muscle tissue. In addition, a preliminary 2-D scan over an inclusion phantom showed the capability to detect features based on the mechanical contrast, albeit, at a reduced accuracy compared to the 1D measurements. With further enhancement of 2-D scanning, we believe that finger-mounted QME has potential to augment existing clinical practices that rely on manual palpation.

Funding

Australian Research Council (ARC); the Cancer Council, Western Australia; OncoRes Medical; War Widows' Guild of Western Australia Scholarship.

7.3 BREAST TISSUE SCANNING

Finger-mounted QME was validated in a clinical scenario by scanning a freshly excised mastectomy specimen at Fiona Stanley Hospital, Western Australia. This study was approved by the Sir Charles Gairdner and Osborne Park Health Care Group Human Research Ethics

Committee (HREC No: 2007-152) and the Fiona Stanley Hospital Research Governance Office (FSH-2015-032), with informed consent obtained from the patient prior to surgery. Immediately after surgery, the breast specimen was transported from the surgical theatre to the pathology department where a pathologist dissected a $\sim 5 \times 5 \times 1$ cm region containing tumour, fibrous tissue, and adipose tissue for imaging. Scans were performed with the probe worn on the finger and manually scanned ~ 3 cm across the sample surface.

The OCT scan is shown in Fig. 7.8(a) where clear optical contrast is visible between regions of dense tissue (DT) and adipose tissue (A). Figure 7.8(b) displays the corresponding elastogram where the regions of dense tissue exhibit an elasticity of ~ 12 kPa, noticeably higher than the regions of adipose tissue which were ~ 0.5 kPa. There is a small region approximately 2 seconds into the scan where the probe was not fully in contact with the silicone layer producing multiple common reference reflection artifacts.

Due to the mechanical heterogeneity at different spatial locations within the scan, the applied strain was deliberately kept low ($< 20\%$) to ensure an approximately linear response from the different tissue types. In contrast to the results presented above, the second Gaussian filter in the processing chain was not applied to the subsampled displacement to prevent the asymptotic effect presented in Fig. 7.7, caused by transitions between compressive and tensile strain, from obscuring tissue boundaries. As a result, there is slightly more noise in the 2-D scans presented in Fig. 7.8.

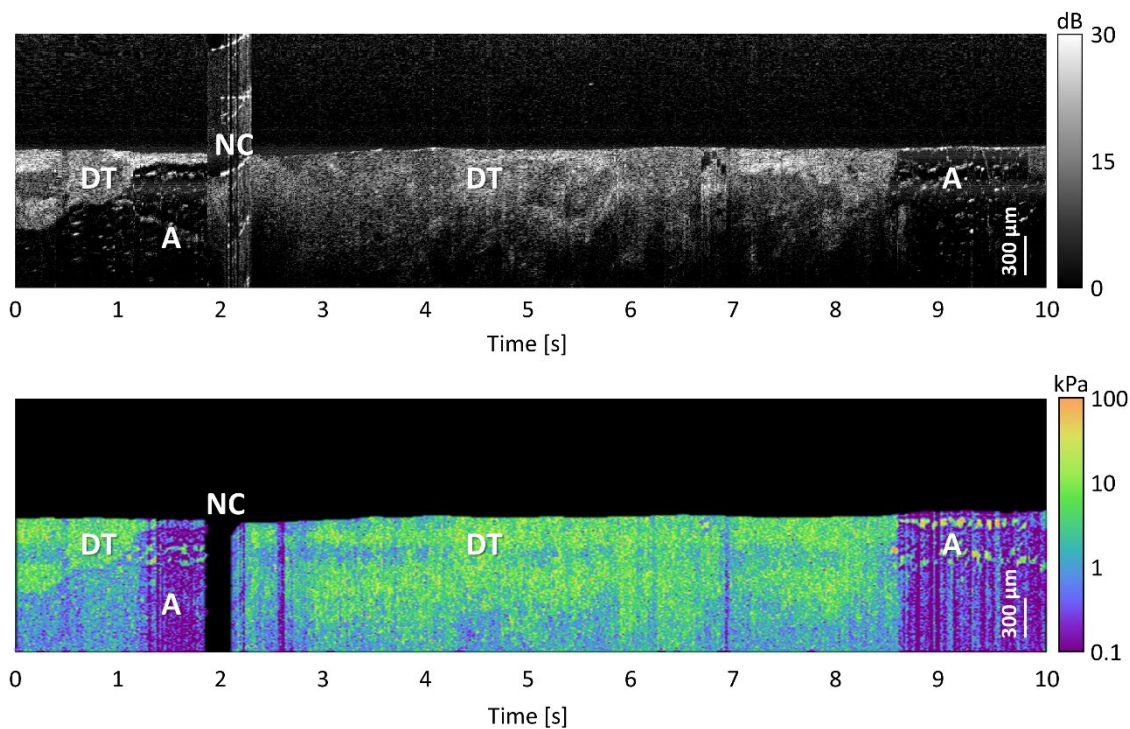


Figure 7.8: Preliminary 2-D scan over freshly excised human breast tissue following mastectomy. (a) The 2-D OCT scan acquired and (b) the corresponding 2-D elasticity map with the x-axis given in seconds (CL masked in black). DT: dense tissue; A: adipose tissue; NC: non-contact.

In this initial demonstration, there was no corresponding histology to validate this specific tissue types in the Fig. 7.8. Therefore, suspected regions of fibrous tissue and tumour have been collectively labelled as dense tissue, in contrast to adipose tissue, which is distinguishable by its honeycomb-like structure in OCT images. Future studies would need to be validated by histology to classify the tissue types present in the acquired scans, particularly as OCT has previously shown low optical contrast between fibrous tissue and tumour. Additionally, follow-up studies will need to investigate the suitability of finger-mounted QME probe for use in the surgical cavity, which is the intended clinical environment. An important objective of these future studies would be to determine the efficacy of finger-mounted QME probe for detecting residual tumour following breast cancer excision. These studies would also likely highlight any limitations of the initial probes design and inform future designs. While this work is outside the scope of this Thesis, the initial work presented here demonstrates that finger-mounted QME has the potential to be adapted as an intraoperative margin assessment technique due to the ability to accurately measure the mechanical properties and provide high resolution images of tissue structure.

CHAPTER 8

CAMERA-BASED OPTICAL PALPATION

8.1 PREFACE

Generally, existing optical elastography techniques rely on expensive and cumbersome components, precluding their use for applications in remote and low-resource settings. Even if imaging probes can be developed to be compact and cost-effective, they still require bulky optical systems such as light sources, spectrometers and free-space optics. The research undertaken in this Chapter seeks to overcome these limitations with the development of a new optical elastography technique, camera-based optical palpation (CBOP). This technique is a variant of optical palpation which, as described in Chapter 4 in the context of an OCT-based implementation, has demonstrated high diagnostic accuracy (sensitivity: 83.3%; specificity: 86.2%), only slightly lower than quantitative micro-elastography (QME) (sensitivity: 92.9%; specificity: 96.4%). In CBOP, most of the cost, bulk, and complexity is removed by replacing the OCT imaging modality with a commercially available digital camera. As the camera alone cannot directly determine axial displacement, a porous silicone layer is used, whereby axial strain is encoded in the optical transmission through the layer. As compression increases, the pores close and reduce in number, permitting more light to transmit through the layer, which is captured by the camera. The results presented in this Chapter demonstrate similar imaging capabilities between CBOP and OCT-based optical palpation, as well as the feasibility of this technique on freshly excised mastectomy samples. In addition, in this Chapter a number of further developments are outlined that can be implemented to increase the clinical suitability of CBOP.

This Chapter consists of a first-authored publication, Rowan W. Sanderson, Qi Fang, Andrea Curatolo, Wayne Adams, Devina D. Lakhiani, Hina M. Ismail, Ken Y. Foo, Benjamin F. Dessauvage, Bruce Latham, Chris Yeomans, Christobel M. Saunders, and Brendan F. Kennedy. “*Camera-based optical palpation*,” *Scientific Reports*, 10(1): pp. 1-13, 2020.

8.2 CAMERA-BASED OPTICAL PALPATION

Rowan W. Sanderson^{1,2}, Qi Fang^{1,2}, Andrea Curatolo^{1,2,3}, Wayne Adams^{1,2}, Devina D. Lakhiani^{1,2}, Hina M. Ismail^{1,2}, Ken Y. Foo^{1,2}, Benjamin F. Dessauvage^{4,5}, Bruce Latham^{4,6}, Chris Yeomans⁴, Christobel M. Saunders^{7,8,9} and Brendan F. Kennedy^{1,2,10}
Scientific Reports, 10(1): pp. 1-13, 2020.

Abstract: Optical elastography is undergoing extensive development as an imaging tool to map mechanical contrast in tissue. Here, we present a new platform for optical elastography by generating sub-millimetre-scale mechanical contrast from a simple digital camera. This cost-effective, compact and easy-to-implement approach opens the possibility to greatly expand applications of optical elastography both within and beyond the field of medical imaging. Camera-based optical palpation (CBOP) utilises a digital camera to acquire photographs that quantify the light intensity transmitted through a silicone layer comprising a dense distribution of micro-pores (diameter, 30–100 μm). As the transmission of light through the micro-pores increases with compression, we deduce strain in the layer directly from intensity in the digital photograph. By pre-characterising the relationship between stress and strain of the layer, the measured strain map can be converted to an optical palpogram, a map of stress that visualises mechanical contrast in the sample. We demonstrate a spatial resolution as high as 290 μm in CBOP, comparable to that achieved using an optical coherence tomography-based implementation of optical palpation. In this paper, we describe the fabrication of the micro-porous layer and present experimental results from structured phantoms containing stiff inclusions as small as $0.5 \times 0.5 \times 1$ mm. In each case, we demonstrate high contrast between the inclusion and the base

¹ BRITelab, Harry Perkins Institute of Medical Research, QEII Medical Centre, Nedlands and Centre for Medical Research, The University of Western Australia, Perth, Western Australia, 6009, Australia

² Department of Electrical, Electronic & Computer Engineering, School of Engineering, The University of Western Australia, Crawley, Western Australia, 6009, Australia

³ Currently with Visual Optics and Biophotonics Group, Instituto de Óptica “Daza de Valdés”, Consejo Superior de Investigaciones Científicas (IO, CSIC), C/Serrano, 121, Madrid, Spain

⁴ PathWest, Fiona Stanley Hospital, 11 Robin Warren Drive, Murdoch, Western Australia, 6150, Australia

⁵ Division of Pathology and Laboratory medicine, Medical School, The University of Western Australia, Crawley, Western Australia, 6009, Australia

⁶ The University of Notre Dame, Fremantle, Western Australia, 6160, Australia

⁷ Division of Surgery, Medical School, The University of Western Australia, Crawley, Western Australia, 6009, Australia

⁸ Breast Centre, Fiona Stanley Hospital, 11 Robin Warren Drive, Murdoch, Western Australia, 6150, Australia

⁹ Breast Clinic, Royal Perth Hospital, 197 Wellington Street, Perth, Western Australia, 6000, Australia

¹⁰ Australian Research Council Centre for Personalised Therapeutics Technologies, Australia

material and validate both the contrast and spatial resolution achieved using finite element modelling. By performing CBOP on freshly excised human breast tissue, we demonstrate the capability to delineate tumour from surrounding benign tissue.

8.2.1 INTRODUCTION

Optical elastography describes a range of techniques used to image the mechanical properties of biological tissue on the micro- to millimetre scale [20,22,155,200,501]. The main application of these techniques is in medical imaging as it is well-established that there is often a correlation between disease and tissue mechanical properties on these scales [1,11,155,249,502,503]. The use of optics invariably provides higher spatial resolution than alternative approaches, namely, ultrasound elastography [504] and magnetic resonance elastography [505], and affords the opportunity to implement small form factor probes which are amenable to *in vivo* imaging [437,440,479]. A range of approaches have been developed that each utilise an optical imaging modality to measure deformation induced by a mechanical load. A mechanical model of the tissue deformation is then used to estimate a mechanical property or parameter that is mapped into an image. The most widely developed approach is optical coherence elastography (OCE) [18,20,22,480,506,507] which combines optical coherence tomography (OCT) and a loading mechanism, typically either a quasi-static compression or an acoustic excitation, to measure the local mechanical response of tissue from which a map of elasticity is derived. OCE has an attractive combination of features, including rapid acquisition, micrometre-scale resolution and millimetre to centimetre field-of-view [21,303], and has been proposed for a number of applications including tumour margin assessment and keratoconus detection [105,208,414,442,478]. Brillouin microscopy is another prominent technique which utilises confocal microscopy to measure the Brillouin frequency shift induced by vibrations of phonons in the tissue. The local longitudinal (bulk) modulus of the sample is derived from this frequency shift and is related to elasticity under simplifying assumptions [26,202,23]. Brillouin microscopy has been demonstrated in cell mechanics [23,508] and ophthalmology [217,509], where particular advantages include its non-contact configuration and the fact that no external loading mechanism is required.

Whilst these existing high resolution variants of optical elastography offer capabilities to image at, or close to, the cellular scale, to imaging depths of hundreds of micrometres to several millimetres, they typically rely on expensive imaging systems that restrict application of optical elastography to niche areas, such as tumour margin assessment [105]. Furthermore, existing techniques may not be practical in low-resource and remote settings [219,417,510]. Another challenge is that techniques such as OCE and Brillouin microscopy are not easily

used by non-optics experts as they contain complex optical components that require careful alignment, thus precluding a broader application of the technology. Also, in some applications, it would be advantageous to have a device with a small footprint and without the burden of optical patch cords obstructing the practical use of the device. For example, there is great promise for optical elastography in the food industry where the elasticity of meats and fruits is an important indicator of food quality [511] and in the robotics industry where tactile feedback is of vital importance [229]. However, these applications remain largely out of reach of existing optical elastography techniques.

In this paper, we begin to address this gap in optical elastography capabilities by proposing camera-based optical palpation (CBOP), a novel approach which provides stress maps, termed optical palpograms, at the tissue surface using a relatively low-cost (<\$1,000 USD), 12.2 megapixel (MP), complementary metal-oxide semiconductor (CMOS) camera and a micro-porous compliant silicone layer. Analogously to the sense of touch, the stress measured in optical palpograms is dependent on the stiffness of the underlying tissue. In CBOP, the light intensity transmitted through the micro-porous layer placed on top of the tissue of interest is detected. The refractive index difference between the silicone and the air inside the micro-pores causes light scattering, such that minimal light is transmitted through the layer in its uncompressed state. However, when compression is applied to the layer, the micro-pore volume decreases leading to an increased transmission of light. In this way, the camera intensity encodes the strain of the layer. Pre-characterisation of the relationship between stress and strain in the layer using standard compression testing allows for optical palpograms to be derived from the measured strain, endowing CBOP with the capability to generate mechanical contrast from a simple digital camera. Another advantage of CBOP is that the images generated are independent of the optical properties of the underlying tissue, as only the light transmitted through the layer is required to generate mechanical contrast. This may provide a benefit over techniques such as OCE and Brillouin microscopy where the optical scattering from the tissue is often inconsistent and can be obscured, for example, by the presence of blood.

CBOP is inspired by OCT-based optical palpation [225], where OCT intensity is used to measure the thickness of a pre-characterised non-porous, transparent silicone layer compressed against the tissue. The strain in the layer is determined by the thickness change measured from the OCT data and the known stress-strain relationship is then used to generate optical palpograms. OCT-based optical palpation has been demonstrated to provide high imaging contrast for skin and human breast tissue [226,234]. For example, in one study of excised human breast tissue from 34 patients, strong correlation was observed between optical palpograms and corresponding gold standard histology [226]. However, a main

drawback of OCT-based optical palpation is the requirement to use an expensive optical imaging system. In addition, a 3-D OCT data set is required, typically restricting the acquisition time needed to generate an optical palpogram to the range of seconds [106], and furthermore, placing a substantial burden on signal processing, limiting its application in scenarios where rapid visualisation of palpograms is essential.

In this paper, we first describe the fabrication and characterisation of the micro-porous silicone layer. We then compare the performance of our technique to OCT-based optical palpation on four structured silicone phantoms, containing stiff inclusions ranging from 0.5–5 mm in size, by analysing the contrast-to-noise ratio (CNR) and spatial resolution in each case. This analysis is accompanied by validation of the mechanical contrast using finite element modelling (FEM). Finally, we demonstrate our technique on human breast specimens freshly excised from mastectomy surgeries. These tissue results are co-registered with and validated against post-operative histology, verifying that CBOP can distinguish tumour from surrounding benign tissue.

8.2.2 METHODS AND MATERIALS

Fabrication of the micro-porous layer

The micro-porous layers used in CBOP consist of a polydimethylsiloxane (PDMS) matrix and an open cell network of ~ 30 – 100 μm diameter pores. While there are several methods for porous layer fabrication, such as the embedding of hollow micro-spheres into the pre-cured base material [512] and gas foaming [513], in CBOP a direct templating technique [514,515] is employed, which involves mixing a sacrificial substrate (sucrose) into the PDMS prior to curing. The sugar is dissolved out after curing, resulting in an open cell network. The layers are cut into 25 mm diameter discs, ~ 900 μm thick, and exhibit an elasticity of 7.3 kPa at 10% strain. The steps in this process are illustrated in Fig. 8.1, and are described in detail below:

Step 1: PDMS resin (Elastosil P7676 Part A, Wacker Chemie, Munich, Germany) and PDMS oil (Wacker AK 50, Wacker Chemie, Munich, Germany) are first mixed at a ratio of 2:1. Adding oil to the resin reduces the overall elasticity of the cured PDMS matrix [481]. Then, fine grain sugar (grain size ~ 30 – 100 μm) is added to the compound in a concentration of 1 g/ml. Grain size uniformity is ensured by passing the sugar grains through both a 106 μm sieve (Product: 003SAW.106, Endecotts, London, United Kingdom) and a 32 μm sieve (Product: 003SAW.032, Endecotts, London, United Kingdom) and collecting the sugar that did not pass through the smaller sieve. Using fine grain sugar allows for uniform dispersion of the grains throughout the matrix, as the suspension is less likely to sediment in

the PDMS [516]. This compound is stirred for 5 minutes using a propeller stirrer, to allow even distribution of the sugar particles.

Step 2: PDMS crosslinker (Elastosil P7676 Part B, Wacker Chemie, Munich, Germany) is mixed with the same type of PDMS oil used in Step 1 at a mixing ratio of 2:1. Then, sugar with the same grain size as in Step 1 is added to the compound at a concentration of 1 g/ml, followed by thorough stirring for 5 minutes to allow even distribution of the sugar particles in the compound. Steps 1 and 2 are performed separately due to the high viscosity of the mixture making it difficult to combine the sugar and PDMS uniformly in the timeframe before the PDMS begins to cure.

Step 3: The resin and crosslinker compounds are combined with additional PDMS oil at a ratio of 1:1:1 and stirred for 5 minutes to provide complete mixing. Then, a portion of the mixture is pipetted into a petri dish, such that the total thickness is 900 μm . The mixture is then placed in an oven at 70°C for 30 minutes, to provide temperature-accelerated curing.

Step 4: After curing, the mixture is cut into cylinders (diameter, 25 mm) using a blade and a circular punch. The cut surfaces of the cylindrical layer provide exposure of the sugar particles to air, which is important for the dissolution process in the next step.

Step 5: The cylindrical layer is placed in a water bath at room temperature, to allow dissolution of the sugar particles. It takes up to 72 hours to fully dissolve the sugar particles, due to the small diameter of the inter-connected channels between sugar particles. To accelerate the dissolution process, the water bath can be kept at 70°C in the oven, increasing the thermal energy used to break intermolecular bonds between sucrose molecules. Using this method, the total period of dissolution can be reduced to 48 hours.

Step 6: The layer with the sugar particles fully dissolved is removed from the water bath, followed by a process of dehydration to remove any residual water inside the layer. This involves placing the layer in the oven at 70°C for 48 hours to remove any residual moisture. After this, the micro-porous layer is ready to be used in imaging.

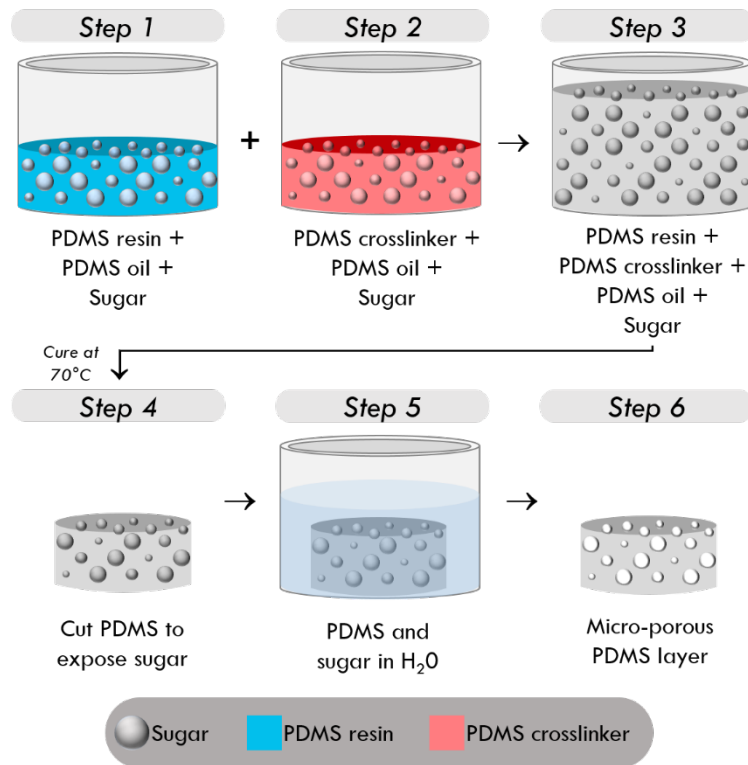


Figure 8.1: Fabrication process of micro-porous silicone layers by sacrificial templating of sugar grains.

Experimental design

CBOP uses a 12.2 MP CMOS camera (Basler ace acA4024-29uc, Basler AG, Ahrensburg, Germany) and a 25 mm fixed focal length lens with a working distance of 100 mm, costing \$550 USD and \$250 USD, respectively. The camera and lens are positioned above a rigid glass window, dimensions: $50.8 \times 50.8 \times 3$ mm, that acts as a compression plate (high efficiency window, Edmund Optics, New Jersey, USA). During acquisition, the sample, a $900 \mu\text{m}$ -thick micro-porous layer and a $\sim 300 \mu\text{m}$ -thick green layer are placed on a rigid plate which is affixed to a translation stage (MTS25-Z8, Thorlabs, New Jersey, USA). The green layer, made from mixing one part of green silicone-based pigment (SP-Green, Barnes Products, Moorebank, Australia) with four parts silicone elastomer (Elastosil P7676, Wacker Chemie, Munich, Germany) serves as a homogeneous colour mask for the underlying sample and ensures that variability in light backscattered from the sample does not affect the estimation of stress. The layer is dyed green as the CMOS camera exhibits a higher spectral sensitivity to this colour channel. $200 \mu\text{L}$ of PDMS oil (Wacker AK 50, Wacker Chemie, Munich, Germany) is applied between each mechanical interface to reduce the effect of friction which restricts the lateral expansion of the sample, the green layer and the micro-porous layer under compression. The translation stage is operated in the z -direction such that the stage compresses the sample and layers against the glass window.

During the experiment, the translation stage is used to bring the sample into contact with the glass window, at which point the total thickness of the sample together with the green layer and micro-porous layer is recorded. The initial thicknesses of the green layer and micro-porous layer are also measured prior to the experiment. Then, the translation stage is used to increase the preloaded strain applied to the overall thickness (sample + green layer + micro-porous layer) in 10% increments until 50% preloaded strain is reached. At each of the strain levels, ten digital photographs are acquired at a rate of 10 fps and are later averaged in post-processing to reduce the effect of shot noise on optical palpograms. Averaging multiple photos at a preloaded strain improves the SNR by as much as 30%, at the expense of longer acquisition times. After imaging, the green and micro-porous layers are removed, and the sample is loaded to the same approximate strain to acquire a digital photograph of the tissue surface to assist with co-registration of features in the optical palpogram.

Figure 8.2 shows a schematic of the experimental setup. In Fig. 8.2(a), at a low level of strain, the light emitted by an array of 6000-6500K SMD 5050 white-light LEDs situated above the imaging window, reaches the micro-porous layer and the air-filled pores scatter light and prevent transmission to the green layer below, resulting in the camera detecting white light as shown by the inset in Fig. 8.2(a). The LEDs in the array each emit ~ 20 lm and draw 60 mA at 3V. Additionally, they are housed in a 3-D printed plastic case which blocks out the ambient light, preventing any light in the surrounding environment from affecting the acquired image. As the compression is increased (Fig. 8.2(b)), the pores become smaller and partially close, allowing a portion of the light to transmit through to the green layer, resulting in the detection of green light on the CMOS sensor. When the compression is increased further, as shown in Fig. 8.2(c), the level of green light detected by the CMOS sensor increases. Characterisation of the relationship between the light transmission and the stress of the micro-porous layer is presented in the next Section.

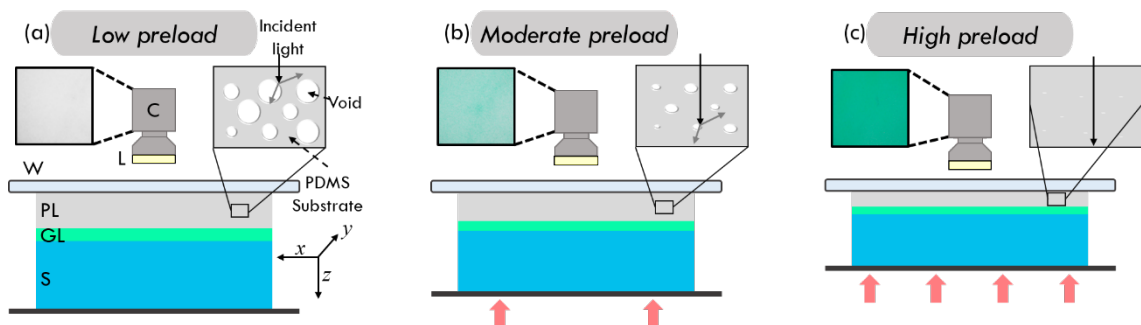


Figure 8.2: Working principle of CBOP. A CMOS camera is used to measure the transmission of light emitted by LEDs through the micro-porous layer and reflected back from the green layer under (a) low preloaded strain, (b) moderate preloaded strain and (c) high preloaded strain; C: camera, L: LEDs, W: glass window, PL: micro-porous layer, GL: green layer, S: sample. The insets from the camera show the change in green intensity with different preloaded strains. The micro-porous layer inset illustrates the reduction in pore size under increasing compression.

Optical transmission through the micro-porous layer

Light travelling through the micro-porous layer undergoes refraction, due to the difference in refractive indices, n , between the silicone matrix ($n = 1.4$) and the pores ($n = 1.0$) [481]. This refraction causes light to scatter multiple times in the layer, reducing optical transmission. Optical transmission of light T , in the micro-porous layer is proportional to the distance a photon will travel before its direction is randomised after scattering by a pore, termed the transport mean free path l_{mfp} , and the reciprocal of the total thickness of the material, L , assuming negligible absorption [517]. Mie scattering theory describes scattering interactions where the pore size is comparable to or greater than the wavelength of light. It suggests that the transport mean free path is inversely proportional to both the number of pores in a given volume, termed, the pore concentration, φ , and the pore scattering cross-section [518,519], defined as the effective area proportional to the probability of an incoming photon interacting with the pore. Provided the pore is non-absorbing and much larger than the wavelength of the incident light, the scattering cross-section is linearly proportional to the pore cross-sectional area, A [520,521]. The micro-porous layers used in CBOP satisfy the material thickness and pore size conditions of Mie scattering theory, and therefore, the optical transmission can be approximated as inversely proportional to the thickness, pore concentration and pore cross-sectional area.

$$T \propto \frac{1}{L\varphi A} \quad (8.1)$$

The above relationship describes the transmission of light through the micro-porous layer under static conditions. However, in CBOP, the optical transmission is dependent on the applied strain. Increasing compressive loading on the micro-porous layer not only reduces the thickness of the material [522], but also causes the internal pores to collapse as the silicone matrix expands into the voids [523], reducing the total pore concentration of the layer, in addition to reducing the geometrical cross-section of the pores. This is a result of the near incompressibility of silicone, which has a Poisson's Ratio close to 0.5 [524,525]. These changes to the pore structure, coupled with the reduction in material thickness, increase the transport mean free path, allowing more light to pass through the micro-porous layer. While compression also reduces the intrinsic backscattering of light from the pores, it affects all colour channels evenly and therefore has negligible impact on colour saturation. As a result, optical transmission can be directly related to the compression applied to the micro-porous layer, as shown in Fig. 8.3(a).

Post-processing

Post-processing of the acquired camera images is performed using MATLAB 2016B (MathWorks, Massachusetts, USA). Averaging of the ten acquired images at each preloaded strain is performed first, generating a 2-D pixel matrix with the average RGB values recorded at each pixel location as shown in Fig. 8.3(d). Colour saturation is then used as a measure of optical transmission, as the micro-porous layer appears white (low saturation) at low preloaded strain and green (high saturation), at high preloaded strain. A 2-D saturation image is generated by measuring the saturation, S , from the RGB values at each pixel location using the following equation:

$$S = \frac{\alpha(C_{max} - C_{min_1}) + (C_{max} - C_{min_2})}{\alpha C_{max} + C_{max}}, \quad (8.2)$$

where S is the saturation value at each pixel. C_{max} , C_{min_1} and C_{min_2} are the highest, lowest and second lowest of the RGB values at each pixel location, normalised between 0 and 1, and α is a user-defined coefficient used to optimise the contrast in the saturation image. This formula is a variation of the conventional colour saturation formula [526] and was used to extend the stress dynamic range by considering RGB values from all three colour channels. In our experimental setup, optimised contrast is achieved with $\alpha = 1.5$, as it provides a sufficiently large stress dynamic range (0-94 kPa), whilst providing minimal trade-off in sensitivity. Figure 8.3 shows the procedure for converting the averaged digital photograph (Fig. 8.3(d)) to the saturation image (Fig. 8.3(e)), then transforming the saturation image into an optical palpogram (Fig. 8.3(f)) for a silicone phantom with an embedded inclusion. First the colour saturation-strain curve of the micro-porous layer is characterised using the CMOS camera (Fig. 8.3(a)). Then, the stress-strain curve of the micro-porous layer is characterised using a uniaxial compression testing system (Fig. 8.3(b)). This system uses a motorised translation stage to increment the strain applied to a sample at a rate of 0.001/s. The strain is determined by measuring the initial thickness of the sample and the displacement of the stage. A load cell measures the applied force at a particular strain, which, along with prior knowledge of the geometric cross-section of the sample allows stress to be estimated. By dividing stress by strain, the elasticity can be estimated. By combining these two curves, we can generate a characteristic stress-saturation curve of the micro-porous layer, as shown in Fig. 8.3(c).

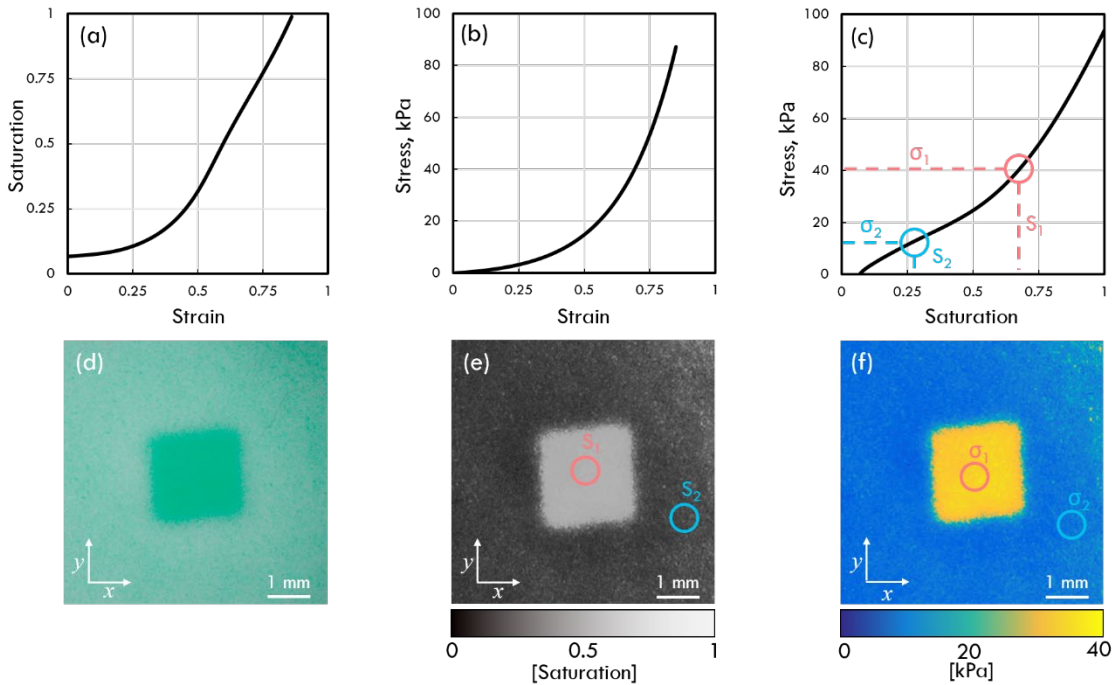


Figure 8.3: Layer characterisation and generation of optical palpograms. (a) The saturation-strain characterisation curve, (b) the stress-strain characterisation curve of the micro-porous silicone layer and (c) the resulting stress-saturation curve. (d) Digital photograph of micro-porous layer of phantom containing a 2.5×2.5 mm inclusion phantom at 50% preloaded strain, and (e) the corresponding colour saturation image where the red and blue circles represent the relative colour saturation through a region of the inclusion and base, respectively. (f) The optical palpogram is produced by equating each pixel in (e) to a stress value using the stress-strain curve in (c).

Layer characterisation and repeatability

The micro-porous layers are mechanically and optically characterised by connecting a load cell (LSB200, Futek Inc., California, USA) to the translation stage of the CBOP set-up. While compression is applied, the camera captures images of colour saturation as light is transmitted through the micro-porous layer and is reflected by the green layer, while the load cell records the resulting force, which along with prior knowledge of the layer surface area, is used to compute stress. To determine the repeatability of this procedure, characterisation is performed on five separate micro-porous layers. The resulting mechanical stress-strain curves demonstrate a mean standard deviation of 0.38 kPa across each of the measured preloaded strains. For the optical properties, the mean standard deviation in saturation values S is 0.03 across any given preloaded strain. This shows that there is a high level of repeatability in the fabrication process between individual layers.

Finite element modelling

In order to validate the stress values measured from CBOP and to simulate the mechanical response of the micro-porous layer, 2-D FEM is performed on each inclusion phantom using Abaqus (Dassault Systèmes, Vélizy-Villacoublay, France). The FEM simulation is designed to match the experimental conditions in CBOP, where a stiff inclusion is embedded $500 \mu\text{m}$

below the surface of a soft silicone phantom. Two additional layers are positioned above the phantom, representing the green layer (300 μm thick) and the micro-porous layer (900 μm thick). The boundary conditions are fixed at the bottom of the phantom and 50% compression is applied axially via the imaging window, which acts as a rigid plate. The friction coefficient between all interfaces is set to 0.2 to account for the PDMS oil applied to the sample in the experiment and the 50% preloaded strain. This value was determined previously by Wijesinghe *et al.* [488] by relating experimental results of OCT-based optical palpation to FEM simulations. 2-D plane stress elements (CPS3) are assigned to all the models, which generate a maximum mesh size of 0.1 mm. Each element of the soft base, and both the green and micro-porous layers are modelled using the Mooney-Rivlin material model for uniaxial compression which relates stress to strain through the coefficients C_{10} and C_{01} [527,528]:

$$\sigma = 2\left(C_{10} + \frac{C_{01}}{\lambda}\right)(\lambda - \lambda^{-2}), \quad (8.3)$$

where σ is the stress and $\lambda = 1 + \varepsilon$ and is defined as the stretch ratio. This model assumes that the materials are homogeneous, isotropic and non-linear. The Mooney-Rivlin coefficients for the soft silicone and green layer are given as $C_{10} = 2.23$ kPa and $C_{01} = 0.70$ kPa, respectively [488]. Similarly, the coefficients for the micro-porous layer are $C_{10} = 0.04$ kPa and $C_{01} = 1.10$ kPa. All coefficients are obtained by fitting Eq. (8.3) to the experimental stress-strain curves of each material which were generated through uniaxial compression testing. The relatively stiff inclusion, however, is modelled as an elastic material to increase the stability of the simulation. This is a valid assumption as the inclusion did not strain to more than 15% in each experiment and the stress-strain curve of the material is approximately linear in this range (elasticity of 160 kPa at 10% strain and Poisson's ratio of 0.45). Stress is computed from the simulated strain using the same steps as in the CBOP experiments. The 2-D FEM is then expanded to 3-D for comparative analysis to the *en face* optical palpograms obtained using CBOP, as shown in Results. *En face* FEM images are imported into MATLAB for analysis and editing [529].

OCT-based optical palpation

OCT-based optical palpation is performed to provide a comparison to CBOP. This is achieved using a spectral-domain OCT system with central wavelength of 1300 nm and spectral bandwidth of 170 nm (TEL320C1, Thorlabs, New Jersey, USA), in a common-path configuration [226]. An objective lens with a 0.055 numerical aperture (LSM03, Thorlabs, New Jersey, USA) is attached to the scan head which provides a measured full width at half maximum axial resolution of 5.5 μm (in air) and lateral resolution of 7.2 μm . A-scans are acquired at a rate of 71 kHz. The optical power on the sample was measured to be 2 mW. Prior to scanning, a 500 μm -thick homogeneous silicone compliant layer is placed on the

sample (Elastosil P7676, Wacker Chemie, Munich, Germany), which ensures that the deforming edge of the layer is within the focus of the OCT system. The sample is then placed on a motorised lab jack to provide axial compression against a fixed glass window, situated between the sample and the OCT scanner. Whilst under compression, the OCT system scans the sample and the axial displacement in the layer is detected at each spatial location, where the smallest detectable displacement in the layer is determined by the axial resolution of the OCT system ($5.5\ \mu\text{m}$) [225]. Stress can then be inferred from the measured OCT data and the pre-characterised stress-strain curve of the compliant layer.

Silicone phantom fabrication

Four tissue-mimicking silicone inclusion phantoms are used as test targets for both CBOP and OCT-based optical palpation. The phantoms are cylindrical with a diameter of 15 mm and a height of 2 mm. The soft base of the phantoms are fabricated from a two-part silicone elastomer (Elastosil P7676, Wacker Chemie, Munich, Germany) which has an elasticity of 20 kPa at 10% strain, using procedures described previously [481]. Four inclusions with sizes of $5 \times 5 \times 1\ \text{mm}$, $2.5 \times 2.5 \times 1\ \text{mm}$, $1 \times 1 \times 1\ \text{mm}$ and $0.5 \times 0.5 \times 1\ \text{mm}$ were fabricated from a silicone elastomer with an elasticity of 160 kPa at 10% strain (Elastosil RT601, Wacker Chemie, Munich, Germany) and embedded 500 μm below the surface of the phantom. The base and inclusions of each phantom contain 0.25 mg/ml and 2 mg/ml of TiO_2 powder, respectively, to provide optical contrast for OCT imaging.

Clinical protocol

Freshly excised human breast samples from two mastectomy surgeries were imaged in this study. After surgery, these samples were immediately transferred from the operating theatre to the pathology department at Fiona Stanley Hospital, Western Australia. A pathologist dissected the sample to extract a $\sim 3 \times 2 \times 1\ \text{cm}$ sample which was then imaged using CBOP. During imaging, the specimen was kept hydrated in saline.

Following imaging, the sample was bisected and placed into two cassettes and a pathologist applied ink to the edges of the specimen to mark the orientation. The sample was then fixed in 10% neutral-buffered formalin and embedded in paraffin following standard histopathological protocols. The paraffin block was sectioned in the same reference plane as optical palpograms and stained with haematoxylin and eosin. This study was approved by the Sir Charles Gairdner and Osborne Park Health Care Group Human Research Ethics Committee (HREC No: 2007-152) and the Fiona Stanley Hospital Research Governance Office (FSH-2015-032), and informed consent was obtained from the patients prior to surgery. All methods were performed in accordance with the relevant guidelines and

regulations, including following good clinical practices described at the International Conference on Harmonisation.

8.2.3 RESULTS

Inclusion phantoms

To validate our technique, we first tested it on the four structured silicone phantoms described in the last Section. During imaging, compression was increased in steps of 10%, causing incremental strain on the micro-porous layers, thus increasing the optical transmission and changing the colour saturation detected by the camera. As the inclusion is much stiffer than the surrounding base material, the strain in the micro-porous layer above the inclusion is larger than that above the base, creating contrast in colour saturation and, subsequently, in optical palpograms. Figure 8.4 shows the photographs and optical palpograms obtained using CBOP for each of the four inclusion phantoms, at 50% preloaded strain. The optical palpograms were obtained using the method described in the last Section, while the photographs were acquired without the micro-porous layer and the green layer.

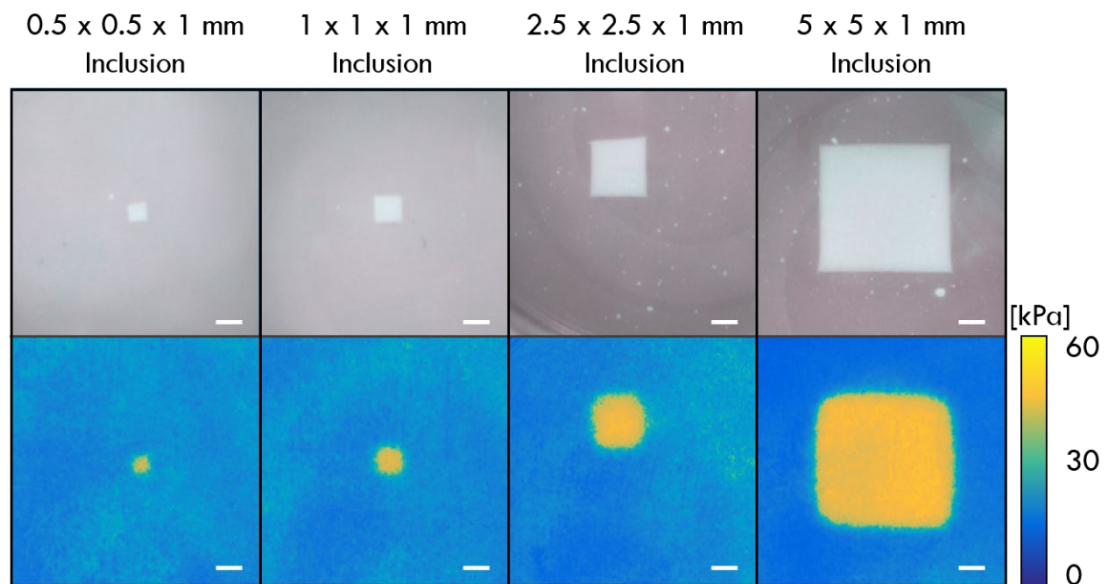


Figure 8.4: Photographs and optical palpograms acquired at 50% preloaded strain for four different-sized inclusion phantoms. Photographs are provided for validation purposes only to show the relative positions of the inclusions and were taken without the micro-porous layer. Scale bars: 1 mm.

In the optical palpograms, the inclusions are clearly distinguished from the base material due to the higher stress in these regions, and the inclusion sizes are comparable to the true values delineated in the photographs. The average stress measured above the four inclusions was 46.5 ± 1.9 kPa, compared to 12.9 ± 0.8 kPa for the soft base, demonstrating a high mechanical contrast between the two materials. Note that in Fig. 8.4 the corners of the inclusions in the optical palpograms are not as sharp as in the photographs, due to the non-

uniaxial stress distribution in the micro-porous layer at the regions above the inclusion corners.

To characterise the optical palpograms generated from CBOP, we compared the phantom results acquired using CBOP with those acquired using OCT-based optical palpation. In particular, we measured the contrast-to-noise ratio (CNR) and lateral resolution in the phantoms using both techniques. Similar to the definition described in previous work [530], we define CNR as:

$$CNR = \frac{|\mu_{inc} - \mu_{base}|}{\sqrt{\sigma_{inc}^2 + \sigma_{base}^2}}, \quad (8.4)$$

where μ_{inc} and μ_{base} are the mean stress values taken from the inclusion and base respectively, and σ_{inc} and σ_{base} are the corresponding standard deviations. These metrics were computed from $200 \times 200 \mu\text{m}$ regions taken at the centre of the inclusions and at the edge of the base material in the field-of-view. This measurement of CNR takes into account the noise over both the inclusion and base, which is essential when measuring materials with non-linear mechanical properties as the noise increases at higher strains. Optimal CNR for CBOP was measured at 50% preloaded strain, where it yielded comparable CNR to OCT-based optical palpation. An average CNR of 35.2 ± 6.5 was measured across the four inclusion phantoms for CBOP, compared to 33.0 ± 9.3 for OCT-based optical palpation. Importantly, this result demonstrates that using the much simpler optical imaging system in CBOP did not substantially degrade image contrast.

Figure 8.5 shows the optical palpograms taken at 50% preloaded strain for the $2.5 \times 2.5 \times 1 \text{ mm}$ inclusion phantom using CBOP (Fig. 8.5(a)), FEM (Fig. 8.5(b)) and OCT-based optical palpation (Fig. 8.5(c)). The lateral resolution of each technique was determined by measuring the step-response in stress measurements across the boundary between the inclusion and base, represented in Figs. 8.5(d)–(f) by the red (CBOP), blue (FEM) and yellow (OCT-based optical palpation) dots. An error function, represented by the black lines in Figs. 8.5(d)–(f), was fitted to the stress measurements and the lateral resolution was defined as the 10–90% rise-distance of the error function. This procedure has previously been used to measure lateral resolution in both OCT [531] and OCE [532]. The lateral resolution was measured at five different locations in each inclusion phantom and averaged to a mean value, as shown in Fig. 8.5(g), where each error bar represents one standard deviation of the five measurements. CBOP demonstrated a lateral resolution of $290 \mu\text{m}$ for the smallest inclusion phantom, which increases with increasing inclusion size as shown in Fig. 8.5(g). This trend of increasing lateral resolution along with increasing inclusion size is consistent with previous work in OCE [532]. The lateral resolution measured from FEM follows the same trend as the experimentally obtained results, albeit generally exhibiting a higher resolution. The lateral

resolution calculated from FEM of the four inclusion phantoms is 430 μm , 390 μm , 340 μm and 240 μm in order of descending feature size with an average R^2 value of 0.994. In Figs. 8.5(a) and (b), the stress values of the base and inclusion measured from the experiment of CBOP correspond to 82.8% and 77.9%, respectively, of that measured in FEM. The differences between the lateral resolution measured in experiment and simulation are likely caused by the different friction conditions. In the experiment, the lubricant PDMS oil was likely squeezed out due to the compression, increasing the friction coefficient, while in the simulation, the friction coefficient was set as a constant, resulting in more lateral expansion and higher strain in the FEM which corresponds to higher stress values. To more accurately estimate the friction coefficient in the FEM, a more thorough measurement is required to characterise the change of friction coefficient in the experiment.

The OCT-based optical palpation measurements provide a baseline for CBOP results to be compared against. As illustrated in Fig. 8.5(g), the measured lateral resolution from OCT-based optical palpation is 280 μm for the smallest inclusion, similar to that measured using CBOP. In both methods, the lateral resolution degrades as the inclusion size increases, until reaching a limit. This trend has been reported previously [532] and is attributed to the restriction on lateral deformation of the base, imposed by the friction between the imaging window and stress layer. As inclusion size increases, the lateral deformation of the base situated between the inclusion and imaging window becomes increasingly restricted, resulting in a flattened strain gradient across the boundary between the inclusion and base thus degrading the lateral resolution. Above a certain inclusion size, the effect of the friction on the strain gradient across the boundary is unchanged, resulting in a limit on the lateral resolution. From Fig. 8.5(g), it is observed that the lateral resolution in OCT-based optical palpation reaches this limit before that of CBOP as friction is more pronounced in thinner layers [533] (the layers used in OCT-based palpation were 500 μm thick compared to 1.2 mm thick layers used in CBOP). In addition, CBOP generally has a lower resolution than OCT-based optical palpation, as the combined thickness of the green layer and the micro-porous layer effectively increase the depth of the inclusion. This effect of degraded resolution while imaging features at a greater depth has previously been reported for OCT-based optical palpation techniques, where optical palpation in general is able to detect mechanical contrast at a depth of 4-5 mm, provided sufficient compression has been applied to deform the sample above these features [225]. Beyond this depth, the assumption of uniaxial stress begins to fail and the stress distribution is no longer localised, making it challenging to generate optical palpograms of the sample features.

Note that the inclusion size in Fig. 8.5(c) appears larger than that in Figs. 8.5(a) and (b), due to more lateral expansion of the inclusion in Fig. 8.5(c). In the experiment, CBOP used

a softer micro-porous layer, where much of the applied strain occurred in the layer, while OCT-based optical palpation used a thinner and stiffer stress layer, made from the same material as the base, resulting in the sample experiencing a higher strain for the same applied preloaded strain. The difference between the sample strains in the two methods is indicated by the higher stress values in Fig. 8.5(c) than those in Figs. 8.5(a) and (b).

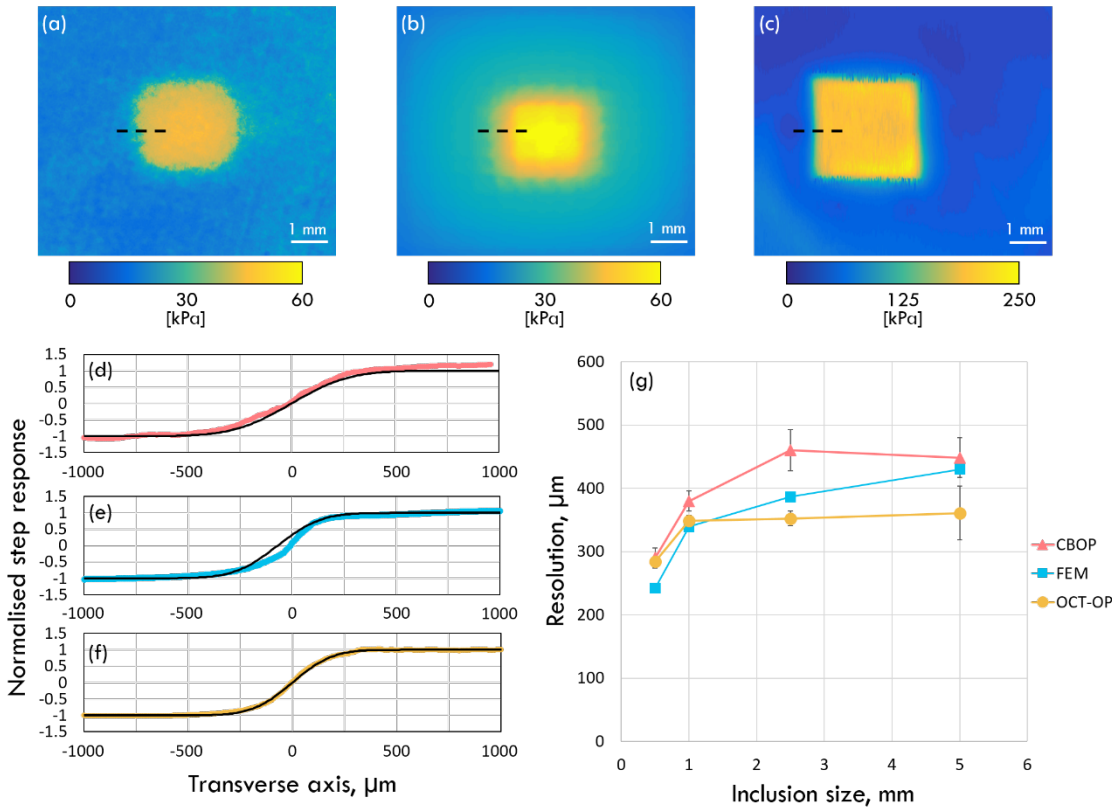


Figure 8.5: Analysis of the lateral resolutions of CBOP and OCT-based optical palpation. Optical palpograms acquired using (a) CBOP at 50% bulk preloaded strain, (b) FEM of CBOP and (c) OCT-based optical palpation at 50% bulk preloaded strain on a $2.5 \times 2.5 \times 1$ mm inclusion embedded within a soft phantom. The normalised step response (coloured points) and error function (black line) of (d) CBOP, (e) FEM and (f) OCT-based optical palpation are taken across the boundary of the same inclusion phantom. (g) The lateral resolution measured using CBOP, OCT-based optical palpation and FEA, across five locations on each inclusion phantom with error bars representing one standard deviation.

Ex vivo human mastectomy samples

To validate the performance of CBOP on human tissue, we imaged freshly excised sections of human breast tissue comprising of tumour and adipose tissue, from mastectomy specimens obtained from patients at Fiona Stanley Hospital, Western Australia. In Fig. 8.6, we compare the photograph, the histology image and the optical palpogram acquired from CBOP in Fig. 8.6. With the aid of expert advice from the pathologists involved in the study, labelling of features in the histology images provided a means to validate contrast obtained in the co-registered optical palpograms.

The first scan was acquired on a specimen from a 59-year-old patient. As shown in Fig. 8.6(a), a photograph of the tissue specimen was acquired after performing CBOP on the same tissue location. The corresponding histology image is presented in Fig. 8.6(b) which

was acquired at a depth of $\sim 100\ \mu\text{m}$ below the tissue surface and is marked with a black circle to denote the CBOP scanning area. Pathologists identified the presence of invasive ductal carcinoma (IDC), fibrous tissue (F) and adipose tissue (A) in the histology image, and these regions have been annotated accordingly on Figs. 8.6(a)–(c). The optical palpogram, shown in Fig. 8.6(c), was acquired at 30% preloaded strain and exhibits a region of elevated stress at the centre of the image, corresponding to invasive ductal carcinoma (IDC) from the histology image. This suggests that IDC is stiffer than surrounding benign tissues, which is consistent with previous results acquired using QME [105,106,303]. Similarly, regions of moderate and low stress match up well with fibrous tissue and adipose tissue detected in the histology image. It is worth highlighting here that while the regions in the histology image correspond with those in the optical palpograms, the imaged area is slightly increased due to the lateral expansion of the tissue under compression during CBOP, when compared to the histology image. Note that there is a region of lower stress in Fig. 8.6(c), marked by a black arrow, which appears to be either fibrous tissue or adipose tissue, however, this is likely to be an artefact caused by variation in the sample thickness, leading to an underestimation of stress. The same region is highlighted by a black arrow in histology Fig. 8.6(b) where IDC was not annotated due to the variation in sample thickness.

The second specimen, taken from a 69-year-old patient, is presented in Figs. 8.6(d)–(f). Figure 8.6(d) shows a photograph acquired after performing CBOP and Fig. 8.6(e) is the histology image of the specimen acquired at $\sim 100\ \mu\text{m}$ below the tissue surface, with a black circle highlighting the same region of the field-of-view of CBOP and photograph. Fig. 8.6(f) is the optical palpogram of the specimen acquired using CBOP. Due to different tissue geometries and mechanical properties, the optimal preloaded strain can vary between samples. For this specimen, CBOP was performed at 60% preloaded strain, which ensures high contrast between the different tissue types present. Postoperative histology of the specimen (Fig. 8.6(e)) revealed the presence of invasive lobular carcinoma (ILC), fibrous tissue (F) and adipose tissue (A). Once again, annotation was performed by a pathologist and the regions of ILC in the histology image correspond well with the regions of elevated stress in the optical palpogram (Fig. 8.6(f)), which is consistent with previous studies of the mechanical properties of ILC [105,534]. In Fig. 8.6(f), an arrow denotes an imaging artefact at the top of the optical palpogram that appears as a region of high stress. This artefact was produced when a portion of the green layer was imaged without the micro-porous layer covering it, giving the appearance of high stress.

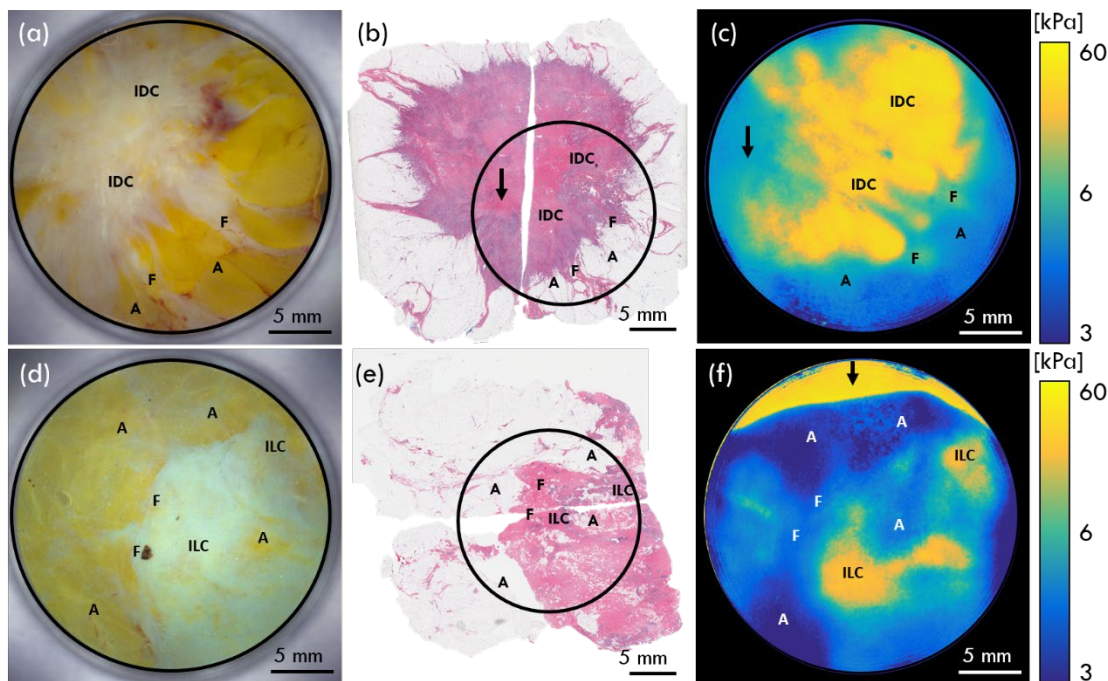


Figure 8.6: CBOP performed on two freshly excised mastectomy specimens containing (a)-(c) IDC and (d)-(f) ILC. (a) Photograph, (b) histology and (c) optical palpogram at 30% preloaded strain. (d) Photograph (e) histology image and (f) optical palpogram at 60% preloaded strain. The images have been annotated to show regions of invasive ductal carcinoma (IDC), invasive lobular carcinoma (ILC), fibrous tissue (F) and adipose tissue (A) and black circles on the histology images mark the approximate region where CBOP was taken relative to the whole specimen. The arrows in (b), (c) and (f) indicate regions of imaging artefacts. Optical palpograms have been displayed on a logarithmic scale to enhance mechanical contrast between tissue types.

8.2.4 DISCUSSION

In this paper, we demonstrate CBOP, a new optical elastography platform, capable of generating 2-D maps of surface stress by using a digital camera and a micro-porous silicone layer. A previous digital-camera-based technique has been proposed in optical elastography by directly imaging the tissue as it is subjected to a tensile loading [535]. Whilst this approach can generate mechanical contrast in tissue, it has the limitation that it relies on visualising tissue features to map deformation. As such, in tissue regions where the contrast is low in the optical image, elastography measurements are not possible. In addition, in many cases, tensile loading is either not easily implemented or undesirable. Our approach with CBOP overcomes these issues by generating contrast from light transmitted through the micro-porous layer and this method is independent of the visual contrast of the tissue. CBOP represents a simple and easy-to-use approach to optical elastography, making it more accessible to a broader range of applications. Furthermore, as the data is acquired from several digital photographs, it greatly simplifies the data processing, readily providing high-speed imaging, which is vital in time-sensitive clinical applications.

In CBOP, we often compress the sample and layers to $\sim 50\%$ preloaded strain to optimise CNR. The issue with this is that the compressive force required to achieve such a high strain

results in the lubricant PDMS oil being forced out, leading to an increase in friction [536] and a degradation in lateral resolution, as described in Results. This issue can be resolved by using a softer material for the substrate of the micro-porous layer, which allows optical palpograms to be acquired at lower preloaded strains. With this approach, we can minimise the effect of friction, thus improving the lateral resolution.

An advantage of CBOP, in common with optical palpation in general, is that the layer complies to the tissue surface to provide a relatively uniform stress distribution at the tissue surface. However, when tissue samples exhibit large variation in surface topography, the layer is not able to fully comply with the sample [458]. While this issue is present in all optical palpation techniques, it is more evident in CBOP than in the OCT-based technique as the micro-porous layer is compressible, meaning it exhibits a lower Poisson's ratio, and is therefore, less likely to conform to the tissue surface. This may lead to non-uniform contact and can lower the contrast between tumour and benign tissue, as seen in Fig. 8.6(c). To achieve more even contact with the tissue sample, the micro-porous layer needs to be thick enough to conform to the surface of the tissue, with some compromise in lateral resolution. Alternatively, uniform contact could be achieved by reducing the elasticity of the homogeneous green layer, allowing it to better conform to the topography of the tissue. In future studies, this improvement may increase the accuracy of CBOP in identifying malignant and benign tissues.

Here we have used CBOP to image breast tissue, a heterogeneous tissue which displays nonlinear mechanical properties. Due to this nonlinearity, the different local strain experienced by the sample during CBOP will have a strong effect on the apparent stiffness of the individual tissue constituents, potentially reducing the contrast between soft adipose tissue and stiff tumour. One solution proposed for use in OCE synthesises a map of stiffness by reassembling A-scans taken from a series of OCE images under increasing load, such that the stress in the layer is uniform over the entire B-scan [458]. Implementation of this type of standardisation in CBOP, however, may prove challenging as CBOP is only able to visualise the strain in the layer rather than the strain in the sample. As CBOP is a qualitative technique, the absolute value of elasticity is less relevant, provided that regions of high stress reliably identifies tumour. Whilst there is scope to explore this further, a previous study using OCT-based optical palpation on 34 freshly excised human breast tissue samples indicates that the effect of nonlinearity is not large enough to obscure the ability to localise tumour [226].

The drawback of CBOP is that it can only generate 2-D optical palpograms, which are qualitative measurements of tissue mechanical properties. In clinical applications, such as tumour margin assessment, detailed knowledge of not only the stress, but also elasticity, which is a quantitative measurement of the mechanical properties of tissue, will likely be

required to remove subjectivity and variability between measurements. In addition, the information of the depth of certain features is critical in guiding clinicians to suspicious regions of tissue. To provide 3-D quantitative measurements of mechanical properties, inverse methods can be used, as has been proposed in tactile imaging applications [537–539], to generate 3-D elastography with higher resolution and accuracy.

To date, optical palpation has been developed primarily for clinical applications, typically suited to advanced healthcare systems, owing to the high cost of OCT. A benefit of CBOP is that it offers a cost-effective implementation of optical palpation, which can broaden the applications of optical palpation, particularly in remote and low-resource settings. For example, CBOP may aid in assessment of the cavity wall following a wide local excision in breast cancer surgery, where other intraoperative techniques would prove too costly for low-resource healthcare [540,541]. In addition, CBOP may be suitable for remote applications beyond medicine, such as agriculture, where the bulk stiffness of plant leaves is an indicator of plant health [542].

In this proof-of-principle study, CBOP was performed using a benchtop design, with a high-resolution CMOS camera to ensure high quality optical palpograms. In future work, this technique can be implemented using more cost-effective CCD/CMOS cameras. As CBOP consists of only a digital camera and the accompanying layers, it can be readily incorporated in a smartphone, with a broad range of potential applications, *e.g.* the detection of malignant skin lesions [543,544]. While there is already a great deal of research into the use of smartphones in diagnostic applications, augmenting these techniques with elastography holds potential for increasing diagnostic accuracy. In addition, the benchtop scanning system is restricted to *ex vivo* studies, whilst development of a small form-factor probe would permit scanning of *in vivo* tissue intraoperatively, *e.g.* the assessment and localisation of hepatic tumours, which present as stiff lesions, during liver surgery [534]. Furthermore, the use of a digital camera allows for the design of a wireless probe, which is preferable in a robust clinical setting due to the dexterity and freedom of motion it offers.

8.2.5 CONCLUSION

In this paper, we have presented CBOP, a cost-effective optical elastography platform capable of mapping stress at the tissue surface. CBOP has demonstrated a resolution of 290 μm and a CNR of 35.2, similar to values obtained with OCT-based optical palpation. In addition, we have demonstrated that CBOP can detect the mechanical contrast between invasive tumour and benign tissue in excised human breast specimens. This technique can be readily developed into a small form factor handheld probe due to the use of a simple digital camera, enhancing the potential for clinical translation.

Acknowledgements

The authors acknowledge the facilities and scientific and technical assistance of the Australian Microscopy & Microanalysis Research Facility at the Centre for Microscopy, Characterisation & Analysis, the University of Western Australia, a facility funded by the University, State and Commonwealth Governments. This work was supported by research grants from the Australian Research Council, the Department of Health, Western Australia and the Cancer Council, Western Australia; a research contract with OncoRes Medical; the Herta Massarik PhD Scholarship for Breast Cancer Research; and the War Widows Guild of Western Australia Top-up Scholarship for Research into Breast Cancer.

CHAPTER 9

SMARTPHONE-BASED OPTICAL PALPATION

9.1 PREFACE

In Chapter 8, a novel optical elastography technique termed camera-based optical palpation (CBOP) was presented. This initial demonstration was performed on freshly excised breast tissue specimens which is an area of particular interest for a number of different optical elastography methods, however, the base technology and principles of CBOP make it suitable for use in a broad variety of applications that were previously out of reach of OCT-based elastography approaches.

The research undertaken in this Chapter adapts CBOP to a commercially available smartphone for portable and convenient optical elastography of pathological burn scars. As discussed in Chapter 2, a reliable and repeatable measurement of burn scar stiffness would provide specialists with valuable information as to the pathology of the scar and whether prescribed therapies are effective. Most current methods for burn scar stiffness evaluation are, however, qualitative and vary greatly between assessors with different experience levels. This issue is exacerbated in remote communities as local clinics rarely have personnel with expertise in treating burns.

In this Chapter, smartphone-based optical palpation (SBOP) is developed towards the characterisation of pathological burn scar stiffness in a format amenable for use in a telehealth environment. Validation of this technique is performed on silicone inclusion phantoms where mechanical contrast was clearly defined and the effect of hand-motion on the image quality was evaluated, before being demonstrated on two pathological burn scars. This work represents a proof-of-principle of SBOP in a compact and handheld design and demonstrates that elastography can be implemented at low cost, which may enable its adoption in other clinical applications. This Chapter consists of a first-author publication, Rowan W. Sanderson, Qi Fang, Andrea Curatolo, Aiden Taba, Helen M. DeJong, Fiona M. Wood, and Brendan F. Kennedy. “*Smartphone-based optical palpation: towards elastography of skin for telehealth applications,*” *Biomedical Optics Express*, 12(6): p. 3117-3132, 2021.

9.2 SMARTPHONE-BASED OPTICAL PALPATION: TOWARDS ELASTOGRAPHY OF SKIN FOR TELEHEALTH APPLICATIONS

Rowan W. Sanderson^{1,2}, Qi Fang^{1,2}, Andrea Curatolo^{2,3}, Aiden Taba^{1,2}, Helen M. DeJong^{1,4,5}, Fiona M. Wood^{5,6,7}, and Brendan F. Kennedy^{1,2,8}

Biomedical Optics Express, 12(6): p. 3117-3132, 2021.

Abstract: Smartphones are now integral to many telehealth services that provide remote patients with an improved diagnostic standard of care. The ongoing management of burn wounds and scars is one area in which telehealth has been adopted, using video and photography to assess the repair process over time. However, a current limitation is the inability to evaluate scar stiffness objectively and repeatedly: an essential measurement for classifying the degree of inflammation and fibrosis. Optical elastography detects mechanical contrast on a micrometre- to millimetre-scale, however, typically requires expensive optics and bulky imaging systems, making it prohibitive for wide-spread adoption in telehealth. More recently, a new variant of optical elastography, camera-based optical palpation, has demonstrated the capability to perform elastography at low cost using a standard digital camera. In this paper, we propose smartphone-based optical palpation, adapting camera-based optical palpation by utilising a commercially available smartphone camera to provide sub-millimetre resolution imaging of mechanical contrast in scar tissue in a form factor that is amenable to telehealth. We first validate this technique on a silicone phantom containing a $5 \times 5 \times 1 \text{ mm}^3$ embedded inclusion, demonstrating comparative image quality between mounted and handheld implementations. We then demonstrate preliminary *in vivo* smartphone-based optical palpation by imaging a region of healthy skin and two scars on a burns patient, showing clear mechanical contrast between regions of scar tissue and

¹ BRITelab, Harry Perkins Institute of Medical Research, QEII Medical Centre, Nedlands and Centre for Medical Research, The University of Western Australia, Perth, Western Australia, 6009, Australia

² Department of Electrical, Electronic & Computer Engineering, School of Engineering, The University of Western Australia, Crawley, Western Australia, 6009, Australia

³ Currently with International Centre for Translational Eye Research, Skierniewicka 10A, 01-230 Warsaw, Poland and Institute of Physical Chemistry, Polish Academy of Sciences, ul. Kasprzaka 44/52, 01-224 Warsaw, Poland

⁴ Perth Scar and Pain Clinic, Mt Pleasant, Western Australia 6160, Australia

⁵ Fiona Wood Foundation, Fiona Stanley Hospital, Murdoch, Western Australia 6150, Australia

⁶ Burn Injury Research Unit, University of Western Australia, Crawley, Western Australia 6009, Australia

⁷ Burn Service of Western Australia, Fiona Stanley Hospital, Murdoch, Western Australia 6150, Australia

⁸ Australian Research Council Centre for Personalised Therapeutics Technologies, Australia

healthy tissue. This study represents the first implementation of elastography on a smartphone device, extending potential application of elastography to telehealth.

© 2021 Optical Society of America under the terms of the OSA Open Access Publishing Agreement

9.2.1 INTRODUCTION

Burn injuries affect approximately 9 million people globally per year and result in over 100,000 deaths [545]. Persistent inflammation and increased mechanical strain on a healing wound leads to the formation of pathological scars, characterised by a palpable increase in scar stiffness and thickness [3,546]. In this process, excessive collagen is deposited (fibrosis) during the healing process, leading to permanent changes in skin structure and extensibility, which is associated with persistent pain and reduced quality of life [547–549]. The optimal treatment method for burn scars includes face-to-face assessment by a clinical expert. Assessments are typically performed several weeks apart in the first two years following an injury, and the burn is monitored over the patient's lifetime, depending on the severity of the scarring. This is a costly, inconvenient and distressing process for patients living in rural and remote communities due to lengthy travel times and time spent away from home. In the USA, 75% of all residents live more than one hour's drive from their nearest verified burns clinic, with coverage lowest in southern states [550]. In Australia, all 15 burns units are located in capital cities [551], despite one-third of the population living outside of these regions. As similar scenarios exist in many countries, telehealth services have been developed globally so that patients can be managed within their local community under the guidance of specialists [552]. Current telehealth services are typically performed over video, aided by a local healthcare practitioner who assists the patient and assesses scar stiffness and texture via manual palpation, relaying this information to a remote specialist [552]. Palpation is an important aspect of burn scar assessment, as the scar mechanical properties indicate the severity of scarring which is critical for prescribing treatments [553,554].

Currently, the most prominent clinical burn scar assessments are the Vancouver Scar Scale and the Patient and Observer Scar Assessment Scale (POSAS), the latter of which rates scars on a scale from 1-10 on several visual and palpable variables as well as pain and itch, where 1 indicates normal skin and 10 indicates severe scarring [553,140]. Despite being widely used, these scales are subjective, thus ratings can vary greatly between assessors with different levels of experience [555,556]. This presents a limitation for telehealth as the local practitioners who assist with assessments often lack the experience and expertise of burns specialists from dedicated clinics, leading to ambiguous measurements. A number of objective burn scar assessment methods have been developed to characterise scar

appearance [557,558], evaluate scar geometry [559], measure blood flow [560] and measure mechanical properties [561]. While these objective measurement tools may potentially enable non-specialists to assess scars in remote settings, they are typically expensive, bulky and impractical to use, and as such are not feasible for many telehealth environments. Therefore, a method to characterise inflammatory biomarkers, objectively, for telehealth may help to identify early signs of pathological healing allowing timely interventions such as laser therapy [562] or massage therapy [134] to be implemented to minimise inflammation, maximise healing and reduce the degree of scar tissue formed.

Optical elastography is a family of techniques that utilise optical imaging to map the mechanical properties of tissue [155,441]. This approach has the potential to quantify burn scar inflammation and fibrosis due to the combination of relatively high spatial resolution and high sensitivity to subtle changes in mechanical properties. While much of the focus of optical elastography has been in oncology [441,442,563] and ophthalmology [208,414,415,564], it has also been applied to imaging of the mechanical properties of skin [234,305,506,565–567]. One such technique is optical palpation, where a pre-characterised compliant silicone layer is placed on the surface of the skin and compressed under an external load [225]. The deformation of the compliant layer is detected using optical coherence tomography (OCT) allowing for the measurement of layer strain. The stress in the sample is then determined from the measured layer strain through knowledge of the mechanical characterisation curve of the silicone layer, enabling the generation of a two-dimensional (2-D) stress map, termed an optical palpogram, indicating the relative stiffness of features in the tissue. This technique provides a spatial resolution of $\sim 200\ \mu\text{m}$ and has demonstrated strong mechanical contrast between skin lesions, scars and surrounding normal skin [225,234]. Despite these promising results, OCT-based optical palpation has similar limitations to existing scar evaluation methods, as it requires a relatively costly and bulky imaging system which would preclude its use in many telehealth applications. More recently, an optical palpation technique that utilises a digital camera rather than an OCT system has been proposed. This technique, known as camera-based optical palpation (CBOP), detects the light transmitted through a porous silicone layer under compression. Of key importance, as compression increases, the pore size decreases and, therefore, refractive index differences between silicone and pores within the layer reduce, allowing more light to be transmitted through the layer. By pre-characterising the relationship between the layer stress and optical transmission, digital photographs can be converted to optical palpograms. It has previously been demonstrated that CBOP can identify the boundaries between healthy adipose tissue, fibrous tissue and tumour in freshly excised human breast tissue specimens [227]. CBOP is potentially well-suited to burn scar assessment in telehealth

scenarios, as it can be implemented using lightweight and cost-effective hardware components.

In this paper, we present the first demonstration of optical elastography on a smartphone by adapting CBOP to a Google Pixel 3 smartphone. This technique, termed smartphone-based optical palpation (SBOP), has the potential to aid in the assessment and diagnosis of burn scars by probing mechanical contrast in scars and represents a step towards developing optical elastography for telehealth applications. Here, we describe the components of SBOP and outline the imaging procedure. We then validate the accuracy of SBOP by imaging a $5 \times 5 \times 1 \text{ mm}^3$ inclusion embedded in a silicone phantom and compare the image quality between both mounted and handheld systems. Finally, we present preliminary *in vivo* SBOP results from a healthy region of skin and two burn scars and, in each case, co-locate the stress in the optical palpograms to corresponding photographs of the skin.

9.2.2 MATERIALS AND METHODS

Smartphone-based optical palpation setup

SBOP can readily be implemented using any smartphone model with a back-facing camera. In our SBOP setup, we utilised a Google Pixel 3 containing a 12.2 megapixel (MP) in-built back-facing camera to acquire photographs of the optical transmission through the porous layer. This camera has a 1/2.55" dual-pixel sensor (Exmor IMX363 RS, Sony Corporation, Japan) and an in-built f/1.8 lens. To optimise the camera for burn scar applications, we increased its magnification by attaching a 10x magnification external macro lens (Moment Inc., USA) which has a 25 mm focal length and a working distance of 18.5 mm. The pixel size at the focus in the specimen (object) plane is $7.9 \times 7.9 \mu\text{m}$ which provides high-resolution imaging of the porous layer compression over a maximum field of view of $32 \times 24 \text{ mm}^2$. The smartphone is housed in a three-dimensional (3-D) printed plastic case to which the macro lens is attached through a twist-and-lock mechanism, as shown in the schematic in Fig. 9.1(a). A glass window housed in a 3-D printed mount is in turn attached to the case over the lens so that the external face of the window is positioned at the focus of the camera. This window is used to apply compression to the sample. All parts are designed using SolidWorks 2019 (Dassault Systèmes, France) and 3-D printed using a Form 2 stereolithography printer (Formlabs, USA). A custom built 30 mm diameter light-emitting diode (LED) ring provides white light illumination to the sample through eight equally-spaced 0603 surface mount diode LEDs (Inolux Corporation, USA) which are fixed within the mount and powered by a USB-C connection to the smartphone. The undiffused LEDs create bright back-reflections at the edges of the glass window which produce imaging artifacts in the optical palpograms. To remove the effect of these artifacts, optical palpograms

are generated over a smaller $14 \times 14 \text{ mm}^2$ field of view. Photographs of the assembled system are shown in Fig. 9.1 (b) and (c).

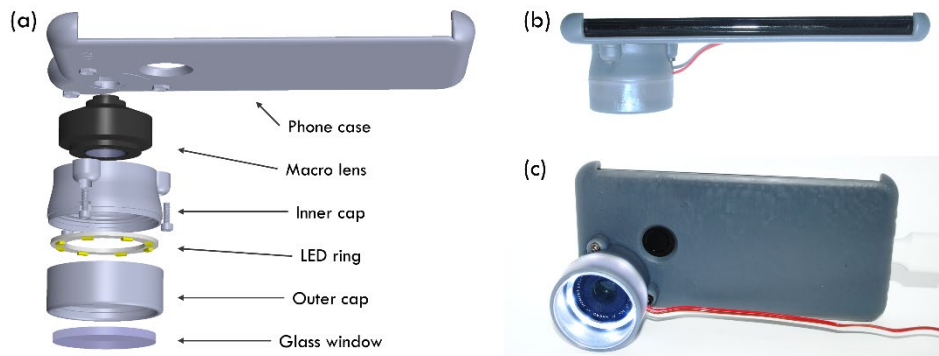


Figure 9.1: Diagram of the SBOP system. (a) An exploded diagram of the SBOP system showing the phone case, macro lens, inner cap and outer cap, LED ring and glass window. Photographs of the assembled SBOP system taken from (b) side-on and (c) front-on.

To generate optical palpograms, we place both a porous silicone layer and a green-dyed homogeneous silicone layer between the sample surface and the glass window (Fig. 9.2). In an uncompressed state, refractive index differences between the silicone and pores result in most of the white-light provided by the LEDs being reflected. In this case, the image of the layer captured by the camera is predominantly white. As compression increases, the pores collapse, reducing in both size and number. In addition, the total thickness of the layer reduces. These effects cause less light scattering from the pores, and in turn, more light to transmit through the layer and reach the green layer below where mostly green light is reflected, resulting in an image with a more intense green colour [227]. This is illustrated in the inset of Fig. 9.2. For a heterogeneous sample, stiffer features will cause the layer to compress more than softer features, producing differences in the optical transmission of the captured images. The relationship between optical transmission and mechanical stress is established prior to imaging using a uniaxial compression test of the porous layers. This characterisation curve is used to convert the acquired digital photographs into 2-D *en face* optical palpograms. Images are acquired using Open Camera (Open Camera, Mark Harman), an open-source camera application for Android devices. Open Camera allows for adjustments to be made to the white balance, ISO and shutter speed to enhance the contrast in transmission based on the illumination from the LEDs. A burst of three photographs are acquired per location at 60 frames per second, which are averaged together to remove the effect of camera noise.

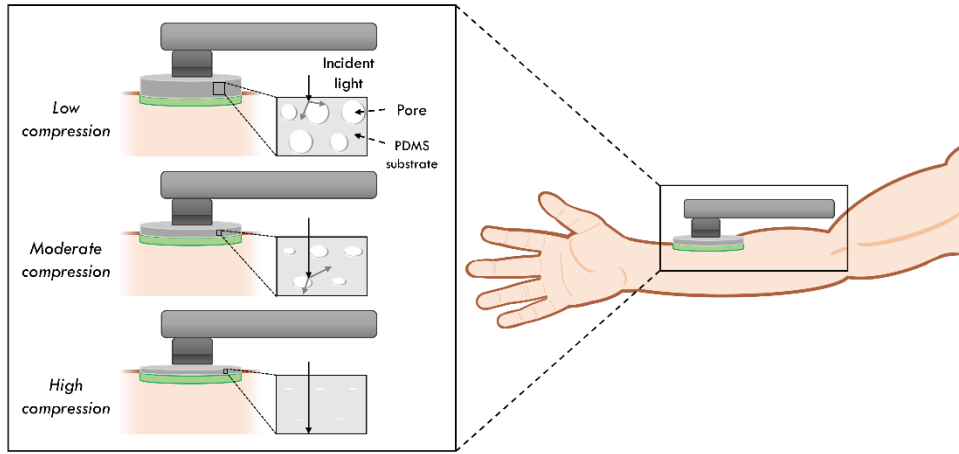


Figure 9.2: Working principle of SBOP. The imaging window on the outside of the outer cap compresses the porous and green silicone layers against a tissue sample. The inset shows that as compression is increased, the voids in the porous layer collapse, allowing more light to transmit and be detected by the smartphone camera.

Signal processing

Signal processing is performed using MATLAB 2016A (MathWorks, USA). Temporal averaging of the three photographs acquired at each location is performed, creating a 2-D photograph of the average red-green-blue (RGB) values. A median filter with a $250 \times 250 \mu\text{m}$ kernel size is applied to the averaged photograph to further reduce the effect of noise in the image. The size of the median filter kernel was selected to be approximately half the resolution in the original optical palpogram. As the porous layer is compressed, the amount of light received by the sensor through each of the RGB channels is different due to the green layer placed below the porous layer. The light transmission through the porous layer is quantified by the relationship between the individual RGB colour channels in the processed digital photograph. In previous work, this quantification was achieved by measuring the saturation in the image according to the following equation [227]:

$$S(x, y) = \frac{\alpha(RGB_{max} - RGB_{min_1}) + (RGB_{max} - RGB_{min_2})}{\alpha RGB_{max} + RGB_{max}}, \quad (9.1)$$

where S is the saturation value at each pixel. RGB_{max} , RGB_{min_1} and RGB_{min_2} are the highest, lowest and second lowest of the RGB values at each pixel location, and α is a user-defined coefficient. This metric is effective at detecting the variation in RGB when using a high-quality industrial camera and leverages the large drop-off in the red colour channel with high strain to maximise contrast, as seen in the histograms for CBOP in Fig. 9.3(a). However, the smartphone camera and LED lighting conditions used in SBOP produce more subtle changes in each colour channel, therefore, Eq. (9.1) produces less accurate stress measurements as it relies on a substantial colour channel variation towards a more intense green image with increasing strain. We address this by developing a new metric, termed *colour contrast*, to quantify the optical transmission through the porous layer, which selectively

compares the RGB values to those acquired from a characterisation image of the layer in its uncompressed state. The expression of colour contrast is given as:

$$C(x, y) = \frac{(B_0(x, y) - G_0(x, y) - B(x, y) - G(x, y))}{G(x, y) - R(x, y)}, \quad (9.2)$$

where R , G and B denote the signal intensities in the camera's red, green and blue colour channels, respectively. The zero subscript indicates measurements that are taken when the layer is uncompressed, *i.e.*, in contact with the imaging window but not under any compressive strain. The uncompressed image was taken during the layer characterisation when the layer was in contact with the imaging window of the uniaxial compression tester and the force measured by a load cell was <0.01 N. This equation compares the relative difference between the three colour channels as well as the difference between the initial colour values for green and blue (the colour channels with the least and most change per compression, respectively). Note that the uncompressed measurements from the layer characterisation are used in the calculation of colour contrast for all experimental results. Figure 9.3(b) shows histograms of the porous layer RGB colour channels under increasing compressive strains to a limit of 60% bulk strain for SBOP. The increasing green hue in the images under increasing strain is mostly caused by a comparatively higher reduction of the blue, foremostly, and red channels than the green channel. It is worth noting that the broader width of the SBOP histograms, compared to CBOP, is likely due to lower spectral sensitivity of the camera sensor as the sensor noise causes a higher deviation from the mean colour values. By using the colour contrast method, we optimise the contrast between the RGB colour channels, providing strong contrast in optical transmission, despite the slight variations in RGB values and the noisy camera sensor. An additional benefit of Eq. (9.2) is that it provides a mostly linear relationship between stress and optical transmission, ensuring the stress sensitivity is uniform, regardless of applied compression or mechanical heterogeneity in the image. This is particularly important for SBOP where compression is applied manually by pressing the smartphone apparatus against the skin, as it is challenging to apply the same level of compression each time. If stress sensitivity is not uniform, this can lead to varying image quality at different levels of mechanical contrast, depending on the amount of applied compression. Finally, the colour contrast image is converted into an optical palpogram by using the stress-colour contrast characterisation as a look-up table to transform each pixel of optical transmission into the corresponding measure of mechanical stress.

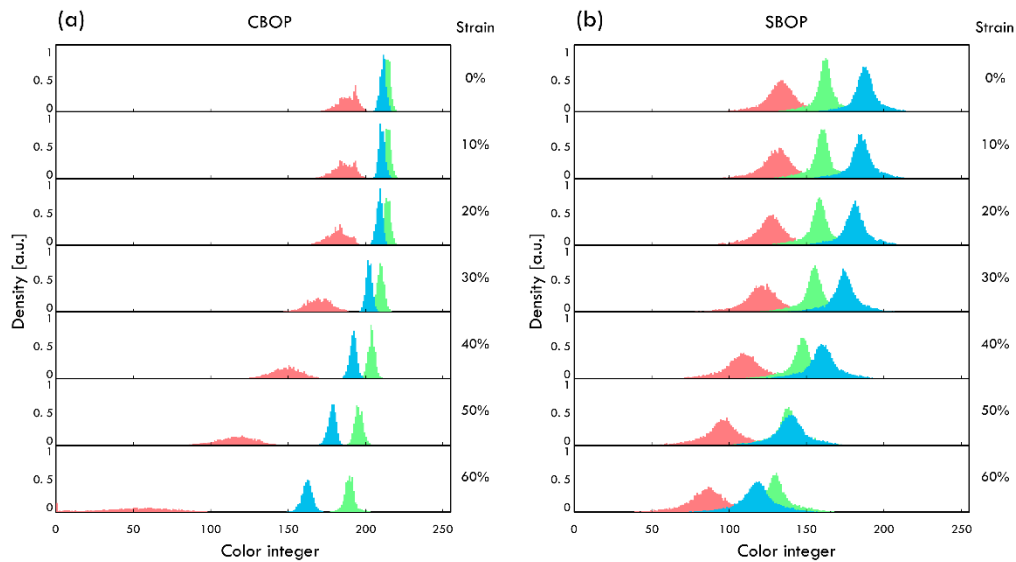


Figure 9.3: Histograms of the red, green and blue colour channels captured from photographs of the layers under uniform increments of compressive strain for (a) CBOP and (b) SBOP. Both measurements were taken from 100×100 pixel central regions of the acquired images. Due to the lower cost hardware where the sensitivity of each of the RGB channels is fixed, SBOP does not present sufficient red channel intensity reduction and colour channel separation with increasing strain as CBOP does, thereby requiring a tailored expression for colour contrast (Eq. (9.2)).

Figure 9.4 illustrates the procedure for converting a colour contrast map into an optical palpogram for the case of a silicone phantom containing a $5 \times 5 \times 1 \text{ mm}^3$ inclusion that is stiffer than the bulk material. The colour contrast image in Fig. 9.4(a) is generated by applying Eq. (9.2) to each pixel in the RGB photograph. The resulting optical palpogram shown in Fig. 9.4(b) is produced by using the stress-colour contrast characterisation curve in Fig. 9.4(c) as a look-up table to perform a pixel-by-pixel transformation of the optical transmission image. The details of this layer characterisation will be described in Section 9.2.4. To verify the accuracy of this technique, we used SBOP to measure the stress of a homogeneous silicone phantom with a 2 mm thickness and 20 mm diameter over 0-60% strain. We compared the resulting stress-strain curve to one generated using a uniaxial compression tester which measured stress via a load cell (LSB205, Futek Inc., USA) as shown in Fig. 9.4(d). In both cases, a motorised translation stage applied strain to the sample which was determined by measuring the initial thickness of the sample and the displacement applied by the stage. The overall trend of the stress-strain curves is similar, with a root mean square error of 0.9 kPa, indicating that SBOP has a high level of accuracy compared to the uniaxial compression tester.

Layer fabrication

A detailed explanation of the porous layer fabrication process is provided in [227]. Here, we briefly describe the main steps. The porous layers are fabricated by mixing equal parts silicone resin, crosslinker (Elastosil P7676, Wacker, Germany) and polydimethylsiloxane (PDMS) oil with fine sugar crystals (particle size, 30-100 μm) at a concentration of 0.25 g/ml. The

mixture is cured in an oven for 30 minutes before the sugar particles are leached out in a water bath for up to 48 hrs. Finally, the layers are dehydrated to remove residual water before being cut into 20 mm diameter disks with a thickness of 1 mm. The green layers are made by combining one part of green silicone-based pigment (SP-Green, Barnes Products, Australia) with four parts of Elastosil P7676 silicone elastomer and are fabricated to a thickness of 0.5 mm and a diameter of 35 mm. The green layer has a larger diameter than the porous layer to prevent the porous layer from sliding off the edge of the green layer under compression. The porous and green layers exhibited a combined elasticity of 8.2 ± 1.5 kPa at 20% compressive strain.

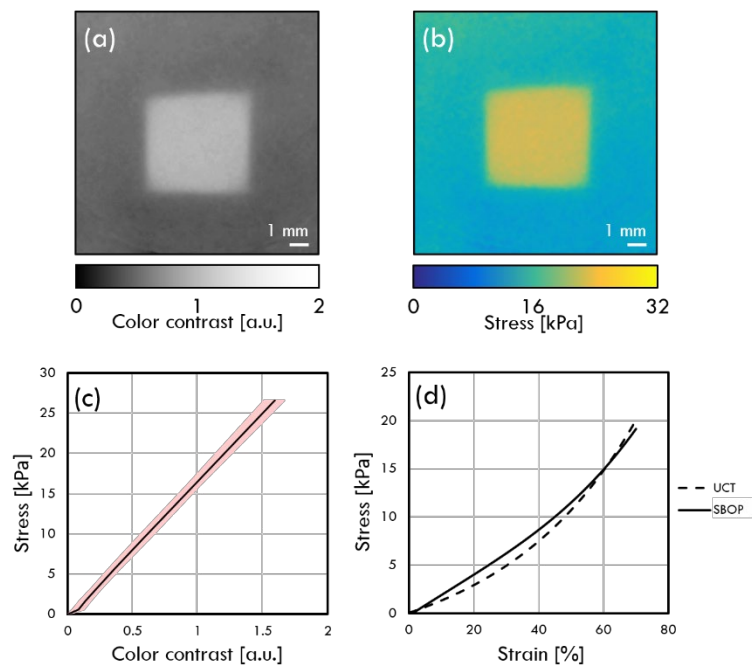


Figure 9.4: Optical palpogram and characterisation of SBOP. (a) Colour contrast image showing the varying optical transmission between inclusion and bulk regions of the phantom and (b) the corresponding optical palpogram, where the stress values are determined from (c) the stress-colour contrast characterisation curve, where the standard deviation of colour contrast is shown in red. (d) A comparison between the measured stress-strain curves of a homogeneous silicone test target acquired using a uniaxial compression (UCT) tester and SBOP.

The three key design parameters of layer material, porosity and thickness determine the elasticity range, sensitivity and spatial resolution that can be measured in an optical palpogram. In general, the elasticity of the silicone material should match that of the imaged tissue type. Furthermore, there exists a trade-off between spatial resolution and sensitivity as thinner layers will provide higher resolutions, however, small variations in colour contrast are better detected in thicker layers. While the values specified above for these parameters are tailored towards imaging burns scars, other clinical applications are likely to require different specifications and, therefore, changes to the layer material, porosity and thickness.

Layer characterisation

To convert the digital photographs to optical palpograms, the porous layers must first be optically and mechanically characterised. Both the porous layer and green layer are placed on a uniaxial compression tester with the smartphone camera positioned above to capture images of the layer transmission as it is compressed against the imaging window of the SBOP setup. Strain is applied by an axially orientated linear translation stage at a rate of $0.1\% \text{ s}^{-1}$ until 70% strain is reached. At each 10% strain interval, three photographs are acquired, which are later averaged to remove the effect of noise from the camera sensor. A load cell records the applied force which is converted to stress using prior knowledge of the layer surface area and a resultant stress-colour contrast characterisation curve of the layers is produced. As the layers are fabricated in batches, a characterisation is performed for each batch to account for slight variations in the fabrication procedure. Repeatability of the porous layers is measured by comparing the mean standard deviation in optical and mechanical properties of three different layers from 0-60% applied strain. The mean standard deviation in mechanical stress is 0.17 kPa (corresponding to $\sim 1\%$ of the maximum stress) and the mean standard deviation in colour contrast is 0.03 across the applied strain range. These results suggest a high level of repeatability between different porous layers.

Inclusion phantom fabrication

A silicone inclusion phantom is used to validate SBOP in both mounted and handheld configurations. The phantom is a 2 mm-thick cylinder with a diameter of 15 mm. The bulk of the phantom is made from Elastosil P7676 (Wacker, Germany), a two-part silicone elastomer in a 1:1 mixing ratio between resin and crosslinker. A $5 \times 5 \times 1 \text{ mm}^3$ stiff silicone inclusion, situated at the surface of the phantom, is made by mixing Elastosil RT601 (Wacker, Germany) with PDMS oil (Wacker, Germany) in a 10:1:10 ratio between the resin, crosslinker and oil. The elasticity of the bulk and inclusion are $18.7 \pm 1.2 \text{ kPa}$ and $277.0 \pm 10.9 \text{ kPa}$ at 20% strain, respectively. The inclusion and bulk materials were selected as their mechanical properties corresponded well with those of burn scar ($\sim 200 \text{ kPa}$) and unscarred tissue ($\sim 10 \text{ kPa}$) [565].

Clinical protocol

Two patients with flame burn scars were recruited to this study and imaged in the State Adult Burns Clinic at Fiona Stanley Hospital, Western Australia. Palpation was performed on the scar site by a clinician and the POSAS score was recorded for both scar stiffness and thickness. A photograph of the tissue was also acquired. To assist with co-location between the photograph and the optical palpogram, three fiduciary marks were drawn on the patient

using a skin-marker pencil, which corresponded with the marks at the same locations on the outer cap. Following this, the green and porous silicone layers were placed onto the surface of the scar with two drops of silicone oil applied between each interface to allow the layers to freely expand under compression, reducing the effects of friction. The clinician, while holding the SBOP system in one hand, positions the imaging window against the layers and applies compression whilst acquiring a set of photographs used to generate optical palpograms of the scar and surrounding tissue. A single optical palpogram was acquired at each scar site due to time constraints during scanning.

This study was approved by South Metropolitan Health Services Ethics Committee (EC00265) in Western Australia and informed consent was obtained from the patients prior to imaging. All methods and procedures were performed in accordance with the relevant guidelines and regulations, including following good clinical practices described at the International Conference on Harmonisation [568].

9.2.3 RESULTS

Inclusion phantom imaging

To validate our technique, we imaged an inclusion phantom described in Section 9.2.2. Firstly, we performed SBOP with the phone mounted to a rigid post and applied compression by driving the sample on an axial translation stage to remove any hand motion artifacts that may be caused while holding the smartphone. Strain was applied incrementally by controlling the position of the stage until the total compression of the layers and the sample was 60%. The resulting optical palpogram is displayed in Fig. 9.5(a), where the inclusion, which exhibited a stress of 23.7 ± 0.5 kPa, can clearly be distinguished from the surrounding region of bulk which displayed a stress of 12.5 ± 0.7 kPa. To determine the effectiveness of temporal averaging on reducing digital noise, ten photographs were acquired in the mounted regime and averaged together before being converted to optical palpograms. Contrast-to-noise ratio (CNR) and spatial resolution are reported as they provide a measure of how variations in mechanical properties between healthy and scar tissue can be detected above the noise (CNR) and the smallest spatial change in mechanical properties (resolution). CNR in each of these averaged optical palpograms was measured at three separate 400×400 μm locations in both the inclusion and the bulk and the average CNR from these locations is plotted in Fig. 9.5(b). CNR is defined as:

$$CNR = \frac{|\mu_{inc} - \mu_{bulk}|}{\sqrt{\sigma_{inc}^2 + \sigma_{bulk}^2}} \quad (9.3)$$

where μ_{inc} and μ_{bulk} are the mean stress values in the inclusion and bulk respectively, and σ_{inc} and σ_{bulk} are the standard deviations. The CNR increases with more photographs averaged, however, there is negligible improvement beyond averaging three photographs. Freehand results were taken by applying compression with the phone held in the user's hand. Once again, the inclusion is clearly distinguishable from the surrounding bulk, as shown in Fig. 9.5(c), and average stresses are measured to be 22.5 ± 0.3 kPa and 13.9 ± 0.4 kPa, respectively. Furthermore, by analysing the CNR of optical palpograms (Fig. 9.5(d)), generated following the same procedure as described for Fig. 9.5(b), it was found that the optimal number of photographs for temporal averaging was also three. Overall, the CNR reduces by $\sim 20\%$ for handheld operation, compared to the mounted setup. In addition to CNR, the resolution degrades slightly from 430 ± 20 μm while mounted, to 540 ± 20 μm for handheld operation. Of note, the resolution of a single optical palpogram generated during handheld operation is 430 ± 100 μm , closely matching the resolution measured for mounted operation. This result strongly suggests that lateral motion resulting from the additional time required to perform averaging causes the resolution to reduce to 540 ± 20 μm . Despite this lower resolution, we performed averaging of three photographs for the handheld operation results presented in Figs. 9.6-9.8, as this results in an increased CNR, as observed in Fig. 9.5(d).

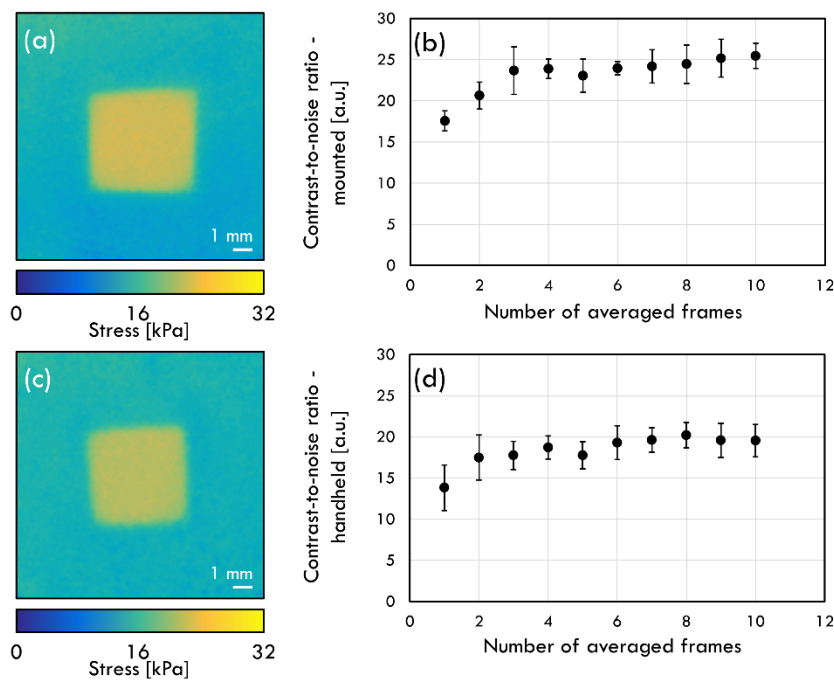


Figure 9.5: Comparison of mounted and freehand SBOP images taken on a $5 \times 5 \times 1$ mm³ silicone inclusion phantom. Optical palpogram from (a) SBOP in a mounted configuration and (b) the effect of increased temporal averaging on the CNR while mounted. Optical palpogram from (c) SBOP for freehand operation and (d) the CNR for increased temporal averaging for freehand operation. Error bars in (b) and (d) represent one standard deviation in CNR.

In vivo skin imaging

The *in vivo* imaging capability of SBOP was demonstrated on an unscarred site which served as a control, in addition to two different burn scars, obtained from the same patient. The control image was taken from the dorsal side of the left forearm which was unscarred and provides a baseline optical palpogram for unscarred tissue. A photograph of the unscarred region can be seen in Fig. 9.6(a). A zoomed-in subsection of the photograph is shown in Fig. 9.6(b) which corresponds to the same field-of-view as in the optical palpogram, presented in Fig. 9.6(c). There is no sign of scarring in the photographs which is consistent with the lack of features detected in the optical palpogram. There is a slight gradient in stress from the top left corner to the bottom right corner, which was likely caused by holding the smartphone at a slight angle relative to the tissue surface while acquiring the image. The distinct lack of features in the optical palpogram in Fig. 9.6(c) suggests that imaged region was relatively homogeneous which is indicative of unscarred tissue [234].

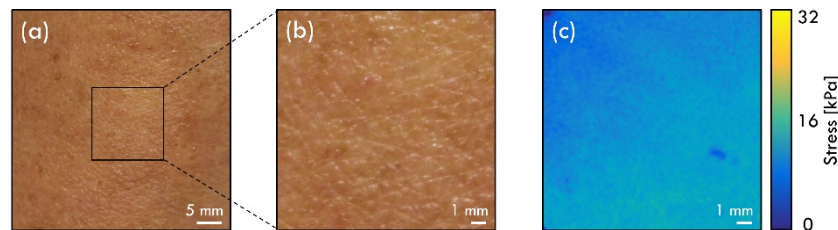


Figure 9.6: Photograph and optical palpogram of the unscarred site. (a) The full-size photograph of the unscarred site where there is no scar present. (b) The zoomed-in section of the photograph that corresponds to the location where (c) the optical palpogram was acquired.

The first burn scar selected for imaging was located on the dorsal side of the right hand. The scar was palpated prior to SBOP by a burns specialist to confirm the presence of mechanical contrast. A score of 3 for stiffness and 4 for thickness was given based on the POSAS, which indicates moderate scarring. The scar site is shown in Fig. 9.7(a) where a region of scarring is visible on the right-hand-side of the image and unscarred tissue is present on the left-hand-side. Figure 9.7(b) shows the zoomed-in region of the scar that corresponds to the same field-of-view as the optical palpogram (Fig. 9.7(c)). The optical palpogram highlights two clear regions of elevated stress on the upper right side and the lower right side of the image in Fig. 9.7(c). The mechanical heterogeneity in the optical palpogram corresponds with the boundaries seen in the photograph, suggesting that these features are stiffer than the surrounding regions of the scar.

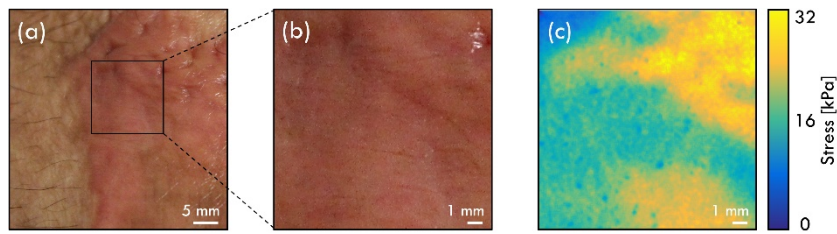


Figure 9.7: Photograph and optical palpogram of a burn scar located on the back of the right hand. (a) The full-size photograph of the scar site and surrounding tissue. (b) The zoomed-in section of the photograph that corresponds to the location where (c) the optical palpogram was acquired.

A second scar site located on the dorsal side of the patient's right forearm was also imaged with SBOP. This scar, shown in Fig. 9.8(a), was approximately 30 mm long and 10 mm wide and was also palpated by a burns specialist prior to imaging, receiving POSAS scores of 5 for stiffness and 2 for thickness, which are indicative of moderate scarring. SBOP was performed at a region where more significant scarring was located next to a region of lesser scarring to demonstrate the difference in mechanical contrast between the two regions. Figure 9.8(b) shows the photograph of the imaged region, where the scarred tissue at the top of the image presents as darker than the less scarred skin. Figure 9.8(c) shows a region of elevated stress towards the top of the optical palpogram, which corresponds well with the approximate region of scar tissue in Fig. 9.8(b). There is a small imaging artifact on the right-hand-side of the optical palpogram which appears as a region of low stress, marked by a black arrow in Fig. 9.8(c). This is likely caused by the presence of air bubbles between the green and porous layers. Note that while the POSAS score indicated that this scar is stiffer than the scar imaged in Fig. 9.7, the relative stress is lower. This is potentially due to different loading mechanisms between manual palpation and SBOP. In addition, manual palpation is a subjective method which can lead to ambiguities between assessments. Despite the lower stress value, contrast is still clearly distinguishable and corresponds well with the scar in the photograph.

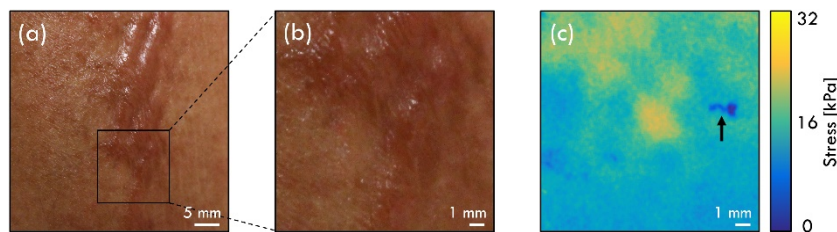


Figure 9.8: Photograph and optical palpogram of a burn scar located on the right forearm. (a) The full-size photograph of the scar site and surrounding tissue. (b) The zoomed-in section of the photograph that corresponds to the location where (c) the optical palpogram was acquired. The black arrow in (c) identifies an imaging artifact due to air bubbles between the layers.

9.2.4 DISCUSSION

In this paper, we have presented the first demonstration of optical elastography on a smartphone device. This technique builds on a previous imaging technique developed by our group, CBOP, and utilises the in-built smartphone camera of a Google Pixel 3 to provide

sub-millimetre resolution imaging of mechanical contrast between regions of *in vivo* burn scars and adjacent tissue. In utilising smartphone devices, we have developed a tool that provides elastography in a widely accessible format. Coupled with the low cost of the additional components, SBOP is well positioned to provide mechanical contrast, in addition to the visual and audial inspection already utilised in a range of telehealth applications [552,569,570].

While the camera used in SBOP was less expensive than that used previously in CBOP, it was also of a lower quality, with a smaller $1/2.55''$ ($5.6 \times 4.2 \text{ mm}^2$) sensor in the Google Pixel 3 compared to the $1/1.7''$ ($7.4 \times 5.6 \text{ mm}^2$) sensor used previously [227]. Despite both cameras providing resolutions of 12.2 MP, the smaller camera sensors typically provide lower dynamic range and higher noise levels as the individual pixels detect less light, resulting in lower quality images [571]. When comparing the relative spatial resolution of the two techniques, both SBOP and CBOP reported spatial resolution of $430 \mu\text{m}$ when imaging a $5 \times 5 \times 1 \text{ mm}^3$ stiff inclusion in a silicone phantom. While this is not a direct comparison as the axial position of the inclusion differed slightly between the two measurements [225], it confirms that the resolution of these camera-based techniques is not limited by the camera sensor but rather by the mechanical deformation of the porous layer and the sample. Therefore, using low-cost smartphone cameras and lenses for telehealth applications will not lead to lower image resolution than higher specification benchtop implementations. Furthermore, the spatial resolution of SBOP is significantly higher than that of manual palpation which has previously reported resolutions of 1-3 mm [10], suggesting SBOP is able to identify finer features within burn scars than the current clinical practice. Despite the resolution being unaffected, there is a drop in CNR from CBOP to SBOP, most likely caused by the higher noise in the smartphone camera sensor and hand motion artifacts when operated freehand. This indicates that the more sophisticated camera used in CBOP can generate higher quality images and mechanical contrast, highlighting the trade-off between CNR and the camera system cost.

In addition, the CNR in the handheld image also reduces by $\sim 20\%$ when compared to mounted SBOP, likely due to a difference in friction conditions between the two scans, which is difficult to match exactly. The mounted set-up is uniaxial; however, it was observed that lateral motion in the handheld set-up (particularly when initially searching for the region containing the inclusion) can cause the lubricating oil to be squeezed out, resulting in increased friction. Increased friction restricts the lateral expansion of the silicone layers under compression, especially at higher preloads, resulting in reduced axial strain on the porous layer for the same stress and, consequently, an underestimation of stress at the inclusion [488]. While the reduction in image quality does not adversely affect the ability to

detect features in the handheld case, there is scope to improve the image quality by incorporating an accurate estimation for the friction coefficient into the measurement of stress. This could be achieved by comparing experimental data to finite element analysis (FEA) simulations to match the friction conditions, from which a computational calculation of 3-D stress in the model layer could be acquired, providing improved spatial resolution and higher image quality [488].

Stress has previously been used as a contrast mechanism in OCT-based optical palpation to distinguish malignant disease [225], however, it is a qualitative measure and does not quantify elasticity. A previous study conducted on 34 freshly excised breast tissue specimens demonstrated that despite this, optical palpograms can localise tumour based on stress contrast [226]. This approach, however, requires mechanical heterogeneity within the field of view of a single image. For SBOP, and indeed all techniques utilising stress as a contrast mechanism, this can lead to ambiguities in cases where there is no heterogeneity, as an entirely stiff sample could appear the same as an entirely soft sample. In this study, we have mitigated this by imaging scar sites at the boundary between soft tissue and stiff scar tissue. Additionally, we aimed to keep the applied loading on the tissue relatively constant, such that optical palpograms were generated at a similar point in the stress-strain curve of different tissues, facilitating direct comparison. In the future, methods could be developed to quantify the mechanical properties of the tissue using inverse methods [537,538] or by utilising an indentation model to approximate elasticity [572,573]. Alternatively, the average stress level in the image could be computed [305] in real-time and used as a trigger for palpogram acquisition. These methods would allow SBOP to better distinguish healthy and diseased tissue as well as more accurately compare scars from different optical palpograms, expanding the clinical feasibility of the technique.

Both scar sites imaged in this study exhibited regions of raised and uneven tissue at the surface. While the thickness of the scar can be used as a diagnostic indicator and is indeed one of the criteria for the POSAS, it is important that our measurements are not incorrectly generating mechanical contrast based on thickness variations. Thickness, however, is unlikely to have produced the contrast in stress observed in the *in vivo* skin optical palpograms presented in the paper, as it has been shown previously that the raised topology of surface features does not lead to an overestimation of stress in OCT-based optical palpation [234].

Tilt is common source of artifacts in handheld imaging probes as it is often difficult to precisely control the orientation of the probe [574]. In SBOP, tilt causes a gradient of stress such as that shown in Fig. 9.6(c), and in extreme cases could lead to incorrect classification of a region of homogeneous non-scarred tissue as scarred. In this initial proof of concept, we utilised Open Camera, an open-source application to acquire images. This application is

not designed to detect the tilt of the camera. In future studies, we seek to develop our own specialised camera application which will incorporate the phone's in-built gyroscope to sense tilt in the camera. This would serve as a simple solution to address tilt as it would not require any additional components, while improving the overall image quality.

A limitation in the clinical application of the current SBOP method is in ensuring that the porous layer undergoes compression sufficient to generate optical palpograms. This is readily achieved when the sample is positioned between a rigid flat plate and the SBOP imaging window, such as in the case of the inclusion phantoms, as it allows for uniform compression to be applied. For *in vivo* scans, however, this may not always be possible depending on the location of the scar site on the body. For example, heightened stress may be observed in the regions above stiff features such as tendons or bones. Similarly, when imaging scars located above large regions of soft tissue, such as the abdomen, or regions with a lot of adipose tissue, the underlying tissue displaces considerably, making it difficult to generate compression in the layer. As a result, the contrast in the current iteration of SBOP is dependent on the anatomical location from which the scan was taken. This can be seen when comparing Fig. 9.7(c) and 9.8(c), where the stress is higher in Fig. 9.7(c) which was acquired on the back of the hand where there is less underlying soft tissue between the scar and skeletal structure. In contrast, Fig. 9.8(c) was taken from the arm where the underlying adipose tissue and muscle tissue was several centimetres thicker. As a result, there is less contrast between the scar and unscarred regions of the skin in this optical palpogram. One approach to mitigate these effects is to reduce the elasticity of the layer so that it is softer than the underlying tissue which would allow the layer to deform more easily. Another potential solution is to reduce the diameter of the imaging window and external cap which would enable the user to apply a more localised force, similar to an indenter, again making it easier to deform the layer and generate contrast while reducing the potential for erroneous measurements caused by spatial variations in the underlying features and tilt [234].

The results presented in this initial work demonstrate that SBOP is capable of distinguishing mechanical heterogeneity in burn scars. While this work has demonstrated strong potential towards telehealth applications, to fully understand the clinical feasibility of this technique, a longitudinal study is required. Such a study would seek to image multiple different scar sites and provide a measure of the inter-sample variability by taking repeat optical palpograms on the same scar site as well as determine the inter- and intra-operator variability. In addition, a detailed comparison between SBOP and POSAS on multiple scar sites would provide an indication of the diagnostic performance of SBOP relative to the current clinical standard.

9.2.5 CONCLUSION

In this paper, we have presented a proof of concept for SBOP, a novel optical palpation device designed to evaluate tissue stiffness on a commercially available smartphone. We have demonstrated this technique on a structured inclusion phantom in both a mounted and handheld setup and shown that there is minimal difference in image quality between the two. In addition, we have demonstrated mechanical contrast in two *in vivo* burn scars using SBOP, highlighting potential application in telehealth treatment of burns. SBOP uses low-cost and readily available components in conjunction with commercially available smartphones making it easily accessible to the public.

Funding

Australian Research Council (ARC); the Cancer Council, Western Australia; War Widows' Guild of Western Australia Scholarship.

CHAPTER 10

CONCLUSION AND PERSPECTIVES

It has been demonstrated that optical elastography is a promising tool for the detection of disease. Optical elastography techniques are at the stage of development with most studies having been performed in laboratory conditions or in *ex vivo* scenarios using large benchtop systems. For optical elastography to be implemented *in vivo*, existing imaging systems need to be adapted from laboratory to clinical use, in many cases, through redesign of imaging probes. The work presented in this Thesis addresses some of the technical requirements for the practical application of optical elastography to intraoperative tumour margin assessment and objective pathological burn scar assessment. This involved designing a novel finger-mounted optical coherence elastography (OCE) imaging probe which mimicked the existing practise of manual palpation. Secondly, a new optical elastography technique, camera-based optical palpation (CBOP), was developed using digital photography to map the local stress on a sample. CBOP was then adapted to a portable imaging probe towards telehealth assessments of pathological burn scars. This work has advanced optical elastography closer to clinical translation through the design of novel imaging probes. However, before optical elastography is ready to be implemented in a clinical environment, there are a number of technical limitations to overcome as well as validation studies required to validate the efficacy of these techniques in their intended applications. In this final Chapter the contribution and significance of this work are discussed, as well as a summary of the current limitations and required future work before concluding with some final remarks.

10.1 RESEARCH CONTRIBUTIONS AND SIGNIFICANCE

A brief summary of the research contributions in each chapter are presented here.

In Chapter 2, an overview of breast cancer and existing intraoperative tumour margin assessment tools for breast conserving surgery were presented. An overview of pathological scar formation and the existing assessment tools was also provided. The benefits and limitations of both sets of assessment tools were described and diagnostic accuracy was reported where relevant. This review highlighted that for both intraoperative margin

assessment and the objective assessment of pathological burn scars, there is a need for diagnostic tools to better identify the presence of disease.

In Chapter 3, optical elastography is presented in the context of the broader field of elastography. Several prominent optical elastography techniques are introduced and a continuum mechanics model for the mechanical response of soft tissue in elastography is presented. The key simplifying assumptions are then described, showing how the model is reduced for practical applications in elastography.

In Chapter 4, a technical overview of optical coherence elastography is presented. Further detail is provided for the techniques of quantitative micro-elastography (QME) and optical palpation.

In Chapter 5, clinical validation of QME and optical palpation is presented. The diagnostic accuracy for these techniques in the assessment of tumour in breast-conserving surgery (BCS) patients is reported, with both techniques exhibiting high sensitivity and specificity.

In Chapter 6, a review of OCE imaging probes is presented and insight is provided on how the design of OCE probes is influenced by the intended clinical application. This chapter identifies the key design parameters in probe development and provides an overview of the current state of OCE probe development.

In Chapter 7, a compact finger-mounted QME probe, capable of providing high-resolution maps of tissue mechanical properties is presented. The probe is designed towards the intraoperative assessment of tumour margins in breast-conserving surgery and seeks to preserve the existing clinical workflow by mimicking manual palpation. The accuracy of the measurements is validated against uniaxial compression tests with mean average percent error of 13% across five different inclusion phantoms. A custom signal processing algorithm was developed to reduce the effect of nonuniform velocity which enabled preliminary two-dimensional (2-D) scans by laterally swiping the finger across the sample surface. The compact nature of this probe allows future iterations to potentially be implemented inside the surgical cavity to provide accurate diagnoses of residual tumour. This would provide a significant advantage over many existing intraoperative techniques which only assess the excised tissue.

In Chapter 8, a new optical elastography technique, CBOP, is presented which utilises a digital camera and porous layer to map mechanical contrast at the tissue surface. This technique can be implemented at a much lower cost (< \$5,000 USD) than OCT-based optical palpation (> \$50,000) while demonstrating comparable spatial resolution of 290 μm . In addition to lower cost, CBOP is less complex to operate than OCT-based imaging technique, which can often limit the clinical adoption of imaging techniques. The clinical feasibility was

demonstrated on two freshly excised mastectomy specimens where CBOP was able to distinguish between regions of adipose tissue, fibrous tissue and tumour based on variations in measured stress. The lower cost of implementation and reduced complexity of CBOP make it suitable in applications that previously would have been beyond optical elastography such as in low-resource healthcare settings.

In Chapter 9, the first implementation of elastography on a smartphone is presented. By adapting the principles of CBOP to a commercial smartphone, we have demonstrated a portable cost effective optical elastography device which is amenable to applications in telehealth. A robust algorithm was developed which enabled optical transmission through the porous layer to be accurately measured despite the lower spectral sensitivity of the camera sensor in smartphone-based optical palpation (SBOP). Despite being operated handheld, SBOP demonstrated comparable image resolution compared to CBOP. This technique was demonstrated *in vivo* where mechanical heterogeneity was detected in two burn scars in contrast to the relatively uniform unscarred site, suggesting SBOP has the potential to provide diagnostic information which could inform the prescription of therapies to prevent the formation of pathological scars.

10.2 STUDY LIMITATIONS AND FUTURE WORK

Limitations and potential solutions

Development of the imaging probes and associated techniques in this thesis have enhanced the viability of optical elastography in intraoperative tumour assessment during breast-conserving surgery and while expanding the potential applications to new fields in telehealth. The studies presented here provide a proof of concept, however, there remain several limitations which must be overcome before implementing these imaging probes in their intended clinical applications. In this section, we explore the main limitations, potential solutions and future clinical studies.

Compression elastography is an appealing technique, as it offers a combination of broad fields of view and rapid image acquisition compared to harmonic [292] and transient [575] loading methods. However, bulk compressive loading results in a mechanically coupled tissue response [488]. This can make it challenging to delineate the local mechanical properties as deformation in one region is influenced by deformation in neighbouring regions, producing strain artifacts in the acquired elastogram. This effect is likely due to tissue incompressibility, where the volume of a deforming sample is preserved and axial compression results in lateral expansion. This effect is present in both the sample and the layer in QME and optical palpation and can lead to erroneous measurements. One method to overcome this is to assess

the stress and strain in three-dimensions (3-D) through finite element analysis (FEA) modelling of the compliant layer. This is known as the computational method and has previously been demonstrated in optical palpation [488]. Another potential solution to this problem is to provide a more localised force through indentation to prevent the confounding effect of lateral expansion from producing strain artifacts. Displacement resulting from micro-indentation has previously been detected using OCT to assess the mechanical properties of tissue [576,577]. Utilising indentation would require a different mechanical model such as Hertzian contact theory to assess the tissue mechanical properties resulting from displacement [578]. One drawback to indentation is the acquisition speed would be quite low, as many measurements are required at each spatial location, similar to how transient loading is applied [21]. A hybrid of compression and indentation elastography may prove an elegant solution, where a broad assessment of the tissue is first determined using compression methods before probing suspicious regions of interest in more depth using indentation to accurately determine the presence of disease.

In the finger-mounted QME probe, 2-D images were acquired by swiping the finger across the sample surface [440]. While this represents a straightforward method to generate 2-D images, it requires the implementation of a more complex mechanical model as the lateral motion introduces shear forces to the sample. Therefore, the assumption that elasticity in a sample can be determined by the ratio of axial stress to axial strain is challenged by the acquisition protocol as the lateral motion in addition to the axial displacement, produces forces perpendicular to the surface of the sample. The resulting strain components are also in two directions, leading to a breakdown in the assumption that loading is only in depth, and therefore, inaccurate measurements. In addition, if the lateral force is sufficiently high (potentially due to a high friction effect at the probe-layer interface) and the sample is confined in place by the boundary conditions, a shear force can be introduced between the upper portion of the sample, which is effectively pulled by the probe tip, and the lower portion, which remains stationary due to the boundary conditions. This shearing introduces tensile forces which create imaging artifacts, particularly at the transition from compression to tension as the strain component approaches zero, resulting in elasticity approaching infinity. The magnitude of the lateral force is dependent on the friction at the probe-layer interface; therefore, this effect could be reduced by reducing this friction. The most logical solution would be to redesign the probe tip to allow smoother transition across the sample surface. The current design has a flat surface with relatively sharp edges. As the probe moves across the surface, these sharp edges 'grip' on the surface, increasing the friction. A spherical tip, possibly made from cured optical adhesive or a spherical fibre optic tip, would reduce the friction effect, allowing the probes to move across the sample with less resistance,

however, a study would need to be carried out to determine if this change sufficiently reduces the lateral forces and shearing in the sample during 2-D swiping. An alternative solution could incorporate a spherical lens which is free to rotate, similar to a ball-bearing, coupled to the fibre optic probe. This would likely greatly reduce the friction effect but also present challenges to the optical design of the probe including aligning the beam through the lens without distortion and reducing the artifacts and signal power loss resulting from multiple reflective surfaces.

In optical palpation, stress at the sample surface is measured [225,227]. While this represents a simpler approach to OCE capable of detecting features beyond the imaging depth of OCT, information such as depth, size, and stiffness of a feature cannot be directly inferred from elastograms of surface stress alone as a stiffer feature located deep within the tissue can produce the same stress profile as a softer feature closer to the surface. Decoupling these parameters is key to improving the clinical feasibility of optical palpation as applications such as the intraoperative detection of breast margins rely on accurate measurements of feature depth, size, and stiffness to determine whether any residual tumour remains in the patient. Inverse methods, which have previously been proposed in tactile imaging applications [537–539] can be applied here to quantify the measurements in optical palpation by analysing the changing stress measurements as compression is incremented. This would be relatively straightforward to accomplish in both optical palpation techniques, however, acquisition of large samples (greater than the lateral field of view for a single OCT image) would become time consuming for OCT-based optical palpation. In contrast CBOP could leverage video rate acquisition of broad fields of view to acquire multiple elastograms at different loading conditions [227,579]. This solution would also resolve the subjectivity of optical palpation, which is currently dependent on the bulk strain applied by the operator. In clinical applications, this bulk strain cannot be determined using optical palpation, however, acquiring multiple elastograms at increasing compressive loads would allow for the reconstruction of relative stress-strain curves for different spatial locations within the sample from which feature depth, size and stiffness can be recovered.

The probes developed in this Thesis have employed the simplified mechanical model to solve for elasticity, in a method known as the algebraic method. While this method is widely used amongst elastography techniques, as described above, it can lead to errors in heterogeneous samples as the simplified mechanical model begins to break down. Alternatively, the inverse elasticity problem can also be solved by using the iterative method, which iterates through different possibilities of mechanical properties [239,359]. This is effectively an optimisation problem, which attempts to reduce the error between the predicted and measured displacements, making far fewer assumptions regarding the sample

mechanical properties, resulting in it being less susceptible to errors compared to the algebraic method. However, these iterative inverse methods remain difficult to implement in practical applications and are computationally intensive, hence the widespread use of the algebraic method in elastography [236].

Future studies

The techniques and probes developed in this thesis have all provided proof of concepts that have the potential to improve the clinical feasibility of optical elastography. Despite this promise, these techniques have only been demonstrated on silicone inclusion phantoms and a select number of *in vivo* tissue samples. While this is representative of the current status of optical elastography techniques, to advance to the point of clinical use first requires large scale *in vivo* studies in the intended clinical application to evaluate the diagnostic accuracy of these techniques.

Finger-mounted QME should be demonstrated on a large number of diverse breast tissue specimens (precursor, invasive and benign tumours, etc.) to determine not only the diagnostic accuracy but the performance of the technique on different cancer types. Furthermore, finger-mounted QME is intended specifically for use in the surgical cavity to determine the presence of residual tumour following excision. Therefore, to evaluate the clinical feasibility of this technique, imaging would eventually have to be performed in the surgical cavity as opposed to scanning the surgical margin of the excised tissue. As validation is typically provided by histology sectioning of the excised tissue, this could present challenges with correlating the histology image to the same location in the QME image. A potential solution would be to image the cavity wall, then taking a shaving from the imaged region to be sectioned for histology. In the case of CBOP a similar study is required to determine its diagnostic accuracy in breast tissue, albeit, on *ex vivo* specimens. For in cavity scans, a purpose-built probe is required which would likely need to trade-off field of view in favour for a more compact design suitable for imaging in the cavity. For SBOP, diagnostic accuracy would need to be confirmed through a study of different scar types, including keloid, hypertrophic, and hypertrophic scars. While validation in breast tissue is performed using histology, this is not possible in the assessment of *in vivo* burn scars. Instead, validation is typically provided by scar scales, however, the objectivity of these assessments makes them poor benchmarks to compare out technique against. Instead, validation could be provided through widefield QME of the scar site which would provide an objective assessment of the scar mechanical properties. Finally, SBOP provides the user with the ability to image themselves, or with the assistance of another person, remotely. Therefore, the clinical feasibility of this technique is partially dependent on how well someone can operate SBOP,

necessitating a structured training program as well. Further studies are required in to how detailed and rigorous this training needs to be and how long is needed before someone is deemed proficient enough to perform SBOP imaging.

In addition to the applications discussed in this thesis, future studies could explore the suitability of these imaging probes in other areas. While the probes in this thesis have been designed specifically for certain applications, the diagnostic capability of these probes would prove beneficial in a number of different applications. For example, the finger-mounted QME probe is designed to detect the presence of residual tumour, to reduce the need for repeat surgical procedures. There are similarities in the excision of brain metastases, where local recurrence rates are $< 46\%$ [580]. Therefore, adapting a similar probe to this application would likely prove beneficial in the detection of tumour and ensure all the tumour was removed.

10.3 FINAL REMARKS

This research has contributed several novel imaging probes and techniques which represent key advances towards the clinical translation of optical elastography. These imaging probes are capable of providing the characteristic high resolution and high sensitivity of optical elastography techniques in a form factor that is suitable for use within the clinical applications of intraoperative breast margin assessment and objective scar assessment. With SBOP, optical elastography has been implemented for the first time on a smartphone in a cost-effective design, expanding this technology to new applications which can benefit from the diagnostic capability of optical elastography.

REFERENCES

1. Y. C. Fung, *Biomechanics: Mechanical Properties of Living Tissues* (Springer Science & Business Media, 2013).
2. K. Hoyt, B. Castaneda, M. Zhang, P. Nigwekar, P. A. di Sant'Agnese, J. V. Joseph, J. Strang, D. J. Rubens, and K. J. Parker, "Tissue elasticity properties as biomarkers for prostate cancer," *Cancer Biomark. Sect. Dis. Markers* **4**, 213–225 (2008).
3. J. A. Clark, J. C. Y. Cheng, and K. S. Leung, "Mechanical properties of normal skin and hypertrophic scars," *Burns* **22**, 443–446 (1996).
4. U. Arena, F. Vizzutti, G. Corti, S. Ambu, C. Stasi, S. Bresci, S. Moscarella, V. Boddi, A. Petrarca, G. Laffi, F. Marra, and M. Pinzani, "Acute viral hepatitis increases liver stiffness values measured by transient elastography," *Hepatology* **47**, 380–384 (2008).
5. E. Mazza, A. Nava, D. Hahnloser, W. Jochum, and M. Bajka, "The mechanical response of human liver and its relation to histology: An in vivo study," *Med. Image Anal.* **11**, 663–672 (2007).
6. C. Mather and S. O'Kelly, "The palpation of pulses," *Anaesthesia* **51**, 189–191 (1996).
7. V. Kataja and M. Castiglione, "Primary breast cancer: ESMO Clinical Recommendations for diagnosis, treatment and follow-up," *Ann. Oncol.* **20**, iv10–iv14 (2009).
8. P. Durani, D. A. McGrouther, and M. W. J. Ferguson, "Current scales for assessing human scarring: A review," *J. Plast. Reconstr. Aesthet. Surg.* **62**, 713–720 (2009).
9. R. W. Van Boven and K. O. Johnson, "The limit of tactile spatial resolution in humans: grating orientation discrimination at the lip, tongue, and finger," *Neurology* **44**, 2361–2366 (1994).
10. H. Manning and F. Tremblay, "Age differences in tactile pattern recognition at the fingertip," *Somatosens. Mot. Res.* **23**, 147–155 (2006).
11. J. Ophir, I. Cespedes, B. Garra, H. Ponnekanti, Y. Huang, and N. Maklad, "Elastography: Ultrasonic imaging of tissue strain and elastic modulus in vivo," *Eur. J. Ultrasound* **3**, 49–70 (1996).
12. R. Muthupillai, D. J. Lomas, P. J. Rossman, J. F. Greenleaf, A. Manduca, and R. L. Ehman, "Magnetic resonance elastography by direct visualization of propagating acoustic strain waves," *Science* **269**, 1854–1857 (1995).
13. V. Ianculescu, L. M. Ciolovan, A. Dunant, P. Vielh, C. Mazouni, S. Delalogue, C. Dromain, A. Blidaru, and C. Balleyguier, "Added value of Virtual Touch IQ shear wave elastography in the ultrasound assessment of breast lesions," *Eur. J. Radiol.* **83**, 773–777 (2014).
14. A. Tang, G. Cloutier, N. M. Szeverenyi, and C. B. Sirlin, "Ultrasound Elastography and MR Elastography for Assessing Liver Fibrosis: Part 1, Principles and Techniques," *Am. J. Roentgenol.* **205**, 22–32 (2015).
15. P. Eaton and P. West, *Atomic Force Microscopy* (Oxford University Press, 2010).
16. P. H. Jones, O. M. Maragò, and G. Volpe, *Optical Tweezers: Principles and Applications* (Cambridge University Press, 2015).
17. R. M. Hochmuth, "Micropipette aspiration of living cells," *J. Biomech.* **33**, 15–22 (2000).
18. J. M. Schmitt, "OCT elastography: imaging microscopic deformation and strain of tissue," *Opt. Express* **3**, 199–211 (1998).
19. S. L. Jacques and S. J. Kirkpatrick, "Acoustically modulated speckle imaging of biological tissues," *Opt. Lett.* **23**, 879–881 (1998).

20. B. F. Kennedy, K. M. Kennedy, and D. D. Sampson, "A Review of Optical Coherence Elastography: Fundamentals, Techniques and Prospects," *IEEE J. Sel. Top. Quantum Electron.* **20**, 272–288 (2014).
21. K. V. Larin and D. D. Sampson, "Optical coherence elastography – OCT at work in tissue biomechanics [Invited]," *Biomed. Opt. Express* **8**, 1172–1202 (2017).
22. S. Wang and K. V. Larin, "Optical coherence elastography for tissue characterization: a review," *J. Biophotonics* **8**, 279–302 (2015).
23. R. Prevedel, A. Diz-Muñoz, G. Ruocco, and G. Antonacci, "Brillouin microscopy: an emerging tool for mechanobiology," *Nat. Methods* **16**, 969–977 (2019).
24. D. A. Boas and A. K. Dunn, "Laser speckle contrast imaging in biomedical optics," *J. Biomed. Opt.* **15**, 011109 (2010).
25. U. Schnars, C. Falldorf, J. Watson, and W. Jüptner, "Digital Holography," in *Digital Holography and Wavefront Sensing: Principles, Techniques and Applications*, U. Schnars, C. Falldorf, J. Watson, and W. Jüptner, eds. (Springer, 2015), pp. 39–68.
26. K. J. Koski and J. L. Yarger, "Brillouin imaging," *Appl. Phys. Lett.* **87**, 061903 (2005).
27. Y. Qiu, Y. Wang, Y. Xu, N. Chandra, J. Haorah, B. Hubbi, B. J. Pfister, and X. Liu, "Quantitative optical coherence elastography based on fiber-optic probe for in situ measurement of tissue mechanical properties," *Biomed. Opt. Express* **7**, 688–700 (2016).
28. Q. Fang, B. Krajancich, L. Chin, R. Zilkens, A. Curatolo, L. Frewer, J. D. Anstie, P. Wijesinghe, C. Hall, B. F. Dessauvagie, B. Latham, C. M. Saunders, and B. F. Kennedy, "Handheld probe for quantitative micro-elastography," *Biomed. Opt. Express* **10**, 4034–4049 (2019).
29. L. Bartolini, F. Feroldi, M. Slaman, J. J. A. Weda, J. F. de Boer, P. van Zuijlen, and D. Iannuzzi, "Toward clinical elastography of dermal tissues: A medical device to probe skin's elasticity through suction, with subsurface imaging via optical coherence tomography," *Rev. Sci. Instrum.* **91**, 074101 (2020).
30. H. Sung, J. Ferlay, R. L. Siegel, M. Laversanne, I. Soerjomataram, A. Jemal, and F. Bray, "Global Cancer Statistics 2020: GLOBOCAN Estimates of Incidence and Mortality Worldwide for 36 Cancers in 185 Countries," *CA. Cancer J. Clin.* **71**, 209–249 (2021).
31. F. Bray, P. McCarron, and D. M. Parkin, "The changing global patterns of female breast cancer incidence and mortality," *Breast Cancer Res.* **6**, 229 (2004).
32. "Understanding breast cancer | Breast Cancer Network Australia," <https://www.bcna.org.au>.
33. M. Kamińska, T. Ciszewski, K. Łopacka-Szatan, P. Miotła, and E. Starosławska, "Breast cancer risk factors," *Przegląd Menopauzalny Menopause Rev.* **14**, 196–202 (2015).
34. K. McPherson, C. M. Steel, and J. M. Dixon, "Breast cancer—epidemiology, risk factors, and genetics," *BMJ* **321**, 624–628 (2000).
35. F. Bray, J. Ferlay, I. Soerjomataram, R. L. Siegel, L. A. Torre, and A. Jemal, "Global cancer statistics 2018: GLOBOCAN estimates of incidence and mortality worldwide for 36 cancers in 185 countries," *CA. Cancer J. Clin.* **68**, 394–424 (2018).
36. "Breast cancer and hormone-replacement therapy in the Million Women Study," *The Lancet* **362**, 419–427 (2003).
37. "Breast cancer and hormonal contraceptives: collaborative reanalysis of individual data on 53 297 women with breast cancer and 100 239 women without breast cancer from 54 epidemiological studies," *The Lancet* **347**, 1713–1727 (1996).
38. A. Bergström, P. Pisani, V. Tenet, A. Wolk, and H.-O. Adami, "Overweight as an avoidable cause of cancer in Europe," *Int. J. Cancer* **91**, 421–430 (2001).

39. C. Magnusson, J. Baron, I. Persson, A. Wolk, R. Bergström, D. Trichopoulos, and H.-O. Adami, "Body size in different periods of life and breast cancer risk in post-menopausal women," *Int. J. Cancer* **76**, 29–34 (1998).
40. W. Y. Chen, B. Rosner, S. E. Hankinson, G. A. Colditz, and W. C. Willett, "Moderate Alcohol Consumption During Adult Life, Drinking Patterns, and Breast Cancer Risk," *JAMA* **306**, 1884–1890 (2011).
41. K. B. Kuchenbaecker, J. L. Hopper, D. R. Barnes, K.-A. Phillips, T. M. Mooij, M.-J. Roos-Blom, S. Jervis, F. E. van Leeuwen, R. L. Milne, N. Andrieu, D. E. Goldgar, M. B. Terry, M. A. Rookus, D. F. Easton, A. C. Antoniou, BRCA1 and BRCA2 Cohort Consortium, L. McGuffog, D. G. Evans, D. Barrowdale, D. Frost, J. Adlard, K.-R. Ong, L. Izatt, M. Tischkowitz, R. Eeles, R. Davidson, S. Hodgson, S. Ellis, C. Nogues, C. Lasset, D. Stoppa-Lyonnet, J.-P. Fricker, L. Faivre, P. Berthet, M. J. Hooning, L. E. van der Kolk, C. M. Kets, M. A. Adank, E. M. John, W. K. Chung, I. L. Andrulis, M. Southey, M. B. Daly, S. S. Buys, A. Osorio, C. Engel, K. Kast, R. K. Schmutzler, T. Caldes, A. Jakubowska, J. Simard, M. L. Friedlander, S.-A. McLachlan, E. Machackova, L. Foretova, Y. Y. Tan, C. F. Singer, E. Olah, A.-M. Gerdes, B. Arver, and H. Olsson, "Risks of Breast, Ovarian, and Contralateral Breast Cancer for BRCA1 and BRCA2 Mutation Carriers," *JAMA* **317**, 2402–2416 (2017).
42. D. R. Youlten, S. M. Cramb, N. A. M. Dunn, J. M. Muller, C. M. Pyke, and P. D. Baade, "The descriptive epidemiology of female breast cancer: An international comparison of screening, incidence, survival and mortality," *Cancer Epidemiol.* **36**, 237–248 (2012).
43. A. J. Darlington, "Anatomy of the Breast," in *Digital Mammography: A Holistic Approach*, P. Hogg, J. Kelly, and C. Mercer, eds. (Springer International Publishing, 2015), pp. 3–10.
44. T. R. Milanese, L. C. Hartmann, T. A. Sellers, M. H. Frost, R. A. Vierkant, S. D. Maloney, V. S. Pankratz, A. C. Degnim, C. M. Vachon, C. A. Reynolds, R. A. Thompson, L. J. Melton III, E. L. Goode, and D. W. Visscher, "Age-Related Lobular Involution and Risk of Breast Cancer," *JNCI J. Natl. Cancer Inst.* **98**, 1600–1607 (2006).
45. S. Zahoor, A. Haji, A. Battoo, M. Qurieshi, W. Mir, and M. Shah, "Sentinel Lymph Node Biopsy in Breast Cancer: A Clinical Review and Update," *J. Breast Cancer* **20**, 217 (2017).
46. S. Pandya and R. G. Moore, "Breast Development and Anatomy," *Clin. Obstet. Gynecol.* **54**, 91–95 (2011).
47. A. E. Giuliano, D. M. Kirgan, J. M. Guenther, and D. L. Morton, "Lymphatic mapping and sentinel lymphadenectomy for breast cancer.," *Ann. Surg.* **220**, 391–401 (1994).
48. M. Akram, M. Iqbal, M. Daniyal, and A. U. Khan, "Awareness and current knowledge of breast cancer," *Biol. Res.* **50**, 33 (2017).
49. Cancer Australia, "Stages of breast cancer," <https://www.canceraustralia.gov.au/affected-cancer/cancer-types/breast-cancer/stages-breast-cancer>.
50. S. A. Narod, J. Iqbal, V. Giannakeas, V. Sopik, and P. Sun, "Breast Cancer Mortality After a Diagnosis of Ductal Carcinoma In Situ," *JAMA Oncol.* **1**, 888–896 (2015).
51. M. van Seijen, E. H. Lips, A. M. Thompson, S. Nik-Zainal, A. Futreal, E. S. Hwang, E. Verschuur, J. Lane, J. Jonkers, D. W. Rea, and J. Wesseling, "Ductal carcinoma in situ: to treat or not to treat, that is the question," *Br. J. Cancer* **121**, 285–292 (2019).
52. Australian Institute of Health and Welfare, Australian Institute of Health and Welfare, and National Breast and Ovarian Cancer Centre (Australia), eds., *Risk of Invasive Breast Cancer in Women Diagnosed with Ductal Carcinoma in Situ in Australia between 1995 and 2005*, Cancer Series No. no. 51 (Australian Institute of Health and Welfare, 2010).

53. D. L. Page, T. E. Kidd, W. D. Dupont, J. F. Simpson, and L. W. Rogers, "Lobular neoplasia of the breast: Higher risk for subsequent invasive cancer predicted by more extensive disease," *Hum. Pathol.* **22**, 1232–1239 (1991).
54. H. Y. Wen and E. Brogi, "Lobular Carcinoma in Situ," *Surg. Pathol. Clin.* **11**, 123–145 (2018).
55. G. N. Sharma, R. Dave, J. Sanadya, P. Sharma, and K. K. Sharma, "VARIOUS TYPES AND MANAGEMENT OF BREAST CANCER: AN OVERVIEW," *J. Adv. Pharm. Technol. Res.* **1**, 109–126 (2010).
56. J. Makki, "Diversity of Breast Carcinoma: Histological Subtypes and Clinical Relevance," *Clin. Med. Insights Pathol.* **8**, 23–31 (2015).
57. S. R. Lakhani, I. O. Ellis, and S. J. Schnitt, *WHO Classification of Tumours of the Breast* (International Agency for Research on Cancer (I A R C) (UN), 2012).
58. W. Street, "Breast Cancer Facts & Figures 2017-2018," 44 (n.d.).
59. L. C. Hartmann, A. C. Degnim, R. J. Santen, W. D. Dupont, and K. Ghosh, "Atypical Hyperplasia of the Breast — Risk Assessment and Management Options," *N. Engl. J. Med.* **372**, 78–89 (2015).
60. M. J. Worsham, U. Raju, M. Lu, A. Kapke, J. Cheng, and S. R. Wolman, "Multiplicity of Benign Breast Lesions Is a Risk Factor for Progression to Breast Cancer," *Clin. Cancer Res.* **13**, 5474–5479 (2007).
61. M. Morrow, J. White, J. Moughan, J. Owen, T. Pajack, J. Sylvester, J. Frank Wilson, and D. Winchester, "Factors Predicting the Use of Breast-Conserving Therapy in Stage I and II Breast Carcinoma," *J. Clin. Oncol.* **19**, 2254–2262 (2001).
62. J. C. Boughey, D. J. Attai, S. L. Chen, H. S. Cody, J. R. Dietz, S. M. Feldman, C. C. Greenberg, R. B. Kass, J. Landercasper, V. Lemaire, F. MacNeill, D. H. Song, A. C. Staley, L. G. Wilke, S. C. Willey, K. A. Yao, and J. A. Margenthaler, "Contralateral Prophylactic Mastectomy (CPM) Consensus Statement from the American Society of Breast Surgeons: Data on CPM Outcomes and Risks," *Ann. Surg. Oncol.* **23**, 3100–3105 (2016).
63. O. M. Fayanju, C. R. T. Stoll, S. Fowler, G. A. Colditz, and J. A. Margenthaler, "Contralateral Prophylactic Mastectomy after Unilateral Breast Cancer: A Systematic Review & Meta-Analysis," *Ann. Surg.* **260**, 1000–1010 (2014).
64. B. Fisher, S. Anderson, J. Bryant, R. G. Margolese, M. Deutsch, E. R. Fisher, J.-H. Jeong, and N. Wolmark, "Twenty-Year Follow-up of a Randomized Trial Comparing Total Mastectomy, Lumpectomy, and Lumpectomy plus Irradiation for the Treatment of Invasive Breast Cancer," *N. Engl. J. Med.* **347**, 1233–1241 (2002).
65. U. Veronesi, N. Cascinelli, L. Mariani, M. Greco, R. Saccozzi, A. Luini, M. Aguilar, and E. Marubini, "Twenty-Year Follow-up of a Randomized Study Comparing Breast-Conserving Surgery with Radical Mastectomy for Early Breast Cancer," *N. Engl. J. Med.* **347**, 1227–1232 (2002).
66. J. K. Harness, A. E. Giuliano, B. A. Pockaj, and E. Downs-Kelly, "Margins: A Status Report from the Annual Meeting of the American Society of Breast Surgeons," *Ann. Surg. Oncol.* **21**, 3192–3197 (2014).
67. J. L. Gwin, B. L. Eisenberg, J. P. Hoffman, F. D. Ottery, M. Boraas, and L. J. Solin, "Incidence of gross and microscopic carcinoma in specimens from patients with breast cancer after re-excision lumpectomy," *Ann. Surg.* **218**, 729–734 (1993).
68. A. Ratanawichitrasin, L. A. Rybicki, E. Steiger, S. Grundfest-Broniatowski, R. E. Hermann, and J. P. Crowe, "Predicting the likelihood of residual disease in women treated for ductal carcinoma in situ," *J. Am. Coll. Surg.* **188**, 17–21 (1999).
69. C. C. Park, M. Mitsumori, A. Nixon, A. Recht, J. Connolly, R. Gelman, B. Silver, S. Hetelekidis, A. Abner, J. R. Harris, and S. J. Schnitt, "Outcome at 8 years after breast-conserving surgery and radiation therapy for invasive breast cancer: influence of margin status and systemic therapy on local recurrence," *J. Clin. Oncol. Off. J. Am. Soc. Clin. Oncol.* **18**, 1668–1675 (2000).

70. M. Morrow, E. A. Strom, L. W. Bassett, D. D. Dershaw, B. Fowble, A. Giuliano, J. R. Harris, F. O'Malley, S. J. Schnitt, S. E. Singletary, and D. P. Winchester, "Standard for Breast Conservation Therapy in the Management of Invasive Breast Carcinoma," *CA. Cancer J. Clin.* **52**, 277–300 (2002).
71. R. G. Pleijhuis, M. Graafland, J. de Vries, J. Bart, J. S. de Jong, and G. M. van Dam, "Obtaining Adequate Surgical Margins in Breast-Conserving Therapy for Patients with Early-Stage Breast Cancer: Current Modalities and Future Directions," *Ann. Surg. Oncol.* **16**, 2717–2730 (2009).
72. M. F. Dillon, A. D. K. Hill, C. M. Quinn, E. W. McDermott, and N. O'Higgins, "A pathologic assessment of adequate margin status in breast-conserving therapy," *Ann. Surg. Oncol.* **13**, 333–339 (2006).
73. J. F. Waljee, E. S. Hu, L. A. Newman, and A. K. Alderman, "Predictors of Re-excision among Women Undergoing Breast-Conserving Surgery for Cancer," *Ann. Surg. Oncol.* **15**, 1297 (2008).
74. M. Morrow, R. Jagsi, A. K. Alderman, J. J. Griggs, S. T. Hawley, A. S. Hamilton, J. J. Graff, and S. J. Katz, "Surgeon recommendations and receipt of mastectomy for treatment of breast cancer," *JAMA* **302**, 1551–1556 (2009).
75. C. Dahlbäck, J. Manjer, M. Rehn, and A. Ringberg, "Determinants for patient satisfaction regarding aesthetic outcome and skin sensitivity after breast-conserving surgery," *World J. Surg. Oncol.* **14**, 303 (2016).
76. C. Baliski, L. Hughes, and B. Bakos, "Lowering Re-excision Rates After Breast-Conserving Surgery: Unraveling the Intersection Between Surgeon Case Volumes and Techniques," *Ann. Surg. Oncol.* **28**, 894–901 (2021).
77. W. Jung, E. Kang, S. M. Kim, D. Kim, Y. Hwang, Y. Sun, C. K. Yom, and S.-W. Kim, "Factors Associated with Re-excision after Breast-Conserving Surgery for Early-Stage Breast Cancer," *J. Breast Cancer* **15**, 412 (2012).
78. O. Riedl, F. Fitzal, N. Mader, P. Dubsy, M. Rudas, M. Mittlboeck, M. Gnant, and R. Jakesz, "Intraoperative frozen section analysis for breast-conserving therapy in 1016 patients with breast cancer," *Eur. J. Surg. Oncol. EJSO* **35**, 264–270 (2009).
79. J. M. Jorns, D. Visscher, M. Sabel, T. Breslin, P. Healy, S. Daignaut, J. L. Myers, and A. Wu, "Intraoperative frozen section analysis of margins in breast conserving surgery significantly decreases reoperative rates: one year experience at an ambulatory surgical center," *Am. J. Clin. Pathol.* **138**, 657–669 (2012).
80. E. R. St John, R. Al-Khudairi, H. Ashrafian, T. Athanasiou, Z. Takats, D. J. Hadjiminas, A. Darzi, and D. R. Leff, "Diagnostic Accuracy of Intraoperative Techniques for Margin Assessment in Breast Cancer Surgery: A Meta-analysis," *Ann. Surg.* **265**, 300–310 (2017).
81. K. Esbona, Z. Li, and L. G. Wilke, "Intraoperative imprint cytology and frozen section pathology for margin assessment in breast conservation surgery: a systematic review," *Ann. Surg. Oncol.* **19**, 3236–3245 (2012).
82. W. P. Weber, S. Engelberger, C. T. Viehl, R. Zanetti-Dallenbach, S. Kuster, S. Dirnhofer, D. Wruk, D. Oertli, and W. R. Marti, "Accuracy of Frozen Section Analysis Versus Specimen Radiography During Breast-Conserving Surgery for Nonpalpable Lesions," *World J. Surg.* **32**, 2599–2606 (2008).
83. M. Bakhshandeh, S. O. Tutuncuoglu, G. Fischer, and S. Masood, "Use of imprint cytology for assessment of surgical margins in lumpectomy specimens of breast cancer patients," *Diagn. Cytopathol.* **35**, 656–659 (2007).
84. F. D'Halluin, P. Tas, S. Rouquette, C. Bendavid, F. Foucher, H. Meshba, J. Blanchot, O. Coué, and J. Levêque, "Intra-operative touch preparation cytology following lumpectomy for breast cancer: A series of 400 procedures," *The Breast* **18**, 248–253 (2009).

85. E. K. Valdes, S. K. Boolbol, J.-M. Cohen, and S. M. Feldman, "Intra-operative touch preparation cytology; does it have a role in re-excision lumpectomy?," *Ann. Surg. Oncol.* **14**, 1045–1050 (2007).
86. J. S. Jeruss, K. K. Hunt, Y. Xing, S. Krishnamurthy, F. Meric-Bernstam, S. B. Cantor, M. I. Ross, and J. N. Cormier, "Is intraoperative touch imprint cytology of sentinel lymph nodes in patients with breast cancer cost effective?," *Cancer* **107**, 2328–2336 (2006).
87. S. H. H. Kim, S. D. Cornacchi, B. Heller, F. Farrokhyar, M. Babra, and P. J. Lovrics, "An evaluation of intraoperative digital specimen mammography versus conventional specimen radiography for the excision of nonpalpable breast lesions," *Am. J. Surg.* **205**, 703–710 (2013).
88. M. Muttalib, M. Tisdall, R. Scawn, S. Shousha, R. S. Cummins, and H. D. Sinnett, "Intra-operative specimen analysis using faxitron microradiography for excision of mammographically suspicious, non-palpable breast lesions," *The Breast* **13**, 307–315 (2004).
89. T. Ihrai, D. Quaranta, Y. Fouche, J.-C. Machiavello, I. Raoust, C. Chapellier, C. Maestro, M. Marcy, J.-M. Ferrero, and B. Flipo, "Intraoperative radiological margin assessment in breast-conserving surgery," *Eur. J. Surg. Oncol.* **40**, 449–453 (2014).
90. C. S. Kaufman, L. Jacobson, B. A. Bachman, L. B. Kaufman, C. Mahon, L.-J. Gambrell, R. Seymour, J. Briscoe, K. Aulisio, A. Cunningham, F. Opstad, N. Schnell, J. Robertson, and L. Oliver, "Intraoperative Digital Specimen Mammography: Rapid, Accurate Results Expedite Surgery," *Ann. Surg. Oncol.* **14**, 1478–1485 (2007).
91. C. Rua, P. Lebas, P. Michenet, and L. Ouldamer, "Evaluation of lumpectomy surgical specimen radiographs in subclinical, in situ and invasive breast cancer, and factors predicting positive margins," *Diagn. Interv. Imaging* **93**, 871–877 (2012).
92. A. Philpott, J. Wong, K. Elder, A. Gorelik, G. B. Mann, and A. Skandarajah, "Factors influencing reoperation following breast-conserving surgery," *ANZ J. Surg.* **88**, 922–927 (2018).
93. R. Santambrogio, E. Opocher, A. P. Ceretti, M. Barabino, M. Costa, S. Leone, and M. Montorsi, "Impact of intraoperative ultrasonography in laparoscopic liver surgery," *Surg. Endosc.* **21**, 181–188 (2007).
94. N. Colakovic, D. Zdravkovic, Z. Skuric, D. Mrda, J. Gacic, and N. Ivanovic, "Intraoperative ultrasound in breast cancer surgery—from localization of non-palpable tumors to objectively measurable excision," *World J. Surg. Oncol.* **16**, 184 (2018).
95. H. Karanlik, I. Ozgur, D. Sahin, M. Fayda, S. Onder, and E. Yavuz, "Intraoperative ultrasound reduces the need for re-excision in breast-conserving surgery," *World J. Surg. Oncol.* **13**, 321 (2015).
96. A. D. Gerrard and A. Shrotri, "Surgeon-led Intraoperative Ultrasound Localization for Nonpalpable Breast Cancers: Results of 5 Years of Practice," *Clin. Breast Cancer* **19**, e748–e752 (2019).
97. C. M. Sehgal, S. P. Weinstein, P. H. Arger, and E. F. Conant, "A Review of Breast Ultrasound," *J. Mammary Gland Biol. Neoplasia* **11**, 113–123 (2006).
98. M. A. Pinkert, L. R. Salkowski, P. J. Keely, T. J. Hall, W. F. Block, and K. W. Eliceiri, "Review of quantitative multiscale imaging of breast cancer," *J. Med. Imaging* **5**, 010901 (2018).
99. A. Evans, P. Whelehan, K. Thomson, D. McLean, K. Brauer, C. Purdie, L. Jordan, L. Baker, and A. Thompson, "Quantitative shear wave ultrasound elastography: initial experience in solid breast masses," *Breast Cancer Res. BCR* **12**, R104 (2010).
100. S. Wojcinski, A. Farrokh, S. Weber, A. Thomas, T. Fischer, T. Slowinski, W. Schmidt, and F. Degenhardt, "Multicenter Study of Ultrasound Real-Time Tissue Elastography in 779 Cases for the Assessment of Breast Lesions: Improved

- Diagnostic Performance by Combining the BI-RADS®-US Classification System with Sonoelastography," *Ultraschall Med. - Eur. J. Ultrasound* **31**, 484–491 (2010).
101. D. O. Cosgrove, W. A. Berg, C. J. Doré, D. M. Skyba, J.-P. Henry, J. Gay, C. Cohen-Bacrie, and the BE1 Study Group, "Shear wave elastography for breast masses is highly reproducible," *Eur. Radiol.* **22**, 1023–1032 (2012).
 102. P. Ricci, E. Maggini, E. Mancuso, P. Lodise, V. Cantisani, and C. Catalano, "Clinical application of breast elastography: State of the art," *Eur. J. Radiol.* **83**, 429–437 (2014).
 103. T. Shiina, K. R. Nightingale, M. L. Palmeri, T. J. Hall, J. C. Bamber, R. G. Barr, L. Castera, B. I. Choi, Y.-H. Chou, D. Cosgrove, C. F. Dietrich, H. Ding, D. Amy, A. Farrokh, G. Ferraioli, C. Filice, M. Friedrich-Rust, K. Nakashima, F. Schafer, I. Sporea, S. Suzuki, S. Wilson, and M. Kudo, "WFUMB Guidelines and Recommendations for Clinical Use of Ultrasound Elastography: Part 1: Basic Principles and Terminology," *Ultrasound Med. Biol.* **41**, 1126–1147 (2015).
 104. A. M. Zysk, K. Chen, E. Gabrielson, L. Tafra, E. A. M. Gonzalez, J. K. Canner, E. B. Schneider, A. J. Cittadine, P. S. Carney, S. A. Boppart, K. Tsuchiya, K. Sawyer, and L. K. Jacobs, "Intraoperative Assessment of Final Margins with a Handheld Optical Imaging Probe During Breast-Conserving Surgery May Reduce the Reoperation Rate: Results of a Multicenter Study," *Ann. Surg. Oncol.* **22**, 3356–3362 (2015).
 105. K. M. Kennedy, R. Zilkens, W. M. Allen, K. Y. Foo, Q. Fang, L. Chin, R. W. Sanderson, J. Anstie, P. Wijesinghe, A. Curatolo, H. E. I. Tan, N. Morin, B. Kunjuraman, C. Yeomans, S. L. Chin, H. DeJong, K. Giles, B. F. Dessauvague, B. Latham, C. M. Saunders, and B. F. Kennedy, "Diagnostic Accuracy of Quantitative Micro-Elastography for Margin Assessment in Breast-Conserving Surgery," *Cancer Res.* **80**, 1773–1783 (2020).
 106. K. M. Kennedy, L. Chin, R. A. McLaughlin, B. Latham, C. M. Saunders, D. D. Sampson, and B. F. Kennedy, "Quantitative micro-elastography: imaging of tissue elasticity using compression optical coherence elastography," *Sci. Rep.* **5**, (2015).
 107. M. E. van Baar, "Epidemiology of Scars and Their Consequences: Burn Scars," in *Textbook on Scar Management: State of the Art Management and Emerging Technologies*, L. Téot, T. A. Mustoe, E. Middelkoop, and G. G. Gauglitz, eds. (Springer International Publishing, 2020), pp. 37–43.
 108. "Injury in Australia: Burns and other thermal causes," <https://www.aihw.gov.au/reports/injury/burns-and-other-thermal-causes>.
 109. E. N. Gangemi, D. Gregori, P. Berchiolla, E. Zingarelli, M. Cairo, D. Bollero, J. Ganem, R. Capocelli, F. Cuccuru, P. Cassano, D. Risso, and M. Stella, "Epidemiology and Risk Factors for Pathologic Scarring After Burn Wounds," *ARCH FACIAL PLAST SURG* **10**, 10 (2008).
 110. H. J. Wallace, M. W. Fear, M. M. Crowe, L. J. Martin, and F. M. Wood, "Identification of factors predicting scar outcome after burn in adults: A prospective case–control study," *Burns* **43**, 1271–1283 (2017).
 111. N. Brusselaers, S. Monstrey, D. Vogelaers, E. Hoste, and S. Blot, "Severe burn injury in europe: a systematic review of the incidence, etiology, morbidity, and mortality," *Crit. Care* **14**, R188 (2010).
 112. M. Sengoelge, Z. El-Khatib, and L. Laflamme, "The global burden of child burn injuries in light of country level economic development and income inequality," *Prev. Med. Rep.* **6**, 115–120 (2017).
 113. M. G. Jeschke, M. E. van Baar, M. A. Choudhry, K. K. Chung, N. S. Gibran, and S. Logsetty, "Burn injury," *Nat. Rev. Dis. Primer* **6**, (2020).
 114. "How a wound heals itself - Sarthak Sinha," <https://ed.ted.com/lessons/how-a-wound-heals-itself-sarthak-sinha>.

115. Y. Qin, "7 - Functional wound dressings," in *Medical Textile Materials*, Y. Qin, ed., Woodhead Publishing Series in Textiles (Woodhead Publishing, 2016), pp. 89–107.
116. "Wound Healing & OCT," <https://wasatchphotonics.com/applications/wound-healing-oct/>.
117. F. B. Rabello, C. D. Souza, and J. A. F. Júnior, "Update on hypertrophic scar treatment," *Clinics* **69**, 565–573 (2014).
118. C.-Y. Huang, C.-H. Feng, Y.-C. Hsiao, S. S. Chuang, and J.-Y. Yang, "Burn scar carcinoma," *J. Dermatol. Treat.* **21**, 350–356 (2010).
119. C. Huang, L. Liu, Z. You, Z. Wu, Y. Du, and R. Ogawa, "Clinical and Pathological Diagnosis of Scars," in *Total Scar Management: From Lasers to Surgery for Scars, Keloids, and Scar Contractures*, R. Ogawa, ed. (Springer, 2020), pp. 83–95.
120. M. T. Clementoni and E. Azzopardi, "Specific Attention Areas in Scar Management: Management of Atrophic Scars," in *Textbook on Scar Management: State of the Art Management and Emerging Technologies*, L. Téot, T. A. Mustoe, E. Middelkoop, and G. G. Gauglitz, eds. (Springer International Publishing, 2020), pp. 353–362.
121. J. Moon, J. Y. Yoon, J. H. Yang, H. H. Kwon, S. Min, and D. H. Suh, "Atrophic acne scar: a process from altered metabolism of elastic fibres and collagen fibres based on transforming growth factor- β 1 signalling," *Br. J. Dermatol.* **181**, 1226–1237 (2019).
122. G. G. Gauglitz, H. C. Korting, T. Pavicic, T. Ruzicka, and M. G. Jeschke, "Hypertrophic scarring and keloids: pathomechanisms and current and emerging treatment strategies," *Mol. Med. Camb. Mass* **17**, 113–125 (2011).
123. C. C. Finnerty, M. G. Jeschke, L. K. Branski, J. P. Barret, P. Dziewulski, and D. N. Herndon, "Hypertrophic scarring: the greatest unmet challenge after burn injury," *The Lancet* **388**, 1427–1436 (2016).
124. W. M. van der Veer, M. C. T. Bloemen, M. M. W. Ulrich, G. Molema, P. P. van Zuijlen, E. Middelkoop, and F. B. Niessen, "Potential cellular and molecular causes of hypertrophic scar formation," *Burns* **35**, 15–29 (2009).
125. J. C. Murray, "Keloids and hypertrophic scars," *Clin. Dermatol.* **12**, 27–37 (1994).
126. I. F. Muir, "On the nature of keloid and hypertrophic scars," *Br. J. Plast. Surg.* **43**, 61–69 (1990).
127. A. Al-Attar, S. Mess, J. M. Thomassen, C. L. Kauffman, and S. P. Davison, "Keloid Pathogenesis and Treatment," *Plast. Reconstr. Surg.* **117**, 286–300 (2006).
128. J. C. Schneider, R. Holavanahalli, P. Helm, R. Goldstein, and K. Kowalske, "Contractures in Burn Injury: Defining the Problem," *J. Burn Care Res.* **27**, 508–514 (2006).
129. B. Leblebici, M. Adam, S. Bağış, A. M. Tarim, T. Noyan, M. N. Akman, and M. A. Haberal, "Quality of Life After Burn Injury: The Impact of Joint Contracture," *J. Burn Care Res.* **27**, 864–868 (2006).
130. A. M. Oosterwijk, L. J. Mouton, H. Schouten, L. M. Disseldorp, C. P. van der Schans, and M. K. Nieuwenhuis, "Prevalence of scar contractures after burn: A systematic review," *Burns* **43**, 41–49 (2017).
131. S. Ud-Din and A. Bayat, "Classification of Distinct Endotypes in Human Skin Scarring: S.C.A.R.—A Novel Perspective on Dermal Fibrosis," *Adv. Wound Care* (2021).
132. A. Anzarut, J. Olson, P. Singh, B. H. Rowe, and E. E. Tredget, "The effectiveness of pressure garment therapy for the prevention of abnormal scarring after burn injury: a meta-analysis," *J. Plast. Reconstr. Aesthet. Surg.* **62**, 77–84 (2009).
133. G. Juckett and H. Hartman-Adams, "Management of Keloids and Hypertrophic Scars," *Am. Fam. Physician* **80**, 253–260 (2009).
134. Y. S. Cho, J. H. Jeon, A. Hong, H. T. Yang, H. Yim, Y. S. Cho, D. H. Kim, J. Hur, J. H. Kim, W. Chun, B. C. Lee, and C. H. Seo, "The effect of burn rehabilitation

- massage therapy on hypertrophic scar after burn: A randomized controlled trial," *Burns* **40**, 1513–1520 (2014).
135. T. S. Alster, "Improvement of erythematous and hypertrophic scars by the 585-nm flashlamp-pumped pulsed dye laser," *Ann. Plast. Surg.* **32**, 186–190 (1994).
 136. J. Poetschke and G. G. Gauglitz, "Treatment of Immature Scars: Evidence-Based Techniques and Treatments," in *Textbook on Scar Management: State of the Art Management and Emerging Technologies*, L. Téot, T. A. Mustoe, E. Middelkoop, and G. G. Gauglitz, eds. (Springer International Publishing, 2020), pp. 193–201.
 137. R. Fearmonti, J. Bond, D. Erdmann, and H. Levinson, "A Review of Scar Scales and Scar Measuring Devices," *Eplasty* **10**, (2010).
 138. Z. F. Tyack, S. Pegg, and J. Ziviani, "Postburn Dyspigmentation: Its Assessment, Management, and Relationship to Scarring—A Review of the Literature," *J. Burn Care Rehabil.* **18**, 435–440 (1997).
 139. L. J. Draaijers, F. R. H. Tempelman, Y. A. M. Botman, R. W. Kreis, E. Middelkoop, and P. P. M. van Zuijlen, "Colour evaluation in scars: tristimulus colorimeter, narrow-band simple reflectance meter or subjective evaluation?," *Burns* **30**, 103–107 (2004).
 140. P. D. H. M. Verhaegen, M. B. A. van der Wal, E. Middelkoop, and P. P. M. van Zuijlen, "Objective Scar Assessment Tools: A Clinimetric Appraisal," *Plast. Reconstr. Surg.* **127**, 1561–1570 (2011).
 141. J. Hambleton, P. G. Shakespeare, and B. J. Pratt, "The progress of hypertrophic scars monitored by ultrasound measurements of thickness," *Burns* **18**, 301–307 (1992).
 142. X.-Q. Wang, J. Mill, O. Kravchuk, and R. M. Kimble, "Ultrasound assessed thickness of burn scars in association with laser Doppler imaging determined depth of burns in paediatric patients," *Burns* **36**, 1254–1262 (2010).
 143. G. V. Oliveira, D. Chinkes, C. Mitchell, G. Oliveras, H. K. Hawkins, and D. N. Herndon, "Objective Assessment of Burn Scar Vascularity, Erythema, Pliability, Thickness, and Planimetry," *Dermatol. Surg.* **31**, 48–58 (2005).
 144. P. P. M. van Zuijlen, A. P. Angeles, M. H. Suijker, R. W. Kreis, and E. Middelkoop, "Reliability and accuracy of techniques for surface area measurements of wounds and scars," *Int. J. Low. Extrem. Wounds* **3**, 7–11 (2004).
 145. K. C. Lee, J. Dretzke, L. Grover, A. Logan, and N. Moiemmen, "A systematic review of objective burn scar measurements," *Burns Trauma* **4**, (2016).
 146. I. Lye, D. W. Edgar, F. M. Wood, and S. Carroll, "Tissue Tonometry Is a Simple, Objective Measure for Pliability of Burn Scar: Is It Reliable?," *J. Burn Care Res.* **27**, 82–85 (2006).
 147. J. Zuccaro, M. M. Perez, A. Mohanta, J. S. Fish, and A. S. Doria, "Quantification of Pediatric Burn Scar Stiffness Using Acoustic Radiation Force Impulse Ultrasound Elastography," *Ultrasound Med. Biol.* **45**, 1918–1923 (2019).
 148. H. DeJong, S. Abbott, M. Zelesco, K. Spilsbury, L. Martin, R. Sanderson, M. Ziman, B. F. Kennedy, and F. M. Wood, "A Novel, Reliable Protocol to Objectively Assess Scar Stiffness Using Shear Wave Elastography," *Ultrasound Med. Biol.* **46**, 1614–1629 (2020).
 149. H. DeJong, S. Abbott, M. Zelesco, K. Spilsbury, M. Ziman, B. F. Kennedy, L. Martin, and F. M. Wood, "Objective quantification of burn scar stiffness using shear-wave elastography: Initial evidence of validity," *Burns* **46**, 1787–1798 (2020).
 150. K. A. Arsenaault, J. McDonald, P. J. Devereaux, K. Thorlund, J. G. Tittley, and R. P. Whitlock, "The use of transcutaneous oximetry to predict complications of chronic wound healing: a systematic review and meta-analysis," *Wound Repair Regen. Off. Publ. Wound Heal. Soc. Eur. Tissue Repair Soc.* **19**, 657–663 (2011).

151. K. D. Paepe, E. Houben, R. Adam, F. Wiesemann, and V. Rogiers, "Validation of the VapoMeter, a closed unventilated chamber system to assess transepidermal water loss vs. the open chamber Tewameter®," *Skin Res. Technol.* **11**, 61–69 (2005).
152. K. L. M. Gardien, D. C. Baas, H. C. W. de Vet, and E. Middelkoop, "Transepidermal water loss measured with the Tewameter TM300 in burn scars," *Burns* **42**, 1455–1462 (2016).
153. K. J. Parker, M. M. Doyley, and D. J. Rubens, "Imaging the elastic properties of tissue: the 20 year perspective," *Phys. Med. Biol.* **56**, R1–R29 (2011).
154. B. F. Kennedy, K. M. Kennedy, A. L. Oldenburg, S. G. Adie, S. A. Boppart, and D. D. Sampson, "Optical Coherence Elastography," in *Optical Coherence Tomography: Technology and Applications*, W. Drexler and J. G. Fujimoto, eds. (Springer International Publishing, 2015), pp. 1007–1054.
155. B. F. Kennedy, P. Wijesinghe, and D. D. Sampson, "The emergence of optical elastography in biomedicine," *Nat. Photonics* **11**, 215–221 (2017).
156. P. G. Newman and G. S. Rozycki, "THE HISTORY OF ULTRASOUND," *Surg. Clin. North Am.* **78**, 179–195 (1998).
157. N. Malhotra, P. K. Shah, P. Acharya, S. Panchal, and J. Malhotra, *Ultrasound in Obstetrics & Gynecology* (JP Medical Ltd, 2014).
158. I. Donald, J. Macvicar, and T. G. Brown, "INVESTIGATION OF ABDOMINAL MASSES BY PULSED ULTRASOUND," *The Lancet* **271**, 1188–1195 (1958).
159. J.-L. Gennisson, T. Defieux, M. Fink, and M. Tanter, "Ultrasound elastography: Principles and techniques," *Diagn. Interv. Imaging* **94**, 487–495 (2013).
160. R. M. Lerner, K. J. Parker, J. Holen, R. Gramiak, and R. C. Waag, "Sono-Elasticity: Medical Elasticity Images Derived from Ultrasound Signals in Mechanically Vibrated Targets," in *Acoustical Imaging: Proceedings of the Sixteenth International Symposium, June 10–12, 1987*, L. W. Kessler, ed., Acoustical Imaging (Springer US, 1988), pp. 317–327.
161. K. J. Parker, S. R. Huang, R. A. Musulin, and R. M. Lerner, "Tissue response to mechanical vibrations for "sonoelasticity imaging,"" *Ultrasound Med. Biol.* **16**, 241–246 (1990).
162. Z. Wu, L. S. Taylor, D. J. Rubens, and K. J. Parker, "Sonoelastographic imaging of interference patterns for estimation of the shear velocity of homogeneous biomaterials," *Phys. Med. Biol.* **49**, 911–922 (2004).
163. J. Ophir, I. Céspedes, H. Ponnekanti, Y. Yazdi, and X. Li, "Elastography: A Quantitative Method for Imaging the Elasticity of Biological Tissues," *Ultrason. Imaging* **13**, 111–134 (1991).
164. B. S. Garra, "Elastography: history, principles, and technique comparison," *Abdom. Imaging* **40**, 680–697 (2015).
165. A. P. Sarvazyan, O. V. Rudenko, S. D. Swanson, J. B. Fowlkes, and S. Y. Emelianov, "Shear wave elasticity imaging: a new ultrasonic technology of medical diagnostics," *Ultrasound Med. Biol.* **24**, 1419–1435 (1998).
166. N. Frulio and H. Trillaud, "Ultrasound elastography in liver," *Diagn. Interv. Imaging* **94**, 515–534 (2013).
167. W. K. Jeong, H. K. Lim, H.-K. Lee, J. M. Jo, and Y. Kim, "Principles and clinical application of ultrasound elastography for diffuse liver disease," *Ultrasonography* **33**, 149–160 (2014).
168. M. Kudo, T. Shiina, F. Moriyasu, H. Iijima, R. Tateishi, N. Yada, K. Fujimoto, H. Morikawa, M. Hirooka, Y. Sumino, and T. Kumada, "JSUM ultrasound elastography practice guidelines: liver," *J. Med. Ultrason.* **40**, 325–357 (2013).
169. R. M. S. Sigrist, J. Liau, A. E. Kaffas, M. C. Chammass, and J. K. Willmann, "Ultrasound Elastography: Review of Techniques and Clinical Applications," *Theranostics* **7**, 1303–1329 (2017).

170. H. Zhi, B. Ou, B.-M. Luo, X. Feng, Y.-L. Wen, and H.-Y. Yang, "Comparison of Ultrasound Elastography, Mammography, and Sonography in the Diagnosis of Solid Breast Lesions," *J. Ultrasound Med.* **26**, 807–815 (2007).
171. T. Rago, F. Santini, M. Scutari, A. Pinchera, and P. Vitti, "Elastography: New Developments in Ultrasound for Predicting Malignancy in Thyroid Nodules," *J. Clin. Endocrinol. Metab.* **92**, 2917–2922 (2007).
172. M. Giovannini, T. Botelberge, E. Bories, C. Pesenti, F. Caillol, B. Esterni, G. Monges, P. Arcidiacono, P. Deprez, R. Yeung, W. Schimdt, H. Schrader, C. Szymanski, C. Dietrich, P. Eisendrath, J.-L. Van Laethem, J. Devière, P. Vilmann, and A. Saftoiu, "Endoscopic ultrasound elastography for evaluation of lymph nodes and pancreatic masses: A multicenter study," *World J. Gastroenterol. WJG* **15**, 1587–1593 (2009).
173. R. G. Barr, R. Memo, and C. R. Schaub, "Shear Wave Ultrasound Elastography of the Prostate: Initial Results," *Ultrasound Q.* **28**, 13–20 (2012).
174. M. Dhyani, A. Anvari, and A. E. Samir, "Ultrasound elastography: liver," *Abdom. Imaging* **40**, 698–708 (2015).
175. E. A. Tsochatzis, K. S. Gurusamy, S. Ntaoula, E. Cholongitas, B. R. Davidson, and A. K. Burroughs, "Elastography for the diagnosis of severity of fibrosis in chronic liver disease: A meta-analysis of diagnostic accuracy," *J. Hepatol.* **54**, 650–659 (2011).
176. B. S. Garra, E. I. Cespedes, J. Ophir, S. R. Spratt, R. A. Zuurbier, C. M. Magnant, and M. F. Pennanen, "Elastography of breast lesions: initial clinical results," *Radiology* **202**, 79–86 (1997).
177. T. J. Hall, Y. Zhu, and C. S. Spalding, "In vivo real-time freehand palpation imaging," *Ultrasound Med. Biol.* **29**, 427–435 (2003).
178. E. S. Burnside, T. J. Hall, A. M. Sommer, G. K. Hesley, G. A. Sisney, W. E. Svensson, J. P. Fine, J. Jiang, and N. J. Hangiandreou, "Differentiating Benign from Malignant Solid Breast Masses with US Strain Imaging," *Radiology* **245**, 401–410 (2007).
179. Y.-M. Sohn, M. J. Kim, E.-K. Kim, J. Y. Kwak, H. J. Moon, and S. J. Kim, "Sonographic elastography combined with conventional sonography: how much is it helpful for diagnostic performance?," *J. Ultrasound Med. Off. J. Am. Inst. Ultrasound Med.* **28**, 413–420 (2009).
180. H. Zhi, X.-Y. Xiao, H.-Y. Yang, Y.-L. Wen, B. Ou, B.-M. Luo, and B. Liang, "Semi-quantitating Stiffness of Breast Solid Lesions in Ultrasonic Elastography," *Acad. Radiol.* **15**, 1347–1353 (2008).
181. G. Sadigh, R. C. Carlos, C. H. Neal, and B. A. Dwamena, "Accuracy of quantitative ultrasound elastography for differentiation of malignant and benign breast abnormalities: a meta-analysis," *Breast Cancer Res. Treat.* **134**, 923–931 (2012).
182. H. J. Kim, S. M. Kim, B. Kim, B. La Yun, M. Jang, Y. Ko, S. H. Lee, H. Jeong, J. M. Chang, and N. Cho, "Comparison of strain and shear wave elastography for qualitative and quantitative assessment of breast masses in the same population," *Sci. Rep.* **8**, 6197 (2018).
183. R. Damadian, "Tumor Detection by Nuclear Magnetic Resonance," *Science* **171**, 1151–1153 (1971).
184. S. W. Atlas, *Magnetic Resonance Imaging of the Brain and Spine* (Lippincott Williams & Wilkins, 2009).
185. D. A. Hamstra, A. Rehemtulla, and B. D. Ross, "Diffusion Magnetic Resonance Imaging: A Biomarker for Treatment Response in Oncology," *J. Clin. Oncol.* **25**, 4104–4109 (2007).
186. S. B. Reeder and C. B. Sirlin, "Quantification of Liver Fat with Magnetic Resonance Imaging," *Magn. Reson. Imaging Clin.* **18**, 337–357 (2010).

187. S. K. Venkatesh and R. L. Ehman, "Introduction," in *Magnetic Resonance Elastography*, S. K. Venkatesh and R. L. Ehman, eds. (Springer, 2014), pp. 1–1.
188. K. J. Glaser and R. L. Ehman, "Perspectives on the Development of Elastography," in *Magnetic Resonance Elastography*, S. K. Venkatesh and R. L. Ehman, eds. (Springer, 2014), pp. 3–18.
189. Y. K. Mariappan, K. J. Glaser, and R. L. Ehman, "Magnetic resonance elastography: A review," *Clin. Anat.* **23**, 497–511 (2010).
190. S. Hoodeshenas, M. Yin, and S. K. Venkatesh, "Magnetic Resonance Elastography of Liver- Current Update," *Top. Magn. Reson. Imaging TMRI* **27**, 319–333 (2018).
191. Y. Liang and D. Li, "Magnetic resonance elastography in staging liver fibrosis in non-alcoholic fatty liver disease: a pooled analysis of the diagnostic accuracy," *BMC Gastroenterol.* **20**, 89 (2020).
192. R. Loomba, T. Wolfson, B. Ang, J. Hooker, C. Behling, M. Peterson, M. Valasek, G. Lin, D. Brenner, A. Gamst, R. Ehman, and C. Sirlin, "Magnetic resonance elastography predicts advanced fibrosis in patients with nonalcoholic fatty liver disease: A prospective study," *Hepatology* **60**, 1920–1928 (2014).
193. S. A. Kruse, G. H. Rose, K. J. Glaser, A. Manduca, J. P. Felmlee, C. R. Jack, and R. L. Ehman, "Magnetic resonance elastography of the brain," *NeuroImage* **39**, 231–237 (2008).
194. P. J. McCracken, A. Manduca, J. Felmlee, and R. L. Ehman, "Mechanical transient-based magnetic resonance elastography," *Magn. Reson. Med.* **53**, 628–639 (2005).
195. L. Xu, Y. Lin, J. C. Han, Z. N. Xi, H. Shen, and P. Y. Gao, "Magnetic resonance elastography of brain tumors: preliminary results," *Acta Radiol.* **48**, 327–330 (2007).
196. M. C. Murphy, J. Huston, C. R. Jack, K. J. Glaser, A. Manduca, J. P. Felmlee, and R. L. Ehman, "Decreased brain stiffness in Alzheimer's disease determined by magnetic resonance elastography," *J. Magn. Reson. Imaging* **34**, 494–498 (2011).
197. B. M. Sandroff, C. L. Johnson, and R. W. Motl, "Exercise training effects on memory and hippocampal viscoelasticity in multiple sclerosis: a novel application of magnetic resonance elastography," *Neuroradiology* **59**, 61–67 (2017).
198. M. C. Murphy, J. Huston, K. J. Glaser, A. Manduca, F. B. Meyer, G. Lanzino, J. M. Morris, J. P. Felmlee, and R. L. Ehman, "Preoperative assessment of meningioma stiffness using magnetic resonance elastography: Clinical article," *J. Neurosurg.* **118**, 643–648 (2013).
199. J. D. Hughes, N. Fattahi, J. Van Gompel, A. Arani, F. Meyer, G. Lanzino, M. J. Link, R. Ehman, and J. Huston, "Higher-Resolution Magnetic Resonance Elastography in Meningiomas to Determine Intratumoral Consistency," *Neurosurgery* **77**, 653–658; discussion 658-659 (2015).
200. V. Y. Zaitsev, A. L. Matveyev, L. A. Matveev, A. A. Sovetsky, M. S. Hepburn, A. Mowla, and B. F. Kennedy, "Strain and elasticity imaging in compression optical coherence elastography: the two-decade perspective and recent advances," *J. Biophotonics* **n/a**, e202000257 (n.d.).
201. B. F. Kennedy, F. G. Malheiro, L. Chin, and D. D. Sampson, "Three-dimensional optical coherence elastography by phase-sensitive comparison of C-scans," *J. Biomed. Opt.* **19**, 076006 (2014).
202. G. Scarcelli and S. H. Yun, "Confocal Brillouin microscopy for three-dimensional mechanical imaging," *Nat. Photonics* **2**, 39–43 (2008).
203. R. Leitgeb, C. K. Hitzenberger, and A. F. Fercher, "Performance of fourier domain vs. time domain optical coherence tomography," *Opt. Express* **11**, 889–894 (2003).
204. J. Kim, W. Brown, J. R. Maher, H. Levinson, and A. Wax, "Functional optical coherence tomography: principles and progress," *Phys. Med. Biol.* **60**, R211–R237 (2015).

205. S. Marschall, B. Sander, M. Mogensen, T. M. Jørgensen, and P. E. Andersen, "Optical coherence tomography—current technology and applications in clinical and biomedical research," *Anal. Bioanal. Chem.* **400**, 2699–2720 (2011).
206. C. Li, G. Guan, Y. Ling, Y. T. Hsu, S. Song, J. T. J. Huang, S. Lang, R. K. Wang, Z. Huang, and G. Nabi, "Detection and characterisation of biopsy tissue using quantitative optical coherence elastography (OCE) in men with suspected prostate cancer," *Cancer Lett.* **357**, 121–128 (2015).
207. A. A. Plekhanov, M. A. Sirotkina, A. A. Sovetsky, E. V. Gubarkova, E. B. Kiseleva, V. Y. Zaitsev, L. A. Matveev, A. L. Matveyev, S. S. Kuznetsov, E. V. Zagaynova, and N. D. Gladkova, "Optical coherence elastography as a new method for estimation of chemotherapy efficacy on triple-negative breast cancer in the experiment," in *Saratov Fall Meeting 2018: Optical and Nano-Technologies for Biology and Medicine* (International Society for Optics and Photonics, 2019), Vol. 11065, p. 1106506.
208. M. A. Kirby, I. Pelivanov, S. Song, L. Ambrozinski, S. J. Yoon, L. Gao, D. Li, T. T. Shen, R. K. Wang, and M. O'Donnell, "Optical coherence elastography in ophthalmology," *J. Biomed. Opt.* **22**, 121720 (2017).
209. A. Nair, M. Singh, S. Aglyamov, and K. V. Larin, "Heartbeat optical coherence elastography: corneal biomechanics in vivo," *J. Biomed. Opt.* **26**, 020502 (2021).
210. F. Zvietcovich, A. Nair, Y. S. Ambekar, M. Singh, S. R. Aglyamov, M. D. Twa, and K. V. Larin, "Confocal air-coupled ultrasonic optical coherence elastography probe for quantitative biomechanics," *Opt. Lett.* **45**, 6567–6570 (2020).
211. R. A. Leitgeb, R. M. Werkmeister, C. Blatter, and L. Schmetterer, "Doppler Optical Coherence Tomography," *Prog. Retin. Eye Res.* **41**, 26–43 (2014).
212. J. F. de Boer, C. K. Hitzenberger, and Y. Yasuno, "Polarization sensitive optical coherence tomography - a review [Invited]," *Biomed. Opt. Express* **8**, 1838–1873 (2017).
213. P. Gong, M. Almasian, G. van Soest, D. M. de Bruin, T. G. van Leeuwen, D. D. Sampson, and D. J. Faber, "Parametric imaging of attenuation by optical coherence tomography: review of models, methods, and clinical translation," *J. Biomed. Opt.* **25**, 040901 (2020).
214. L. Brillouin, "Diffusion de la lumière et des rayons X par un corps transparent homogène - Influence de l'agitation thermique," *Ann. Phys.* **9**, 88–122 (1922).
215. G. Antonacci, R. M. Pedrigi, A. Kondiboyina, V. V. Mehta, R. de Silva, C. Paterson, R. Krams, and P. Török, "Quantification of plaque stiffness by Brillouin microscopy in experimental thin cap fibroatheroma," *J. R. Soc. Interface* **12**, 20150843 (2015).
216. G. Antonacci, M. R. Foreman, C. Paterson, and P. Török, "Spectral broadening in Brillouin imaging," *Appl. Phys. Lett.* **103**, 221105 (2013).
217. G. Scarcelli, R. Pineda, and S. H. Yun, "Brillouin Optical Microscopy for Corneal Biomechanics," *Invest. Ophthalmol. Vis. Sci.* **53**, 185–190 (2012).
218. C. W. Ballmann, J. V. Thompson, A. J. Traverso, Z. Meng, M. O. Scully, and V. V. Yakovlev, "Stimulated Brillouin Scattering Microscopic Imaging," *Sci. Rep.* **5**, 18139 (2015).
219. G. Scarcelli, W. J. Polacheck, H. T. Nia, K. Patel, A. J. Grodzinsky, R. D. Kamm, and S. H. Yun, "Noncontact three-dimensional mapping of intracellular hydromechanical properties by Brillouin microscopy," *Nat. Methods* **12**, 1132–1134 (2015).
220. G. Scarcelli, P. Kim, and S. H. Yun, "In Vivo Measurement of Age-Related Stiffening in the Crystalline Lens by Brillouin Optical Microscopy," *Biophys. J.* **101**, 1539–1545 (2011).
221. G. Scarcelli, S. Kling, E. Quijano, R. Pineda, S. Marcos, and S. H. Yun, "Brillouin Microscopy of Collagen Crosslinking: Noncontact Depth-Dependent Analysis of Corneal Elastic Modulus," *Invest. Ophthalmol. Vis. Sci.* **54**, 1418–1425 (2013).

222. G. Scarcelli, S. Besner, R. Pineda, P. Kalout, and S. H. Yun, "In Vivo Biomechanical Mapping of Normal and Keratoconus Corneas," *JAMA Ophthalmol.* **133**, 480–482 (2015).
223. I. Remer and A. Bilenca, "Background-free Brillouin spectroscopy in scattering media at 780 nm via stimulated Brillouin scattering," *Opt. Lett.* **41**, 926–929 (2016).
224. C. W. Ballmann, Z. Meng, A. J. Traverso, M. O. Scully, and V. V. Yakovlev, "Impulsive Brillouin microscopy," *Optica* **4**, 124–128 (2017).
225. K. M. Kennedy, S. Es'haghian, L. Chin, R. A. McLaughlin, D. D. Sampson, and B. F. Kennedy, "Optical palpation: optical coherence tomography-based tactile imaging using a compliant sensor," *Opt. Lett.* **39**, 3014–3017 (2014).
226. W. M. Allen, P. Wijesinghe, B. F. Dessauvage, B. Latham, C. M. Saunders, and B. F. Kennedy, "Optical palpation for the visualization of tumor in human breast tissue," *J. Biophotonics* **12**, e201800180 (2019).
227. R. W. Sanderson, Q. Fang, A. Curatolo, W. Adams, D. D. Lakhiani, H. M. Ismail, K. Y. Foo, B. F. Dessauvage, B. Latham, C. Yeomans, C. M. Saunders, and B. F. Kennedy, "Camera-based optical palpation," *Sci. Rep.* **10**, 15951 (2020).
228. R. S. Dahiya, G. Metta, M. Valle, and G. Sandini, "Tactile Sensing—From Humans to Humanoids," *IEEE Trans. Robot.* **26**, 1–20 (2010).
229. M. I. Tiwana, S. J. Redmond, and N. H. Lovell, "A review of tactile sensing technologies with applications in biomedical engineering," *Sens. Actuators Phys.* **179**, 17–31 (2012).
230. V. Egorov, H. van Raalte, and A. P. Sarvazyan, "Vaginal Tactile Imaging," *IEEE Trans. Biomed. Eng.* **57**, 1736–1744 (2010).
231. P. S. Wellman, R. D. Howe, N. Dewagan, M. A. Cundari, E. Dalton, and K. A. Kern, "Tactile imaging: a method for documenting breast masses," in *Proceedings of the First Joint BMES/EMBS Conference. 1999 IEEE Engineering in Medicine and Biology 21st Annual Conference and the 1999 Annual Fall Meeting of the Biomedical Engineering Society (Cat. N (1999), Vol. 2, p. 1131 vols.2-*
232. P. S. Wellman, E. P. Dalton, D. Krag, K. A. Kern, and R. D. Howe, "Tactile Imaging of Breast Masses: First Clinical Report," *Arch. Surg.* **136**, 204–208 (2001).
233. C. Pan, L. Dong, G. Zhu, S. Niu, R. Yu, Q. Yang, Y. Liu, and Z. L. Wang, "High-resolution electroluminescent imaging of pressure distribution using a piezoelectric nanowire LED array," *Nat. Photonics* **7**, 752–758 (2013).
234. S. Es'haghian, K. M. Kennedy, P. Gong, D. D. Sampson, R. A. McLaughlin, and B. F. Kennedy, "Optical palpation *in vivo*: imaging human skin lesions using mechanical contrast," *J. Biomed. Opt.* **20**, 016013 (2015).
235. F. Irgens, *Continuum Mechanics* (Springer Science & Business Media, 2008).
236. P. Wijesinghe, L. Chin, A. A. Oberai, and B. F. Kennedy, "Tissue mechanics," in *Optical Coherence Elastography: Imaging Tissue Mechanics on the Micro-Scale* (AIP Publishing, 2021).
237. M. M. Doyley, "Model-based elastography: a survey of approaches to the inverse elasticity problem," *Phys. Med. Biol.* **57**, R35 (2012).
238. A. F. Bower, *Applied Mechanics of Solids* (CRC Press, 2009).
239. L. Dong, P. Wijesinghe, J. T. Dantuono, D. D. Sampson, P. R. T. Munro, B. F. Kennedy, and A. A. Oberai, "Quantitative Compression Optical Coherence Elastography as an Inverse Elasticity Problem," *IEEE J. Sel. Top. Quantum Electron.* **22**, 277–287 (2016).
240. Y. Qiu, Y. Wang, Y. Xu, N. Chandra, J. Haorah, B. Hubbi, B. J. Pfister, and X. Liu, "Quantitative optical coherence elastography based on fiber-optic probe for in situ measurement of tissue mechanical properties," *Biomed. Opt. Express* **7**, 688–700 (2016).

241. P. Wijesinghe, R. A. McLaughlin, D. D. Sampson, and B. F. Kennedy, "Parametric imaging of viscoelasticity using optical coherence elastography," *Phys. Med. Biol.* **60**, 2293–2307 (2015).
242. E. E. Konofagou, T. P. Harrigan, J. Ophir, and T. A. Krouskop, "Poroelastography: imaging the poroelastic properties of tissues," *Ultrasound Med. Biol.* **27**, 1387–1397 (2001).
243. Y. Qiu, F. R. Zaki, N. Chandra, S. A. Chester, and X. Liu, "Nonlinear characterization of elasticity using quantitative optical coherence elastography," *Biomed. Opt. Express* **7**, 4702–4710 (2016).
244. K. A. Athanasiou and R. M. Natoli, *Introduction to Continuum Biomechanics* (Morgan & Claypool Publishers, 2008).
245. R. W. Ogden, "Nonlinear elasticity, anisotropy, material stability and residual stresses in soft tissue," in *Biomechanics of Soft Tissue in Cardiovascular Systems* (Springer, 2014).
246. M. A. Meyers, P.-Y. Chen, A. Y.-M. Lin, and Y. Seki, "Biological materials: Structure and mechanical properties," *Prog. Mater. Sci.* **53**, 1–206 (2008).
247. U. G. K. Wegst and M. F. Ashby, "The mechanical efficiency of natural materials," *Philos. Mag.* **84**, 2167–2186 (2004).
248. M. Stolz, R. Raiteri, A. U. Daniels, M. R. VanLandingham, W. Baschong, and U. Aebi, "Dynamic Elastic Modulus of Porcine Articular Cartilage Determined at Two Different Levels of Tissue Organization by Indentation-Type Atomic Force Microscopy," *Biophys. J.* **86**, 3269–3283 (2004).
249. M. Plodinec, M. Loparic, C. A. Monnier, E. C. Obermann, R. Zanetti-Dallenbach, P. Oertle, J. T. Hyotyla, U. Aebi, M. Bentires-Alj, R. Y. H. Lim, and C.-A. Schoenenberger, "The nanomechanical signature of breast cancer," *Nat. Nanotechnol.* **7**, 757–765 (2012).
250. A. Fuhrmann, J. R. Staunton, V. Nandakumar, N. Banyai, P. C. W. Davies, and R. Ros, "AFM stiffness nanotomography of normal, metaplastic and dysplastic human esophageal cells," *Phys Biol* **11** (2011).
251. S. E. Cross, Y.-S. Jin, J. Rao, and J. K. Gimzewski, "Nanomechanical analysis of cells from cancer patients," *Nat. Nanotechnol.* **2**, 780–783 (2007).
252. A. Nowicki and K. Dobruch-Sobczak, "Introduction to ultrasound elastography," *J. Ultrason.* **16**, 113–124 (2016).
253. D. T. Butcher, T. Alliston, and V. M. Weaver, "A tense situation: forcing tumour progression," *Nat. Rev. Cancer* **9**, 108–122 (2009).
254. T. A. Krouskop, T. M. Wheeler, F. Kallel, B. S. Garra, and T. Hall, "Elastic Moduli of Breast and Prostate Tissues under Compression," *Ultrason. Imaging* **20**, 260–274 (1998).
255. W. Drexler, U. Morgner, R. K. Ghanta, F. X. Kärtner, J. S. Schuman, and J. G. Fujimoto, "Ultrahigh-resolution ophthalmic optical coherence tomography," *Nat. Med.* **7**, 502–507 (2001).
256. A. M. Hagag, S. S. Gao, Y. Jia, and D. Huang, "Optical coherence tomography angiography: Technical principles and clinical applications in ophthalmology," *Taiwan J. Ophthalmol.* **7**, 115–129 (2017).
257. A. J. Tatham and F. A. Medeiros, "Detecting Structural Progression in Glaucoma with Optical Coherence Tomography," *Ophthalmology* **124**, S57–S65 (2017).
258. T. Yonetsu, B. E. Bouma, K. Kato, J. G. Fujimoto, and I.-K. Jang, "Optical Coherence Tomography," *Circ. J. advpub*, (2013).
259. H. G. Bezerra, M. A. Costa, G. Guagliumi, A. M. Rollins, and D. I. Simon, "Intracoronary Optical Coherence Tomography: A Comprehensive Review," *JACC Cardiovasc. Interv.* **2**, 1035–1046 (2009).
260. L. J. Diaz-Sandoval, B. E. Bouma, G. J. Tearney, and I.-K. Jang, "Optical coherence tomography as a tool for percutaneous coronary interventions," *Catheter. Cardiovasc. Interv.* **65**, 492–496 (2005).

261. L. P. Hariri, G. T. Bonnema, K. Schmidt, A. M. Winkler, V. Korde, K. D. Hatch, J. R. Davis, M. A. Brewer, and J. K. Barton, "Laparoscopic optical coherence tomography imaging of human ovarian cancer," *Gynecol. Oncol.* **114**, 188–194 (2009).
262. H. Pahlevaninezhad, M. Khorasaninejad, Y.-W. Huang, Z. Shi, L. P. Hariri, D. C. Adams, V. Ding, A. Zhu, C.-W. Qiu, F. Capasso, and M. J. Suter, "Nano-optic endoscope for high-resolution optical coherence tomography in vivo," *Nat. Photonics* **12**, 540–547 (2018).
263. J. M. Schmitt, "Optical coherence tomography (OCT): a review," *IEEE J. Sel. Top. Quantum Electron.* **5**, 1205–1215 (1999).
264. D. Huang, E. A. Swanson, C. P. Lin, J. S. Schuman, W. G. Stinson, W. Chang, M. R. Hee, T. Flotte, K. Gregory, C. A. Puliafito, and J. G. Fujimoto, "Optical Coherence Tomography," *Science* **254**, 1178–1181 (1991).
265. A. G. Podoleanu, "Optical coherence tomography," *Br. J. Radiol.* **78**, 976–988 (2005).
266. C. Boudoux, *Fundamentals of Biomedical Optics: From Light Interactions with Cells to Complex Imaging Systems*, First (Pollux, 2017).
267. M. L. Gabriele, G. Wollstein, H. Ishikawa, J. Xu, J. Kim, L. Kagemann, L. S. Folio, and J. S. Schuman, "Three dimensional optical coherence tomography imaging: Advantages and advances," *Prog. Retin. Eye Res.* **29**, 556–579 (2010).
268. A. F. Fercher, C. K. Hitzenberger, G. Kamp, and S. Y. El-Zaiat, "Measurement of intraocular distances by backscattering spectral interferometry," *Opt. Commun.* **117**, 43–48 (1995).
269. M. A. Choma, M. V. Sarunic, C. Yang, and J. A. Izatt, "Sensitivity advantage of swept source and Fourier domain optical coherence tomography," *Opt. Express* **11**, 2183–2189 (2003).
270. J. F. de Boer, B. Cense, B. H. Park, M. C. Pierce, G. J. Tearney, and B. E. Bouma, "Improved signal-to-noise ratio in spectral-domain compared with time-domain optical coherence tomography," *Opt. Lett.* **28**, 2067–2069 (2003).
271. N. Nassif, B. Cense, B. H. Park, S. H. Yun, T. C. Chen, B. E. Bouma, G. J. Tearney, and J. F. de Boer, "In vivo human retinal imaging by ultrahigh-speed spectral domain optical coherence tomography," *Opt. Lett.* **29**, 480–482 (2004).
272. T. C. Chen, B. Cense, M. C. Pierce, N. Nassif, B. H. Park, S. H. Yun, B. R. White, B. E. Bouma, G. J. Tearney, and J. F. de Boer, "Spectral Domain Optical Coherence Tomography: Ultra-high Speed, Ultra-high Resolution Ophthalmic Imaging," *Arch. Ophthalmol.* **123**, 1715–1720 (2005).
273. R. F. Spaide, H. Koizumi, and M. C. Pozzoni, "Enhanced Depth Imaging Spectral-Domain Optical Coherence Tomography," *Am. J. Ophthalmol.* **146**, 496–500 (2008).
274. S. H. Yun, G. J. Tearney, J. F. de Boer, N. Iftimia, and B. E. Bouma, "High-speed optical frequency-domain imaging," *Opt. Express* **11**, 2953–2963 (2003).
275. S. R. Chinn, E. A. Swanson, and J. G. Fujimoto, "Optical coherence tomography using a frequency-tunable optical source," *Opt. Lett.* **22**, 340–342 (1997).
276. R. Huber, M. Wojtkowski, and J. G. Fujimoto, "Fourier Domain Mode Locking (FDML): A new laser operating regime and applications for optical coherence tomography," *Opt. Express* **14**, 3225–3237 (2006).
277. J. F. Bille, *High Resolution Imaging in Microscopy and Ophthalmology: New Frontiers in Biomedical Optics* (Springer, 2019).
278. M. S. Hepburn, K. Y. Foo, L. Chin, R. A. Leitgeb, and B. F. Kennedy, "Optical coherence tomography," in *Optical Coherence Elastography: Imaging Tissue Mechanics on the Micro-Scale* (AIP Publishing, [To be published]).
279. J. Fujimoto and W. Drexler, "Introduction to Optical Coherence Tomography," in *Optical Coherence Tomography: Technology and Applications*, W. Drexler and J. G.

- Fujimoto, eds., *Biological and Medical Physics, Biomedical Engineering* (Springer, 2008), pp. 1–45.
280. J. Rogowska, N. A. Patel, J. G. Fujimoto, and M. E. Brezinski, "Optical coherence tomographic elastography technique for measuring deformation and strain of atherosclerotic tissues," *Heart* **90**, 556–562 (2004).
 281. R. C. Chan, A. H. Chau, W. C. Karl, S. Nadkarni, A. S. Khalil, N. Iftimia, M. Shishkov, G. J. Tearney, M. R. Kaazempur-Mofrad, and B. E. Bouma, "OCT-based arterial elastography: robust estimation exploiting tissue biomechanics," *Opt. Express* **12**, 4558 (2004).
 282. A. Curatolo, B. Kennedy, D. Sampson, and T. R. Hilman, "Speckle in optical coherence tomography," *Adv. Biophotonics Tissue Opt. Sect.* 212–277 (2014).
 283. D. D. Duncan and S. J. Kirkpatrick, "Processing algorithms for tracking speckle shifts in optical elastography of biological tissues," *J. Biomed. Opt.* **6**, 418–426 (2001).
 284. C. Sun, B. A. Standish, B. Vuong, X.-Y. Wen, and V. X. D. Yang, "Digital image correlation–based optical coherence elastography," *J. Biomed. Opt.* **18**, 121515 (2013).
 285. A. Nahas, M. Bauer, S. Roux, and A. C. Boccara, "3D static elastography at the micrometer scale using Full Field OCT," *Biomed. Opt. Express* **4**, 2138–2149 (2013).
 286. B. F. Kennedy, T. R. Hillman, A. Curatolo, and D. D. Sampson, "Speckle reduction in optical coherence tomography by strain compounding," *Opt. Lett.* **35**, 2445–2447 (2010).
 287. B. F. Kennedy, S. H. Koh, R. A. McLaughlin, K. M. Kennedy, P. R. T. Munro, and D. D. Sampson, "Strain estimation in phase-sensitive optical coherence elastography," *Biomed. Opt. Express* **3**, 1865–1879 (2012).
 288. R. K. Wang, S. Kirkpatrick, and M. Hinds, "Phase-sensitive optical coherence elastography for mapping tissue microstrains in real time," *Appl. Phys. Lett.* **90**, 164105 (2007).
 289. R. K. Wang, Z. Ma, and S. J. Kirkpatrick, "Tissue Doppler optical coherence elastography for real time strain rate and strain mapping of soft tissue," *Appl. Phys. Lett.* **89**, 144103 (2006).
 290. S. J. Kirkpatrick, R. K. Wang, and D. D. Duncan, "OCT-based elastography for large and small deformations," *Opt. Express* **14**, 11585–11597 (2006).
 291. B. H. Park, M. C. Pierce, B. Cense, S.-H. Yun, M. Mujat, G. J. Tearney, B. E. Bouma, and J. F. de Boer, "Real-time fiber-based multi-functional spectral-domain optical coherence tomography at 1.3 μm ," *Opt. Express* **13**, 3931–3944 (2005).
 292. W. Qi, R. Li, T. Ma, J. Li, K. Kirk Shung, Q. Zhou, and Z. Chen, "Resonant acoustic radiation force optical coherence elastography," *Appl. Phys. Lett.* **103**, 103704 (2013).
 293. G. Lan, K. V. Larin, S. Aglyamov, and M. D. Twa, "Characterization of natural frequencies from nanoscale tissue oscillations using dynamic optical coherence elastography," *Biomed. Opt. Express* **11**, 3301–3318 (2020).
 294. P.-C. Huang, E. J. Chaney, R. L. Shelton, and S. A. Boppart, "Magnetomotive Displacement of the Tympanic Membrane Using Magnetic Nanoparticles: Toward Enhancement of Sound Perception," *IEEE Trans. Biomed. Eng.* **65**, 2837–2846 (2018).
 295. S. G. Adie, X. Liang, B. F. Kennedy, R. John, D. D. Sampson, and S. A. Boppart, "Spectroscopic optical coherence elastography," *Opt. Express* **18**, 25519–25534 (2010).
 296. L. Chin, P. Wijesinghe, A. L. Oldenburg, and B. F. Kennedy, "Optical Coherence Elastography Techniques," in *Optical Coherence Elastography*, AIP Publishing Books (AIP Publishing LLC, 2021), pp. 6-1-6–34.

297. C. Li, G. Guan, X. Cheng, Z. Huang, and R. K. Wang, "Quantitative elastography provided by surface acoustic waves measured by phase-sensitive optical coherence tomography," *Opt. Lett.* **37**, 722–724 (2012).
298. J. A. Mulligan, G. R. Untracht, S. N. Chandrasekaran, C. N. Brown, and S. G. Adie, "Emerging Approaches for High-Resolution Imaging of Tissue Biomechanics With Optical Coherence Elastography," *IEEE J. Sel. Top. Quantum Electron.* **22**, 246–265 (2016).
299. M. Singh, C. Wu, C.-H. Liu, J. Li, A. Schill, A. Nair, and K. V. Larin, "Phase-sensitive optical coherence elastography at 1.5 million A-Lines per second," *Opt. Lett.* **40**, 2588–2591 (2015).
300. S. Song, W. Wei, B.-Y. Hsieh, I. Pelivanov, T. T. Shen, M. O'Donnell, and R. K. Wang, "Strategies to improve phase-stability of ultrafast swept source optical coherence tomography for single shot imaging of transient mechanical waves at 16 kHz frame rate," *Appl. Phys. Lett.* **108**, 191104 (2016).
301. B. F. Kennedy, R. A. McLaughlin, K. M. Kennedy, L. Chin, A. Curatolo, A. Tien, B. Latham, C. M. Saunders, and D. D. Sampson, "Optical coherence micro-elastography: mechanical-contrast imaging of tissue microstructure," *Biomed. Opt. Express* **5**, 2113–2124 (2014).
302. K. M. Kennedy, C. Ford, B. F. Kennedy, M. B. Bush, and D. D. Sampson, "Analysis of mechanical contrast in optical coherence elastography," *J. Biomed. Opt.* **18**, 121508 (2013).
303. W. M. Allen, K. M. Kennedy, Q. Fang, L. Chin, A. Curatolo, L. Watts, R. Zilkens, S. L. Chin, B. F. Dessauvague, B. Latham, C. M. Saunders, and B. F. Kennedy, "Wide-field quantitative micro-elastography of human breast tissue," *Biomed. Opt. Express* **9**, 1082 (2018).
304. K. Y. Foo, K. M. Kennedy, R. Zilkens, W. M. Allen, Q. Fang, R. W. Sanderson, J. Anstie, B. F. Dessauvague, B. Latham, C. M. Saunders, L. Chin, and B. F. Kennedy, "Optical palpation for tumor margin assessment in breast-conserving surgery," *Biomed. Opt. Express* **12**, 1666–1682 (2021).
305. B. Krajancich, A. Curatolo, Q. Fang, R. Zilkens, B. F. Dessauvague, C. M. Saunders, and B. F. Kennedy, "Handheld optical palpation of turbid tissue with motion-artifact correction," *Biomed. Opt. Express* **10**, 226–241 (2019).
306. J. Landercasper, D. Attai, D. Atisha, P. Beitsch, L. Bosserman, J. Boughey, J. Carter, S. Edge, S. Feldman, J. Froman, C. Greenberg, C. Kaufman, M. Morrow, B. Pockaj, M. Silverstein, L. Solin, A. Staley, F. Vicini, L. Wilke, W. Yang, and H. Cody, "Toolbox to Reduce Lumpectomy Reoperations and Improve Cosmetic Outcome in Breast Cancer Patients: The American Society of Breast Surgeons Consensus Conference," *Ann. Surg. Oncol.* **22**, 3174–3183 (2015).
307. J. Landercasper, E. Whitacre, A. C. Degnim, and M. Al-Hamadani, "Reasons for Re-Excision After Lumpectomy for Breast Cancer: Insight from the American Society of Breast Surgeons MasterySM Database," *Ann. Surg. Oncol.* **21**, 3185–3191 (2014).
308. L. E. McCahill, R. M. Single, E. J. Aiello Bowles, H. S. Feigelson, T. A. James, T. Barney, J. M. Engel, and A. A. Onitilo, "Variability in Reexcision Following Breast Conservation Surgery," *JAMA* **307**, 467–475 (2012).
309. C. C. Kimball, C. I. Nichols, and J. G. Vose, "The Payer and Patient Cost Burden of Open Breast Conserving Procedures Following Percutaneous Breast Biopsy," *Breast Cancer Basic Clin. Res.* **12**, 1178223418777766 (2018).
310. L. N. Metcalfe, A. M. Zysk, K. S. Yemul, L. K. Jacobs, E. E. Oker, H. R. Underwood, and A. M. Thompson, "Beyond the Margins—Economic Costs and Complications Associated With Repeated Breast-Conserving Surgeries," *JAMA Surg.* **152**, 1084–1086 (2017).

311. K. Esbona, Z. Li, and L. G. Wilke, "Intraoperative Imprint Cytology and Frozen Section Pathology for Margin Assessment in Breast Conservation Surgery: A Systematic Review," *Ann. Surg. Oncol.* **19**, 3236–3245 (2012).
312. M. R. Decker, A. Trentham-Dietz, N. K. Loconte, H. B. Neuman, M. A. Smith, R. S. Punglia, C. C. Greenberg, and L. G. Wilke, "The Role of Intraoperative Pathologic Assessment in the Surgical Management of Ductal Carcinoma In Situ," *Ann. Surg. Oncol.* **23**, 2788–2794 (2016).
313. J. K. Harness, A. E. Giuliano, B. A. Pockaj, and E. Downs-Kelly, "Margins: A Status Report from the Annual Meeting of the American Society of Breast Surgeons," *Ann. Surg. Oncol.* **21**, 3192–3197 (2014).
314. C. L. Miller, "Comparison of intra-operative specimen mammography to standard specimen mammography for excision of non-palpable breast lesions: a randomized trial," *Breast Cancer Res Treat* **7** (2016).
315. D. Rhee, B. Pockaj, N. Wasif, C.-C. Stucky, V. Pizzitola, M. Giurescu, B. Patel, J. McCarthy, and R. Gray, "Operative outcomes of conventional specimen radiography versus in-operating room specimen radiography in radioactive seed-localized segmental mastectomies," *Am. J. Surg.* **215**, 151–154 (2018).
316. P. D. Britton, L. I. Sonoda, A. K. Yamamoto, B. Koo, E. Soh, and A. Goud, "Breast surgical specimen radiographs: How reliable are they?," *Eur. J. Radiol.* **79**, 245–249 (2011).
317. D. M. Layfield, D. J. May, R. I. Cutress, C. Richardson, A. Agrawal, M. Wise, and C. Yiangou, "The effect of introducing an in-theatre intra-operative specimen radiography (IOSR) system on the management of palpable breast cancer within a single unit," *The Breast* **21**, 459–463 (2012).
318. N. M. Krekel, M. H. Haloua, A. M. Lopes Cardozo, R. H. de Wit, A. M. Bosch, L. M. de Widt-Levert, S. Muller, H. van der Veen, E. Bergers, E. S. de Lange de Klerk, S. Meijer, and M. P. van den Tol, "Intraoperative ultrasound guidance for palpable breast cancer excision (COBALT trial): a multicentre, randomised controlled trial," *Lancet Oncol.* **14**, 48–54 (2013).
319. M. Ramos, J. C. Díaz, T. Ramos, R. Ruano, M. Aparicio, M. Sancho, and J. M. González-Orús, "Ultrasound-guided excision combined with intraoperative assessment of gross macroscopic margins decreases the rate of reoperations for non-palpable invasive breast cancer," *The Breast* **22**, 520–524 (2013).
320. M. Ahmed and M. Douek, "Intra-operative ultrasound versus wire-guided localization in the surgical management of non-palpable breast cancers: systematic review and meta-analysis," *Breast Cancer Res. Treat.* **140**, 435–446 (2013).
321. O. Olsha, D. Shemesh, M. Carmon, O. Sibirsky, R. Abu Dalo, L. Rivkin, and I. Ashkenazi, "Resection Margins in Ultrasound-Guided Breast-Conserving Surgery," *Ann. Surg. Oncol.* **18**, 447–452 (2011).
322. I. Pappo, R. Spector, A. Schindel, S. Morgenstern, J. Sandbank, L. T. Leider, S. Schneebaum, S. Lelcuk, and T. Karni, "Diagnostic Performance of a Novel Device for Real-Time Margin Assessment in Lumpectomy Specimens," *J. Surg. Res.* **160**, 277–281 (2010).
323. F. Schnabel, S. K. Boolbol, M. Gittleman, T. Karni, L. Tafra, S. Feldman, A. Police, N. B. Friedman, S. Karlan, D. Holmes, S. C. Willey, M. Carmon, K. Fernandez, S. Akbari, J. Harness, L. Guerra, T. Frazier, K. Lane, R. M. Simmons, A. Estabrook, and T. Allweis, "A Randomized Prospective Study of Lumpectomy Margin Assessment with Use of MarginProbe in Patients with Nonpalpable Breast Malignancies," *Ann. Surg. Oncol.* **21**, 1589–1595 (2014).
324. L. E. Lamberts, M. Koch, J. S. de Jong, A. L. L. Adams, J. Glatz, M. E. G. Kranendonk, A. G. T. T. van Scheltinga, L. Jansen, J. de Vries, M. N. L. Hooge, C. P. Schröder, A. Jorritsma-Smit, M. D. Linssen, E. de Boer, B. van der Vegt, W. B. Nagengast, S. G. Elias, S. Oliveira, A. J. Witkamp, W. P. T. M. Mali, E. V. der Wall,

- P. J. van Diest, E. G. E. de Vries, V. Ntziachristos, and G. M. van Dam, "Tumor-Specific Uptake of Fluorescent Bevacizumab–IRDye800CW Microdosing in Patients with Primary Breast Cancer: A Phase I Feasibility Study," *Clin. Cancer Res.* **23**, 2730–2741 (2017).
325. Q. R. J. G. Tummers, F. P. R. Verbeek, B. E. Schaafsma, M. C. Boonstra, J. R. van der Vorst, G.-J. Liefers, C. J. H. van de Velde, J. V. Frangioni, and A. L. Vahrmeijer, "Real-time intraoperative detection of breast cancer using near-infrared fluorescence imaging and Methylene Blue," *Eur. J. Surg. Oncol. EJSO* **40**, 850–858 (2014).
326. J. T. Unkart, S. L. Chen, I. L. Wapnir, J. E. González, A. Harootunian, and A. M. Wallace, "Intraoperative Tumor Detection Using a Ratiometric Activatable Fluorescent Peptide: A First-in-Human Phase 1 Study," *Ann. Surg. Oncol.* **24**, 3167–3173 (2017).
327. M. J. Whitley, D. M. Cardona, A. L. Lazarides, I. Spasojevic, J. M. Ferrer, J. Cahill, C.-L. Lee, M. Snuderl, D. G. Blazer, E. S. Hwang, R. A. Greenup, P. J. Mosca, J. K. Mito, K. C. Cuneo, N. A. Larrier, E. K. O'Reilly, R. F. Riedel, W. C. Eward, D. B. Strasfeld, D. Fukumura, R. K. Jain, W. D. Lee, L. G. Griffith, M. G. Bawendi, D. G. Kirsch, and B. E. Brigman, "A mouse-human phase 1 co-clinical trial of a protease-activated fluorescent probe for imaging cancer," *Sci. Transl. Med.* **8**, 320ra4–320ra4 (2016).
328. Y. "Winston" Wang, N. P. Reder, S. Kang, A. K. Glaser, Q. Yang, M. A. Wall, S. H. Javid, S. M. Dintzis, and J. T. C. Liu, "Raman-Encoded Molecular Imaging with Topically Applied SERS Nanoparticles for Intraoperative Guidance of Lumpectomy," *Cancer Res.* **77**, 4506–4516 (2017).
329. J. Q. Brown, T. M. Bydlon, S. A. Kennedy, M. L. Caldwell, J. E. Gallagher, M. Junker, L. G. Wilke, W. T. Barry, J. Geradts, and N. Ramanujam, "Optical Spectral Surveillance of Breast Tissue Landscapes for Detection of Residual Disease in Breast Tumor Margins," *PLOS ONE* **8**, 14 (2013).
330. E. Kho, L. L. de Boer, K. K. V. de Vijver, F. van Duijnhoven, M.-J. T. F. D. V. Peeters, H. J. C. M. Sterenborg, and T. J. M. Ruers, "Hyperspectral Imaging for Resection Margin Assessment during Cancer Surgery," *Clin. Cancer Res.* **25**, 3572–3580 (2019).
331. D. W. Shipp, E. A. Rakha, A. A. Koloydenko, R. D. Macmillan, I. O. Ellis, and I. Notingher, "Intra-operative spectroscopic assessment of surgical margins during breast conserving surgery," *Breast Cancer Res.* **20**, 69 (2018).
332. S. J. Erickson-Bhatt, R. M. Nolan, N. D. Shemonski, S. G. Adie, J. Putney, D. Darga, D. T. McCormick, A. J. Cittadine, A. M. Zysk, M. Marjanovic, E. J. Chaney, G. L. Monroy, F. A. South, K. A. Cradock, Z. G. Liu, M. Sundaram, P. S. Ray, and S. A. Boppart, "Real-time Imaging of the Resection Bed Using a Handheld Probe to Reduce Incidence of Microscopic Positive Margins in Cancer Surgery," *Cancer Res.* **75**, 3706–3712 (2015).
333. R. Ha, L. C. Friedlander, H. Hibshoosh, C. Hendon, S. Feldman, S. Ahn, H. Schmidt, M. K. Akens, M. Fitzmaurice, B. C. Wilson, and V. L. Mango, "Optical Coherence Tomography: A Novel Imaging Method for Post-lumpectomy Breast Margin Assessment—A Multi-reader Study," *Acad. Radiol.* **25**, 279–287 (2018).
334. X. Yao, Y. Gan, E. Chang, H. Hibshoosh, S. Feldman, and C. Hendon, "Visualization and tissue classification of human breast cancer images using ultrahigh-resolution OCT," *Lasers Surg. Med.* **49**, 258–269 (2017).
335. A. M. Zysk, K. Chen, E. Gabrielson, L. Tafra, E. A. May Gonzalez, J. K. Canner, E. B. Schneider, A. J. Cittadine, P. Scott Carney, S. A. Boppart, K. Tsuchiya, K. Sawyer, and L. K. Jacobs, "Intraoperative Assessment of Final Margins with a Handheld Optical Imaging Probe During Breast-Conserving Surgery May Reduce the Reoperation Rate: Results of a Multicenter Study," *Ann. Surg. Oncol.* **22**, 3356–3362 (2015).

336. B. F. Kennedy, R. A. McLaughlin, K. M. Kennedy, L. Chin, P. Wijesinghe, A. Curatolo, A. Tien, M. Ronald, B. Latham, C. M. Saunders, and D. D. Sampson, "Investigation of Optical Coherence Microelastography as a Method to Visualize Cancers in Human Breast Tissue," *Cancer Res.* **75**, 3236–3245 (2015).
337. L. Scolaro, R. A. McLaughlin, B. F. Kennedy, C. M. Saunders, and D. D. Sampson, "A review of optical coherence tomography in breast cancer," *Photonics Lasers Med.* **3**, 225–240 (2014).
338. C. Zhou, D. W. Cohen, Y. Wang, H.-C. Lee, A. E. Mondelblatt, T.-H. Tsai, A. D. Aguirre, J. G. Fujimoto, and J. L. Connolly, "Integrated Optical Coherence Tomography and Microscopy for Ex Vivo Multiscale Evaluation of Human Breast Tissues," *Cancer Res.* **70**, 10071–10079 (2010).
339. B. W. Maloney, D. M. M. Iii, B. W. Pogue, K. D. Paulsen, W. A. W. M.d, and R. J. B. M.d, "Review of methods for intraoperative margin detection for breast conserving surgery," *J. Biomed. Opt.* **23**, 100901 (2018).
340. M. P. McEvoy, J. Landercasper, H. R. Naik, and S. Feldman, "Update of the American Society of Breast Surgeons Toolbox to address the lumpectomy reoperation epidemic," *Gland Surg.* **7**, 536–553 (2018).
341. M. Plodinec, M. Loparic, C. A. Monnier, E. C. Obermann, R. Zanetti-Dallenbach, P. Oertle, J. T. Hyotyla, U. Aebi, M. Bentires-Alj, R. Y. H. Lim, and C.-A. Schoenenberger, "The nanomechanical signature of breast cancer," *Nat. Nanotechnol.* **7**, 757–765 (2012).
342. S. M. Dua, R. J. Gray, and M. Keshtgar, "Strategies for localisation of impalpable breast lesions," *The Breast* **20**, 246–253 (2011).
343. H. Xu, T. Varghese, J. Jiang, and J. A. Zagzebski, "In Vivo Classification of Breast Masses Using Features Derived From Axial-Strain and Axial-Shear Images," *Ultrason. Imaging* **34**, 222–236 (2012).
344. B. F. Kennedy, P. Wijesinghe, and D. D. Sampson, "The emergence of optical elastography in biomedicine," *Nat. Photonics* **11**, 215–221 (2017).
345. W. M. Allen, K. Y. Foo, R. Zilkens, K. M. Kennedy, Q. Fang, L. Chin, B. F. Dessauvage, B. Latham, C. M. Saunders, and B. F. Kennedy, "Clinical feasibility of optical coherence micro- elastography for imaging tumor margins in breast-conserving surgery," **9**, 6331–6349 (2018).
346. K. M. Kennedy, L. Chin, R. A. McLaughlin, B. Latham, C. M. Saunders, D. D. Sampson, and B. F. Kennedy, "Quantitative micro-elastography: imaging of tissue elasticity using compression optical coherence elastography," *Sci. Rep.* **5**, 15538 (2015).
347. W. M. Allen, K. M. Kennedy, Q. Fang, L. Chin, A. Curatolo, L. Watts, R. Zilkens, S. L. Chin, B. F. Dessauvage, B. Latham, C. M. Saunders, and B. F. Kennedy, "Wide-field quantitative micro-elastography of human breast tissue," *Biomed. Opt. Express* **9**, 1082–1096 (2018).
348. C. A. Schneider, W. S. Rasband, and K. W. Eliceiri, "NIH Image to ImageJ: 25 years of image analysis," *Nat. Methods* **9**, 671–675 (2012).
349. O. Assayag, M. Antoine, B. Sigal-Zafrani, M. Riben, F. Harms, A. Burcheri, K. Grieve, E. Dalimier, B. Le Conte de Poly, and C. Boccara, "Large Field, High Resolution Full-Field Optical Coherence Tomography: A Pre-Clinical Study of Human Breast Tissue and Cancer Assessment," *Technol. Cancer Res. Treat.* **13**, 455–468 (2014).
350. F. T. Nguyen, A. M. Zysk, E. J. Chaney, J. G. Kotynek, U. J. Oliphant, F. J. Bellafiore, K. M. Rowland, P. A. Johnson, and S. A. Boppart, "Intraoperative Evaluation of Breast Tumor Margins with Optical Coherence Tomography," *Cancer Res* **8** (2009).

351. K. S. Yemul, A. M. Zysk, A. L. Richardson, K. V. Tangella, and L. K. Jacobs, "Interpretation of Optical Coherence Tomography Images for Breast Tissue Assessment," *Surg. Innov.* **26**, 50–56 (2019).
352. L. D. Brown, T. T. Cai, and A. DasGupta, "Interval Estimation for a Binomial Proportion," *Stat. Theory Appl.* **18** (2021).
353. S. Kim and W. Lee, "Does McNemar's test compare the sensitivities and specificities of two diagnostic tests?," *Stat. Methods Med. Res.* **26**, 142–154 (2017).
354. J. L. Fleiss, "Measuring nominal scale agreement among many raters," *Psychol. Bull.* **76**, 378–382 (1971).
355. M. Sharma, A. H. Beck, J. A. Webster, I. Espinosa, K. Montgomery, S. Varma, M. van de Rijn, K. C. Jensen, and R. B. West, "Analysis of stromal signatures in the tumor microenvironment of ductal carcinoma in situ," *Breast Cancer Res. Treat.* **123**, 397–404 (2010).
356. A. Curatolo, M. Villiger, D. Lorenser, P. Wijesinghe, A. Fritz, B. F. Kennedy, and D. D. Sampson, "Ultrahigh-resolution optical coherence elastography," *Opt. Lett.* **41**, 21–24 (2016).
357. P. Wijesinghe, N. J. Johansen, A. Curatolo, D. D. Sampson, R. Ganss, and B. F. Kennedy, "Ultrahigh-Resolution Optical Coherence Elastography Images Cellular-Scale Stiffness of Mouse Aorta," *Biophys. J.* **113**, 2540–2551 (2017).
358. L. Dong, P. Wijesinghe, J. T. Dantuono, D. D. Sampson, P. R. T. Munro, B. F. Kennedy, and A. A. Oberai, "Quantitative Compression Optical Coherence Elastography as an Inverse Elasticity Problem," *IEEE J. Sel. Top. Quantum Electron.* **22**, 277–287 (2016).
359. L. Dong, P. Wijesinghe, D. D. Sampson, B. F. Kennedy, P. R. T. Munro, and A. A. Oberai, "Volumetric quantitative optical coherence elastography with an iterative inversion method," *Biomed. Opt. Express* **10**, 384–398 (2019).
360. Q. Fang, L. Frewer, P. Wijesinghe, W. M. Allen, L. Chin, J. Hamzah, D. D. Sampson, A. Curatolo, and B. F. Kennedy, "Depth-encoded optical coherence elastography for simultaneous volumetric imaging of two tissue faces," *Opt. Lett.* **42**, 1233–1236 (2017).
361. T. Klein and R. Huber, "High-speed OCT light sources and systems [Invited]," *Biomed. Opt. Express* **8**, 828–859 (2017).
362. Q. Fang, B. Krajancich, L. Chin, R. Zilkens, A. Curatolo, L. Frewer, J. D. Anstie, P. Wijesinghe, C. Hall, B. F. Dessauvage, B. Latham, C. M. Saunders, and B. F. Kennedy, "Handheld probe for quantitative micro-elastography," *Biomed. Opt. Express* **10**, 4034–4049 (2019).
363. C. E. DeSantis, J. Ma, M. M. Gaudet, L. A. Newman, K. D. Miller, A. G. Sauer, A. Jemal, and R. L. Siegel, "Breast cancer statistics, 2019," *CA. Cancer J. Clin.* **69**, 438–451 (2019).
364. E. L. Vos, J. Gaal, C. Verhoef, K. Brouwer, C. H. M. van Deurzen, and L. B. Koppert, "Focally positive margins in breast conserving surgery: Predictors, residual disease, and local recurrence," *Eur. J. Surg. Oncol.* **43**, 1846–1854 (2017).
365. H. Ballal, D. B. Taylor, A. G. Bourke, B. Latham, and C. M. Saunders, "Predictors of re-excision in wire-guided wide local excision for early breast cancer: a Western Australian multi-centre experience," *ANZ J. Surg.* **85**, 540–545 (2015).
366. L. G. Wilke, T. Czechura, C. Wang, B. Lapin, E. Liederbach, D. P. Winchester, and K. Yao, "Repeat Surgery After Breast Conservation for the Treatment of Stage 0 to II Breast Carcinoma: A Report From the National Cancer Data Base, 2004-2010," *JAMA Surg.* **149**, 1296–1305 (2014).
367. J. Landercasper, E. Whitacre, A. C. Degnim, and M. Al-Hamadani, "Reasons for Re-Excision After Lumpectomy for Breast Cancer: Insight from the American Society of Breast Surgeons MasterySM Database," *Ann. Surg. Oncol.* **21**, 3185–3191 (2014).

368. L. E. McCahill, R. M. Single, E. J. A. Bowles, H. S. Feigelson, T. A. James, T. Barney, J. M. Engel, and A. A. Onitilo, "Variability in reexcision following breast conservation surgery," *JAMA J. Am. Med. Assoc.* **307**, 467–475 (2012).
369. R. Jeevan, D. A. Cromwell, M. Trivella, G. Lawrence, O. Kearins, J. Pereira, C. Sheppard, C. M. Caddy, and J. H. P. van der Meulen, "Reoperation rates after breast conserving surgery for breast cancer among women in England: retrospective study of hospital episode statistics," *BMJ* **345**, e4505 (2012).
370. M. S. Moran, S. J. Schnitt, A. E. Giuliano, J. R. Harris, S. A. Khan, J. Horton, S. Klimberg, M. Chavez-MacGregor, G. Freedman, N. Houssami, P. L. Johnson, and M. Morrow, "Society of Surgical Oncology–American Society for Radiation Oncology Consensus Guideline on Margins for Breast-Conserving Surgery With Whole-Breast Irradiation in Stages I and II Invasive Breast Cancer," *Ann. Surg. Oncol.* **21**, 704–716 (2014).
371. E. R. St John, R. Al-Khudairi, H. Ashrafiyan, T. Athanasiou, Z. Takats, D. J. Hadjiminas, A. Darzi, and D. R. Leff, "Diagnostic Accuracy of Intraoperative Techniques for Margin Assessment in Breast Cancer Surgery: A Meta-analysis," *Ann. Surg.* **265**, 300–310 (2017).
372. N. B. Kouzminova, S. Aggarwal, A. Aggarwal, M. D. Allo, and A. Y. Lin, "Impact of initial surgical margins and residual cancer upon re-excision on outcome of patients with localized breast cancer," *Am. J. Surg.* **198**, 771–780 (2009).
373. M. Thill, "MarginProbe®: intraoperative margin assessment during breast conserving surgery by using radiofrequency spectroscopy," *Expert Rev. Med. Devices* **10**, 301–315 (2013).
374. A. Munshi, S. Kakkar, R. Bhutani, R. Jalali, A. Budrukkar, and K. A. Dinshaw, "Factors Influencing Cosmetic Outcome in Breast Conservation," *Clin. Oncol.* **21**, 285–293 (2009).
375. J. J. Keating, C. Fisher, R. Batiste, and S. Singhal, "Advances in Intraoperative Margin Assessment for Breast Cancer," *Curr. Surg. Rep.* **4**, 15 (2016).
376. R. J. Gray, B. A. Pockaj, E. Garvey, and S. Blair, "Intraoperative Margin Management in Breast-Conserving Surgery: A Systematic Review of the Literature," *Ann. Surg. Oncol.* **25**, 18–27 (2018).
377. S. L. Blair, K. Thompson, J. Rococco, V. Malcarne, P. D. Beitsch, and D. W. Ollila, "Attaining Negative Margins in Breast-Conservation Operations: Is There a Consensus among Breast Surgeons?," *J. Am. Coll. Surg.* **209**, 608–613 (2009).
378. R. G. Pleijhuis, M. Graafland, J. de Vries, J. Bart, J. S. de Jong, and G. M. van Dam, "Obtaining Adequate Surgical Margins in Breast-Conserving Therapy for Patients with Early-Stage Breast Cancer: Current Modalities and Future Directions," *Ann. Surg. Oncol.* **16**, 2717–2730 (2009).
379. K. Butler-Henderson, A. H. Lee, R. I. Price, and K. Waring, "Intraoperative assessment of margins in breast conserving therapy: A systematic review," *The Breast* **23**, 112–119 (2014).
380. C. H. Lee and D. Carter, "Detecting residual tumor after excisional biopsy of impalpable breast carcinoma: efficacy of comparing preoperative mammograms with radiographs of the biopsy specimen.," *Am. J. Roentgenol.* **164**, 81–86 (1995).
381. B. W. Maloney, D. M. McClatchy, B. W. Pogue, K. D. Paulsen, W. A. Wells, and R. J. Barth, "Review of methods for intraoperative margin detection for breast conserving surgery," *J. Biomed. Opt.* **23**, 100901 (2018).
382. W. M. Allen, L. Chin, P. Wijesinghe, R. W. Kirk, B. Latham, D. D. Sampson, C. M. Saunders, and B. F. Kennedy, "Wide-field optical coherence micro-elastography for intraoperative assessment of human breast cancer margins," *Biomed. Opt. Express* **7**, 4139–4153 (2016).
383. F. T. Nguyen, A. M. Zysk, E. J. Chaney, J. G. Kotynek, U. J. Oliphant, F. J. Bellafiore, K. M. Rowland, P. A. Johnson, and S. A. Boppart, "Intraoperative

- Evaluation of Breast Tumor Margins with Optical Coherence Tomography," *Cancer Res.* **69**, 8790–8796 (2009).
384. K. M. Kennedy, R. Zilkens, W. M. Allen, K. Y. Foo, Q. Fang, L. Chin, R. W. Sanderson, J. Anstie, P. Wijesinghe, A. Curatolo, H. E. I. Tan, N. Morin, B. Kunjuraman, C. Yeomans, S. L. Chin, H. DeJong, K. Giles, B. F. Dessauvage, B. Latham, C. M. Saunders, and B. F. Kennedy, "Diagnostic Accuracy of Quantitative Micro-Elastography for Margin Assessment in Breast-Conserving Surgery," *Cancer Res.* **80**, 1773–1783 (2020).
385. W. M. Allen, K. M. Kennedy, Q. Fang, L. Chin, A. Curatolo, L. Watts, R. Zilkens, S. L. Chin, B. F. Dessauvage, B. Latham, C. M. Saunders, and B. F. Kennedy, "Wide-field quantitative micro-elastography of human breast tissue," *Biomed. Opt. Express* **9**, 1082–1096 (2018).
386. W. M. Allen, P. Wijesinghe, B. F. Dessauvage, B. Latham, C. M. Saunders, and B. F. Kennedy, "Optical palpation for the visualization of tumor in human breast tissue," *J. Biophotonics* **12**, e201800180 (2019).
387. V. Egorov and A. P. Sarvazyan, "Mechanical Imaging of the Breast," *IEEE Trans. Med. Imaging* **27**, 1275–1287 (2008).
388. Y. Al-Handarish, O. M. Omisore, T. Igbe, S. Han, H. Li, W. Du, J. Zhang, and L. Wang, "A Survey of Tactile-Sensing Systems and Their Applications in Biomedical Engineering," *Adv. Mater. Sci. Eng.* **2020**, 4047937 (2020).
389. M. I. Tiwana, S. J. Redmond, and N. H. Lovell, "A review of tactile sensing technologies with applications in biomedical engineering," *Sens. Actuators Phys.* **179**, 17–31 (2012).
390. K.-S. Sohn, J. Chung, M.-Y. Cho, S. Timilsina, W. B. Park, M. Pyo, N. Shin, K. Sohn, and J. S. Kim, "An extremely simple macroscale electronic skin realized by deep machine learning," *Sci. Rep.* **7**, 11061 (2017).
391. Y. Gao, H. Ota, E. W. Schaler, K. Chen, A. Zhao, W. Gao, H. M. Fahad, Y. Leng, A. Zheng, F. Xiong, C. Zhang, L.-C. Tai, P. Zhao, R. S. Fearing, and A. Javey, "Wearable Microfluidic Diaphragm Pressure Sensor for Health and Tactile Touch Monitoring," *Adv. Mater.* **29**, 1701985 (2017).
392. X. Wang, H. Zhang, L. Dong, X. Han, W. Du, J. Zhai, C. Pan, and Z. L. Wang, "Self-Powered High-Resolution and Pressure-Sensitive Triboelectric Sensor Matrix for Real-Time Tactile Mapping," *Adv. Mater.* **28**, 2896–2903 (2016).
393. K. K. Choi, S. L. Jiang, and Z. Li, "Multifingered robotic hands: contact experiments using tactile sensors," in *Proceedings. 1998 IEEE International Conference on Robotics and Automation (Cat. No.98CH36146)* (1998), Vol. 3, pp. 2268–2273 vol.3.
394. R. S. Dahiya, G. Metta, and M. Valle, "Development of fingertip tactile sensing chips for humanoid robots," in *2009 IEEE International Conference on Mechatronics* (2009), pp. 1–6.
395. K. M. Kennedy, S. Es'haghian, L. Chin, R. A. McLaughlin, D. D. Sampson, and B. F. Kennedy, "Optical palpation: optical coherence tomography-based tactile imaging using a compliant sensor," *Opt. Lett.* **39**, 3014–3017 (2014).
396. S. Es'haghian, K. M. Kennedy, P. Gong, D. D. Sampson, R. A. McLaughlin, and B. F. Kennedy, "Optical palpation in vivo: imaging human skin lesions using mechanical contrast," *J. Biomed. Opt.* **20**, 016013–016013 (2015).
397. M. Plodinec, M. Loparic, C. A. Monnier, E. C. Obermann, R. Zanetti-Dallenbach, P. Oertle, J. T. Hyotyla, U. Aebi, M. Bentières-Alj, R. Y. H. Lim, and C.-A. Schoenenberger, "The nanomechanical signature of breast cancer," *Nat. Nanotechnol.* **7**, 757–765 (2012).
398. M. Morrow, E. A. Strom, L. W. Bassett, D. D. Dershaw, B. Fowble, A. Giuliano, J. R. Harris, F. O'Malley, S. J. Schnitt, S. E. Singletary, and D. P. Winchester, "Standard for Breast Conservation Therapy in the Management of Invasive Breast Carcinoma," *CA. Cancer J. Clin.* **52**, 277–300 (2002).

399. S. M. Dua, R. J. Gray, and M. Keshtgar, "Strategies for localisation of impalpable breast lesions," *The Breast* **20**, 246–253 (2011).
400. S. T. Philipp, T. Kalisch, T. Wachtler, and H. R. Dinse, "Enhanced tactile acuity through mental states," *Sci. Rep.* **5**, 13549 (2015).
401. J. A. Woods, L. F. Leslie, D. B. Drake, and R. F. Edlich, "Effect of puncture resistant surgical gloves, finger guards, and glove liners on cutaneous sensibility and surgical psychomotor skills," *J. Biomed. Mater. Res.* **33**, 47–51 (1996).
402. K. M. Kennedy, L. Chin, R. A. McLaughlin, B. Latham, C. M. Saunders, D. D. Sampson, and B. F. Kennedy, "Quantitative micro-elastography: imaging of tissue elasticity using compression optical coherence elastography," *Sci. Rep.* **5**, 15538 (2015).
403. D. W. Shipp, E. A. Rakha, A. A. Koloydenko, R. D. Macmillan, I. O. Ellis, and I. Notingher, "Intra-operative spectroscopic assessment of surgical margins during breast conserving surgery," *Breast Cancer Res.* **20**, 69 (2018).
404. A. M. Zysk, K. Chen, E. Gabrielson, L. Tafra, E. A. May Gonzalez, J. K. Canner, E. B. Schneider, A. J. Cittadine, P. Scott Carney, S. A. Boppart, K. Tsuchiya, K. Sawyer, and L. K. Jacobs, "Intraoperative Assessment of Final Margins with a Handheld Optical Imaging Probe During Breast-Conserving Surgery May Reduce the Reoperation Rate: Results of a Multicenter Study," *Ann. Surg. Oncol.* **22**, 3356–3362 (2015).
405. W. M. Allen, K. Y. Foo, R. Zilkens, K. M. Kennedy, Q. Fang, L. Chin, B. F. Dessauvage, B. Latham, C. M. Saunders, and B. F. Kennedy, "Clinical feasibility of optical coherence micro-elastography for imaging tumor margins in breast-conserving surgery," *Biomed. Opt. Express* **9**, 6331–6349 (2018).
406. B. F. Kennedy, K. M. Kennedy, and D. D. Sampson, "A Review of Optical Coherence Elastography: Fundamentals, Techniques and Prospects," *IEEE J. Sel. Top. Quantum Electron.* **20**, 272–288 (2014).
407. A. Sarvazyan, "Mechanical imaging: A new technology for medical diagnostics," *Int. J. Med. Inf.* **49**, 195–216 (1998).
408. K. S. Yemul, A. M. Zysk, A. L. Richardson, K. V. Tangella, and L. K. Jacobs, "Interpretation of Optical Coherence Tomography Images for Breast Tissue Assessment," *Surg. Innov.* **26**, 50–56 (2019).
409. D. Mojahed, R. S. Ha, P. Chang, Y. Gan, X. Yao, B. Angelini, H. Hibshoosh, B. Taback, and C. P. Hendon, "Fully Automated Postlumpectomy Breast Margin Assessment Utilizing Convolutional Neural Network Based Optical Coherence Tomography Image Classification Method," *Acad. Radiol.* **27**, e81–e86 (2019).
410. R. Ha, L. C. Friedlander, H. Hibshoosh, C. Hendon, S. Feldman, S. Ahn, H. Schmidt, M. K. Akens, M. Fitzmaurice, B. C. Wilson, and V. L. Mango, "Optical Coherence Tomography: A Novel Imaging Method for Post-lumpectomy Breast Margin Assessment—A Multi-reader Study," *Acad. Radiol.* **25**, 279–287 (2018).
411. M. Morrow, K. J. Van Zee, L. J. Solin, N. Houssami, M. Chavez-MacGregor, J. R. Harris, J. Horton, S. Hwang, P. L. Johnson, M. L. Marinovich, S. J. Schnitt, I. Wapnir, and M. S. Moran, "Society of Surgical Oncology–American Society for Radiation Oncology–American Society of Clinical Oncology Consensus Guideline on Margins for Breast-Conserving Surgery with Whole-Breast Irradiation in Ductal Carcinoma In Situ," *Ann. Surg. Oncol.* **23**, 3801–3810 (2016).
412. A. A. Sovetsky, A. L. Matveyev, L. A. Matveev, E. V. Gubarkova, A. A. Plekhanov, M. A. Sirotkina, N. D. Gladkova, and V. Y. Zaitsev, "Full-optical method of local stress standardization to exclude nonlinearity-related ambiguity of elasticity estimation in compressional optical coherence elastography," *Laser Phys. Lett.* **17**, 065601 (2020).

413. P. Wijesinghe, D. D. Sampson, and B. F. Kennedy, "Computational optical palpation: a finite-element approach to micro-scale tactile imaging using a compliant sensor," *J. R. Soc. Interface* **14**, 20160878 (2017).
414. M. R. Ford, W. J. Dupps Jr, A. M. Rollins, A. S. Roy, and Z. Hu, "Method for optical coherence elastography of the cornea," *J. Biomed. Opt.* **16**, 016005 (2011).
415. S. Wang and K. V. Larin, "Noncontact depth-resolved micro-scale optical coherence elastography of the cornea," *Biomed. Opt. Express* **5**, 3807–3821 (2014).
416. H.-J. Ko, W. Tan, R. Stack, and S. A. Boppart, "Optical coherence elastography of engineered and developing tissue," *Tissue Eng.* **12**, 63–73 (2006).
417. M. S. Hepburn, P. Wijesinghe, L. G. Major, J. Li, A. Mowla, C. Astell, H. W. Park, Y. Hwang, Y. S. Choi, and B. F. Kennedy, "Three-dimensional imaging of cell and extracellular matrix elasticity using quantitative micro-elastography," *Biomed. Opt. Express* **11**, 867–884 (2020).
418. J. C. Mankins, *Technology Readiness Levels [White Paper]* (NASA, 1995), p. 5.
419. G. Lan, S. R. Aglyamov, K. V. Larin, and M. D. Twa, "In Vivo Human Corneal Shear-wave Optical Coherence Elastography," *Optom. Vis. Sci. Off. Publ. Am. Acad. Optom.* **98**, 58–63 (2021).
420. G. Lan and M. D. Twa, "Theory and design of Schwarzschild scan objective for Optical Coherence Tomography," *Opt. Express* **27**, 5048–5064 (2019).
421. V. S. De Stefano, M. R. Ford, I. Seven, and W. J. Dupps, "Depth-Dependent Corneal Biomechanical Properties in Normal and Keratoconic Subjects by Optical Coherence Elastography," *Transl. Vis. Sci. Technol.* **9**, 4–4 (2020).
422. A. Ramier, A. M. Eltony, Y. Chen, F. Clouser, J. S. Birkenfeld, A. Watts, and S.-H. Yun, "In vivo measurement of shear modulus of the human cornea using optical coherence elastography," *Sci. Rep.* **10**, 17366 (2020).
423. S. Kling, "Optical coherence elastography by ambient pressure modulation for high-resolution strain mapping applied to patterned cross-linking," *J. R. Soc. Interface* **17**, 20190786 (2020).
424. C.-H. Liu, S. Assassi, S. Theodore, C. Smith, A. Schill, M. Singh, S. Aglyamov, C. Mohan, and K. V. Larin, "Translational optical coherence elastography for assessment of systemic sclerosis," *J. Biophotonics* **12**, e201900236 (2019).
425. K. M. Kennedy, R. Zilkens, W. M. Allen, K. Y. Foo, Q. Fang, L. Chin, R. W. Sanderson, J. Anstie, P. Wijesinghe, A. Curatolo, H. E. I. Tan, N. Morin, B. Kunjuraman, C. Yeomans, S. L. Chin, H. DeJong, K. Giles, B. F. Dessauvague, B. Latham, C. M. Saunders, and B. F. Kennedy, "Diagnostic Accuracy of Quantitative Micro-Elastography for Margin Assessment in Breast-Conserving Surgery," *Cancer Res.* **80**, 1773–1783 (2020).
426. Q. Fang, L. Frewer, R. Zilkens, B. Krajancich, A. Curatolo, L. Chin, K. Y. Foo, D. D. Lakhiani, R. W. Sanderson, P. Wijesinghe, J. D. Anstie, B. F. Dessauvague, B. Latham, C. M. Saunders, and B. F. Kennedy, "Handheld volumetric manual compression-based quantitative microelastography," *J. Biophotonics* **13**, e201960196 (2020).
427. L. Bartolini, F. Feroldi, M. Slaman, J. J. A. Weda, J. F. de Boer, P. van Zuijlen, and D. Iannuzzi, "Toward clinical elastography of dermal tissues: A medical device to probe skin's elasticity through suction, with subsurface imaging via optical coherence tomography," *Rev. Sci. Instrum.* **91**, 074101 (2020).
428. A. Parmar, G. Sharma, S. Sharma, and K. Singh, "Portable Optical Coherence Elastography System With Flexible and Phase Stable Common Path Optical Fiber Probe," *IEEE Access* **9**, 56041–56048 (2021).
429. X. Liu, F. R. Zaki, H. Wu, C. Wang, and Y. Wang, "Temporally and spatially adaptive Doppler analysis for robust handheld optical coherence elastography," *Biomed. Opt. Express* **9**, 3335–3353 (2018).

430. Y. Qu, T. Ma, Y. He, M. Yu, J. Zhu, Y. Miao, C. Dai, P. Patel, K. K. Shung, Q. Zhou, and Z. Chen, "Miniature probe for mapping mechanical properties of vascular lesions using acoustic radiation force optical coherence elastography," *Sci. Rep.* **7**, 4731 (2017).
431. R. Bu, S. Balakrishnan, H. Price, C. Zdanski, S. Mitran, and A. L. Oldenburg, "Localized compliance measurement of the airway wall using anatomic optical coherence elastography," *Opt. Express* **27**, 16751–16766 (2019).
432. C. Robertson, S.-W. Lee, Y.-C. Ahn, S. Mahon, Z. Chen, M. Brenner, and S. C. George, "Investigating in vivo airway wall mechanics during tidal breathing with optical coherence tomography," *J. Biomed. Opt.* **16**, 106011 (2011).
433. W. Qi, R. Li, T. Ma, K. Kirk Shung, Q. Zhou, and Z. Chen, "Confocal acoustic radiation force optical coherence elastography using a ring ultrasonic transducer," *Appl. Phys. Lett.* **104**, 123702 (2014).
434. K. Nakamura, R. Isago, and D. Koyama, "Endoscopic optical coherence elastography using acoustic radiation force and a vibrating fiber," in (2012), pp. 247–250.
435. A. B. Karpiouk, D. J. VanderLaan, K. V. Larin, and S. Y. Emelianov, "Integrated optical coherence tomography and multielement ultrasound transducer probe for shear wave elasticity imaging of moving tissues," *J. Biomed. Opt.* **23**, 105006 (2018).
436. Q. Fang, A. Curatolo, P. Wijesinghe, Y. L. Yeow, J. Hamzah, P. B. Noble, K. Karnowski, D. D. Sampson, R. Ganss, J. K. Kim, W. M. Lee, and B. F. Kennedy, "Ultrahigh-resolution optical coherence elastography through a micro-endoscope: towards in vivo imaging of cellular-scale mechanics," *Biomed. Opt. Express* **8**, 5127–5138 (2017).
437. K. M. Kennedy, B. F. Kennedy, R. A. McLaughlin, and D. D. Sampson, "Needle optical coherence elastography for tissue boundary detection," *Opt. Lett.* **37**, 2310–2312 (2012).
438. K. M. Kennedy, R. A. McLaughlin, B. F. Kennedy, A. Tien, B. Latham, C. M. Saunders, and D. D. Sampson, "Needle optical coherence elastography for the measurement of microscale mechanical contrast deep within human breast tissues," *J. Biomed. Opt.* **18**, 121510 (2013).
439. S. Latus, C. Otte, M. Schlüter, J. Rehra, K. Bizon, H. Schulz-Hildebrandt, T. Saathoff, G. Hüttmann, and A. Schlaefel, "An Approach for Needle Based Optical Coherence Elastography Measurements," in *Medical Image Computing and Computer-Assisted Intervention – MICCAI 2017*, M. Descoteaux, L. Maier-Hein, A. Franz, P. Jannin, D. L. Collins, and S. Duchesne, eds., Lecture Notes in Computer Science (Springer International Publishing, 2017), pp. 655–663.
440. R. W. Sanderson, A. Curatolo, P. Wijesinghe, L. Chin, and B. F. Kennedy, "Finger-mounted quantitative micro-elastography," *Biomed. Opt. Express* **10**, 1760 (2019).
441. W. M. Allen, L. Chin, P. Wijesinghe, R. W. Kirk, B. Latham, D. D. Sampson, C. M. Saunders, and B. F. Kennedy, "Wide-field optical coherence micro-elastography for intraoperative assessment of human breast cancer margins," *Biomed. Opt. Express* **7**, 4139–4153 (2016).
442. B. F. Kennedy, R. A. McLaughlin, K. M. Kennedy, L. Chin, P. Wijesinghe, A. Curatolo, A. Tien, M. Ronald, B. Latham, C. M. Saunders, and D. D. Sampson, "Investigation of Optical Coherence Microelastography as a Method to Visualize Cancers in Human Breast Tissue," *Cancer Res.* **75**, 3236–3245 (2015).
443. G. Lan, B. Gu, K. V. Larin, and M. D. Twa, "Clinical Corneal Optical Coherence Elastography Measurement Precision: Effect of Heartbeat and Respiration," *Transl. Vis. Sci. Technol.* **9**, 3–3 (2020).
444. G. Lan, M. Singh, K. V. Larin, and M. D. Twa, "Common-path phase-sensitive optical coherence tomography provides enhanced phase stability and detection sensitivity for dynamic elastography," *Biomed. Opt. Express* **8**, 5253–5266 (2017).

445. B. F. Kennedy, R. A. McLaughlin, K. M. Kennedy, L. Chin, A. Curatolo, A. Tien, B. Latham, C. M. Saunders, and D. D. Sampson, "Optical coherence micro-elastography: mechanical-contrast imaging of tissue microstructure," *Biomed. Opt. Express* **5**, 2113 (2014).
446. K. Schwarzschild, *Untersuchungen zur geometrischen Optik: Einleitung in die Feblerttheorie optischer Instrumente auf Grund des Eikonalebegriffs. I* (Weidmann, 1905).
447. Ł. Ambroziński, S. Song, S. J. Yoon, I. Pelivanov, D. Li, L. Gao, T. T. Shen, R. K. Wang, and M. O'Donnell, "Acoustic micro-tapping for non-contact 4D imaging of tissue elasticity," *Sci. Rep.* **6**, 38967 (2016).
448. Y. Zhou, Y. Wang, M. Shen, Z. Jin, Y. Chen, Y. Zhou, J. Qu, and D. Zhu, "In vivo evaluation of corneal biomechanical properties by optical coherence elastography at different cross-linking irradiances," *J. Biomed. Opt.* **24**, (2019).
449. S. Wang, K. V. Larin, J. Li, S. Vantipalli, R. K. Manapuram, S. Aglyamov, S. Emelianov, and M. D. Twa, "A focused air-pulse system for optical-coherence-tomography-based measurements of tissue elasticity," *Laser Phys. Lett.* **10**, 075605 (2013).
450. M. Singh, J. Li, S. Vantipalli, Z. Han, K. V. Larin, and M. D. Twa, "Optical coherence elastography for evaluating customized riboflavin/UV-A corneal collagen crosslinking," *J. Biomed. Opt.* **22**, 091504 (2017).
451. J. J. Pitre, M. A. Kirby, D. S. Li, T. T. Shen, R. K. Wang, M. O'Donnell, and I. Pelivanov, "Nearly-incompressible transverse isotropy (NITI) of cornea elasticity: model and experiments with acoustic micro-tapping OCE," *Sci. Rep.* **10**, 12983 (2020).
452. M. Singh, J. Li, Z. Han, C. Wu, S. R. Aglyamov, M. D. Twa, and K. V. Larin, "Investigating Elastic Anisotropy of the Porcine Cornea as a Function of Intraocular Pressure With Optical Coherence Elastography," *J. Refract. Surg. Thorofare NJ* 1995 **32**, 562–567 (2016).
453. L. Yuting, C. Li, K. Zhou, G. Guan, P. L. Appleton, S. Lang, D. McGloin, Z. Huang, and G. Nabi, "Microscale characterization of prostate biopsies tissues using optical coherence elastography and second harmonic generation imaging," *Lab. Invest.* **98**, 380–390 (2018).
454. B. F. Kennedy, T. R. Hillman, R. A. McLaughlin, B. C. Quirk, and D. D. Sampson, "In vivo dynamic optical coherence elastography using a ring actuator," *Opt. Express* **17**, 21762–21772 (2009).
455. L. Chin, B. Latham, C. M. Saunders, D. D. Sampson, and B. F. Kennedy, "Simplifying the assessment of human breast cancer by mapping a micro-scale heterogeneity index in optical coherence elastography," *J. Biophotonics* **10**, 690–700 (2017).
456. W. M. Allen, K. Y. Foo, R. Zilkens, K. M. Kennedy, Q. Fang, L. Chin, B. F. Dessauvague, B. Latham, C. M. Saunders, and B. F. Kennedy, "Clinical feasibility of optical coherence micro-elastography for imaging tumor margins in breast-conserving surgery," *Biomed. Opt. Express* **9**, 6331 (2018).
457. K. M. Kennedy, L. Chin, P. Wijesinghe, R. A. McLaughlin, B. Latham, D. D. Sampson, C. M. Saunders, and B. F. Kennedy, "Investigation of optical coherence micro-elastography as a method to visualize micro-architecture in human axillary lymph nodes," *BMC Cancer* **16**, 874 (2016).
458. A. A. Sovetsky, A. L. Matveyev, L. A. Matveev, E. V. Gubarkova, A. A. Plekhanov, M. A. Sirotkina, N. D. Gladkova, and V. Y. Zaitsev, "Full-optical method of local stress standardization to exclude nonlinearity-related ambiguity of elasticity estimation in compressional optical coherence elastography," *Laser Phys. Lett.* **17**, 065601 (2020).

459. R. W. Kirk, B. F. Kennedy, D. D. Sampson, and R. A. McLaughlin, "Near Video-Rate Optical Coherence Elastography by Acceleration With a Graphics Processing Unit," *J. Light. Technol.* **33**, 3481–3485 (2015).
460. O. Assayag, K. Grieve, B. Devaux, F. Harms, J. Pallud, F. Chretien, C. Boccara, and P. Varlet, "Imaging of non-tumorous and tumorous human brain tissues with full-field optical coherence tomography," *NeuroImage Clin.* **2**, 549–557 (2013).
461. C. Kut, K. L. Chaichana, J. Xi, S. M. Raza, X. Ye, E. R. McVeigh, F. J. Rodriguez, A. Quiñones-Hinojosa, and X. Li, "Detection of human brain cancer infiltration ex vivo and in vivo using quantitative optical coherence tomography," *Sci. Transl. Med.* **7**, 292ra100-292ra100 (2015).
462. X. Liang, S. G. Adie, R. John, and S. A. Boppart, "Dynamic spectral-domain optical coherence elastography for tissue characterization," *Opt. Express* **18**, 14183–14190 (2010).
463. X. Liu, F. Zaki, and Y. Wang, "Quantitative Optical Coherence Elastography for Robust Stiffness Assessment," *Appl. Sci.* **8**, 1255 (2018).
464. D. N. H. Enomoto, J. R. Mekkes, P. M. M. Bossuyt, R. Hoekzema, and J. D. Bos, "Quantification of cutaneous sclerosis with a skin elasticity meter in patients with generalized scleroderma," *J. Am. Acad. Dermatol.* **35**, 381–387 (1996).
465. H. Dobrev, "Study of human skin mechanical properties by mean of Cutometer," *Folia Med. (Plovdiv)* **44**, 5–10 (2002).
466. T. A. Bowden, V. H. Hooks, and A. R. Mansberger, "Intraoperative gastrointestinal endoscopy," *Ann. Surg.* **191**, 680–687 (1980).
467. Z. Sun, R. J. Winder, B. E. Kelly, P. K. Ellis, P. T. Kennedy, and D. G. Hirst, "Diagnostic Value of CT Virtual Intravascular Endoscopy in Aortic Stent-Grafting," *J. Endovasc. Ther.* **11**, 13–25 (2004).
468. S. I. Rosenberg, H. Silverstein, T. O. Willcox, and M. A. Gordon, "Endoscopy in otology and neurotology," *Am. J. Otol.* **15**, 168–172 (1994).
469. Y. Kawase, Y. Suzuki, F. Ikeno, R. Yoneyama, K. Hoshino, H. Q. Ly, G. T. Lau, M. Hayase, A. C. Yeung, R. J. Hajjar, and I.-K. Jang, "Comparison of nonuniform rotational distortion between mechanical IVUS and OCT using a phantom model," *Ultrasound Med. Biol.* **33**, 67–73 (2007).
470. N. Uribe-Patarroyo and B. E. Bouma, "Rotational distortion correction in endoscopic optical coherence tomography based on speckle decorrelation," *Opt. Lett.* **40**, 5518 (2015).
471. M. C. Antonetti, B. Killelea, and R. Orlando III, "Hand-Assisted Laparoscopic Liver Surgery," *Arch. Surg.* **137**, 407–412 (2002).
472. R. H. Wilkins, "Neurosurgical Classic—XVII," *J. Neurosurg.* **21**, 240–244 (1964).
473. D. Field and J. S. O. Hutchinson, *Field's Anatomy, Palpation, and Surface Markings* (Elsevier Health Sciences, 2006).
474. L. Castera, X. Forns, and A. Alberti, "Non-invasive evaluation of liver fibrosis using transient elastography," *J. Hepatol.* **48**, 835–847 (2008).
475. M. Yin, J. A. Talwalkar, K. J. Glaser, A. Manduca, R. C. Grimm, P. J. Rossman, J. L. Fidler, and R. L. Ehman, "Assessment of Hepatic Fibrosis With Magnetic Resonance Elastography," *Clin. Gastroenterol. Hepatol.* **5**, 1207-1213.e2 (2007).
476. S. Wang and K. V. Larin, "Shear wave imaging optical coherence tomography (SWI-OCT) for ocular tissue biomechanics," *Opt. Lett.* **39**, 41–44 (2014).
477. V. Y. Zaitsev, L. A. Matveev, A. L. Matveyev, G. V. Gelikonov, and V. M. Gelikonov, "Elastographic mapping in optical coherence tomography using an unconventional approach based on correlation stability," *J. Biomed. Opt.* **19**, 021107 (2013).
478. S. Wang, M. Singh, T. T. Tran, J. Leach, S. R. Aglyamov, I. V. Larina, J. F. Martin, and K. V. Larin, "Biomechanical assessment of myocardial infarction using optical coherence elastography," *Biomed. Opt. Express* **9**, 728–742 (2018).

479. G. van Soest, F. Mastik, N. de Jong, and A. F. W. van der Steen, "Robust intravascular optical coherence elastography by line correlations," *Phys. Med. Biol.* **52**, 2445 (2007).
480. A. A. Sovetsky, A. L. Matveyev, L. A. Matveev, D. V. Shabanov, and V. Y. Zaitsev, "Manually-operated compressional optical coherence elastography with effective aperiodic averaging: demonstrations for corneal and cartilaginous tissues," *Laser Phys. Lett.* **15**, 085602 (2018).
481. G. Lamouche, B. F. Kennedy, K. M. Kennedy, C.-E. Bissaillon, A. Curatolo, G. Campbell, V. Pazos, and D. D. Sampson, "Review of tissue simulating phantoms with controllable optical, mechanical and structural properties for use in optical coherence tomography," *Biomed. Opt. Express* **3**, 1381–1398 (2012).
482. E. Tornberg, "Effects of heat on meat proteins – Implications on structure and quality of meat products," *Meat Sci.* **70**, 493–508 (2005).
483. G. J. Lewis and P. P. Purslow, "The strength and stiffness of perimysial connective tissue isolated from cooked beef muscle," *Meat Sci.* **26**, 255–269 (1989).
484. K. Li, R. Nataraj, T. L. Marquardt, and Z.-M. Li, "Directional Coordination of Thumb and Finger Forces during Precision Pinch," *PLoS ONE* **8**, e79400 (2013).
485. P. Wijesinghe, L. Chin, and B. F. Kennedy, "Strain Tensor Imaging in Compression Optical Coherence Elastography," *IEEE J. Sel. Top. Quantum Electron.* 1–1 (2018).
486. T. A. Krouskop, T. M. Wheeler, F. Kallel, B. S. Garra, and T. Hall, "Elastic Moduli of Breast and Prostate Tissues under Compression," *Ultrason. Imaging* **20**, 260–274 (1998).
487. L. Castéra, J. Vergniol, J. Foucher, B. Le Bail, E. Chanteloup, M. Haaser, M. Darriet, P. Couzigou, and V. de Lédinghen, "Prospective comparison of transient elastography, Fibrotest, APRI, and liver biopsy for the assessment of fibrosis in chronic hepatitis C," *Gastroenterology* **128**, 343–350 (2005).
488. P. Wijesinghe, D. D. Sampson, and B. F. Kennedy, "Computational optical palpation: a finite-element approach to micro-scale tactile imaging using a compliant sensor," *J. R. Soc. Interface* **14**, 20160878 (2017).
489. C. D. Lu, M. F. Kraus, B. Potsaid, J. J. Liu, W. Choi, V. Jayaraman, A. E. Cable, J. Hornegger, J. S. Duker, and J. G. Fujimoto, "Handheld ultrahigh speed swept source optical coherence tomography instrument using a MEMS scanning mirror," *Biomed. Opt. Express* **5**, 293–311 (2014).
490. K. H. Kim, B. H. Park, G. N. Maguluri, T. W. Lee, F. J. Rogomentich, M. G. Bancu, B. E. Bouma, J. F. de Boer, and J. J. Bernstein, "Two-axis magnetically-driven MEMS scanning catheter for endoscopic high-speed optical coherence tomography," *Opt. Express* **15**, 18130–18140 (2007).
491. P. H. Tran, D. S. Mukai, M. Brenner, and Z. Chen, "In vivo endoscopic optical coherence tomography by use of a rotational microelectromechanical system probe," *Opt. Lett.* **29**, 1236–1238 (2004).
492. Y. Pan, H. Xie, and G. K. Fedder, "Endoscopic optical coherence tomography based on a microelectromechanical mirror," *Opt. Lett.* **26**, 1966–1968 (2001).
493. B. Y. Yeo, R. A. McLaughlin, R. W. Kirk, and D. D. Sampson, "Enabling freehand lateral scanning of optical coherence tomography needle probes with a magnetic tracking system," *Biomed. Opt. Express* **3**, 1565–1578 (2012).
494. C. E. DeSantis, C. C. Lin, A. B. Mariotto, R. L. Siegel, K. D. Stein, J. L. Kramer, R. Alteri, A. S. Robbins, and A. Jemal, "Cancer treatment and survivorship statistics, 2014," *CA- Cancer J. Clin.* **64**, 252–271 (2014).
495. S. E. Singletary, "Surgical margins in patients with early-stage breast cancer treated with breast conservation therapy," *Am. J. Surg.* **184**, 383–393 (2002).
496. H. Ballal, D. B. Taylor, A. G. Bourke, B. Latham, and C. M. Saunders, "Predictors of re-excision in wire-guided wide local excision for early breast cancer: a Western Australian multi-centre experience," *ANZ J. Surg.* **85**, 540–545 (2015).

497. J. A. Knol, C. S. Marn, I. R. Francis, J. M. Rubin, J. Bromberg, and A. E. Chang, "Comparisons of dynamic infusion and delayed computed tomography, intraoperative ultrasound, and palpation in the diagnosis of liver metastases," *Am. J. Surg.* **165**, 81–88 (1993).
498. T. C. Böttger, W. Weber, J. Beyer, and T. Junginger, "Value of tumor localization in patients with insulinoma," *World J. Surg.* **14**, 107–112 (1990).
499. W. Wieser, B. R. Biedermann, T. Klein, C. M. Eigenwillig, and R. Huber, "Multi-Megahertz OCT: High quality 3D imaging at 20 million A-scans and 4.5 GVoxels per second," *Opt. Express* **18**, 14685–14704 (2010).
500. S. J. Wilson, D. Sellu, A. Uy, and M. A. Jaffer, "Subjective effects of double gloves on surgical performance.," *Ann. R. Coll. Surg. Engl.* **78**, 20–22 (1996).
501. X. Liang, V. Crecea, and S. A. Boppart, "Dynamic optical coherence elastography: a review," *J. Innov. Opt. Health Sci.* **03**, 221–233 (2010).
502. J. F. Greenleaf, M. Fatemi, and M. Insana, "Selected Methods for Imaging Elastic Properties of Biological Tissues," *Annu. Rev. Biomed. Eng.* **5**, 57–78 (2003).
503. Q. S. Li, G. Y. H. Lee, C. N. Ong, and C. T. Lim, "AFM indentation study of breast cancer cells," *Biochem. Biophys. Res. Commun.* **374**, 609–613 (2008).
504. R. Righetti, S. Srinivasan, and J. Ophir, "Lateral resolution in elastography," *Ultrasound Med. Biol.* **29**, 695–704 (2003).
505. A. Manduca, T. E. Oliphant, M. A. Dresner, J. L. Mahowald, S. A. Kruse, E. Amromin, J. P. Felmlee, J. F. Greenleaf, and R. L. Ehman, "Magnetic resonance elastography: Non-invasive mapping of tissue elasticity," *Med. Image Anal.* **5**, 237–254 (2001).
506. X. Liang and S. A. Boppart, "Biomechanical Properties of In Vivo Human Skin From Dynamic Optical Coherence Elastography," *IEEE Trans. Biomed. Eng.* **57**, 953–959 (2010).
507. A. A. Plekhanov, M. A. Sirotkina, A. A. Sovetsky, E. V. Gubarkova, S. S. Kuznetsov, A. L. Matveyev, L. A. Matveev, E. V. Zagaynova, N. D. Gladkova, and V. Y. Zaitsev, "Histological validation of in vivo assessment of cancer tissue inhomogeneity and automated morphological segmentation enabled by Optical Coherence Elastography," *Sci. Rep.* **10**, (2020).
508. J. Margueritat, A. Virgone-Carlotta, S. Monnier, H. Delanoë-Ayari, H. C. Mertani, A. Berthelot, Q. Martinet, X. Dagany, C. Rivière, J.-P. Rieu, and T. Dehoux, "High-Frequency Mechanical Properties of Tumors Measured by Brillouin Light Scattering," *Phys. Rev. Lett.* **122**, 018101 (2019).
509. D. Cherfan, E. E. Verter, S. Melki, T. E. Gisel, F. J. Doyle, G. Scarcelli, S. H. Yun, R. W. Redmond, and I. E. Kochevar, "Collagen Cross-Linking Using Rose Bengal and Green Light to Increase Corneal Stiffness," *Invest. Ophthalmol. Vis. Sci.* **54**, 3426–3433 (2013).
510. A. Curatolo, M. Villiger, D. Lorensen, P. Wijesinghe, A. Fritz, B. F. Kennedy, and D. D. Sampson, "Ultrahigh-resolution optical coherence elastography," *Opt. Lett.* **41**, 21–24 (2016).
511. E. Kress-Rogers and C. J. B. Brimelow, *Instrumentation and Sensors for the Food Industry* (Woodhead Publishing, 2001).
512. V. Y. Zaitsev, A. Dyskin, E. Pasternak, and L. Matveev, "Microstructure-induced giant elastic nonlinearity of threshold origin: Mechanism and experimental demonstration," *EPL Europhys. Lett.* **86**, 44005 (2009).
513. T. Kobayashi, H. Saitoh, N. Fujii, Y. Hoshino, and M. Takanashi, "Porous membrane of polydimethylsiloxane by hydrosilylation cure: Characteristics of membranes having pores formed by hydrogen foams," *J. Appl. Polym. Sci.* **50**, 971–979 (1993).

-
514. S.-J. Choi, T.-H. Kwon, H. Im, D.-I. Moon, D. J. Baek, M.-L. Seol, J. P. Duarte, and Y.-K. Choi, "A Polydimethylsiloxane (PDMS) Sponge for the Selective Absorption of Oil from Water," *ACS Appl. Mater. Interfaces* **3**, 4552–4556 (2011).
515. D. Zhu, S. Handschuh-Wang, and X. Zhou, "Recent progress in fabrication and application of polydimethylsiloxane sponges," *J. Mater. Chem. A* **5**, 16467–16497 (2017).
516. M. Larsson, A. Hill, and J. Duffy, "Suspension Stability; Why Particle Size, Zeta Potential and Rheology are Important," *Annu. Trans. Nord. Rheol. Soc.* **20**, 7 (2012).
517. D. J. Durian, D. A. Weitz, and D. J. Pine, "Multiple Light-Scattering Probes of Foam Structure and Dynamics," *Science* **252**, 686–688 (1991).
518. C. F. Bohren and D. R. Huffman, *Absorption and Scattering of Light by Small Particles* (John Wiley & Sons, 2008).
519. X. Deng, X. Gan, and M. Gu, "Monte Carlo simulation of multiphoton fluorescence microscopic imaging through inhomogeneous tissue-like turbid media," *J. Biomed. Opt.* **8**, 440 (2003).
520. H. C. van de Hulst, *Light Scattering by Small Particles* (Courier Corporation, 1981).
521. A. J. Cox, A. J. DeWeerd, and J. Linden, "An experiment to measure Mie and Rayleigh total scattering cross sections," *Am. J. Phys.* **70**, 620–625 (2002).
522. M. Borovinšek, M. Vesenjak, Y. Higa, K. Shimojima, and Z. Ren, "Characterization of Geometrical Changes of Spherical Advanced Pore Morphology (APM) Foam Elements during Compressive Deformation," *Materials* **12**, (2019).
523. R. A. Smith, M. J. Paulus, J. M. Branning, and P. J. Phillips, "X-Ray Computed Tomography on a Cellular Polysiloxane under Compression," *J. Cell. Plast.* **37**, 231–248 (2001).
524. D. Tscharnuter, M. Jerabek, Z. Major, and R. W. Lang, "Time-dependent poisson's ratio of polypropylene compounds for various strain histories," *Mech. Time-Depend. Mater.* **15**, 15–28 (2011).
525. B. Wang and S. Krause, "Properties of dimethylsiloxane microphases in phase-separated dimethylsiloxane block copolymers," *Macromolecules* **20**, 2201–2208 (1987).
526. A. R. Smith, "Color gamut transform pairs," in *Proceedings of the 5th Annual Conference on Computer Graphics and Interactive Techniques - SIGGRAPH '78* (ACM Press, 1978), pp. 12–19.
527. M. Mooney, "A Theory of Large Elastic Deformation," *J. Appl. Phys.* **11**, 582–592 (1940).
528. R. S. Rivlin and E. K. Rideal, "Large elastic deformations of isotropic materials IV. further developments of the general theory," *Philos. Trans. R. Soc. Lond. Ser. Math. Phys. Sci.* **241**, 379–397 (1948).
529. G. Papazafeiropoulos, M. Muñoz-Calvente, and E. Martínez-Pañeda, "Abaqus2Matlab: A suitable tool for finite element post-processing," *Adv. Eng. Softw.* **105**, 9–16 (2017).
530. M. J. Tapiovaara and R. F. Wagner, "SNR and noise measurements for medical imaging: I. A practical approach based on statistical decision theory," *Phys. Med. Biol.* **38**, 71–92 (1993).
531. A. Curatolo, B. F. Kennedy, and D. D. Sampson, "Structured three-dimensional optical phantom for optical coherence tomography," *Opt. Express* **19**, 19480–19485 (2011).
532. M. S. Hepburn, P. Wijesinghe, L. Chin, and B. F. Kennedy, "Analysis of spatial resolution in phase-sensitive compression optical coherence elastography," *Biomed. Opt. Express* **10**, 1496–1513 (2019).
533. H. Kuhn, "Uniaxial Compression Testing," in *Mechanical Testing and Evaluation* (ASM International, 2000), pp. 143–151.

534. A. L. McKnight, J. L. Kugel, P. J. Rossman, A. Manduca, L. C. Hartmann, and R. L. Ehman, "MR Elastography of Breast Cancer: Preliminary Results," *Am. J. Roentgenol.* **178**, 1411–1417 (2002).
535. Y. Zhang, R. T. Brodell, E. N. Mostow, C. J. Vinyard, and H. Marie, "In vivo skin elastography with high-definition optical videos," *Skin Res. Technol.* **15**, 271–282 (2009).
536. G. Carbone and B. N. J. Persson, "Dewetting at soft viscoelastic interfaces," *J. Chem. Phys.* **121**, 2246–2252 (2004).
537. P. S. Wellman, R. D. Howe, N. Dewagan, M. A. Cundari, E. Dalton, and K. A. Kern, "Tactile imaging: a method for documenting breast masses," in *Proceedings of the First Joint BMES/EMBS Conference* (1999), Vol. 2, pp. 1131–1132.
538. S. M. Hosseini, M. Amiri, S. Najarian, and J. Dargahi, "Application of artificial neural networks for the estimation of tumour characteristics in biological tissues," *Int. J. Med. Robot.* **3**, 235–244 (2007).
539. J.-H. Lee and C.-H. Won, "The Tactile Sensation Imaging System for Embedded Lesion Characterization," *IEEE J. Biomed. Health Inform.* **17**, 452–458 (2013).
540. J. B. Osborn, G. L. Keeney, J. W. Jakub, A. C. Degnim, and J. C. Boughey, "Cost-Effectiveness Analysis of Routine Frozen-Section Analysis of Breast Margins Compared with Reoperation for Positive Margins," *Ann. Surg. Oncol.* **18**, 3204 (2011).
541. T. A. James, S. Harlow, J. Sheehy-Jones, M. Hart, C. Gaspari, M. Stanley, D. Krag, T. Ashikaga, and L. E. McCahill, "Intraoperative Ultrasound Versus Mammographic Needle Localization for Ductal Carcinoma In Situ," *Ann. Surg. Oncol.* **16**, 1164–1169 (2009).
542. B. W. Touchette, S. E. Marcus, and E. C. Adams, "Bulk elastic moduli and solute potentials in leaves of freshwater, coastal and marine hydrophytes. Are marine plants more rigid?," *AoB Plants* **6**, (2014).
543. A. Esteva, B. Kuprel, R. A. Novoa, J. Ko, S. M. Swetter, H. M. Blau, and S. Thrun, "Dermatologist-level classification of skin cancer with deep neural networks," *Nature* **542**, 115–118 (2017).
544. N. Chuchu, Y. Takwoingi, J. Dinnes, R. N. Matin, O. Bassett, J. F. Moreau, S. E. Bayliss, C. Davenport, K. Godfrey, S. O'Connell, A. Jain, F. M. Walter, J. J. Deeks, H. C. Williams, and C. S. C. D. T. A. Group, "Smartphone applications for triaging adults with skin lesions that are suspicious for melanoma," *Cochrane Database Syst. Rev.* (2018).
545. S. L. James, L. R. Lucchesi, C. Bisignano, C. D. Castle, Z. V. Dingels, J. T. Fox, E. B. Hamilton, N. J. Henry, D. McCracken, N. L. S. Roberts, D. O. Sylte, A. Ahmadi, M. B. Ahmed, F. Alahdab, V. Alipour, Z. Andualem, C. A. T. Antonio, J. Arabloo, A. D. Badiye, M. Bagherzadeh, A. Banstola, T. W. Bärnighausen, A. Barzegar, M. Bayati, S. Bhaumik, A. Bijani, G. Bukhman, F. Carvalho, C. S. Crowe, K. Dalal, A. Daryani, M. D. Nasab, H. T. Do, H. P. Do, A. Y. Endries, E. Fernandes, I. Filip, F. Fischer, T. Fukumoto, K. B. B. Gebremedhin, G. G. Gebremeskel, S. A. Gilani, J. A. Haagsma, S. Hamidi, S. Hostiuc, M. Househ, E. U. Igumbor, O. S. Ilesanmi, S. S. N. Irvani, A. U. Jayatilleke, A. Kahsay, N. Kapoor, A. Kasaeian, Y. S. Khader, I. A. Khalil, E. A. Khan, M. Khazae-Pool, Y. Kokubo, A. D. Lopez, M. Madadin, M. Majdan, V. Maled, R. Malekzadeh, N. Manafi, A. Manafi, S. Mangalam, B. B. Massenburg, H. G. Meles, R. G. Menezes, T. J. Meretoja, B. Miazgowski, T. R. Miller, A. Mohammadian-Hafshejani, R. Mohammadpourhodki, S. D. Morrison, I. Negoi, T. H. Nguyen, S. H. Nguyen, C. T. Nguyen, M. R. Nixon, A. T. Olagunju, T. O. Olagunju, J. R. Padubidri, S. Polinder, N. Rabiee, M. Rabiee, A. Radfar, V. Rahimi-Movaghar, S. Rawaf, D. L. Rawaf, A. Rezapour, J. Rickard, E. M. Roro, N. Roy, R. Safari-Faramani, P. Salamati, A. M. Samy, M. Satpathy, M. Sawhney, D. C. Schwebel, S. Senthilkumaran, S. G. Sepanlou, M. Shigematsu, A. Soheili, M. A.

- Stokes, H. R. Tohidinik, B. X. Tran, P. R. Valdez, T. Wijeratne, E. Yisma, Z. Zaidi, M. Zamani, Z.-J. Zhang, S. I. Hay, and A. H. Mokdad, "Epidemiology of injuries from fire, heat and hot substances: global, regional and national morbidity and mortality estimates from the Global Burden of Disease 2017 study," *Inj. Prev. J. Int. Soc. Child Adolesc. Inj. Prev.* **26**, i36–i45 (2020).
546. I. A. Darby, B. Laverdet, F. Bonté, and A. Desmoulière, "Fibroblasts and myofibroblasts in wound healing," *Clin. Cosmet. Investig. Dermatol.* **7**, 301–311 (2014).
547. A. L. Browne, R. Andrews, S. A. Schug, and F. Wood, "Persistent Pain Outcomes and Patient Satisfaction With Pain Management After Burn Injury," *Clin. J. Pain* **27**, 136–145 (2011).
548. H. M. DeJong, M. Phillips, D. W. Edgar, and F. M. Wood, "Patient opinion of scarring is multidimensional: An investigation of the POSAS with confirmatory factor analysis," *Burns* **43**, 58–68 (2017).
549. C. Öster, M. Kildal, and L. Ekselius, "Return to Work After Burn Injury: Burn-Injured Individuals' Perception of Barriers and Facilitators," *J. Burn Care Res.* **31**, 540–550 (2010).
550. M. B. Klein, C. B. Kramer, J. Nelson, F. P. Rivara, N. S. Gibran, and T. Concannon, "Geographic Access to Burn Center Hospitals," *JAMA J. Am. Med. Assoc.* **302**, 1774–1781 (2009).
551. ANZBA, "Burn Units – ANZBA: Australian & New Zealand Burn Association," <https://anzba.org.au/resources/burn-units/>.
552. T. McWilliams, J. Hendricks, D. Twigg, F. Wood, and M. Giles, "Telehealth for paediatric burn patients in rural areas: a retrospective audit of activity and cost savings," *Burns* **42**, 1487–1493 (2016).
553. N. Brusselaers, A. Pirayesh, H. Hoeksema, J. Verbelen, S. Blot, and S. Monstrey, "Burn Scar Assessment: A Systematic Review of Different Scar Scales," *J. Surg. Res.* **164**, e115–e123 (2010).
554. H. Goei, C. H. van der Vlies, W. E. Tuinebreijer, P. P. M. van Zuijlen, E. Middelkoop, and M. E. van Baar, "Predictive validity of short term scar quality on final burn scar outcome using the Patient and Observer Scar Assessment Scale in patients with minor to moderate burn severity," *Burns* **43**, 715–723 (2017).
555. P. S. Powers, S. Sarkar, D. B. Goldgof, C. W. Cruse, and L. V. Tsap, "Scar Assessment: Current Problems and Future Solutions," *J. Burn Care Rehabil.* **20**, 54–60 (1999).
556. L. Forbes-Duchart, S. Marshall, A. Strock, and J. E. Cooper, "Determination of Inter-Rater Reliability in Pediatric Burn Scar Assessment Using a Modified Version of the Vancouver Scar Scale," *J. Burn Care Res.* **28**, 460–467 (2007).
557. A. J. Singer, H. C. Thode, and S. A. McClain, "Development of a Histomorphologic Scale to Quantify Cutaneous Scars after Burns," *Acad. Emerg. Med.* **7**, 1083–1088 (2000).
558. J. M. Rawlins, W. L. Lam, R. O. Karoo, I. L. Naylor, and D. T. Sharpe, "Quantifying Collagen Type in Mature Burn Scars: A Novel Approach Using Histology and Digital Image Analysis," *J. Burn Care Res.* **27**, 60–65 (2006).
559. M. C. T. Bloemen, M. S. van Gerven, M. B. A. van der Wal, P. D. H. M. Verhaegen, and E. Middelkoop, "An objective device for measuring surface roughness of skin and scars," *J. Am. Acad. Dermatol.* **64**, 706–715 (2011).
560. Y. M. Liew, R. A. McLaughlin, F. M. Wood, and D. D. Sampson, "Motion correction of in vivo three-dimensional optical coherence tomography of human skin using a fiducial marker," *Biomed. Opt. Express* **3**, 1774–1786 (2012).
561. S. S. L. Fong, L. K. Hung, and J. C. Y. Cheng, "The cutometer and ultrasonography in the assessment of postburn hypertrophic scar — a preliminary study," *Burns* **23**, S12–S18 (1997).

562. B. M. Willows, M. Ilyas, and A. Sharma, "Laser in the management of burn scars," *Burns* **43**, 1379–1389 (2017).
563. C. Li, G. Guan, Y. Ling, Y. T. Hsu, S. Song, J. T. J. Huang, S. Lang, R. K. Wang, Z. Huang, and G. Nabi, "Detection and characterisation of biopsy tissue using quantitative optical coherence elastography (OCE) in men with suspected prostate cancer," *Cancer Lett.* **357**, 121–128 (2015).
564. V. Y. Zaitsev, A. L. Matveyev, L. A. Matveev, G. V. Gelikonov, A. I. Omelchenko, O. I. Baum, S. E. Avetisov, A. V. Bolshunov, V. I. Siplivy, D. V. Shabanov, A. Vitkin, and E. N. Sobol, "Optical coherence elastography for strain dynamics measurements in laser correction of cornea shape," *J. Biophotonics* **10**, 1450–1463 (2017).
565. S. Es'haghian, K. M. Kennedy, P. Gong, Q. Li, L. Chin, P. Wijesinghe, D. D. Sampson, R. A. McLaughlin, and B. F. Kennedy, "In vivo volumetric quantitative micro-elastography of human skin," *Biomed. Opt. Express* **8**, 2458–2471 (2017).
566. L. Bartolini, F. Feroldi, M. Slaman, J. J. A. Weda, J. F. de Boer, P. van Zuijlen, and D. Iannuzzi, "Toward clinical elastography of dermal tissues: A medical device to probe skin's elasticity through suction, with subsurface imaging via optical coherence tomography," *Rev. Sci. Instrum.* **91**, 074101 (2020).
567. S. J. Kirkpatrick, R. K. Wang, D. D. Duncan, M. Kulesz-Martin, and K. Lee, "Imaging the mechanical stiffness of skin lesions by in vivo acousto-optical elastography," *Opt. Express* **14**, 9770–9779 (2006).
568. J. R. Dixon, "The International Conference on Harmonization Good Clinical Practice Guideline," *Qual. Assur.* **6**, 65–74 (1999).
569. S. Govender and M. Mars, "The use of telehealth services to facilitate audiological management for children: A scoping review and content analysis," *J. Telemed. Telecare* **23**, 392–401 (2017).
570. G. Novara, E. Checcucci, A. Crestani, A. Abrate, F. Esperto, N. Pavan, C. De Nunzio, A. Galfano, G. Giannarini, A. Gregori, G. Liguori, R. Bartoletti, F. Porpiglia, R. M. Scarpa, A. Simonato, C. Trombetta, A. Tubaro, and V. Ficarra, "Telehealth in Urology: A Systematic Review of the Literature. How Much Can Telemedicine Be Useful During and After the COVID-19 Pandemic?," *Eur. Urol.* **78**, 786–811 (2020).
571. A. J. P. Theuwissen, "CMOS image sensors: State-of-the-art," *Solid-State Electron.* **52**, 1401–1406 (2008).
572. C. Pailler-Mattei, S. Bec, and H. Zahouani, "In vivo measurements of the elastic mechanical properties of human skin by indentation tests," *Med. Eng. Phys.* **30**, 599–606 (2008).
573. V. L. Popov, M. Heß, and E. Willert, *Handbook of Contact Mechanics : Exact Solutions of Axisymmetric Contact Problems* (Springer Nature, 2019).
574. Q. Fang, L. Frewer, R. Zilkens, B. Krajancich, A. Curatolo, L. Chin, K. Y. Foo, D. D. Lakhiani, R. W. Sanderson, P. Wijesinghe, J. D. Anstie, B. F. Dessauvage, B. Latham, C. M. Saunders, and B. F. Kennedy, "Handheld volumetric manual compression-based quantitative microelastography," *J. Biophotonics* **13**, e201960196 (2020).
575. J. Zhu, Y. Qu, T. Ma, R. Li, Y. Du, S. Huang, K. K. Shung, Q. Zhou, and Z. Chen, "Imaging and characterizing shear wave and shear modulus under orthogonal acoustic radiation force excitation using OCT Doppler variance method," *Opt. Lett.* **40**, 2099–2102 (2015).
576. Y. Yang, P. O. Bagnaninchi, M. Ahearne, R. K. Wang, and K.-K. Liu, "A novel optical coherence tomography-based micro-indentation technique for mechanical characterization of hydrogels," *J. R. Soc. Interface* **4**, 1169–1173 (2007).
577. M. Marrese, N. Antonovaite, B. K. A. Nelemans, T. H. Smit, and D. Iannuzzi, "Micro-indentation and optical coherence tomography for the mechanical

-
- characterization of embryos: Experimental setup and measurements on chicken embryos," *Acta Biomater.* **97**, 524–534 (2019).
578. D. C. Lin, D. I. Shreiber, E. K. Dimitriadis, and F. Horkay, "Spherical indentation of soft matter beyond the Hertzian regime: numerical and experimental validation of hyperelastic models," *Biomech. Model. Mechanobiol.* **8**, 345 (2008).
579. R. W. Sanderson, Q. Fang, A. Curatolo, A. Taba, H. M. DeJong, F. M. Wood, and B. F. Kennedy, "Smartphone-based optical palpation: towards elastography of skin for telehealth applications," *Biomed. Opt. Express* **12**, 3117–3132 (2021).
580. A. J. Patel, D. Suki, M. A. Hatiboglu, H. Abouassi, W. Shi, D. M. Wildrick, F. F. Lang, and R. Sawaya, "Factors influencing the risk of local recurrence after resection of a single brain metastasis," *J. Neurosurg.* **113**, 181–189 (2010).